5th International Conference

ELMECO-5

ELECTROMAGNETIC DEVICES AND PROCESSES IN ENVIRONMENT PROTECTION

Nałęczów, Poland
September 2005

Conference Proceedings

Institute of Electrical Engineering
& Electrotechnologies

Centre of Excellence for the Application
of Superconducting and Plasma Technologies
in Power Engineering

Lublin University of Technology, Poland

38A Nadbystrzycka St.
20-618 Lublin
Poland
http://ipee.pollub.pl
e-mail: we.ipee.pollub.pl
tel./fax (+48-81) 5384 289, 538 4643

The conference has been supported by the European Commission
within the 5th Framework Programme - ASPPECT No ENK6-CT-2002-80668

5th International Conference
ELECTROMAGNETIC DEVICES AND PROCESSES IN ENVIRONMENT PROTECTION
ELMECO - 5

September 2005

Nałęczów – Poland

Organised by:

Institute of Electrical Engineering and Electrotechnologies
Centre of Excellence for the Application of Superconducting and Plasma Technologies in Power Engineering
Lublin University of Technology, Poland

ISBN

Wydawnictwo Drukarnia Liber

CONTENTS

5th International Conference **ELMECO**
Nałęczów, Poland
September 2005

MODIFICATION OF POLYMER SURFACES USING ATMOSPHERIC PRESSURE BARRIER DISCHARGES

P. Sťahel, V. Buršíková, M. Šíra, Z. Navrátil, P. Kloc and J. Janča

Department of Physical Electronics Masaryk University,
Kotlářská 2, 611 37 Brno, Czech Republic
jan92@physics.muni.cz

ABSTRACT

Plasma deposition at an atmospheric pressure becomes a promising technology due to its economical and ecological advantages. The objective of the present work is the development of a technique for the deposition of thin films, by means of an atmospheric pressure discharge, onto a pulp board surface, with the desired surface energy, permeability and wear resistant surface. The deposition of thin films was carried out by a surface barrier discharge at the atmospheric pressure. The films were deposited from mixtures of C_4F_8 *with nitrogen. The properties of the thin film substrate systems were investigated by means of contact angle measurement and industrial permeability tests. The chemical composition of the films was studied by means of a Fourier transform infrared spectroscopy. The mechanical properties of the films were studied by means of depth sensing indentation tests performed on samples deposited upon glass plate. The surface topographies of coated and uncoated samples were investigated using a scanning electron microscope.*

Keywords: plasma, atmospheric pressure, modification, wettability

INTRODUCTION

Over the past two decades plasma techniques for the surface activation of polymeric materials have been extensively reported (which included the surface treatment of: paper, wood and other cellulose based materials [1 - 5]). Plasma treatment has the advantage of its relative ease of application and it's comparatively ecologicically friendly nature. The treatment enables the modification of the surface properties of polymeric materials in order to increase, or decrease, surface free energy, whilst retaining their useful bulk properties.

The hydroxyl group is the most abundant functional group of the polymeric components of cellulose based materials, followed by other oxygen containing functionalities. The cellulose materials have very high affinity to water, due to the presence of hydroxyl and other polar groups. These characteristics can be the cause several disadvantageous factors, such as: weathering degradation, biological degradation or swelling. Considerable work has been done in the plasma treatment of cellulose based materials in recent years in order to protect their surface from water penetration. The majority of applications were carried out at reduced pressures e.g. [1-3], where the spatially homogeneous low-temperature plasma can be easily generated and brought into direct contact with the treated surfaces. However, the use of expensive vacuum systems, necessitated by batch processing, has discouraged the application of low-pressure plasmas on a larger industrial scale in the treatment of low-cost materials. Thus it is apparent that such low-pressure plasma systems cannot be utilized for standard paper production lines. Atmospheric-pressure plasma processes offer several advantages for the modification of low-cost cellulose based materials: costly vacuum equipment is not necessary, processing times are reduced, and plasma modification is simpler in a low pressure plasma reactor.

Recently, atmospheric corona or silent discharge devices have been mainly used in the surface treatment of polymeric materials. In these cases the needed plasma conditions are achieved only in small volume plasma channels, termed "streamers", developing perpendicularly to the material’s surface. As a consequence of which, the plasma is h as a very limited contact with the surface, resulting in low processing speeds, typically in the order of 1 m/min. Moreover, the localised arcing(?) may result in the formation of pinholes in the treated material, because plasma channels and arcing are an intrinsic phenomenon associated with this type of the discharge. Disadvantages of corona and silent discharges can be eliminated using atmospheric pressure glow discharge (APGD). APGD is very sensitive to gas purity and to the optimisation of electrode arrangement, these factors limiting its application [7]. A good compromise between low pressure systems and APGD is the atmospheric pressure surface barrier discharge (SD). The objective of the present project is to develop techniques for surface modification of cellulose based materials using SD [8].

The surface barrier discharge is the one alternative discharge, which enables the elimination of the above listed disadvantages of the standard barrier discharge treatments.

EXPERIMENTAL

The deposition of thin films was carried out by the barrier surface discharge at the atmospheric pressure with the operation frequency of 5 kHz. The surface discharge was created on the surface of an insulating glass plate, which was fully covered with metal electrode on one side.

On the other side of the glass plate a metal electrode was placed, which consisted of 9 connected rotating rods with 9 mm spacings (the rods being 6 cm in length). The whole arrangement was placed in a deposition chamber. Paper strips were drawn through the chamber between the metal electrodes and the glass insulator plate at a controlled speed. The surface power density was kept to 1.5 W/cm^2 in all cases. In this study, the deposition time was constant, in all cases, at 90s.

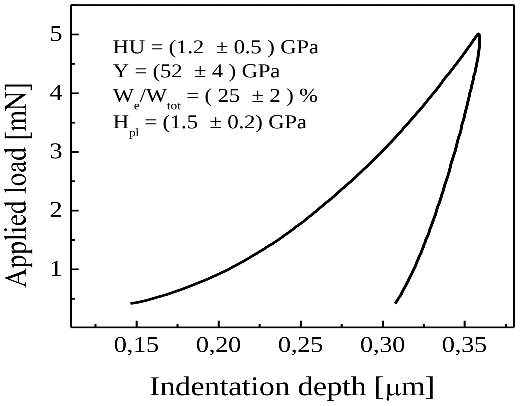

Fig. 1. Load - penetration curve obtained by microhardness measurements on thin film deposited from C_4F_8 and nitrogen mixture on the glass substrate

The films were deposited from different mixtures of oktafluorcyclobutane (C_4F_8) with nitrogen. Filter paper was used as a substrate because of its similar properties to pulp. The discharge was studied by means of the optical emission spectroscopy. The spectra emitted by the discharge were recorded by means of the Jobin –Yvon TRIAX 550 monochromator, with the liquid nitrogen cooled CCD detector.

The total surface free energy of the film was investigated by means of the sessile drop technique using the Surface Energy Evaluation System (SEE System), developed by our research team. The contact angles were measured directly from the images of the solid-liquid meniscus of a liquid drop set on the film, taken with CCD camera. The surface free energy of the deposited films was calculated according Lifshitz-Van der Waals/acid-base approach, proposed by Van Oss, Good and Chaudury [5]. This method enables the determination of the electron-acceptor and electron-donor parameters of the surface tension. The total surface tension is a sum of its apolar and polar components:

$$\gamma = \gamma^{LW} + \gamma^{AB}, \tag{1}$$

where LW indicates the total apolar (dispersive) Lifshitz-Van der Walls interaction and AB refers to the acid-base, or electron-acceptor/ electron-donor interaction according to Lewis.

The surface free energy can be calculated according to the Young-Dupré equation expressed in the terms of acid component γ^+ (acceptor effect) and basic component γ^- (donor effect):

$$(1+\cos\theta_i)\gamma_i = 2\left(\sqrt{\gamma_i^{LW}\gamma_j^{LW}} + \sqrt{\gamma_i^+\gamma_j^-} + \sqrt{\gamma_i^-\gamma_j^+}\right), \tag{2}$$

where i refers to the liquid and j refers to the solid material. The values can be determined from the contact angle measurement with three liquids of which two must have a polar component. The polar component is given by

$$\gamma^{AB} = 2\sqrt{\gamma^+\gamma^-} \tag{3}$$

The wetting properties were studied by means of industrial permeability tests. The permeability was measured as the time necessary for the penetration of 5 ml of the testing liquid through the sample to special wettable paper ERT FF3. This measurement is consistent with the norm ISO 9073-8:1995.

The mechanical properties were studied by means of the depth sensing indentation technique using a Fischerscope H100 tester. In the case of the mechanical tests, polycarbonate or glass plates were used as the substrate. The morphology of the paper surface before and after deposition was observed using a Philips SEM 505 scanning electron microscope.

Examples of the load-penetration curve of thin film deposited from the mixture of C_4F_8 and nitrogen is shown in Fig. 1. HU is the universal hardness, $Y=E/(1-\nu^2)$ is the indentation elastic modulus, where E is the Young´s modulus and ν is the Poisson´s ratio, W_{tot} is the total indentation work and We is its elasticity factor, H_{pl} is the plastic hardness. The studied film was about 0,6 μm thick and was deposited on a glass substrate.

RESULTS AND DISCUSSION

The fluorinated ("teflon-like") materials have been known for along time to posses the lowest surface energies and, therefore the lowest wettability of any class of known materials [9,10]. For example, CF_4 [11] or fluortrimethylsilane [12] was used in order to create highly hydrophobic natural polymeric surfaces in low pressure r.f. discharges on several differing cellulose based surfaces.

We report here on the formation of fluorinated "Teflon-like" hydrophobic films deposited from octafluorbutane in order to protect the papers, of several types, surface against water penetration. A typical spectrum of the discharge created in mixture of nitrogen and C_4F_8 is shown in Figure 2.

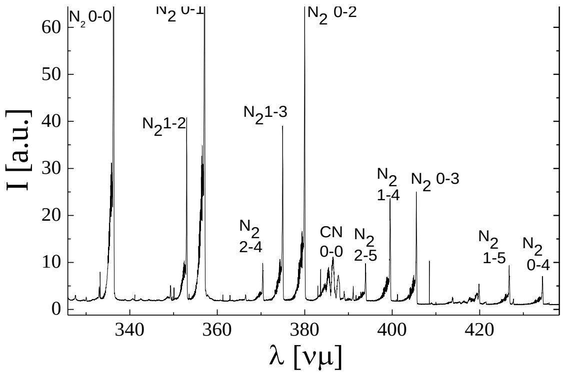

Fig. 2. The emission spectrum of the surface discharge in nitrogen with the admixture of C_4F_8

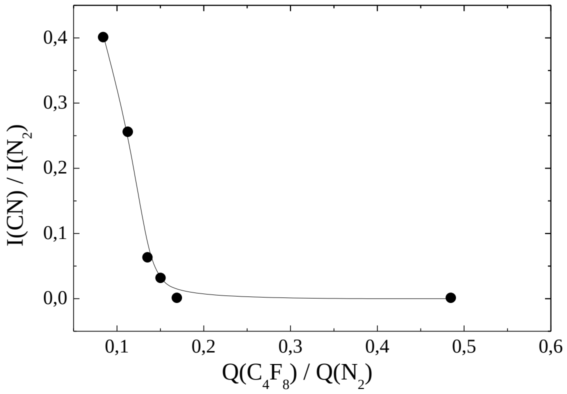

Fig. 3. The ratio of integrated intensities of CN and N_2 bands for different flow of C_4F_8 to N_2

The spectra consist of the molecular bands of second positive system of nitrogen (C $^3\Pi_u \rightarrow$ B $^3\Pi_g$). The spectrum is plotted in the range 300 - 500 nm, because only the second spectral order was registered in excess of 500 nm. When octafluorbutane was mixed into the nitrogen, intensive bands of CN violet system ($^2\Pi \rightarrow {}^2\Sigma$) at 388 nm and 422 nm were observed. Intensity of N_2 and CN system depends on the octafluorbutane to nitrogen flow rate ratio Q_{C4F8}/Q_{N2}. Therefore integrated intensity of the CN band at 388 nm and integrated intensity of N_2 system was calculated. The ratio of integrated intensities of CN and N_2 bands as a function of C_4F_8 to nitrogen flow rate ratio Q_{C4F8}/Q_{N2} is shown in Figure 3. The CN/N_2 ratio increases with decreasing C_4F_8 concentration.

Tab. 1. Examples of the deposition conditions together with the results of the permeability test and total surface free energy

sample	Q_{C4F8} [slm]	Q_{N2} [slm]	penetration time [s]	γ^{tot} [mJ/m^2]
1	0	0	3	52
2	2	0	20	45
3	2	1	38	42.5
4	2	2	1300	10.4
5	2	3	18000	8.5
6	2	4	50000	8.2
7	2	6	50000	6.0
8	2	8	50000	6.5
9	2	10	50000	8.8
10	2	15	50000	9.2
11	2	20	50000	12.3
12	0.5	20	50000	18.2

In Tab. 1 the deposition conditions, together with the results of water penetration tests and total surface energies, are given.

Vibrational temperature was calculated from the bands of the second positive system of nitrogen N_2 0-2, N_2 1-3 and N_2 2-4. The value of the vibrational temperature varied only minimally with the flow rate of the octafluorbutane admixed to the pure nitrogen, its value being approximately 2100 K in all cases.

The water permeability of coated paper increases when the ratio of Q_{C4F8}/Q_{N2} increases. The water permeability has similar evolution with ratio of integrated intensities of CN/N_2 and evolution of free surface energy.

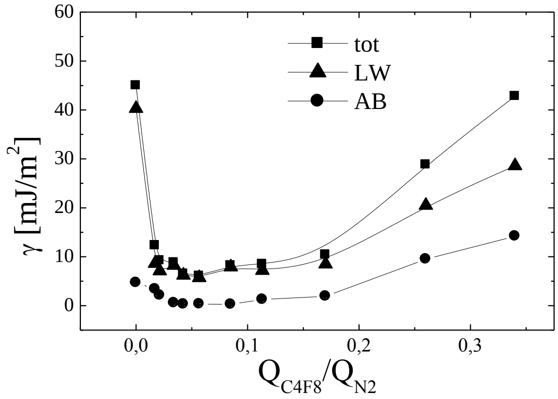

Fig. 4. The dependence of the coating total surface free energy γ^{tot} and its apolar γ^{LW}, polar γ^{AB}components on the C_4F_8 to N_2 flow rate ratio

The evolution of surface free energy and its polar and dispersive components of coatings as a function of flow rate ratio Q_{C4F8}/Q_{N2} is shown in Figure 4. The acid base model was used for evaluation of free surface energy. The first point at 0 represents uncoated paper. The surface energy of coated papers decreases with flow rate ratio. The total surface energy and its components initially decreases and then slightly increases with increasing flow rate ratio Q_{C4F8}/Q_{N2}. The surface energy and its components show similar behaviour as the CN/N_2 ratio and the permeability factor. The acid and basic component of the polar element of free surface energy is not plotted for better clarity of the figure.

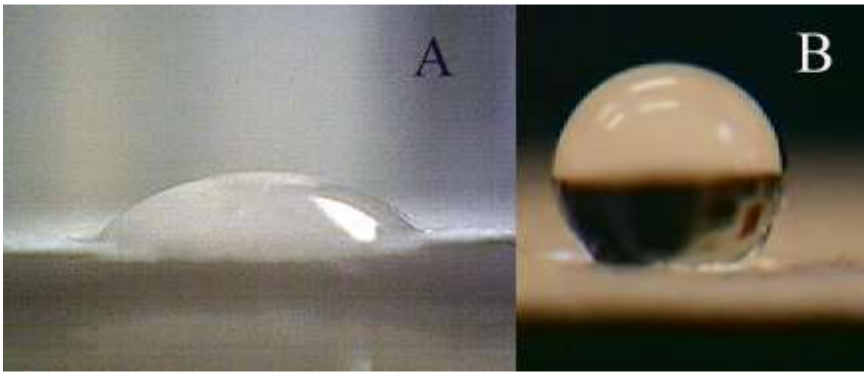

Fig. 5. The image of the uncoated paper substrate (A) and coated filter paper (B)

The Figure 5 shows the images of the water drop set on the coated and uncoated substrate. In the case of uncoated paper the contact angle is at approx. 40^o, however, after deposition, the water contact angle increased to 135^o.

CONCLUSION

Highly hydrophobic thin films were prepared using a new deposition technique based on the atmospheric pressure surface barrier discharge. The thin films were prepared from a mixture of oktafluorcyclobutane C_4F_8 with nitrogen. The water contact angle with the paper surface was increased from 46.3^o to approx. (87-144^o). This correlates with a decrease in the surface energy from 52 to 9 mJ/m^2. The water permeability of coated paper was negligible even after a one day period of testing.

ACKNOWLEDGEMENT

This work has been supported by Grant Agency of Czech Republic, contract No. 202/05/0777 and MSMT 00216225411.

REFERENCES

[1] Z. Q. Hua, R. Sitaru, F. Denes, and R. A. Young: Plasmas and Polymers 2(3), (1998) 196

[2] J. Behnisch, Plasma Processing of Polymers, In: R.d'Agostino, P. Favia, F. Fracassi (Eds.), Plasma Processing of polymers, NATO ASI Series. Vol. 346, (1996) p. 345

[3] R. Mahlberg, H. E.- M. Niemi, F. Denes, R.M. Rowell, International Journal of Adhesion 62 Adhesives 18 (1998) p. 283

[4] D. Lee, S. Manolache, M. Sarmadi and F. Denes, Polymer Bulletin 43, (1999) p. 409

[5] M. N. Belgacem, A. Blayo and A. Gandini, Journal of Colloid and Interface Science 182(No. 0484), (1996) p. 431

[6] A.V. Rajnen, X. H. Li, L. G. Devi, G. B. Rao, Y. Z. Meng, Cellulose 10 (2003) p. 179

[7] R. Prat, Y. J. Koh, Y. Babukutty, M. Kogoma, S. Osakazaki, M. Kodama, Polymer 41 (2000) p.7355

[8] V. Buršíková, P. Sťahel and J. Janča, Czech. J. Phys., Vol.52 (2002), Suppl. D, p. 866

[9] Sapieha S., Verrault M., Klemberg-Sapieha J. E. Sacher E., Wertheimer M. R. App. Surface Sci. 44 (1990). p. 171

[10] Hua Z. Q., Sitaru R., Denes F. Young R. A. Plasmas and Polymers, 2(3) p. 199

[11] Sahin, H. T., Monolache S., Young R. A. and Denes F. Cellulose 9(2002) p. 171

[12] Navarro F., Davalos F., Denes F., Cruz L. E., Young, R. A., Ramos J. Cellulose 10 (2003) p.411

5th International Conference **ELMECO**
Nałęczów, Poland
September 2005

ANALYSIS OF ACOUSTIC SIGNAL IN THE MICRO DISCHARGES USING CONTINUOUS WAVELET TRANSFORM

Toshiyuki Nakamiya[1], Daiki Sasahara[2], Kenji Ebihara[2], Tomoaki Ikegami[2] and Ryoichi Tsuda[1]

[1]Department of Information Science, Kyushu Tokai University,
Toroku9-1-1, Kumamoto 862-8652,Japan
[2]Graduate School of Science and Technology, Kumamoto University,
Kurokami 2-39-1, Kumamoto 860-0082, Japan
e-mail: nakamiya@ktmail.ktokai-u.ac.jp

Abstract

The fundamental experiments were carried to examine the tracking phenomenon that was one of the main causes of fire breaking. AC high voltage was applied to one of the electrode. As the electrode, the following samples were prepared: the mesh plate, the flat ribbon cable and the ignition plug. The current, voltage waveforms of micro discharge and the sound signal detected by the condenser microphone were stored in the memory Hi-coder. In this scheme, Continuous Wavelet Transform (CWT) were applied to discriminate the acoustic sound of the micro discharge and the dominant frequency components were studied. In addition, the energy distribution of acoustic signal was examined by CWT, when the frequency of power supply was increased from 10kHz to 30kHz.

Keywords: Continuous Wavelet Transform, dielectric barrier discharge, mesh type electrode, micro discharge

INTRODUCTION

The fires caused by arc tracking phenomenon are about 700/year in Japan. The dust accumulated in the plug for the power supply of household utensils is main reason for the arc tracking phenomena. Electrical current will flow through dusts only when the dusts contain water. If the moisture is continuously replenished, the currents will be sustained. It is thought that small leakage currents through such contamination cause degradation of the plug material leading to the micro discharge, charring or igniting combustible materials around the discharge. The combined effects of surface moisture and pollutants cause leakage currents across the surface of the insulator, which can lead to formation of carbonized tracks [1]. A more energetic arc through the carbonized dusts might cause a fire under the right conditions. The similar phenomenon occurs on the electronic circuit board of computer and household electric appliance. The deposited dust carbonizes with a long time, and it becomes a cause of the arc tracking phenomenon [2]. The development of fire breaking prevention technique using the electric discharge sound is expected [1], [2]. We proposed the procedure to detect the tracking phenomenon using the acoustic signal due to the micro discharge. The fundamental experiments to examine the characteristics of the discharge were performed. The high voltage was applied to one of the electrode. The micro discharge was generated by the applying high voltage and initiated the acoustic sound. In this scheme, the CWT was applied to discriminate the acoustic sound of the micro discharge and the dominant frequency components were studied.

The micro discharge is also observed between electrodes, when the ozone is generated by the dielectric barrier discharge (DBD). Physics of DBD is based on the initial avalanche-to-streamer transition that is followed by the formation of micro discharge and their arrangement in the specific pattern [3]. It was shown recently that dielectric barrier discharge can exhibit two major discharge modes: filamentary mode and homogeneous or glow mode [4]. The filamentary mode was a topic for active investigations in the past several years. Most industrial DBD applications utilize filamentary mode. However, for a homogeneous treatment of surfaces, or for the deposition of thin films, the glow discharge mode has obvious advantages over the filamentary one [5]. Unfortunately the DBD glow discharge is very unstable and prone to spontaneous transition to more stable filamentary mode. The electric discharge sound may be considered the utilization of the monitor of the effective ozone generation.

EXPERIMENTAL PROCEDURES

The fundamental experiments were carried to examine the tracking phenomenon that was one of the main causes of fire breaking. The schematic diagram of experimental equipment is shown in Fig.1.

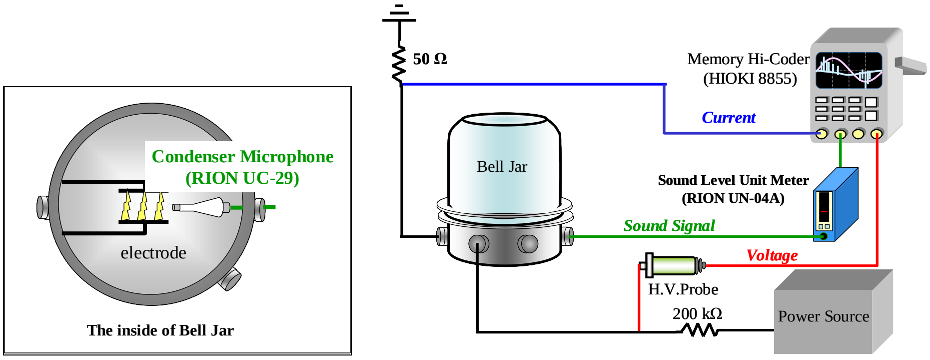

Fig. 1. Measurement circuit of waveforms

The following three type of electrode were used to simulate the arc tracking phenomenon: the mesh type electrode, the flat ribbon cable and the ignition plug. The structure of the mesh type electrode is shown in Fig. 2.

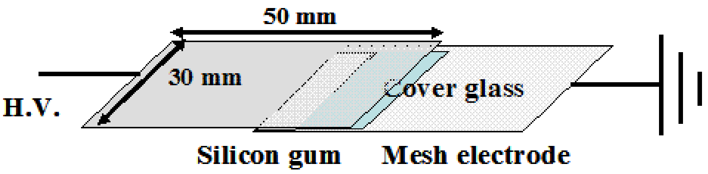

Fig. 2. Mesh type electrode

In the mesh type electrode, the microscopic hole of 20μm diameters has been opened in great numbers. The cover glass (22mm x 4mm,Thickness: 0.12～0.17mm) is held between mesh electrode (30mm x 50mm) of the 2 sheets, and the gap length of mesh type electrode is 0.5～1.0mm. The flat ribbon cable (ϕ:1.1mm, length:100mm) is used in order to connect the mother boards of personal computer. The ignition plug (gap: 1.5mm) is used for automobile engine.

We generated the micro discharges using the electrode in order to understand the fundamental relationship between the micro discharge and the acoustic sound properties. One of the electrode was connected to the high voltage terminal through the resistance 200kΩ. Other terminal was grounded. The sound signal was generated by the discharge of the electrode. The high voltage produced by the power source was applied to the electric wire. The current, voltage waveforms of micro discharge and the sound signal detected by the condenser microphone were stored in the memory Hi-coder 8855(Hioki). The sampling frequency was 1 MHz and the measurement time was 1 second. Data analysis was performed using MATLAB with the Signal Processing toolbox and Wavelet toolbox (The Mathworks, Inc.).

CONTINUOUS WAVELET TRANSFORM (CWT)

The wavelet transform converts a signal from time domain to the time-scale domain. Wavelet analysis involves the breaking up of a single prototype function called the mother wavelet. $\psi^{(a,b)}(t)$ is obtained by scaling the mother wavelet $\psi(t)$ at time b and scale a

$$\psi^{(a,b)}(t) = \frac{1}{\sqrt{a}}\psi\left(\frac{t-b}{a}\right) \tag{1}$$

When a becomes large, the basis function $\psi^{(a,b)}$ becomes a stretched version of the prototype, which can be useful for analysis of the low-frequency components of the signal. On the other hand, when the scale parameter is small, the basis function $\psi^{(a,b)}$ will be contracted, which is useful for the analysis of the high-frequency components of the signal [3].

As a mother wavelet, the gabor wavelet is used.

$$\psi(t) = \frac{1}{2\sqrt{\pi\sigma}} e^{-\frac{t^2}{\sigma^2}} e^{-it} \tag{2}$$

Equation (2) is similar to the Short Time Fourier Transform (STFT) which is used the Gaussian function in window function. So it is easy to compare with the analytical results of the STFT and the CWT. In this paper, real part of gabor function is used as a mother wavelet (σ =8).

$$\psi(t) = \frac{1}{2\sqrt{\pi\sigma}} e^{-\frac{t^2}{\sigma^2}} \cos(t) \tag{3}$$

Therefore the wavelet transform of a continuous signal is defined as:

$$\hat{f}(a,b) = \frac{1}{\sqrt{a}} \int_{-\infty}^{\infty} \frac{1}{2\sqrt{\pi\sigma}} e^{-\frac{(t-b)^2}{\sigma^2 a^2}} \cos\left(\frac{t-b}{a}\right) f(t)dt \tag{4}$$

where the signal $f(t)$ is transformed by the mother wavelet (Eq. (2)). The squared magnitude of the CWT, $\left|\hat{f}(a,b)\right|^2$ is called scalogram and can be used to obtained the energy distribution of the signal over the entire time-scale plane. The time-scale expression has an equivalent time-frequency expression, obtained by using the formal identification

$$Fa = \frac{\Delta \cdot Fc}{a} \tag{5}$$

where Δ is the sampling time of sound signal and Fc is the central frequency of the mother wavelet.

RESULTS AND DISCUSSION

Neon transformer

The high voltage (2～15kV, 60Hz) was produced by the neon transformer and was applied to the electrode by the atmospheric pressure. The following three type of electrode were used: the mesh type electrode, the flat ribbon cable and the ignition plug.

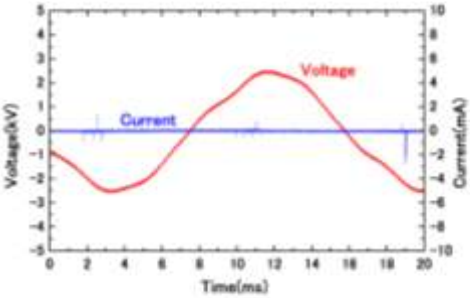

Fig. 3. Voltage and current waveforms with applied voltage of 2.5kV

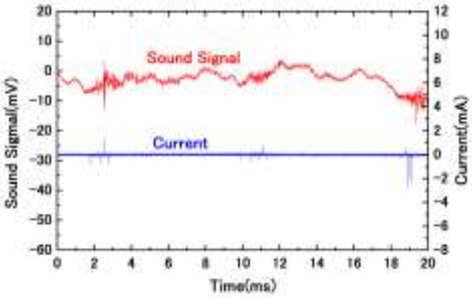

Fig. 4. Sound signal and Current waveforms with applied voltage of 2.5kV

Mesh type electrode

There was no discharge at the applied voltage of 2kV in the mesh type electrode. The discharge appeared at the applied voltage of 2.5kV. Figure 3 shows the voltage and the current waveforms with applied voltage of 2.5kV. The discharge current appears within 1/4 half-cycles which increase or decrease from 0V. The discharge current flows during 1.7ms～2.8ms, 9.9ms～11.3ms and 18.7～19ms. The current value is 2.7mA even in the maximum. The current waveform is pulse-like, and it seems to generate the dielectric barrier discharge, because the cover glass has been inserted between the electrodes.

When AC 2.5kV voltage is applied in the electrode, the measurement result of sound and current waveforms are shown in Fig.4. The acoustic signal is observed in the form superimposed on the drift signal, and the maximum value of the amplitude is 2.6mV.

The time-frequency representation of sound signal with dielectric barrier discharge is shown in Fig.5. AC 2.5kV is applied to the mesh type electrode. The frequency components over 20kHz appear during 2.1ms～3.3ms, 10.9～11.3ms and 19.2～19.7ms. The maximum frequency components of the sound signal are over 45kHz. These results of the CWT are good agreement with the time period of acoustic signal with the dielectric barrier discharge.

When AC 2.5kV is applied to the mesh type electrode, the scalogram of sound signal with dielectric barrier discharge is shown in Fig.5. This figure shows the energy distribution of the sound signal over the time-frequency plane. The peak value of the sound energy is shown at 2.1ms and 35kHz of the time-frequency plane.

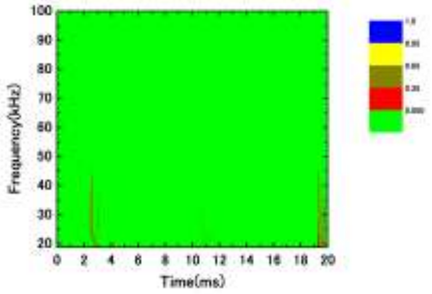

Fig. 5. Time-frequency representation of sound signal using CWT with applied voltage of 2.5kV

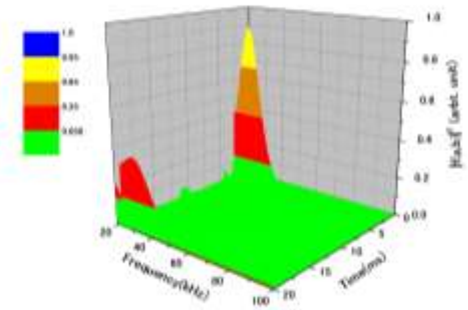

Fig. 6. CWT scalogram of sound signal with applied voltage of 2.5kV

Flat ribbon cable

The flat ribbon cable is used as an electrode. Figure 7 shows the voltage and the current waveforms with applied voltage of 15kV. The pulse-like discharge current flows during 0.3ms～4.3ms, 8.6ms～12.6ms and 16.6～19.7ms. The current value is 32.9mA even in the maximum. The discharge current appears within 1/4 half-cycles which increase or decrease from 0V at the voltage value. The flat ribbon cable is covered with vinyl chloride and the pulse-like waveforms of the discharge current indicate dielectric barrier discharge.

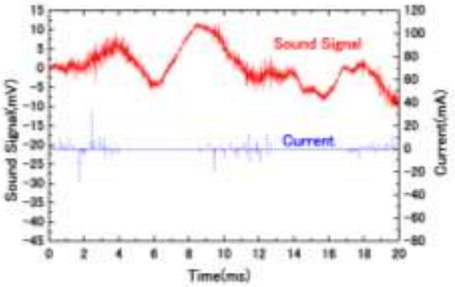

Fig. 7. Voltage and current waveforms
with applied voltage of 15kV

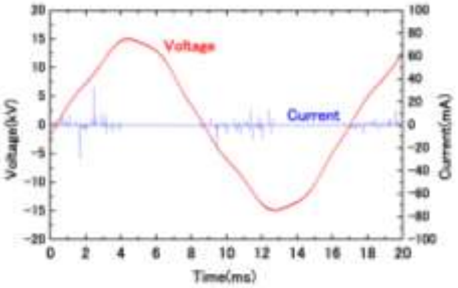

Fig. 8. Sound signal and Current
waveforms with applied voltage of 15kV

Figure 8 shows the sound signal and the current waveforms with applied voltage of 15kV. The acoustic signal is observed in the form superimposed on the 8ms period (125Hz) signal, and the maximum value of the amplitude is 8.3mV.

When AC 15kV is applied to the flat ribbon cable, the time-frequency representation of sound signal with dielectric barrier discharge is shown in Fig.9. The frequency components over 30kHz appear during 1.3ms～4.3ms, 9.6ms～13.2ms and 18.9～19.7ms. These results by CWT are comparatively well agreement with the time of acoustic signal by the dielectric barrier discharge.

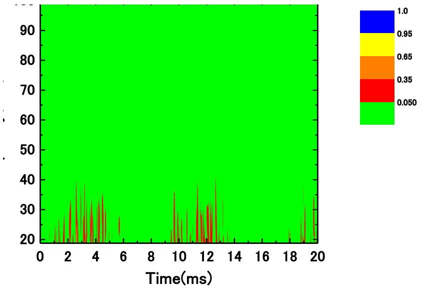

Fig. 9. Time-frequency representation of
sound signal using CWT with applied
voltage of 15kV

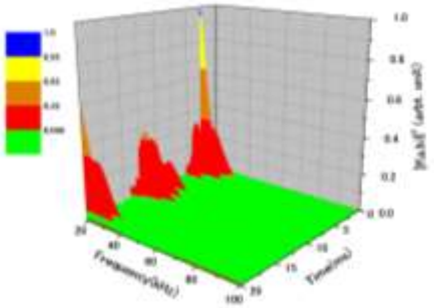

Fig. 10. CWT scalogram of sound signal
with applied voltage of 15kV

When AC 15kV is applied to the mesh type electrode, the scalogram of sound signal with dielectric barrier discharge is shown in Fig.10. The time-frequency characteristic of the sound signal is shown by the three-dimensional display. This figure shows the three peaks and the maximum peak appear at 2.7ms and 20kHz of the time-frequency plane.

Ignition plug

When AC 7kV voltage is applied in the ignition plug, the measurement result of sound and current waveforms are shown in Fig. 11.

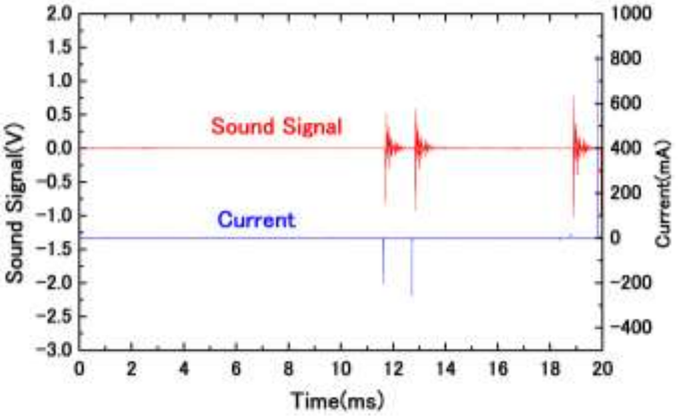

Fig. 11. Sound signal and Current waveforms with applied voltage of 7kV

As well as electrode using the mesh type electrode or the flat ribbon cable, the pulse-like current with the electric discharge is generated. The electric discharge has been generated at 11.6ms, 12.7ms and 18.8ms. The current maximum value is 270mA. This value is large compared with the electrode using meshed electrode or the flat ribbon cable. In addition, the acoustic signal also shows 1.8V in the maximum. This result shows that the arc discharge has been generated.

The acoustic signal has been retarded from arc discharge at 0.1ms. It propagates at 3cm in 0.1ms, as the temperature in the laboratory is made to be 30℃, and The propagation distance is almost same with the distance of the microphone and the ignition plug.

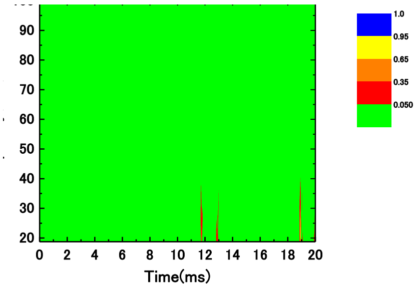

Fig. 12. Time-frequency representation of sound signal using CWT with applied voltage of 15kV

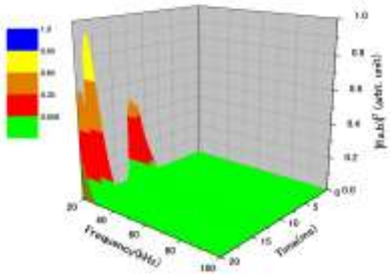

Fig. 13. CWT scalogram of sound signal with applied voltage of 7kV

Figure 12 shows the analyzing result of the acoustic signal by CWT with applied voltage of 7kV to the ignition plug. The frequency components over 35kHz appear at 11.7ms, 12.8ms and 18.9ms. These values by CWT are fairly good agreement with the time of acoustic signal by the arc discharge.

When AC 7kV is applied to the ignition plug, the scalogram of sound signal with dielectric barrier discharge is shown in Fig.13. The time-frequency characteristic of the sound signal is shown by the three-dimensional display. This figure shows the energy distribution of the sound signal over the time-frequency plane.

Impulse high frequency and high voltage power supply

The high voltage (4〜6kV:peak to peak voltage, 10〜30kHz) was produced by the Impulse high frequency and high voltage power supply. The voltage was applied to the mesh type electrode in atmospheric pressure.

Figure 14 shows the voltage and the current waveforms with applied voltage of 5kV and 10kHz. The discharge current flows at 1.5μs and 9.2μs. The maximum current value is 30mA and the current waveform is pulse-like. The luminescence began on the edge of the mesh type electrode.

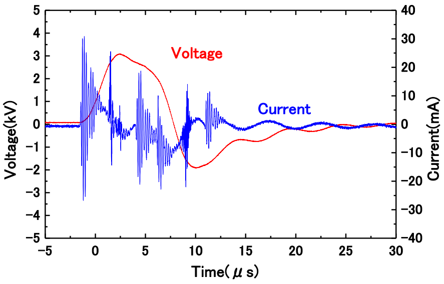

Fig. 14. Voltage and current waveforms with applied voltage of 5kV (f=10kHz)

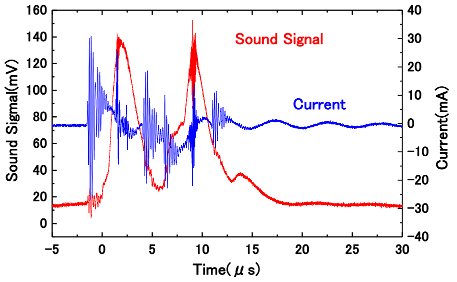

Fig. 15. Sound signal and Current waveforms with applied voltage of 5kV (f=10kHz)

When 5kV voltage is applied in the electrode, the measurement result of sound and current waveforms are shown in Fig.15. The acoustic signal is observed in the form superimposed on the drift signal, and the maximum value of the amplitude is 67mV.

Figure 16 shows the analyzing result of the acoustic signal by CWT with applied voltage of 5kV to the mesh type electrode. The frequency components over 20kHz appear at 1.5μs and 9.1μs. These values by CWT are fairly good agreement with the time of acoustic signal by the dielectric barrier discharge. The dominant frequency components at the time of 1.5μs contain from 45kHz to 65kHz. The sound signal at the time of 9.1μs has the wide frequency components from 20kHz to 145kHz.

The scalogram of sound signal with dielectric barrier discharge is shown in Fig. 17. The time-frequency characteristic of the sound signal is shown by the three-dimensional display and it shows the energy distribution of the sound signal.

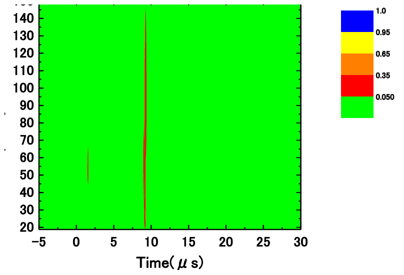

Fig. 16. Time-frequency representation of sound signal using CWT with applied voltage of 5kV (f=10kHz)

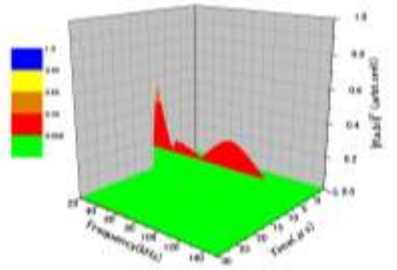

Fig. 17. CWT scalogram of sound signal with applied voltage of 5kV (f=10kHz)

The frequency of power supply increases to 30kHz. When the high frequency of 5kV is applied to the electrode, the CWT scalogram of sound signal is shown in Fig.14. The frequency components over 20kHz appear at 1.5μs and 9.1μs. These values by CWT are fairly good agreement with the time of acoustic signal by the dielectric barrier discharge.

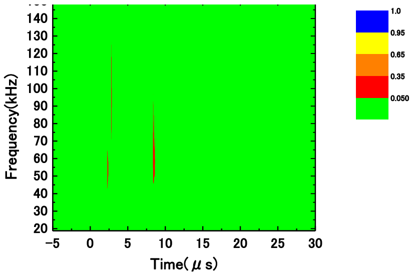

Fig. 18. Time-frequency representation of sound signal using CWT with applied voltage of 5kV (f=30kHz)

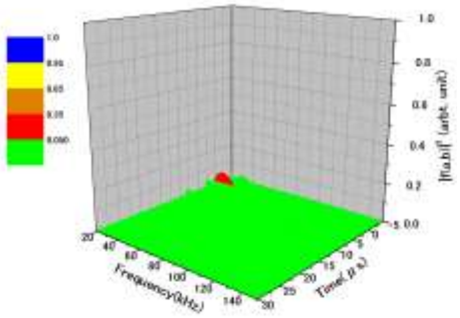

Fig. 19. CWT scalogram of sound signal with applied voltage of 5kV (f=30kHz)

The dominant frequency components are contained between 42kHz and 125kHz at 1.5μs. At the time of 9.1μs, the dominant frequency components are contained between 40kHz and 100kHz.

The scalogram of sound signal with dielectric barrier discharge is shown in Fig.19. The time-frequency characteristic of the sound signal is shown by the three-dimensional display. This figure shows the energy distribution of the sound signal over the time-frequency plane. The peak value of the sound energy of 30kHz(frequency of applied voltage) is smaller than that of 10kHz.

CONCLUSIONS

The fundamental experiments to examine the tracking phenomenon were carried. The high voltage of alternating current was applied to the electrode such as the mesh type electrode, the flat ribbon cable and the ignition plug. CWT was applied to discriminate the acoustic sound of the micro discharge and the dominant frequency components were studied. The following results are obtained:

1. When AC 2.5kV is applied to the mesh type electrode, the discharge current flows during 1.7ms～2.8ms, 9.9ms～11.3ms and 18.7～19ms. The current waveform is pulse-like, and it seemed to generate the dielectric barrier discharge. CWT scalogram of sound signal shows that the frequency components over 20kHz appear during 2.1ms～3.3ms, 10.9～11.3ms and 19.2～19.7ms.
2. The pulse-like discharge current flows during 0.3ms～4.3ms, 8.6ms～12.6ms and 16.6～19.7ms, when AC 15kV is applied to the electrode of flat ribbon cable. The CWT scalogram of sound signal with dielectric barrier discharge shows that the frequency components over 30kHz appear during 1.3ms～4.3ms, 9.6ms～13.2ms and 18.9～19.7ms.
3. When AC 7kV voltage is applied in the ignition plug, the electric discharge has been generated at 11.6ms, 12.7ms and 18.8ms. The CWT scalogram of sound signal shows that the frequency components over 35kHz appear at 11.7ms, 12.8ms and 18.9ms.
4. When the frequency of the power supply increases from 10kHz to 30kHz, the peak value of the sound signal energy of 30kHz is smaller than that of 10kHz.
5. The analytical results by the CWT are good agreement with the experimental results.

LITERATURE

[1] T. Nakamiya, T. Tanaka, K. Ebihara, T. Ikegami, Chung-Seog Choi and R. Tsuda, “Acoustic Signal Analysis in the Partial Discharge”, The 21st Symposium on Plasma Processing, 2004, pp. 282-283

[2] T. Nakamiya, T. Tanaka, K. Ebihara, T. Ikegami and R. Tsuda, “Acoustic Signal Analysis in the Partial Discharge by Short Time Fourier Transformation”, The Papers of Technical Meeting on Plasma Science and Technology, IEE Japan, PST-04-80, 2004, pp. 45-49

[3] Chirokov A., Gutsol A., Fridman A., Sieber K. D., Grace J. M., Robinson K. S., “Analysis of two-dimentional microdischarge distribution in dielectric-barrier discharges”, *Plasma Sources Science &Technology*, 13(4), 2004, pp. 623-625

[4] Kanazawa S., Kogoma M., Moriwaki T., Okazaki S., “Stable glow plasma at atmospheric pressure”, *Journal of Physics D: Applied Physics*, 21(5), 1988, pp. 838-840

[5] Martin S., Massines F., Gherardi N., Jimenez C., “Atmospheric pressure PECVD of silicon based coating using a glow dielectric barrier discharge”, *Surface and coatings Technology*, 177-178, 2004, pp. 693-698

[6] Abry P., *Ondelettes et turbulence. Multirésolutions, algorithmes de décomposition, invariance d’échelles*, Diderot Editeur, Paris, 1997

5th International Conference **ELMECO**
Nałęczów, Poland
September 2005

IN-FLIGHT PROCESSING OF POST-INCINERATION ASH IN A DC THERMAL PLASMA JET

Wincenty W. Płotczyk, Aleksandra Sadowska, Michał Bystrzejewski,
Andrzej Huczko

Department of Chemistry, Warsaw University
Pasteur 1, 02-093 Warsaw
Poland, e-mail:wwplot@chem.uw.edu.pl

Abstract

Bottom ash resulting from the incineration of municipal solid waste (MSW) in the Warsaw incinerator has been in-flight processed in a direct current (DC) thermal plasma jet. The arc power varied between 4 – 12 kW. The influence of the specific energy of ash and construction of the reaction chamber on the starting material transformation was investigated. At high specific energy the melting degree exceeding 80 wt.% was achieved.

Keywords: thermal plasma , waste treatment, incineration, melting

INTRODUCTION

The growing interest in the use of thermal plasma in environmental engineering [1-3] has been observed for the last 20 years. This has been stimulated by existing both European and Polish regulations [4] which prohibit the dumping of solid residues from MSW incinerators. They usually contain heavy metals and other harmfull compounds which may migrate to the environment. Thus, the new techniques to neutralize them are urgently sought.

There are several advantages as far as it concerns the application of plasmas in waste utilization [5]:

- heat generation is independent of process thermal effects;
- relatively low volume of gases at high temperature;
- in the case of pyrolysis the hydrogen, carbon monoxide and lower unsaturated hydrocarbons formed can be utilizated as an energy source;
- inorganic wastes are melted thus decreasing its volume and leachibility;
- due to high energy density in plasma environment the processing is highly effective (high rate of reactions);
- only gases and low-volume solids (any liquid compounds) are reaction products;

- plasma processes are not sensitive regarding the composition and chemical stability of processed waste.

The investigation of the plasma treatment of solid waste carried out in the Laboratory of Plasma Chemistry has been reported earlier [5-7]. In the present study thermal DC arc plasma was used to process the post-incineration waste resulting from the Warsaw MSW incineration plant at various energetic conditions for three different arrangements of the reaction chamber which is crucial for efficient mixing of reactants with plasma environment.

EXPERIMENTAL AND METHODOLOGY

The experiments were carried out in the thermal plasma arc reactor presented schematically in Fig.1 which contained a DC plasma torch generating an argon plasma jet. A welding machine was used as a current source (130 – 480 A, 20 –32 V). The ash was transported by argon using a pneumatic-vibration feeder. As-obtained ash powder fraction (designed as fraction) 0.1 – 0.4 and below 0.1 mm was introduced into the reaction chamber through a hole perpendiculary to the direction of a plasma jet flow. The argon was used as the plasma gas and transport gas and its flow was 2.6 and 1.0 m^3/h, respectively. The products were cooled in a quenching zone. The solid product was separated from gases in a system of cyclones. The similar reactor was earlier used for hydrocarbon and carbonaceous matter pyrolysis [8-10].

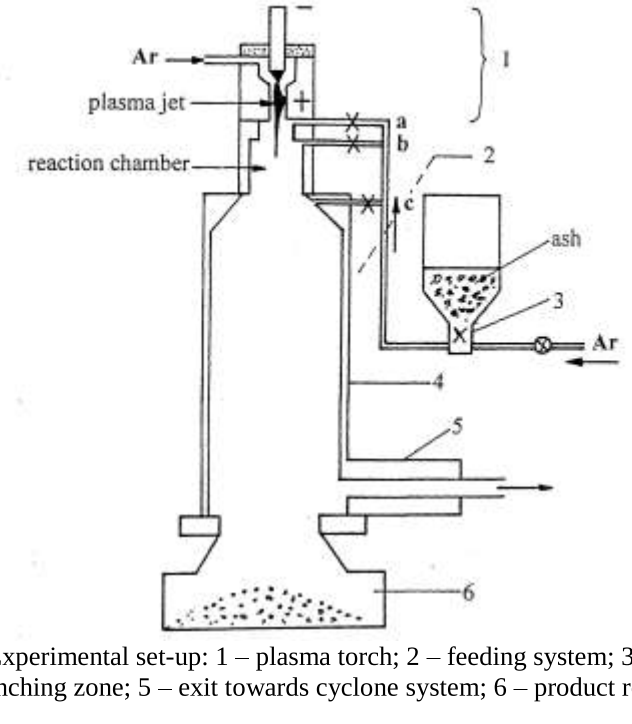

Fig. 1. Experimental set-up: 1 – plasma torch; 2 – feeding system; 3 – feeder; 4 – quenching zone; 5 – exit towards cyclone system; 6 – product receptacle

As it is shown in Fig. 1, three different modes of ash feeding (designed as “a”, “b” and “c”) were used. In the “a” case the reaction chamber (18 mm dia and 52 mm length) had a relatively small initial cross-section (ca 10 mm) with four feeding parts. In the “b” and “c” cases the ash was introduced through one hole only (at 18 and 60 mm dia cross-section respectively). The parameters characterising the process were calculated from the following formulas:

- feeding rate of ash (FR):

$$FR = \frac{m_o}{t} \qquad [kg/h] \qquad (1)$$

- specific energy of ash (SE), defined as the ratio of arc power and the feeding rate of ash:

$$SE = \frac{P}{FR} \qquad [kWh/kg] \qquad (2)$$

From sieve analysis of solid product the melting efficiency of ash (ME) was calculated. It was defined as a ratio between a mass product with a size exceeding the upper one the starting material fraction m_{pr} to the mass of the starting reactant (m_o):

$$ME = \frac{m_{pr}}{m_o} \cdot 10^2 \qquad [wt.\ \%] \qquad (3)$$

The energy consumption in the processes of ash melting (EC) was calculated from the formula:

$$EC = \frac{P}{m_{pr}} \qquad [kWh/kg] \qquad (4)$$

where:

m_o – mass of fed ash; t – feeding duration; P – arc power;

m_{pr} – mass of melted fraction

RESULTS AND DISCUSSION

The operating parameters and the results are shown in Tables 1-3 and Figs 2-3 (as an example).

Table 1. Experimental conditions and results of melting carried out in the reactor “a”

No.	Fraction [mm]	P [kW]	FR [kg/h]	SE [kWh/kg]	ME [wt. %]	EC [kWh/ kg]
1	0.1 – 0.4	4.3	2.0	2.2	7.2	30.4
2	0.1 – 0.4	4.2	1.6	2.5	3.1	82.9
3	0.1 – 0.4	4.3	1.3	3.2	7.7	42.2
4	0.1 – 0.4	7.3	1.8	4.1	47.7	8.5
5	0.1 – 0.4	6.5	1.2	5.2	33.9	15.3
6	0.1 – 0.4	7.0	0.8	5.5	44.1	15.7
7	<0.1	4.1	1.8	2.2	71	3.1

Table 2. Experimental condition and results of melting carried out in the reactor “b”

No.	Fraction [mm]	P [kW]	FR [kg/h]	SE [kWh/kg]	ME [wt. %]	EC [kWh/kg]
8	<0.1	3.9	2.6	1.6	41.3	3.7
9	<0.1	3.8	1.8	2.2	57.1	3.8
10	<0.1	6.4	2.9	2.2	44.1	4.9
11	<0.1	6.0	1.6	3.7	51.6	7.3
12	<0.1	6.1	1.5	4.1	60.0	6.9
13	0.1 – 0.4	6.3	1,5	4.2	36.4	11.5
14	0.1 – 0.4	7.9	1.3	5.8	37.8	15.4
15	0.1 – 0.4	8.6	1.4	6.3	46.2	13.7
16	<0.1	4.7	1.05	4.5	80.4	5.6
17	<0.1	5.1	0.86	5.1	62.9	6.6
18	<0.1	6.5	1.06	6.1	78.9	7.7
19	<0.1	4.4	0.72	6.1	67.5	9.1
20	<0.1	7.7	0.82	9.3	93.3	10.0

Table 3. Experimental condition and results of melting carried out in the reactor “c”

No.	Fraction [mm]	P [kW]	FR [kg/h]	SE [kWh/kg]	ME [wt. %]	EC [kWh/kg]
21	<0.1	3.9	2.3	1.7	25.1	6.7
22	<0.1	6.0	1.7	3.5	34.3	10.2
23	<0.1	8.6	1.5	5.6	80.6	6.9
24	0.1-0.4	6.4	1.4	4.6	2.1	311.9
25	0.1-0.4	9.4	1.3	7.4	14.3	52.2
26	0.1-0.4	11.9	1.3	8.8	48.1	18.4

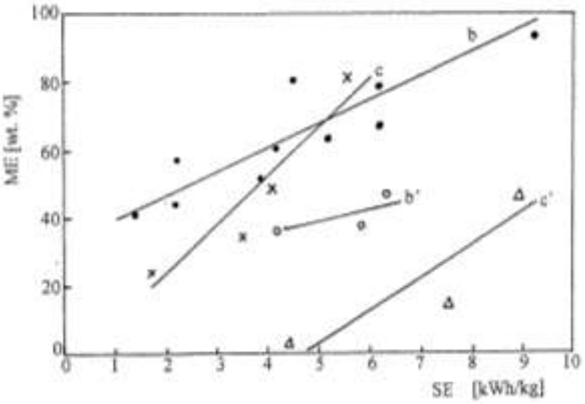

Fig. 2. Melting efficiency vs. specific energy of bottom ash: ● , ○ - mode “b”, fine and coarse ash; ×, Δ - mode “c” , fine and coarse ash

It can be seen from Fig. 2 that the higher melting degree was obtained when specific energy of ash increased. Higher process efficiency was achieved for a fine powder as expected. Also mode “b” of operation was better compared to the feeding with a hole located both at the higher and the lowest position. The energetics of the process (Fig. 3) is, however, much more complicated. There is, however, a tendency of the increase of energy consumption with an increase of the specific energy. Lower melting was observed when the ash was introduced into high temperature zone further from the plasma jet.

The best results was obtained with the fraction of ash below 0.1 mm. For specific energy of ash equal to 2.2 kWh/kg, the melting efficiency 71 wt. % and energy consumption 3.1 kWh/kg was achieved. Solid reaction products, produced specially at higher specific energy, were highly uniform, mostly melted into basalt-like rock.

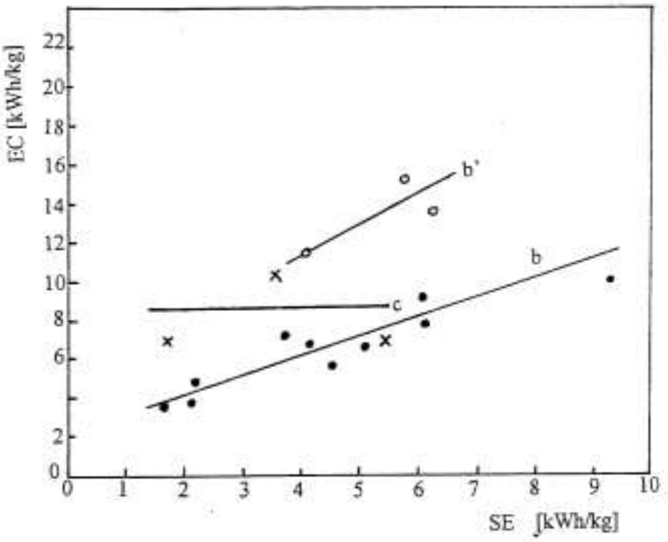

Fig. 3. Energy consumption vs. specific energy of bottom ash : ●, ○ - mode “b” fine and coarse ash, × - mode “c”, fine ash

The starting ash and products from experiments 6, 12 and 20 were examined by the chemical analyses to compare the mobility of different metals (including toxic ones). The leaching tests with distilled water were performed at ambient temperature, with continuous stirring at water-to-sample mass ratio 10:1. Table 4 contains the results of ICP AES analyses of heavy metals in extracts of starting material (fraction below 0.1 and 0.1 – 0.4 mm) and products from experiments 6, 12 and 20. The results of analyses show that the chemical nature of the processed ash changes distinctly as a result of plasma treatment. The leachibility of some heavy metals (eg. As, Cd, Ni, Zn) was generally decreased.

Table 4. Content of selected heavy metals in water extracts [mg/dm3]

		Reactant [mm] Fraction [mm]						
	metal	As	Cd	Cr	Cu	Ni	Pb	Zn
Starting	< 0.1	0.18	17.0	0.10	2.68	0.19	0.80	819
Exp.12	< 0.1	0.09	14.9	0.02	2.66	0.18	1.54	367
Exp.12	>0.1	0.07	3.9	0.25	7.33	0.11	3.44	185
Starting	0.1 – 0.4	0.15	17.0	0.24	3.02	0.16	5.97	729
Exp.6	>0.4	0.05	16.7	0.11	1.75	0.14	7.76	50
Exp.6	>3	0.05	1.9	0.16	4,22	0.10	0.05	1.3
Starting	< 0.1	0.63	19.8	0.53	9.43	0.13	1.7	883
Exp. 20	< 0.1	0.05	16.6	0.02	0.45	0.11	1.3	305
Exp. 20	> 0.1	0.15	11.0	0.04	0.52	0.10	2.6	275

CONCLUSIONS

In-flight thermal plasma treatment of incineration ash results in its partial melting. The melting degree increases with the increasing specific energy of ash. Higher melting was obtained for fine ash comparing to the coarse one with the process efficiency exceeding 70 % at energy consumption ca 3 kWh/kg. The distinct decrease of the leachibility of some heavy metals from the melt was observed, too.

REFERENCES

[1] H. M. Freeman in Incinerating Hazardous Wastes, Ed. by H.M. Freeman, Technomic Publishing Co inc. Lancaster Bosal 1988, p. 247

[2] A. Huczko, H. Lange, G. Chojecki, and D. Dziadko, Przem. Chem. **79**/10, 333 (2000)

[3] A. Stübes, A. Hauck and D. Neuschütz, VDI Berichte **1166**, 583 (1995)

[4] Dz. U. z 2001r., Nr 62, poz. 627.

[5] A. Huczko, G. Chojecki, J. Golimowski, J. Kowalska, D. Dziadko, H. Tanaka and T. Ishigaki, Chem. Inż. Ekol. **9**, Nr 1, 9 (2002)

[6] H. Lange, A. Huczko, G. Chojecki, J. Golimowski, W. W. Płotczyk, B.Krasnodębska-Ostręga, D. Dziadko, J. Pacheco, T. Ishigaki and H. Tanaka, Acta Agrophysica, **80**, 327 (2002)

[7] H. Lange, A. Huczko, G. Chojecki, J. Golimowski, W. W. Płotczyk, B. Krasnodębka-Ostręga, T. Ishigaki, and H. Tanaka, Progress in Plasma Processing of Materials 2003, Ed. P. Fauchais p. 765

[8] W. W. Płotczyk, A Resztak, T.Opalińska, A. Szymański, Acta Phys. Slov. **39**, Nr 2, 126 (1990)

[9] W. W. Płotczyk, A. Resztak, A. Szymański, Coll. De Physique Coll. 5, 51 (1990) C-43

[10] A. Huczko, W.W. Płotczyk, T. Opalińska, A. Resztak, ISPC-8, Symp. Proceed., Tokio 1987, p. 725

DEVELOPMENT OF AGRICULTURAL SOIL STERILIZATION USING OZONE GENERATED BY HIGH FREQUENCY DIELECTRIC BARRIER DISCHARGE

Kenji Ebihara[1], Masahiro Takayama[1], Tomoaki Ikegami[1], Kouichi Ogata[1], H. D. Stryczewska[2], Yutaka Gyoutoku[3] and Takamasa Sakai[4]

[1] Department of Electrical and Computer Engineering and Graduate School of Science and Technology, Kumamoto University
Kurokami 2-39-1, Kumamoto 860-8555 Japan
[2] Faculty of Electrical Engineering and Computer Science , Lublin University of Technology,
Nadbystrzycka 38A,20-618 Lublin,Poland
[3] Kumamoto Prefecture Agricultural Research Center,
Sakae 3801, Goshi, Kikuchi,Kumamoto 861-1113,Japan
[4] Kumamoto Technology and Industry Foundation,
Tabaru 2081-01, Mashiki, Kamimashiki, Kumamoto 861-2202, Japan
e-mail:ebihara@eecs.kumamoto-u.ac.jp

Abstract

We have developed the ozone generation system suitable to soil sterilization and ozone supplying system into the soil. The coaxial dielectric barrier discharge produced the ozone with high concentration at high efficiency. Injection of the on- site generated ozone gas into the soil resulted in decreasing soil pathogen and changing chemical properties of the soil. We studied ozone sterilization of agricultural soil when it was treated by varying ozone dosages and process duration. The temporal and spatial properties of the soil were monitored using the pH and electrical conductivity. The bacteria populations, pathogen and soil-borne fungi were measured after various ozone treatment procedures. Ozone with 100g/m3 was injected into the soil at a flow rate of 2 liter/min during 60min. The pH shows drastic change in 40min that will be one of indexes indicating the sterilization level. In this treatment 100% of the bacteria in the agricultural soil was killed.

Keywords: ozone, soil sterilization, barrier discharge, screw electrode, pH

INTRODUCTION

The objective of soil sterilization is to destroy/eliminate microbial cells without significantly altering the chemical and physical characteristics of the soil. Methyl bromide, a fumigant for agricultural soil, has been identified as a significant atmospheric ozone depleting substance. In accordance with the Montreal Protocol, the international treaty designated to protect the Earth’s ozone layer, production of methyl bromide was reduced, in stages, beginning in January,1999. Complete production phase-out is scheduled for this year(2005). Uses of this pesticide include fumigation for elimination of insects , nematodes and virus in soil.

Numerous technologies including autoclaving (moist heat), dry heat and microwaves have been developed to sterilize soil or inhibit microbial activities in soil. The worldwide need to develop environmentally benign alternatives to methyl bromide for soil sterilization requires new technologies for the agricultural and horticultural fumigation.

Ozone , which has been recognized as the most powerful oxidant next to hydroxyl, is a highly reactive and unstable molecule and oxidizing agent which quickly kills insect, bacteria, fungi and contact. Ozone also has many benefits based on on-site generation, minimum human toxicity, low persistent chemicals in the soil. In order to generate ozone and related radicals, dielectric barrier discharge, pulsed discharge, corona discharge and surface discharge have been utilized.

We have developed the ozone generation system suitable to soil sterilization and ozone injection system into the soil. The coaxial dielectric barrier discharge using the pyramid type electrode or the screw type electrode produced the ozone with high concentration at high efficiency [1-5]. Ozone treatment of soil using the on- site generated ozone gas resulted in decreasing soil pathogen and changing chemical properties of the soil [6].

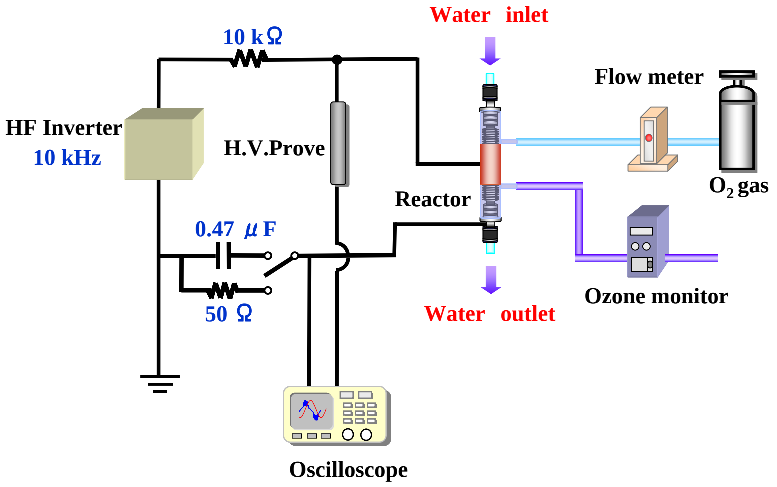

Fig. 1. Dielectric barrier discharge system

We report here the development of ozone generation systems using high frequency dielectric barrier discharge which will be useful for soil sterilization in the farmland. The ozone diffusion and sterilization of agricultural soil when it was treated by varying ozone dosages and process duration were studied. The temporal and spatial properties of the soil were monitored using the pH and electrical conductivity. The bacteria populations, pathogen and soil-borne fungi were measured after various ozone treatment procedures.

EXPERIMENTAL

Fig.1 shows the outline of the ozone generation system. An electric power of high frequency inverter (10kHz) was applied to the electrodes in the range of applied voltage (1.7 kV-5.5 kV). Material gas (oxygen 99.9 %) was supplied to the reactor of the dielectric quartz glass tube (ϕ 8 mm) with an inner electrode. The inner electrode is the structure of a water-cooled screw type electrode of stainless steel rod (ϕ□ 6 mm) . The ground electrode is cupper foil wrapped around the quartz tube. The gap separation between the inner electrode and the insulator tube was kept at 1 mm.

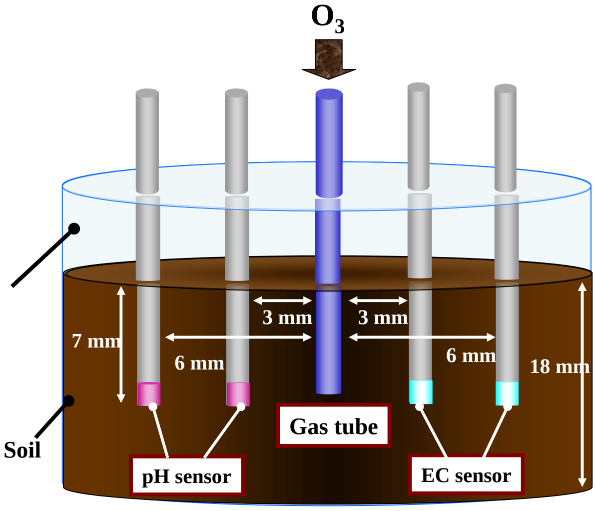

Fig. 2. pH and EC sensors in the ozone injection vessel

Fig.2 shows the ozone injection system into the agricultural soil (Audisols: Kumamoto soil). Ozone was introduced into the soil through the drip tube of 1/4 inch Teflon pipe. Two sets of the pH sensor and the electrical conductivity (EC) probe were placed at appropriate separation. The soil temperature was also measured. The treatment container was arranged in an incubator of which temperature and light illumination can be automatically controlled. These measured data can be transmitted to the PC through the wireless network system.

RESULTS AND DISCUSSION

Fig.3 shows the ozone concentration as a function of applied voltage at a flow rate of 2 liter/min. The maximum ozone concentration for the water–cooled electrode was 38g/ m^3 at 5.3kV. In the case of the non-cooling apparatus, rapid decrease by dissociation of ozone appears over 4.6kV due to dielectric heating of the quartz tube.

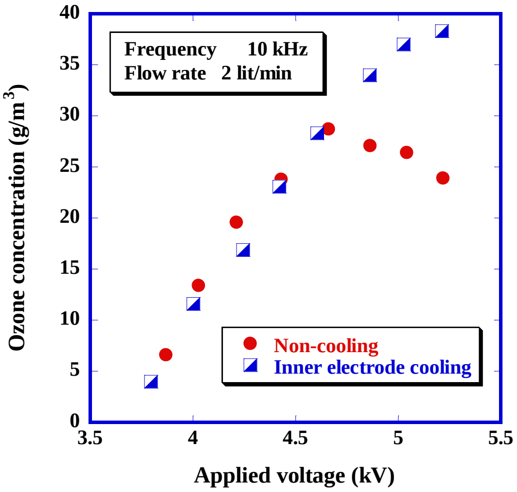

Fig. 3. Ozone concentration as a function of applied voltage

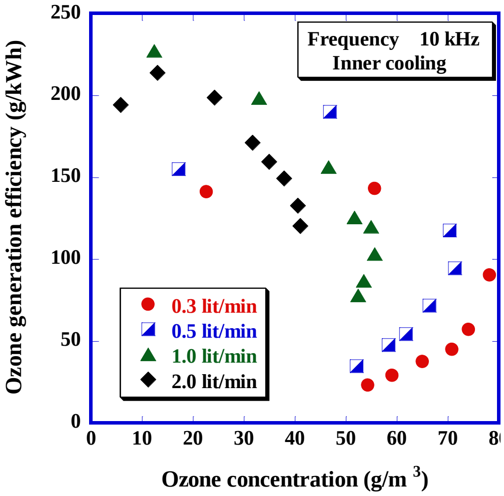

Fig. 4. Ozone generation efficiency as a function of ozone concentration

The ozone generation efficiency is shown in Fig.4 as a function of ozone concentration at various O_2 flow rates [6]. The high ozone concentration of 80g/ m^3 is generated at a low gas flow rate of 0.3 liter/min. The high value of ozone generation efficiency of 220g/kWh was obtained at 1-2 liter/min where a low ozone concentration of 10g/m^2 was generated. It is shown that the maximum concentration obtained decreases with increase of O_2 flow rate.

Nitric monoxide(NO) is a free radical which makes it very reactive and unstable. In air, it quickly reacts with oxygen to form the poisonous nitrogen dioxide(NO2). The NO also has been expected to kill or eliminate microbial cells. We generated the NO radical using the dielectric barrier discharge.

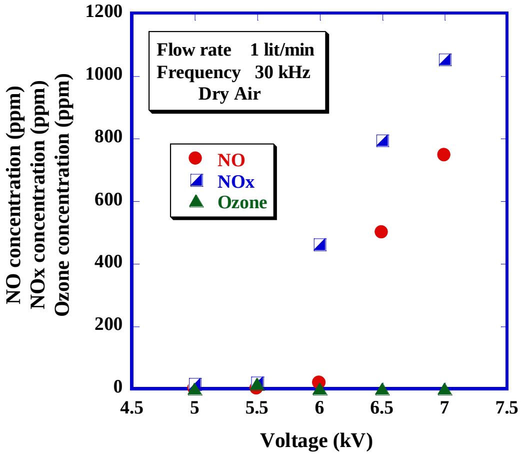

Fig. 5. NO,NOX concentration as a function of applied voltage(30kHz)

Fig.5 shows the NO concentration when the applied voltage was changed. In this case we used the high frequency oscillator operating at 30kHz and dry air of 1 liter/min was introduced into the same discharge tube shown in Fig.1.

NO began to generate at applied voltage of 6kV. The concentration increases with the applied voltage. The maximum concentration of 780ppm was attained at 7kV.

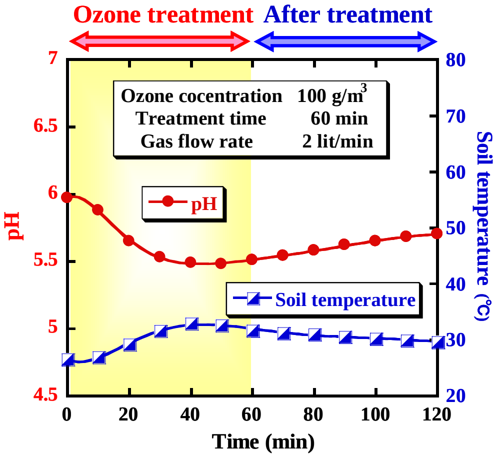

Fig. 6. pH and soil temperature as a function of ozone treatment time

We have studied the soil properties when ozone or NO was injected into the agricultural soil as shown in Fig.2. Typical behavior of the soil property of the pH is shown in Fig.6. Ozone with 100g/m^3 was injected into the soil at a flow rate of 2 liter/min during 60min. The pH at position of 30mm from the injection pipe shows drastic change in 40min and then gradually increases. Fig.7 shows time development of electrical conductivity(EC) as well as soil temperature. The EC also shows rapid decrease till 20 min and gradually recovers to steady value. After termination of the ozone treatment, normal value of EC of 70mS/m is attained. We also found that soil temperature drastically increases and decreases as the EC and pH change rapidly. The interesting phenomena is considered to be accompanied with chemical exothermic reaction of the soil with ozone. Fig.8 shows the change of the pH and the EC during and after NO treatment. We notice only slow decrease of the EC. In this treatment, NO concentration of 500ppm was injected into the soil at a flow rate of 2 liter/min.

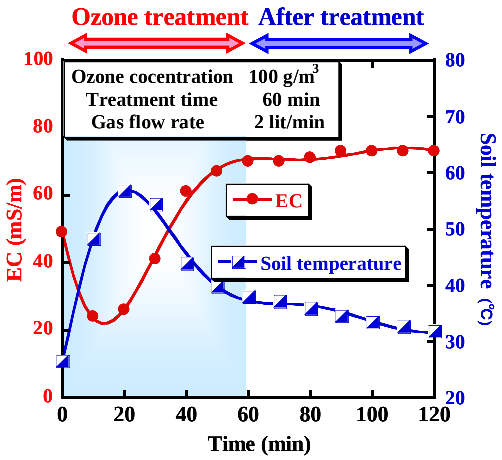

Fig. 7. Time development of EC and soil temperature as a function of treatment time
Position d=30mm

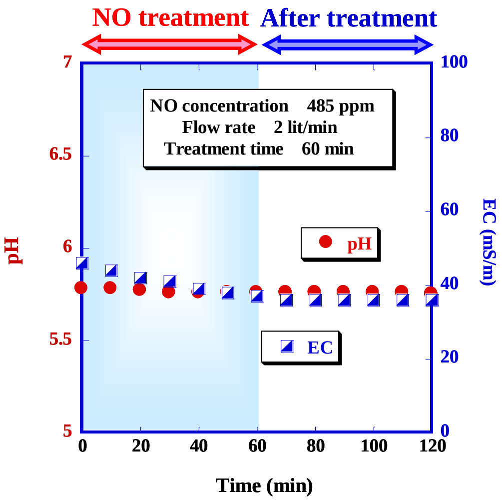

Fig. 8. pH and EC of NO treated soil as a function of treatment time

We sterilized the agricultural soil by supplying ozone. Fig. 9 is the previous result published [6]. This is the ozone sterilization results when the agricultural soil (50g) was treated varying the ozone dosages (0-40gO_3/m^3) and the duration (1-60min). In this experiment the agricultural soil was filled in an chamber(ϕ 70mm) and ozone gas was supplied from the top of the chamber and evacuated from the bottom exit. The soil samples subjected to the sterilization process were sterile. Fasarium oxysporum of 10^6 conidal/mL was inoculated into the soil. The CFU(colony forming unit) counting was used to evaluate the number survivors after 72 hours. The total ozone amount (g) is calculated from the product of ozone concentration, gas flow rate, and treatment duration. For example, the test soil of $7.2x10^6$ CFU shows $1.7x10^2$ CFU after the treatment of ozone dosage of 6.39g where ozone concentration of 38.5 g/m^3 at gas flow rate of 3 liter/min and treating time of 60min were used. The resulting sterilization rate is 100% as shown in Fig.9 (left end data).

It is shown that the sterilization by ozone injection is effective when the ozone dosage becomes over 0.3g for the 50g soil.

We carried out another experiment for soil sterilization. We prepared the agricultural soil contaminated with root-knot nematode (M.incognita J2). The ozone of the concentration of 45g/m^3 was injected during 20min at a flow rate of 3 liter/min. We did not find the nematode in the depth range from the surface to 50mm of the treated soil. After 30days, the root-knot index (the number of knots of root for planted melon) was measured. The measured index (2.0) for the ozone treated soil is decreased about half of the index (3.8) for the untreated soil. The result also shows that ozone treatment is effective for sterilization of the contaminated agricultural soil.

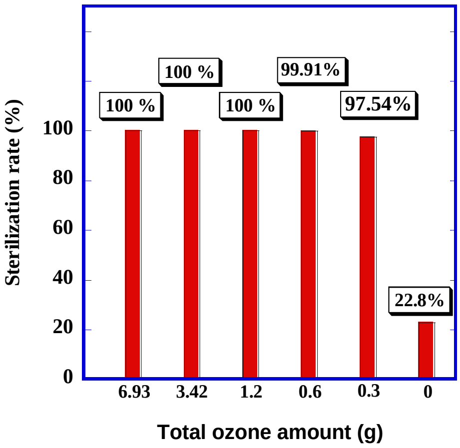

Fig. 9. Sterilization as a function of ozone amount. The inoculated soil initially has 4-7x106 CFU/cc of Fasarium oxysporum

CONCLUSION

We have studied the soil sterilization by using ozone and nitric monoxide which are generated by the coaxial dielectric barrier discharge. The high ozone concentration of 80g/m^3 was generated at a low gas flow rate of 0.3 liter/min. The high value of ozone generation efficiency of 220g/kWh was obtained at 1-2 liter/min. The maximum concentration of 780ppmNO was attained at 7kV. The pH at position of 30mm from the injection pipe shows drastic change in 40min and then gradually increases. The EC also shows rapid decrease till 20 min and gradually recovers to steady value. The soil temperature drastically increases and decreases when the EC and pH change rapidly. These phenomena are considered to be accompanied with chemical exothermic reaction of the soil with ozone.

The sterilization of the agricultural soil was investigated using ozone injection into the soil. The ozone sterilization rate was clarified from several analytical methods.

ACNOWLEDGEMENT

This work have been supported by Research Project for utilizing Advanced Technologies in Agriculture, Forestry and Fisheries(the Ministry of Agriculture, Forest and Fisheries), and the Strategic Research Promotion Program of Information Technology of the Ministry of Internal Affairs and Communications.

REFERENCES

[1] K. Ebihara,Y. Shibuya, H. D. Stryczewska, Y. Gyoutoku, K. Kubo and M. Tachibana, ”Soil treatment process using ozone and NO generated by Electric discharges”, The 21st Symposium on Plasma Processing (Hokkaido, 2004 Jan. 28-30), P2-35, pp. 268 – 269(2004)

[2] M. Takayama, K. Ebihara, H. Stryczewska, T. Ikegami, Y. Gyoutoku, K. Kubo and M. Tachibana,”Ozone generation by high frequency dielectric barrier discharge for soil sterilization”, Abstracts of 7th APCPST and 17th SPSM (Fukuoka, June 29-July 2, 2004), 30 p-85 (2004)

[3] H. D. Stryczewska, K. Ebihara, Y. Shibuya, Y. Gyoutoku, M. Tachibana, ”Non-thermal plasma based technology for soil sterilization”, Ninth International Symposium on High Pressure, Low Temperature Plasma Chemistry (Padova, Italy, Aug. 23-27, 2004), No. 7.06 (2004)

[4] Henryka D. Stryczewska, Kenji Ebihara, Masahiro Takayama, Yutaka Gyoutoku, Mashiro Tachibana, ”Non-thermal plasama-based technology for soil treatment”, Plasma Processes and Polymers, Vol.2, No.3, pp. 238-245 (2005)

[5] M. Takayama, K. Ebihara, H. Stryczewska, T. Ikegami, Y. Gyoutoku, K. Kubo and M. Tachibana, ”Ozone generation by dielectric barrier discharge for soil sterilization”, Thin Solid Films, 2005 (in press)

[6] K. Ebihara, M. Takayama, T. Ikegami, H. Stryczewska, Y. Gyoutoku, T. Yokoyama, N. Gunjikake, M. Tachibana, and T. Sakai, ”Soil sterilization using ozone generated by dielectric barrier discharge”, Proceeding of 17th International Symposium on Plasma Chemistry (August 7th-12th, 2005, Toronto, Canada), CD (1201)

5th International Conference **ELMECO**
Nałęczów, Poland
September 2005

SIMULTANEOUS DECOMPOSITION OF DPM AND NO*x* USING DIELECTRIC BARRIER DISCHARGE

Y. Yamagata1), K. Niho1), T. Jono1), K. Muraoka2)

1 Interdisciplinary Graduate School of Engineering Sciences, Kyushu University,
6-1 Kasugakoen, Kasuga, Fukuoka 816-8580, Japan
2 School of Engineering, Chubu University,
1200 Matsumoto, Kasugai, Aichi 487-8501, Japan
E-mail: yamagata@ence.kyushu-u.ac.jp

Abstract

We propose a new technique for simultaneous decomposition of diesel particulate material (DPM) and nitric oxides (NOx) exhausted from a diesel engine. DPM and NOx are collected in a reactor using an electrostatic precipitation and a honeycomb-shaped adsorbent, respectively. After the sufficient collections, a dielectric barrier discharge (DBD) is generated in the closed space to condense DPM and NOx, and decomposes these simultaneously. DPM and NOx were decomposed simultaneously and effectively by the DBD, which act as the oxidant and reductant, respectively. It is considered that this technique is the most suitable for the decomposition of DPM and NOx with small concentration and high gas flow rate.

Keywords: Dielectric Barrier Discharge, Diesel Particulate Material, Electrostatic Precipitation, Nitric Oxides

INTRODUCTION

Exhaust gas from diesel engines and other combustion processes contains diesel particulate material (DPM), nitric oxides (NO*x*) and hydrocarbons (HC), which cause atmospheric environmental pollution and the health damage. It is very difficult to decrease DPM and NO*x* by means of the combustion control simultaneously. Therefore, in order to satisfy a big social demand to reduce these materials, there are a lot of investigations for aftertreatment of these emissions using diesel particulate filters, catalysts, adsorption/ thermal-desorption or by combinations of these effects [1-5]. However, because of lack of sufficient action and/or excessive cost, promising techniques are yet to be explored.

Thermodynamically non-equilibrium gas discharges, such as packed-bed discharge [6], corona discharge [7] and dielectric barrier discharge (DBD) [2-5, 8], have attracted much attention for these purposes. For instance, packed-bed discharge has been recognized to be able to decompose NO*x* and volatile organic compounds (VOC). However, it is not suitable for the process in high gas flow rate due to large pressure loss caused by its own structure. Moreover, most of the electrical energy are consumed for excitation and ionization of predominantly existing N_2 and O_2 instead of decomposition of these materials, because these hazardous materials are exhausted in very small concentrations of a few tens to hundreds ppm. Therefore, the decomposition efficiency using any kinds of discharges for these hazardous materials is still low. In order to extract the potential of these discharges for the decomposition, densification or localization of these hazardous materials is prerequisite.

Recently, we have proposed a new decomposition technique for environmentally hazardous materials with low concentration, and achieved a successful decomposition of volatile organic compounds [9, 10]. This technique is based on the combination of a DBD with densification/localization using honeycomb-shaped adsorbents. This combination does not spoil the high gas flow rate, and the DBD can easily generate non-equilibrium plasmas on a large discharge space. Therefore, this technique is also useful to decompose DPM and NO*x* exhausted from a diesel engine. In these situations, we demonstrated a usefulness of the filter trapping – low temperature burning scheme using DBD [3], and fabricated a model discharge reactor and installed it onto a diesel engine exhaust pipe [4]. In this previous experiment, DPM localized by a trapping filter and NO*x*, which exist in the exhaust gas, were exposed and decomposed by a DBD to CO, CO_2 and N_2 molecules [11]. However, the problem of pressure loss has to be solved as this technique is widely applied to actual diesel engines.

In order to overcome this problem, we have developed a new method that is based on a combination of DBD with electrostatic precipitation. DPM and NO*x* are collected in a reactor using an electrostatic precipitation and a honeycomb-shaped adsorbent without apparent pressure loss, respectively. In this paper, electrostatic precipitation of DPM and simultaneous decomposition of DPM and NO*x* using this method are mainly shown.

EXPERIMENTAL SETUP AND RESULTS

NO*x* in exhaust gases is adsorbed in catalysts deposited on a haneycomb-shaped sheet inserted in a DBD region, similarly as VOC described above. On the other hand, DPM is collected to the adsorbent surface and/or a collectiong electrode by electrostatic precipitation. Then, DBD are generated between the parallel electrodes, then inducing desorption and simultaneous decomposition of the NO*x* and DPM. In order to show that the proposal method is useful to decompose DPM and NO*x* simultaneously, it is necessary to clarify the following items.

Adsorption/desorption of NO*x* using honeycomb-shaped catalyst

We have chosen a recently developed Pt-ZrO_2-Al_2O_3 (PZA) catalyst as the adsorbent of NO*x*. This adsorbent has advantages of rapid and large adsorption of NO even in the presence of O_2 and CO_2 in the atmosphere hardly affected the adsorption and desorption properties, and selective catalytic decomposition of NO easily proceeds on Pt during desorption in the reducing atmosphere [13]. In order to clarify the adsorption/desorption of NO*x* by a honeycomb-shaped catalyst of PZA, the PZA honeycomb were placed in a quartz tube surrounded by an electric furnace controlling the temperature. An imitative gas including 800 ppm of NO in 10 % of O_2 and 90 % of He, was fed into the quartz tube at 200 ºC that is typical temperature of exhaust gas from actual diesel engine.

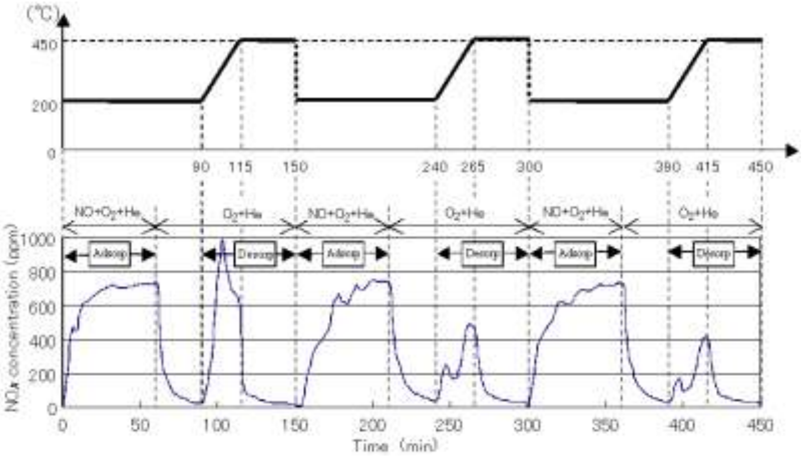

Fig. 1. Temporal change of NO*x* concentration at the outlet of the reactor (lower) together with the temperature change of the PZA honeycomb (upper)

After sufficient adsorption of NO, the flowing gas was changed to another imitative one without NO (O_2 10 % – He 90 %) then the temperature was increased to desorb NO from the PZA honeycomb. During the experiment, the gas flow rates were fixed at 0.1 ℓ/min, and the NO concentration at outlet of the quartz tube was monitored to measure the adsorbed- and desorbed-NO molecules. Figure 1 shows the temporal change of NO*x* concentration measured at the outlet of the reactor together with the temperature change of the honeycomb-shaped PZA catalyst. The NO molecules were first adsorbed at relatively low temperature of 200 ºC by the PZA honeycomb sheet, then were desorbed around 400 ºC from it. Periodic behavior of adsorption/desorption can also be seen in this figure. The amounts of NO*x* adsorption and desorption at each cycle are found to be $(3.3 – 6.0)\times10^{-5}$ and $(3.0 – 6.0)\times10^{-5}$ mol/g, respectively.

Electrostatic precipitation of DPM

Figure 2 (a) and (b) show the schematic illustrations of experimental setup for DPM collection, and the structure of electrostatic precipitator, respectively. Both sides of a stainless steel sheet (thickness of 0.02 mm) were covered by a specially-designed mica sheet (0.26 mm thick) except only the one edge processed to shape of saw tooth. This structure ensures to easily generate a corona discharge to charge DPM negatively. A raw stainless steel sheet (0.15 mm thick) as a collection electrode was faced to the corona electrode with the 2.0 mm separation. The set of these electrodes was accumulated by 18 steps, then which formed a electrostatic precipitator (Fig. 2(b)). Di-Octyl-Phthalate (DOP, $C_6H_4[COOCH_2(CH_2)_6CH_3]_2$) having a mean diameter of 0.3 μm was used as a model particulate. The DC applied voltage and the gas flow rate were ranged 0 – 2 kV and 8 – 20 ℓ/min, respectively. Optical absorption measurement was done to estimate the DOP reduction rate by the reactor. Reduction rate of the DOP versus DC applied voltage is shown in Fig. 3 as a function of gas flow rate. As can be seen in this figure, 68 % of DOP was collected into the reactor at DC 2 kV and 8 ℓ/min.

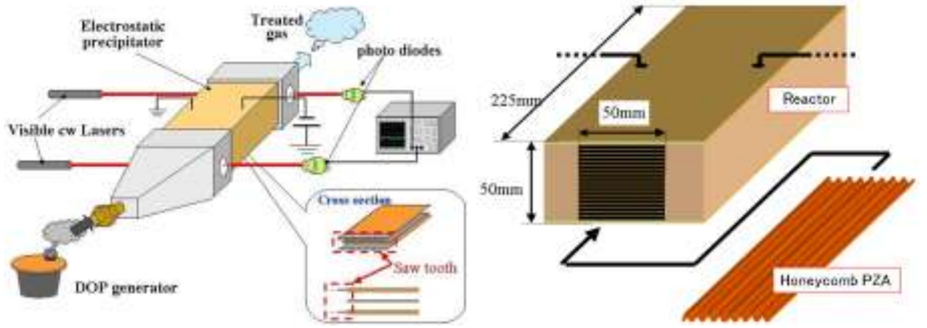

(a) (b)

Fig. 2. Schematic illustrations of (a) experimental setup for DPM collection, and (b) the structure of electrostatic precipitator

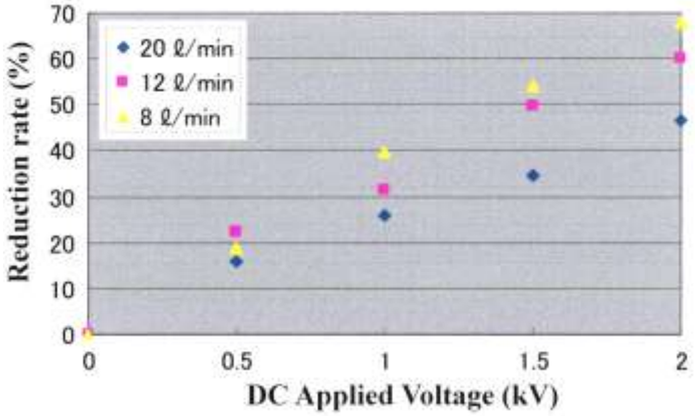

Fig. 3. Reduction rate of the DOP versus DC applied voltage as a function of gas flow rate

DBD generation in the space inserted honeycomb-shaped adsorbent

As described above, the PZA honeycomb is useful as adsorbent/desorbent for NO*x*, when it is controlled by the temperature. As the PZA honeycomb is installed into the proposed method, it is necessary that DBD has to be generated in the insertion of the PZA honeycomb between the electrodes, and should be able to control its temperature. In order to clarify these, we made a DBD reactor that is almost same as the one used in the DPM collection experiment (Fig. 2(b)). The only exception was that all of electrodes were fully covered by mica. Photographs of the front view of the reactor and the DBD generated at 12 kV of 60 Hz are shown in Figs. 4 (a) and (b), respectively. The DBD was uniformly generated at whole of the area. In this figure, however, we can see brighter color of discharge on the center part of the reactor because of very low solid angle due to the long length of the reactor. Figure 5 shows the temporal change of temperature inside the reactor generating DBD (8 kV, 2 kHz). The temperature was increased with time by the DBD, and reached from a room temperature to 300 ºC for 40 min DBD operation.

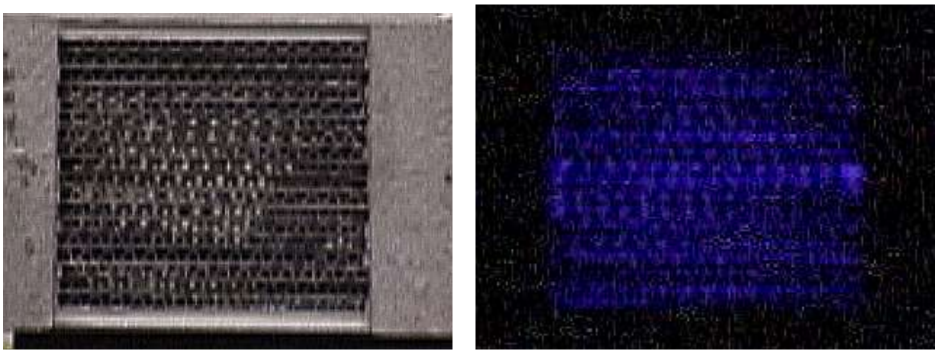
(a) (b)

Fig. 4. Photographs of (a) the front view of the reactor and (b) the DBD (12 kV, 60 Hz)

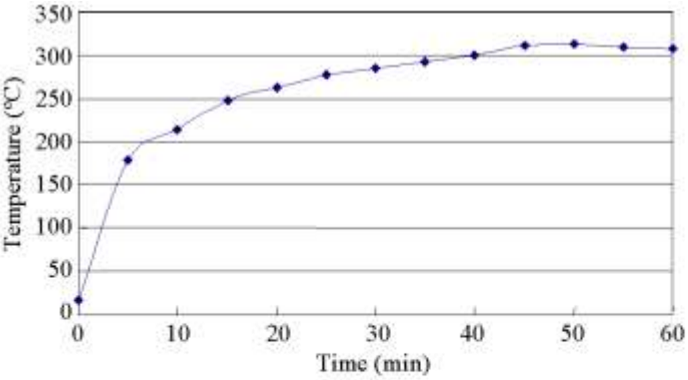

Fig. 5. Temporal change of temperature inside the reactor generating DBD (8 kV, 2 kHz)

Simultaneous decomposition DPM and NO*x*

The most important feature of this proposed method is that DPM and NO*x* with high concentrations in a closed (DBD) space are acts as the oxidant and reductant, respectively. It ensures the simultaneous decomposition of DPM and NO*x* with high energy efficiency. Therefore, we demonstrated decomposition of DPM and NO*x* by DBD under the conditions with and without each other. Using the same reactor as the one used at the DBD generation, carbon black (CB) imitating the DPM, because the DPM mainly consists of carbon and HC, was spread on the surface of the DBD electrode. Decompositions of NO in a model gas (NO 2250 ppm in O_2:10 %/N_2:90 %) by continuous DBD were comparatively investigated at the conditions with and without CB. Also, sum of CO and CO_2 concentrations at the outlet of the reactor was measured during DBD operation in some of model gases (O_2:10 % – N_2:90 % basis). The sum is corresponding to the amount of CB decomposition, because the CB is only the carbon source. The DBD was generated at 10 kV at 60 Hz, and the gas flow rate was kept at 2 ℓ/min. Figure 6 shows the NO concentration measured at the outlet of the reactor with and without CB. As for the case with CB, about 1400 ppm of NO was decomposed by the DBD, while about 650 ppm of NO was decomposed without CB. Also, the concentrations decrease with time for both cases. Figure 7 shows the sum of CO and CO_2 concentrations at the outlet of the reactor as a function of the ambient gas. The CB decomposition in NO containing gas is remarkably large compared with that without NO molecule. The concentration difference was about 400 – 600 ppm. It should be noted that drastic changes at first few minutes in Figs. 6 and 7 are caused by the response delay of the NO*x* and CO-CO_2 meters.

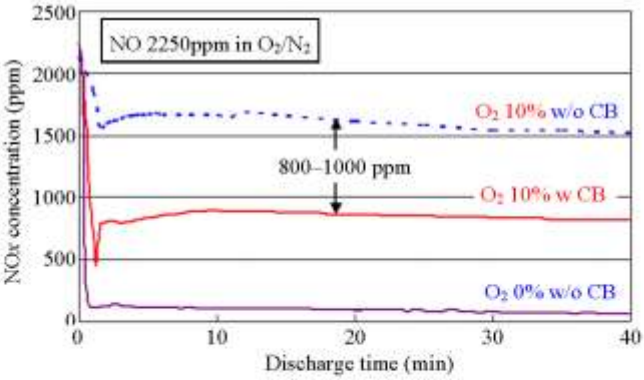

Fig. 6. NO*x* concentration at the outlet of the reactor with and without CB

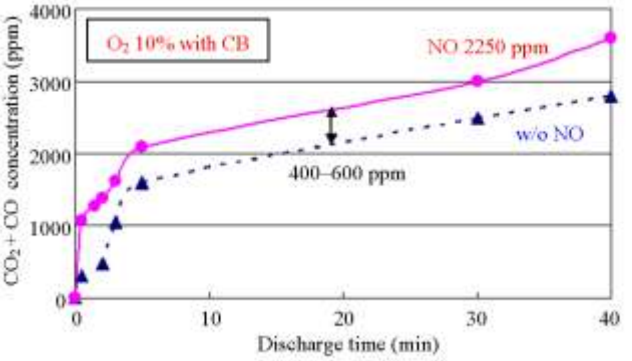

Fig. 7. Sum of CO and CO_2 concentrations at the outlet of the reactor as a function of the ambient gas

DISCUSSION

The PZA catalyst is seem to be useful as adsorbent/desorbent of NO*x* in diesel exhaust gases, because the adsorbing temperature is almost same as typical exhaust temperature (200 ºC), and the desorbing temperature around 400 ºC is not so high. The DBD generated with honeycomb-shaped PZA can easily increase the temperature to 400 ºC for 10 min when the treated gas temperature is 200 ºC (Fig. 3). DPM can be collected using the almost same design of the reactor that is used by DBD, therefore NO*x* and DPM densifications in a reactor using PZA honeycomb and electrostatic precipitator, respectively, can be easily achieved.

A nitric monoxide (NO), which is a main content in diesel exhaust gas, is easily oxidized to NO_2 in the DBD as following reaction (1). Then the DPM is directly oxidized by NO_2 as following reaction (2).

$$NO + O \rightarrow NO_2 \tag{1}$$

$$NO_2 + DPM \rightarrow CO_2\ (CO) + N_2 \qquad (2)$$

Actually, the difference between the NO*x* decompositions with and without CB is of about 800 – 1000 ppm (Fig. 6), and these values are almost two times larger than 400 – 600 ppm obtained from the difference between the CB decompositions with and without NO*x*. This result supports the simultaneous decomposition of DPM and NO*x* as following equation (3).

$$2NO + C\,(DPM) \rightarrow CO_2\ (CO) + N_2 \qquad (3)$$

Furthermore, as can be seen in Figs. 6 and 7, the decrease of NO*x* concentration and the increase of CO-CO_2 concentration with time passage are considered due to the temperature increase. In exact operation of this technique to the diesel engine, more effective decomposition is suggested because the decomposition takes place around 400 ºC in actual exhaust gas. These results suggest that this combination method of the DBD with a densification/localization technique can actually achieve a simultaneous decomposition of the DPM and the NO*x* from the diesel exhaust gas.

CONCLUSION

Series of the experiments aiming to effective and simultaneous decomposition of DPM and NO*x* in diesel exhaust gases using a combination of DBD with densification technique by electrostatic precipitation and honeycomb-shaped adsorbent have been demonstrated. Over 68 % of DPM was collected on the electrodes at DC 2 kV, and cyclic adsorption/desorption of NO*x* was shown to be achievable by the temperature control using the DBD. The NO*x* decomposition using the DBD in the existence of DPM was obtained to be about two times larger than that without DPM. DPM and NO*x* act as the oxidant and reductant, respectively, and are decomposed simultaneously and effectively by the DBD. It is considered that this technique is the most suitable for the aftertreatment of diesel exhaust gas.

ACKNOWLEDGEMENTS

This work has been partially supported by Grant-in-Aid for Scientific Research from the Ministry of Education, Science, Sports, Culture and Technology of Japan.

LITERATURE

[1] P. Hawker, G. Hüthwohl, J. Henn, W. Koch, H. Lüdders, B Lüers, P. Stommel, Effect of a continuously regenerating diesel particulate filter on non-regulated emissions and particle size distribution, *Society of Automotive Engineers*, No. 980189, 1998, pp. 374-380

[2] J. O. Chae, J. W. Hwang, J. Y. Jung, J. H. Han, H. J. Hwang, S. Kim, V. I. Demidiouk, Reduction of the particulate and nitric oxide from the diesel engine using a plasma chemical hybrid system, *Phys. Plasmas*, Vol. 8, 2001, pp. 1403-1410

[3] K. Muraoka, Y. Yamagata, Applications of barrier discharges for environmental problems, *Proceedings of the 1st Korea-Japan Joint Symposium on Energy and Environment (KIER, Korea, December 13-14, 2001)*, pp. 3-4

[4] Y. Yamagata, T. Matsui, T. Ebihara, K. Muraoka, Treatments of Environmentally Hazardous Materials by Combinations of Barrier Discharges with Densification by Adsorption/Trapping, *Proceedings of the 2nd Japan-Korea Joint Symposium on Energy and Environment (Kyushu University, Japan, October 15, 2002),* pp. 29-30

[5] B. Eliasson, V. Kogelschatz, Modeling and applications of silent discharge plasmas, *IEEE Trans. Plasma Sci.,* Vol. 19, 1991, pp. 309-323

[6] T. Yamamoto, K. Ramanathan, P. A. Lawless, D. S. Ensor, J. R. Newsome, G. H. Ramsey, N. Plaks, Control of volatile organic-compounds by an ac energized ferroelectric pellet reactor and a pulsed corona reactor, *IEEE Trans. Indust. Applicat.,* Vol. 28, No. 3, 1992, pp. 528-534

[7] H. H. Kim, K. Takashima, S. Katsura, A. Mizuno, Low-temperature NO*x* reduction processes using combined systems of pursed corona discharge and catalysts, *J. Phys. D – Appl. Phys.,* Vol. 34, No. 4, 2001, pp. 604-613

[8] N. Goto, S. Kudo, H. Motoyama, S. Ohyama, Direct decomposition technique for NO in O_2-N_2 mixture using barrier discharge and Cu zeolite, *Jpn. J. Appl. Phys. Part 2,* Vol. 41, 2002, pp. L64-L66

[9] H. Urae, Y. Yamagata, K. Muraoka, K. Yamada, H. Ymauchi, H. Okano, Removal of volatile organic compounds at low concentration using a combination of densification by a zeolite adsorption with a barrier discharge, *Trans. IEE Japan,* Vol. 122-A, No. 11, 2002, pp. 965-976 (*Japanese*)

[10] Y. Yamagata, T. Ebihara, S. Kuba, K. Muraoka, Aftertreatments of environmentally hazardous materials by combinations of barrier discharges with densification by adsorption/trapping, *Abstract for the 56th Gaseous Electronics Conference (San Francisco, CA, USA, Oct. 21-24, 2003),* No. QR2-3, p. 64

[11] Y. Yamagata, T. Matsui, T. Ebihara, K. Muraoka, Decomposition of diesel particulate materials and nitric oxides using a dielectric barrier discharge, *Proceedings of Electrostatics 2003 Conference (Edinburgh Conference Centre, Heriot-Watt University, Edinburgh, UK, Mar. 23-27, 2003), IOP Conf. SN 178,* 2004, pp.367-372

[12] Y. Yamagata, T. Ebihara, K. Misumi, K. Muraoka, Aftertreatment of diesel exhaust gas by combinations of dielectric barrier discharges with electrostatic precipitation, *Abstract of 7th APCPST/17th SPSM (Fukuoka, Japan, June29- July 2, 2004),* No. 30P-97, p. 637

[13] K. Eguchi, T. Kondo, T. Hayashi, H. Arai, Sorption of nitrogen oxides on MnO_y-ZrO_2 and Pt-ZrO_2-Al2O_3, *Appl. Cataly. B*, Vol. 16, No. 1, 1998, pp. 69-77

5th International Conference **ELMECO**
Nałęczów, Poland
September 2005

MEASUREMENT OF LOW GAS CONCENTRATION USING PHOTONIC CRYSTAL FIBER

Joanna Pawłat and Toshitsugu Ueda

Graduate School of Information, Production and Systems, Waseda University
808-0135 Fukuoka ken, Kitakyushu-shi, Wakamatsu-ku, 2-7 Hibikino, Japan
askmik@hotmail.com

Abstract

A high-sensitivity, compact set-up, enabling the precise measurement of a very low concentration of gas was designed. The micro-capillary gas flow phenomenon and the gas absorption inside fiber were estimated. Darcy - Weisbach equation for non-compressible flow and quasi - Panhandle equation for compressible gas flow were used for the calculation of the gas flow rate and gas velocity inside the PhC fiber. It was assumed that gas flowed mostly in the core. During the experimental part of work several types of PhC fiber of various parameters were used. The core diameters ranged from 10.9 to 19.9 μm. It was possible to measure the flow rate of the nitrogen gas inside the PhC fiber with various pressure differences on the opposite ends. Average velocity (Δp = 0.9 atm) ranged 0.17 m/s and was a little bit lower than expected.

Keywords: Low Gas Concentration Sensing, Photonic Crystal Fiber, Microcapillary Gas Flow

INTRODUCTION

The fast development of a semiconductor manufacturing industry encouraged our research group to engage in the development of a new measurement system. The results of preliminary research on in-situ measurement using tunable laser and glass or metal tanks as the gas cells were quite promising.

Precise measurement system for very low concentration of gas was designed. Besides high sensitivity, the priority was put on a low cost, portability, simplicity and possibility of completing the measurement in a relatively short time.

The goals of the research might be reported as follows:

1. Analysis of the micro-capillary gas flow phenomenon and the gas absorption inside fiber,
2. Examination of properties of photonic crystal fiber and design of the proper fiber for our device,

3. Engineering application: construction of in-situ measurement device, which will be able to work with small gas samples (0.01 cm^3), having the high resolution order (ppb level at MHz order of laser frequency).

In this paper study on the first task is presented. Ammonia (NH_3) and nitrogen were used as a model gases during the calculations. Ammonia causes various environmental and technical problems as a pollutant. Main of them is the contamination of clean rooms, where NH_3 decreases photolithography yield [1,2] and its detection requires an expensive and time-consuming ion chromatography measurement. Precise detection of low concentrations of ammonia is important for the monitoring of NH_3 seasonal changes in urban atmosphere. Proposed set-up might be used in automotive industry and for medical purposes as well.

EXPERIMENTAL SET UP

The system consisted of 3 sub-systems and optical fiber as a main measuring cell:

- gas providing sub-system,
- optical sub-system,
- chemical analysis sub-system and other measurements sub systems.

The main goal of the experiment was to measure sub-ppb concentration of ammonia where 19.5 ppm ammonia gas was diluted with high purity nitrogen to ppb level. Precise dilution process could be performed inside the 6-step mixing device. Gas was dosed into the gas cell of special design and it passed throughout the optic fiber for proper measurement of light absorption.

Two small control volumes: 0.64 and 1.27 cm^3 were used during measurement of the gas flow rate and its velocity. The inlet and outlet pressures were measured using MKS Baratron Type 622 pressure control with power supply readout MKS type 113 and Yokogawa Baratron, FP101A-ZZZ-LZ0A*B/Z with voltmeter. Typical manostats were also installed to roughly establish the pressure ranges. The gas- providing system is presented in Fig. 1.

1550 nm emission wavelength tunable laser was chosen for the optical measurement system. Light passed LPMM-05 objective lens, the zero-order waveplate 10RPO2-40 and was spitted using 12,7 mm cube beam splitter. The output light was guided inside the optic fiber from and to the gas cells, and passed LPMM-05 objective lens with the zero-order waveplate 10RPO2-40. Finally both: measurement light wave front and reference light wavefront (adjusted using mirror) were received by two photodetectors New Focus 2011-S. The working scheme of optical sub-system is depicted in Fig. 2. The emitted laser light, which wavelength corresponded with the absorption of the pollutant molecule should be partly absorbed by the ammonia gas within the optical fiber. The absorption would be strictly related to the concentration of NH_3 in the carrying gas (high-purity nitrogen).

Optical fiber is a glass or plastic fiber that has the ability to guide light along its axis in the centre with higher refractive index called core. The other elements of the fiber are lower refractive index cladding (which usually by total internal reflection traps the light in the core) and coating [3]. The single mode Photonic Bandgap fiber (PBG fiber) was used in the experiment. Relatively small core and single mode light-wave virtually eliminated most of distortion that could result from overlapping light pulses, providing the least signal attenuation and the highest transmission speeds.

The microscope photo of the photonic band gap fiber is shown in Fig. 3. The photonic crystal fiber had the unique structure, where the light guiding process was different than in the typical optic fiber: light was confined throughout a photonic bandgap.

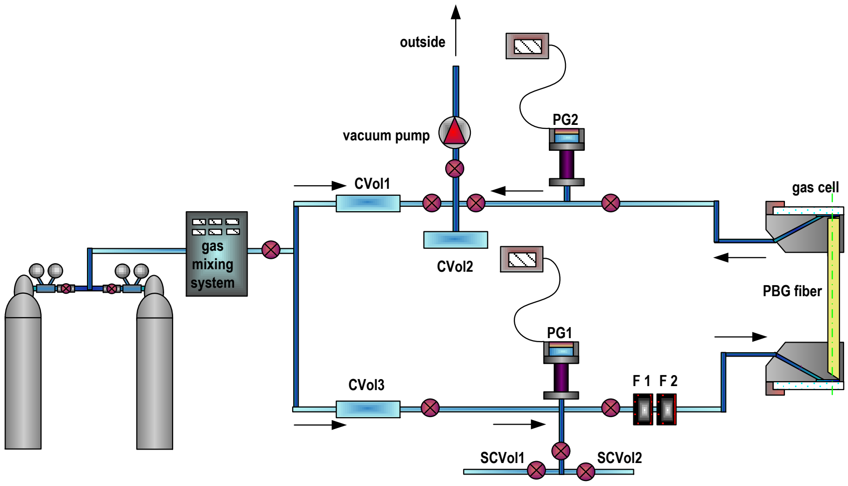

Fig. 1. Scheme of gas-providing sub-system:
PG1, PG2- pressure control, NV1-NV10- control valves, RF- relief valve, F1, F2- filters, CVol1-CVol3- control volumes, SmallCVol1, SmallCVol2- small control volumes, S1- spare connection

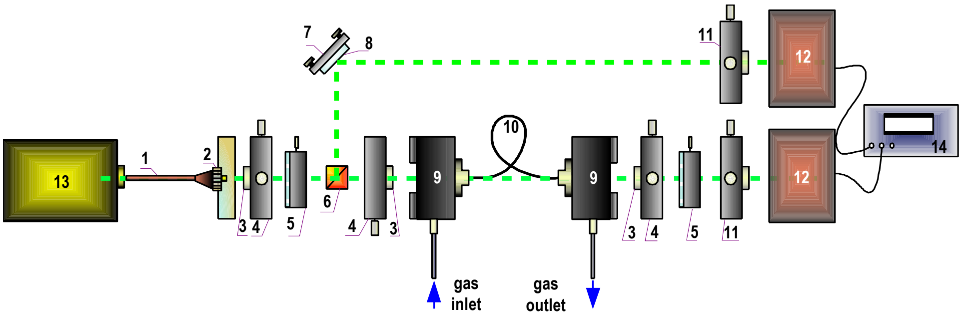

Fig. 2. Scheme of optical subsystem:
1- optical fiber, 2- optical fiber connector FC, 3- objective lens with adapter, 4, 11- stage, 5- rotary stage with zero-order waveplate, 6- beam splitter, 7- New Focus 9882, 8- mirror, 9- gas cell, 10- photonic crystal fiber, 12- auto receiver- photodetector, 13-tunable laser or lamp, 14-differential amperometer

It was mostly guided in a hollow, circular core surrounded by a microstructured cladding formed by a periodic arrangement of air holes in undoped silica. Up to 65 % of the fiber cross-section was composed of solid silica but less than 5 % of light propagated in glass. More than 90% of optical power was located in the hollow core or in the holes of cladding.

Holes of core and cladding were filled with the tested gas. Fiber was coated by single acrylate layer.

The new PBG fibers of 1960 nm center operating wavelength were especially developed for the research purpose. The core diameters of new fibers used in the experiment were: 15.2 µm, 16.2 µm, 19.4 µm, and 19.6 µm.

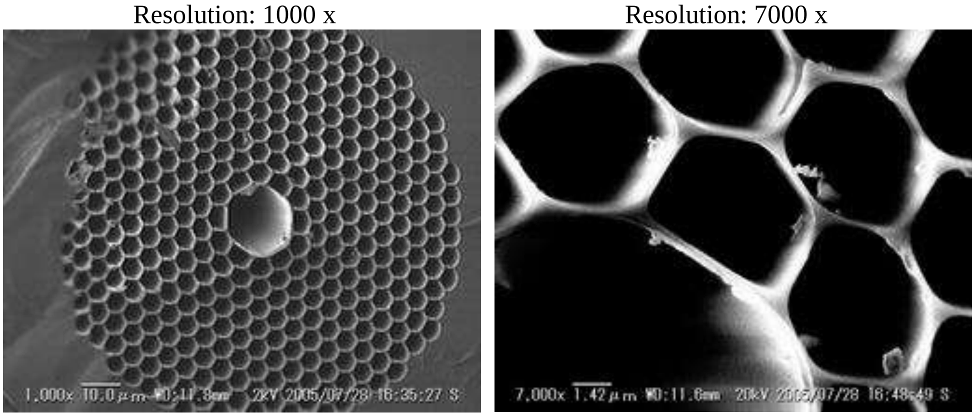

Resolution: 1000 x

Resolution: 7000 x

Fig. 3. Photos of photonic crystal fiber: core 16.2 μm (SEM) after cutting using adjustable fiber cutter

10 meters of fiber or using of etalon with short lengths are required to measure the ppb level of ammonia. However, on presented stage of the research, also shorter fibers from 20 cm up to 5 m were tested to check the pressure losses and to establish gas velocity, its flow rate and the lowest possible pressure difference between both ends of the fiber.

The optical microscope Keyence VQ-Z50, the scanning electron microscope (SEM) V-7800 and the violet laser microscope Keyence VK-9510 were used to take pictures of the optic fiber.

Avoiding of the pollution and the proper cutting of optic fiber had a crucial importance for the experiment. After adjusting the length, the coating of the ending part of fiber was removed and the core surrounded by cladding was put into ferrule and sealed with a CEMENT glue to prevent the leak of the gas. Ferrule was then attached to the gas cell. To enable the capillary gas flow within fiber of a very small diameter it was necessary to find the simple and appropriate cutting technique. The known ones could be particularized as follows: adjustable fiber cutter and vacuum pump, hot scissors, breaking after freezing in the liquid nitrogen, microtome, etching, laser ablation. The cut using most of above methods caused serious damages of the surface. In spite of the immediate cleaning with a high-pressure air gun on the microscopic photos damages and the remains of glass were easily seen. The most of the perforated area was blocked and the gas flow stopped. The best results were achieved using adjustable fiber cutter, what is shown in Fig. 3.

RESULTS AND DISCUSSION

Microcapillary nitrogen gas flow simulations were performed employing the standard mathematical software.

Both, the core and the cladding of optical fiber were perforated, but the calculations proved that the gas flow within the cladding might be neglected from the engineering point of view.

All presented results were obtained assuming gas flow within the core and 20°C temperature. Velocity of the gas was calculated from the pressure difference $\Delta p = p_1 - p_2$.

At first, the Darcy- Weisbach equation for non-compressible flow was applied to experimental conditions:

$$\Delta p = \lambda\,(l / d)\,(\rho v^2 / 2),\ [\mathrm{Pa}] \qquad (1)$$

Δp – pressure difference on both ends of the optical fiber, [Pa],
l - length of the reactor, [m],
d - core diameter, [m],
ρ - gas density at certain pressure, [kg/m^3],
v - gas velocity, [m/s],
μ - dynamic (absolute) viscosity, [Pa*s],
λ - coefficient, which depends on Reynolds number, for laminar flow ($Re < 2300$):

$$\lambda = 64/Re,\ [-] \qquad (2)$$

$$Re = (d\,v\,\rho)/\mu,\ [-] \qquad (3)$$

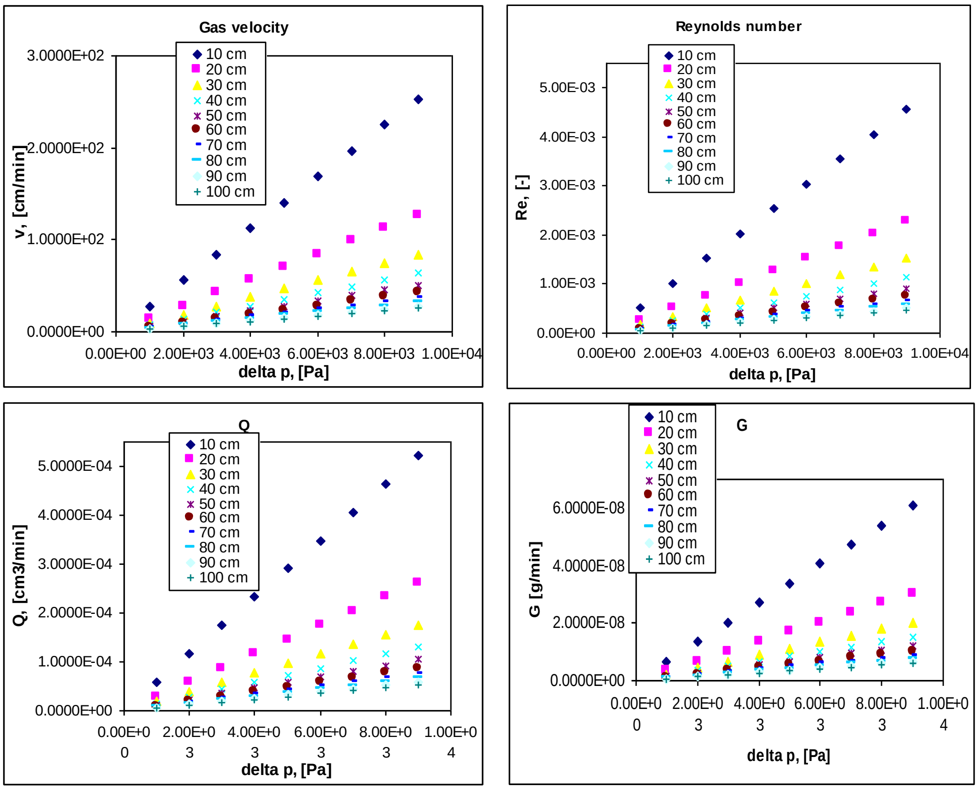

Fig. 4. Simulation of gas velocity, Reynolds number, flow rate and mass flow rate in dependence on the pressure difference for non-compressible flow

The result of gas velocity simulation is presented in Fig. 4. Velocity was calculated from the equation (1) for 16.2 μm core PBG fiber and various lengths from 10 cm to 1 m (primarily up to 10 m).

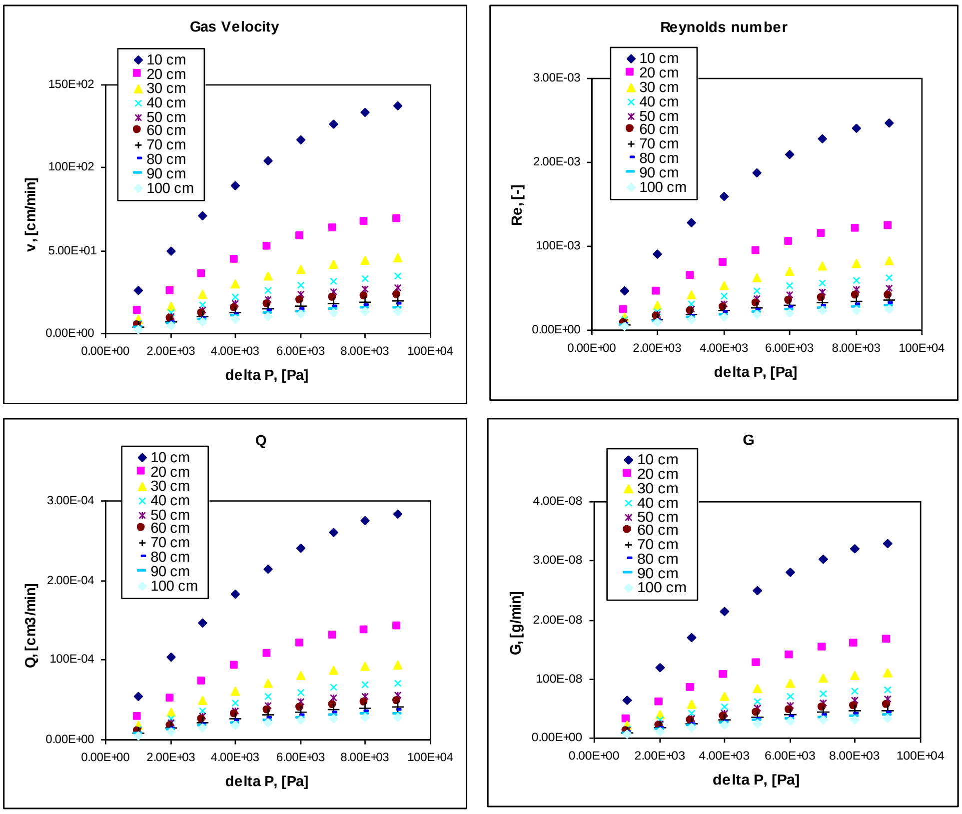

Fig. 5. Simulation of gas velocity, Reynolds number, flow rate and mass flow rate in dependence on the pressure difference for compressible flow

Gas flow rate Q was calculated after the establishing gas velocity inside the optic fiber using the equation (4):

$$Q = F\ v,\ [m^3/s] \qquad (4)$$

F - core cross-section area, $[m^2]$

The final calculation based on the previous was mass flow rate G inside the optic fiber.

$$G = \rho\ F\ v,\ [kg/s] \qquad (5)$$

Darcy-Weisbach equation does not take the compressibility into an account and obtained values for gas are different from the real case. Therefore, quasi-Panhandle equation (6) for modelling of the compressible fluid flow was also taken unto account.

$$p_1^2-p_2^2 = G^2RT/F^2\ (\lambda\ (l/d) + 2\log_e\ (v_2/v_1)),\ [Pa] \qquad (6)$$

Predicted gas flows were confirmed by the experimental results. It was possible to measure the flow rate of the nitrogen gas inside the PBG fiber with various pressure differences on the opposite ends. Time of pressure balancing time for such a fiber is depicted in Fig. 6.

Average velocity ranged 99.7 cm/min and 146.1 cm/min at p_1 and p_2, respectively. Average flow rates were 2.1 x 10^{-3} and 3 x 10^{-3} at 0.9 atm pressure differences for 16.2 μm core PBG fiber and p_1 and p_2, respectively.

That was in the order range between compressible and non-compressible flow simulation results. Such a flow still would be too slow for in-situ measurement in the case of set-up with 10 m length fiber.

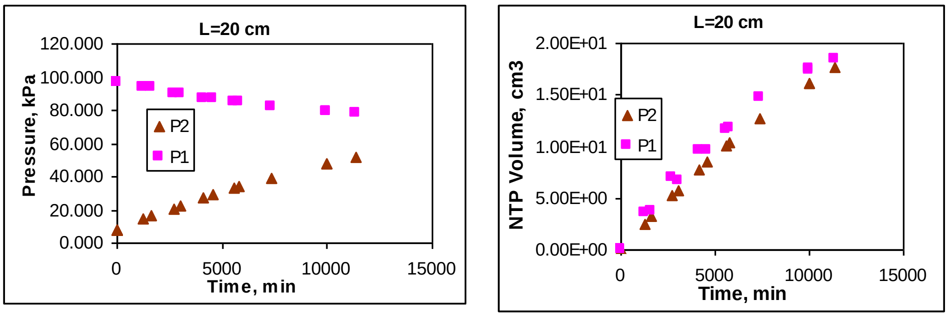

Fig. 6. The pressure change and volume change versus time for 16,2 μm core BPG fiber

Changing of the gas temperature would not significantly influence gas velocity. Only increasing of the core diameter of the fiber would cause an improvement in the gas conditions. In such a case, however, it might be difficult to preserve the single-mode character of the fiber.

To solve this problem in the next stage of experiment two solutions will be tested:
- using of etalon in optical circuit and short 1 m length fiber,
- designing of new single-mode fiber with the larger core with BANDSOLVE CAD tool.

CONCLUSIONS

The set-up for measuring of ppb concentration of ammonia was designed.

Simulations of mass flow rate and gas velocity in dependence on applied pressure, temperature and diameter of the optical fiber's core were performed.

Gas flow rate in the experimental condition was corresponding to the simulated one. Still, it was too slow to apply 10 m fiber. In that case, etalon should be used during the optical measurements. Eventually, the single mode light guiding fiber of maximal possible core diameter will be designed in the next stage of the research using BANDSOLVE software.

ACKNOWLEDGEMENT

This research was supported by the Grant-in-Aid of Japanese Ministry of Ecology and Natural Resources.

LITERATURE

[1] Dean K. and Carpio R., Proc. Interface ’94 OCG *Microlithography Seminar*, 1994, pp. 199-212

[2] MacDonald S., Clecak N., Wendt H., Willson C., Snyder C., Knors C., Deyoe N., Maltabes J., Morrow J., McGuire A. and Holmes S., *Advances in Resist Technology and Processing VIII, Proc.SP*IE, vol.1466, 1991, pp. 2-12

[3] Bjarklev A., Broeng J., Sanchez-Bjarklev A., *Photonic Crystal Fibers*, KLUWER Academic Publishers, 2003

5th International Conference **ELMECO**
Nałęczów, Poland
September 2005

INFLUENCE OF SILICON, OXYGEN AND NITROGEN ADMIXTURES UPON THE PROPERTIES OF PLASMA DEPOSITED AMORPHOUS DIAMOND-LIKE CARBON COATINGS

V. Buršíková[1], L. Zajíčková[1], P. Dvořák[1], D. Franta[1], V. Peřina[2]
and J. Janča[1]

[1]Department of Physical Electronics, Faculty of Science, Masaryk University,
Kotlářská 2, 611 37 Brno, Czech Republic
[2]Institute of Nuclear Physics, Czech Academy of Science,
25068 Rez near Prague, Czech Republic

Abstract

Amorphous diamond-like carbon films (DLC) with various silicon, oxygen and nitrogen content were deposited by plasma enhanced chemical vapor deposition (PECVD) technique. The films were prepared from the mixture of methane and hexamethyldisiloxane (HMDSO) in r.f. capacitively coupled discharges (13.56 MHz). The reactive plasma was investigated by optical emission spectroscopy and capacitive coupled planar probe. A combination of RBS, ERDA, FTIR and XPS methods was used to study the films' chemical composition and structure. The mechanical properties were studied using a depth sensing indentation technique. The films were mainly composed of C-C, C-H and C-Si bonds. The optimum deposition conditions for the preparation of DLC films, with enhanced thermo-mechanical stability, were determined.

INTRODUCTION

This paper discusses the unusual properties and possibilities of being able to grow uniformly over large areas of set thin DLC (hydrogenated amorphous diamond-like carbon) films as attractive protective coatings. The properties of these films are determined by the relative contribution of the sp^3 (diamond) and sp^2 (graphite) bonding configurations of carbon. In the case of plasma enhanced chemical vapour deposition (PECVD), the substrate is exposed to intense ion bombardment and therefore the carbon sp^3 hybridisation is preferentially created. One of the main problems for the application of DLC films is the high compressive intrinsic stress created in films due to intense ion bombardment. Moreover, the application of DLC films is limited, due to thermal degradation. According to our observations, the DLC films present stable properties up to about 280°C. When reaching this temperature the hydrogen loss commences an increased sp^2 character in the film.

In the present work, substantial success was achieved in the enhancement of the film's thermo mechanical stability by incorporating impurities, such as, silicon, oxygen or nitrogen into the carbon network. The modified DLC films were deposited in capacitively coupled r.f. discharge (13.56 MHz). The structure of the prepared films was studied with infrared absorption spectroscopy (FTIR) and X-ray photoelectron spectroscopy. Complete atomic compositions, including hydrogen content and film densities, were determined by combination of RBS and ERD analyses. The complex dielectric function of the films was determined from ellipsometric measurements in the range 1.5-5.2 eV. The mechanical properties were determined by depth sensing indentation technique, using the Fischerscope H100 tester. The surface energy was determined utilizing contact angle measurements using the SEE System. To determine the plasma diagnostics, optical emission spectroscopy, capacitively coupled planar ion flux probe measurements and gas chromatography, with mass spectrometry of stable plasma products, were used.

EXPERIMENTAL PROCEDURES

The DLC:SiOx films were prepared in r.f. capacitive discharges at low pressures (8-11 Pa) from a mixture of methane (CH_4) and HMDSO. The reactor was a glass cylinder with two, inner parallel plate electrodes, made of graphite. The bottom electrode, with the diameter of 150 mm, was coupled to the r.f. generator (13.56 MHz) via a blocking capacitor. The substrates, for deposition (silicon wafers and glass), were placed on the r.f. electrode, the r.f. voltage of which was superimposed with a negative d.c. self-bias. The r.f. power was in the range 50 to 250 W . The corresponding self-bias voltage varied from -250 V to -600 V depending on the gas mixture, applied power and deposition pressure. The DLC:SiO_x films were prepared from a mixture of methane and HMDSO (hexamethyldisiloxane - $Si_2OC_6H_{12}$). This basic mixture was used either, without any additional gas, or with an admixture of argon, hydrogen or nitrogen. In the second case the flow rate of admixed gas ranged from 0.35sccm to 7sccm. The CH_4 flow rate was varied in the range; 1.4 sccm to 2.85 sccm. The HMDSO flow rate Q_{HMDSO} varied from 0 to 0.87 sccm.

RESULTS AND DISCUSSION

The dissociation and excitation of the deposition gas mixtures were observed by means of optical emission spectroscopy (Jobin-Yvon TRIAX 550 spectrometer equipped with CCD detector).

As concern atoms the only hydrogen emission lines were detected suggesting that the dissociation of original gases is not completed. However, the hydrogen radicals are important for deposition of hard DLC films because they are able to etch, weak sp^2 bonded carbon. Alongside hydrogen Balmer serie the emission of H_2 molecules dominated in the emission spectra. From the "film building" radicals we have observed relative weak emission from excited CH_2 and CH radicals. The emission of CH_3 radicals, often referred to as "the most abundant species in case of DLC deposition", could not be observed because it's position in VUV/UV was beyond our detection range. The products, exclussive of the HMDSO molecule, were evidenced by an increased deposition rate, [6] but, however, not by emission lines or bands. However, an effect of the HMDSO addition was observed as changed dissipation of energy into rotational and vibrational molecular states. This was estimated by vibrational and rotational temperatures calculated from the nitrogen second positive system, when a small amount of nitrogen was added into the gas feed. The vibrational and rotational temperatures increased from 2500 K to 4000 K and from 340 K to 390 K, respectively, with increasing HMDSO flow rate up to 0.36 sccm (see Fig. 1 and 2). Above this flow rate, both the temperatures were constant, within the range of experimental error.

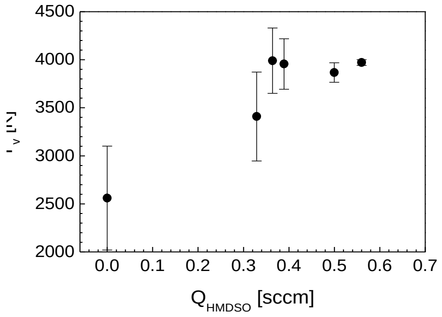

Fig. 1. Vibrational temperature calculated from the nitrogen second positive system, sequence Δν=-2, as function of the HMDSO flow rate

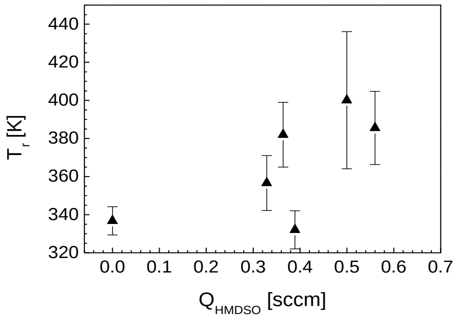

Fig. 2. Rotational temperature calculated from the nitrogen (0,2) second positive system as function of the HMDSO flow rate

For the properties of the growing layers the ion current density to the substrate is of great significance. The measurement of the saturated ion current was carried out by means of the capacitively coupled planar probe [7]. In this experimental procedure, the upper electrode was used as the planar probe. It was found that the current density was constant for the HMDSO flow rate from 0 to 0.4 sccm. Above this value, the current density fell to 80% of the original value in case of the highest HMDSO flow rate used. This effect can be related to increasing mass of the ions related to oligo-/polymer formation in the plasma [8].

Table 1. Parameters describing the atomic concentrations of DLC:SiO$_x$ films

atoms	ai	bi	ci
C	2.7	63.9	60
H	2	35.4	130
Si	2.4	0.2	46
O	5	0.5	20

The films were investigated by infrared absorption spectroscopy (FTIR), X-ray photoelectron spectroscopy (XPS) and Rutherford backscattering, spectrometry, (RBS) combined with elastic recoil detection analysis (ERDA) in order to assess the film’s chemical structure and composition. The bulk concentrations of carbon, hydrogen, silicon and oxygen atoms, composing the DLC:SiOx films were obtained by RBS and ERDA. Similarly to the atomic concentrations in the gas feeds, the atomic concentrations in the films can be generally described using the formula

$$f_i(q) = \frac{b_i + c_i q}{1_i + a_i q} \qquad (1)$$

where *q* is the HMDSO-to-methane flow rate ratio, *i* indexes the atoms and a_i, b_i , c_i are corresponding parameters. The parameters ai, bi, ci found by fitting the experimental dependences obtained on 11 samples are summarized in Table 1. The carbon content decreases from 65 to 40 % with increasing HMDSO flow rate while silicon, oxygen and hydrogen increase from 0 to 12 %, from 1 to 3 % and from 35 to 46 %, respectively. It has been already shown that the oxygen-to-silicon ratio was about 0.29, independently on the HMDSO flow rate [6].

The chemical bonds were qualitatively observed by FTIR. A typical IR transmittance of the films is shown in Fig. 3 for the film deposited at the HMDSO flow rate of 0.5 sccm. The broad band in the range 2800-3000 cm^{-1} is related to C-Hn stretch absorption bands (n=1,2,3) where carbon is in the sp^3 or sp^2 hybridisation [9,10]. The peaks corresponding to the sp2 hybridisation, typical for soft graphite-like films, are situated above 2950 cm^{-1}. I can be seen below that the DLC:SiO_x films deposited at HMDSO flow rate of 0.5 sccm still exhibit relatively high hardness, in agreement with very low absorption above 2950 cm^{-1}.

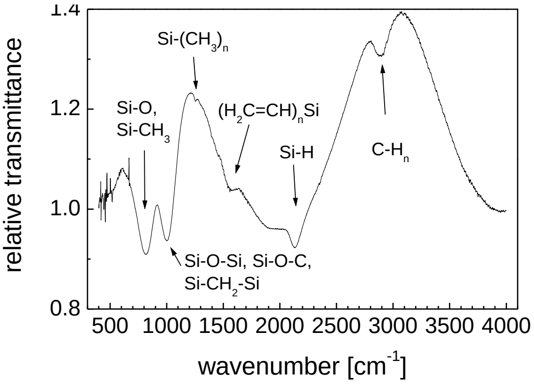

Fig. 3. Transmittance of the DLC:SiO_x film divided by the transmittance of bare silicon substrate. The 1400 nm thick film was deposited at the HMDSO flow rate of 0.5 sccm

Several absorption features caused by the presence of Si can be found in the FTIR spectra. The band around 2130 cm^{-1} is associated with Si-H bonds [11,12]. Its position suggests that Si is further bonded to C or H rather than in siloxane structure. The broad band around 1580cm^{-1} is related to the $(H_2C=CH)_nSi$ groups [13] and the small peak at 1255 cm^{-1} can, with little reason for doubt, be assigned to Si-$(CH_3)_n$ bonds [11]. The broad peaks at 1002 and 815cm^{-1} are hard to relate to some single bonds because there are characteristic frequencies for the vibrations of different chemical groups there. Moreover, the relative high width of the peaks suggests they may be even composed of several absorption bands. In the range 1020-1090 cm^{-1} one can find Si-O-Si, Si-O-C or Si-CH_2-Si [11,14]. The SiO-CH_3 and Si-CH_3 bonds cause absorption in the range 1000-1100 cm^{-1} and 980-990 cm^{-1}, respectively [11,14]. In the position around 815 cm^{-1} the absorption due to Si-CH_3 or Si-O-Si groups can be found [11]. Therefore, an important question, concerning, the presence of Si-O-Si bonds in the films arises. It may be answered with a help of the Si-O-Si rocking band positioned at 450 cm^{-1} that do not coincide with other bonds and therefore has been already used for the determination of the Si-O-Si incorporation rate [14].

The transmittance is very noisy in this region but it seems that the amount of silicon oxide bonds in the films has to be very low.

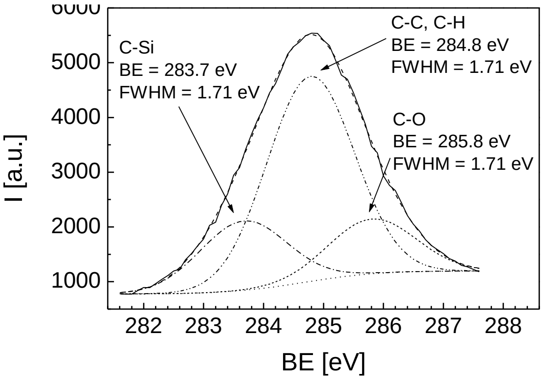

Fig. 4. C1s XPS signal deconvoluted into three Gaussian profiles associated with C-Si, C-C (C-H) and C-O bonds for the films deposited at 0.54 sccm HMDSO flow rate

XPS analyses showed that the surface regions of the DLC:SiOx films (maximum depth of 5 nm) contain more oxygen than the bulk film. In fact, the oxygen-to-silicon ratio decreases from 2.5 in case of the HMDSO flow rate of 0.17 sccm, to about 1.0 for higher HMDSO flow rates, which is still more than three times higher than in the film. The deconvolution of the C1s and Si2p atomic signals into several Gauss profiles give the information about the chemical bonds in the surface region. In general, the C1s signal was deconvoluted into three Gaussian profiles assigned to the C-C, C-H bonds (the most intensive peak), the C-Si and C-O bonds [15]. Such deconvolution is depicted in Fig. 4 where the position of the whole C1s signal was shifted in such a way that the C-C, C-H peak was centered at 284.8 eV (correction for charging). The percentage of C-C, C-H bonds decreased with increasing HMDSO flow rate from 85 to 69 % on the cost of the C-Si bonds. The maximum of C-Si bonds was 27 %. The percentage of C-O bonds oscillated between 5 and 17 % without any clear dependence on the deposition conditions. It is worth to noting that, although we did not observed any C-O bonds in the FTIR spectra of the films, the carbon was obviously bonded to oxygen in the surface region. Similar results were found for silicon bonded, either to carbon, or to oxygen in the surface region.

The depth sensing indentation (DSI) with Fisherscope H100 tester was used to determine the microhardness HU_{pl} and the elastic modulus Y of the DLC:SiO_x films. Here, $Y= E/(1-\nu^2)$ where E is the Young’s modulus and ν is the Poisson’s ratio. In the case of relatively thin films, the substrate material parameters may substantially influence the measured values, due to combined elastic and plastic responses to the coating and the substrate. Therefore, the mechanical properties of the coating/substrate systems were measured for several different maximum applied loads. In this way several values of the apparent plastic hardness, i.e. plastic hardness of the coating/substrate system was obtained and the substrate influence was successively eliminated on the basis of these measurements.

The HMDSO addition had a beneficial effect on the mechanical properties of the DLC:SiO_x films as far as the fracture toughness and the mechanical stability were concerned. The deposited films were smooth, homogenous and pinhole-free. The optimum microhardness was found for coatings deposited on silicon substrates at HMDSO flow rate

Q_{HMDSO} ranging approximately from 0.1 to 0.5 sccm. The film microhardness in this range reached the microhardness of DLC films prepared without HMDSO addition.

The fracture toughness of the DLC:SiO_x films was studied on the basis of the critical indentation depth. The critical indentation depth at which the first cracking or delamination occur was determined from load/penetration curves and from optical micrographs of the indentation prints after removing the indenter. The fracture toughness of the DLC:SiO_x films increased with the HMDSO flow rate up to 0.4 sccm and than decreased again. The lowest fracture toughness was observed for the coatings prepared either from pure methane or pure HMDSO.

CONCLUSION

We have deposited DLC:SiO_x films with different amounts of SiO_x groups. The films were mainly composed of C-C, C-H and C-Si bonds. No C-O bonds were detected in the films. The presence of Si-O bonds in the films could not undoubtedly be determined by FTIR. The concentration of silicon and oxygen increased with increasing HMDSO flow rate. The film surfaces were richer in oxygen and consequently the Si-O and C-O bonds were observed by XPS. The film hardness, elastic modulus, interfacial fracture toughness was studied in dependence on silicon and oxygen concentration. It was found that the incorporation of silicon and oxygen (SiO_x) into the DLC network significantly increased the interfacial fracture toughness and decreased the compressive stress in the films compared to pure DLC coatings. We have determined the optimum silicon and oxygen percentage in the DLC network at which the thermo-mechanical stability of the DLC films was improved, whilst keeping the useful DLC properties.

ACKNOWLEDGEMENT

The present work was supported by the Ministry of Education of the Czech Republic, contracts MSM0021622411.

REFERENCES

[1] L. Martinu, Plasma Processing of Polymers, ed. R.D. Agostino et. al., Kluwer Academic Publisher, NATO ASI Series E: **346**, 247,1996

[2] C. De Martino, G. Fusco, G. Mina, A. Tagliaferro, L. Vanzetti, L. Calliari and M. Anderle, *Diamond and Related Materials* 6, 559, 1997

[3] S. S. Camargo Jr., R. A. Santos, A. L. Baia Neto, R. Carius and F. Finger, *Thin Solid Films* **332**, 130, 1998

[4] V. Buršíková, V. Navrátil, L. Zajíčková and J. Janča, *Mater. Sci. Eng*. **A324**, 251, 2001

[5] D. Franta, I. Ohlídal, V. Buršíková and L. Zajíčková, Diamond Rel. Mater.**12**, 9,1532-1538, 2003

[6] L. Zajíčková, V. Buršíková, V. Peřina, A. Macková and J. Janča, *Surface and Coating Technology* **174 – 175** (2003) 281 – 285

[7] N. St. J. Braithwaite, J. P. Booth and G. Gunge, *Plasma Sources Sci. Technol*. 5, 667, 1996

[8] D. Franta, I. Ohlídal, V. Buršíková and L. Zajíčková. *Thin Solid Films,* **455-456**, 1 393-398,

[9] B. Dischler, A. Bubenzer and P. Koidl, Solid *State Communications***, 48** (2), 105, 1983

[10] G. Herzberg, Infrared and Raman spectra of polyatomic molecules, Van Nostrand, Princeton N. J., 1945

[11] S. F. Durrant, R.P. Mota and M.A. Bica de Moraes, *Vacuum*, 4**7**(2), 187, 1996

[12] K. Aumaille, C. Vallee, A. Granier, A. Goullet, F. Gaboriau, and G. Turban, *Thin Solid Films*, **359**, 188, 2000

[13] M. Horák and D. Papoušek, Infrared Spectra and Molecular Structure, Academia, Praha, 1976

[14] M. T. Kim *Thin Solid Films*, **311**, 157, 1997

[15] N. Fourches, G. Turban and B. Grolleau, *Appl. Surf. Sci.*, 68, 149, 1993

[16] J. Malzbender, G. de With, and J. M. J. den Toonder, *Thin Solid Films*, **366**, 139, 2000

5th International Conference **ELMECO**
Nałęczów, Poland
September 2005

STARK BROADENING TO DETERMINE THE ELECTRON DENSITY IN MICROWAVE TORCH PLASMAS

Mariusz Jasiński, Jerzy Mizeraczyk, Zenon Zakrzewski

Centre for Plasma and Laser Engineering
The Szewalski Institute of Fluid-Flow Machinery, Polish Academy of Sciences
Address: J. Fiszera 14, 80-231 Gdańsk, Poland
E-mail: mj@imp.gda.pl

Abstract

We present results of the spectroscopic investigation of the electron density in a microwave torch plasma (MTP) generated in atmospheric pressure Ar flow. The electron density in the MTP was determined using two approaches based on the Stark broadening of H_β *spectral line emitted by the plasma.*

Keywords: electron density, microwave torch plasma, stark broadening

INTRODUCTION

Recently, the microwave torch plasma (MTP) in gases at atmospheric pressure has been found attractive for decomposition of gaseous pollutants (e.g. [1-4]). Since electron reactions play an important role in the gas pollutants decomposition in MTPs, the knowledge of the electron density in such plasmas is crucial for understanding the chemical kinetics of the gas decomposition process and its optimization.

In this paper we present results of the spectroscopic investigations of the electron density in a microwave torch plasma in atmospheric pressure Ar flow. A small amount (about 1 % vol.) of water vapour was added to the Ar flow to obtain a detectable intensity of H_β emission spectral line for the electron density measurement. The electron density in the MTP was determined using the method based on the Stark broadening of H_β spectral line spontaneously emitted by the plasma. The H_β spectral line (486.13 nm) of the hydrogen Balmer series was observed in the MTP emission spectrum due to dissociation of the water vapour in the Ar MTP flame.

The measured profile of an emission line can be affected by different mechanisms of broadening [5]: natural, thermal Doppler, Stark (collisional) broadening, instrumental, etc.

Generally, majority of the broadening mechanisms result in the emission lines with the Gaussian profile, except for the Stark broadening, which generates the Lorentzian profile in the emission lines [5]. The convolution of the Lorentzian (Stark) and Gaussian profiles results in the so-called Voigt profile.

In this investigations, the measured H_β line profile was fitted using the Voigt function in order to estimate the full width at half maximum (FWHM) of the Lorentzian (Stark) profile $\Delta\lambda^{Stark}(H_\beta)$.

The electron density in the MTP was determined using either GKS theory or Gig-Card theory.

In the GKS theory (Griem, Kolb and Shen [6]), the Stark broadening is estimated in a quasi-static approximation using the classic Holtsmark field, resulting in the relation [5]:

$$n_e = [10^9 \cdot \Delta\lambda^{Stark}(H_\beta)/(2.5 \cdot \alpha_{1/2})]^{1.5} \quad [cm^{-3}], \qquad (1)$$

where $\Delta\lambda^{Stark}(H_\beta)$ is measured in nm when n_e is expressed in cm^{-3}. The $\alpha_{1/2}$ parameter (fractional semi-half-width) is tabulated in [7]. We interpolated these discrete points as shown in Fig. 1. The simple relation obtained by Goktas et al [8], for the electron temperature in the range of 1-4 eV and for electron densities between 10^{14} and 10^{18} cm^{-3}, is

$$n_e = 1.09 \cdot 10^{16} \cdot [\Delta\lambda^{Stark}(H_\beta)]^{1.458} \quad [cm^{-3}], \qquad (2)$$

where $\Delta\lambda^{Stark}(H_\beta)$ is in nm.

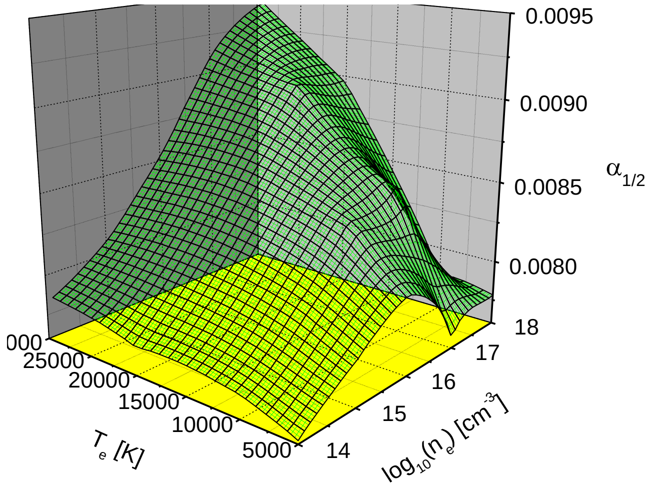

Fig. 1. Approximated values of $\alpha_{1/2}$ as a function of electron temperature T_e and electron density n_e based on discrete points tabulated in [7]. The $\alpha_{1/2}$ parameter is in nm per cgs field strength unit

The Gig-Card theory (Gigosos and Cardenoso [9]) is a more recent and it incorporates the ion dynamics to evaluate the Stark broadening of lines spontaneously emitted by the plasma [5], resulting in the relation between $\Delta\lambda^{Stark}(H_\beta)$, n_e and T_e tabulated in [9]. We interpolated these discrete points as shown in Fig. 2.

From the data shown in Fig. 2, we obtained a simple relation between $\Delta\lambda^{Stark}(H_\beta)$ and n_e in the form of:

$$n_e = 10^{16} \cdot [\Delta\lambda^{Stark}(H_\beta)]^{1.55} \quad [cm^{-3}], \tag{3}$$

where $\Delta\lambda^{Stark}(H_\beta)$ is in nm.

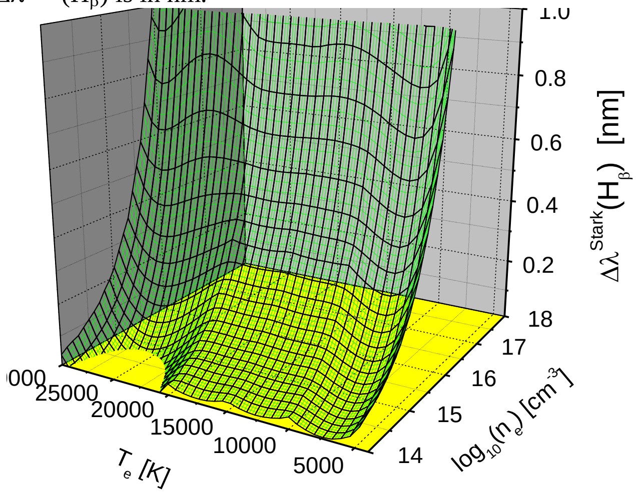

Fig. 2. Approximated values of $\Delta\lambda^{Stark}(H_\beta)$ as a function of electron temperature T_e and electron density n_e based on discrete points tabulated in [9]

EXPERIMENTAL SETUP

The main components of the experimental setup used in this investigation were the 2.45 GHz magnetron generator, the microwave plasma torch, the microwave power supplying and measuring system, the gas supplying and flow control system, the spectrograph for emission line analysis terminated with a CCD camera, and a PC computer. The MTP uses a TIAGO concept disclosed by Moisan et al [10]. The microwave torch structure is based on a modified WR 430 rectangular waveguide. A conical nozzle is placed in a reduced-height section of the waveguide. The inner diameter of the nozzle channel was about 1 mm. A hollow circular Teflon seal was placed around the nozzle inside the reduced-height section of the waveguide. The microwave power, up to 500 W was fed directly through the waveguide from the magnetron generator at one end of the torch structure while the opposite end was terminated with a movable plunger. The plasma was sustained in the form of a "plasma flame" at the end of the nozzle protruding from the reduced-height waveguide section.

The working gas (atmospheric pressure Ar with a small amount of water vapour) flowed at atmospheric pressure at a rate of 1÷2 l/min and exited through the nozzle at its conical tip to be ionized and form the plasma flame. The microwave power delivered to the discharge was calculated as P_I-P_R, where P_I and P_R are the incident and reflected powers, respectively.

To investigate the H_β spectral line profile, the light emitted by the plasma flame was focused onto the entrance slit of the spectrograph [DK-480 (CVI), (1200 grooves/mm)], where the emission lines were selected and then their intensities recorded with the CCD camera. In this investigations the width of the entrance slit of the spectrograph was 10 μm.

Two horizontal slits (that is, in a plane perpendicular to the plasma flame axis) were placed between the plasma flame and the optical lens to collimate the light from a selected section of the plasma flame, about 1 mm in height and covering the whole plasma flame width.

The instrumental line profile is assumed to be nearly Gaussian with a FWHM of about 0.015 nm. The gas temperature in argon MPT flame ranged about 1000-4000 K [11, 12], depending on the location within the flame. For this temperature interval, the corresponding Doppler widths are of the order of 0.01 and 0.02 nm for H_β spectral line. Hence, the resulting Gaussian line width was of the same order. This is small compared to the $\Delta\lambda^{Stark}(H_\beta)$ measured by us.

Fig. 3 shows the photo of a typical MTP flame generated in atmospheric-pressure argon flow at a microwave power of 100 W and argon flow rate of 1 l/min. For these conditions the MTP flame mainly consisted of a dense core, surrounded by a tenuous plasma shell.

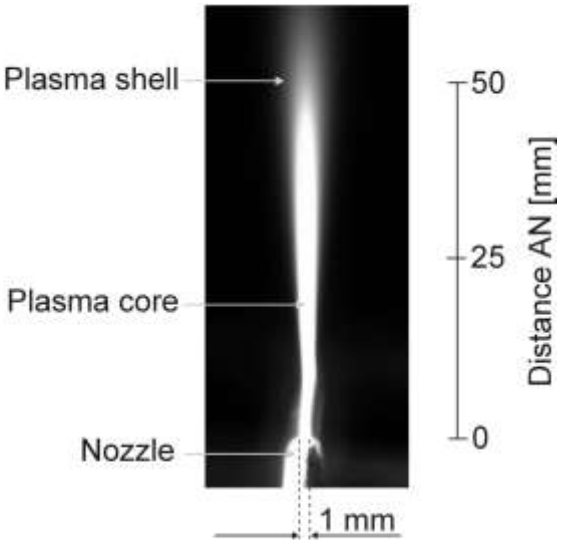

Fig. 3. Photo of the atmospheric-pressure argon MTP flame. Microwave power – 100 W, argon flow rate – 1 l/min. The MTP flame mainly exhibits a strong core; AN – above the nozzle

RESULTS AND DISCUSSION

Fig. 4 shows an example of the measured H_β spectral line profile and the Voigt profile fitted to the experimental points. The measured H_β line profile was fitted using the Voigt function with a Gaussian line width of 0.02 nm. The found value of the FWHM of the Lorentzian (Stark) profile $\Delta\lambda^{Stark}(H_\beta)$ allowed to calculate the electron density using the formula (2) [GKS theory] or (3) [Gig-Card theory].

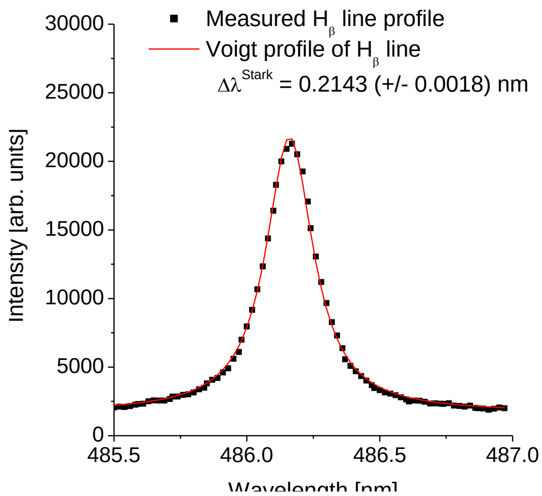

Fig. 4. Measured H$_\beta$ line profile and the Voigt function fit. Microwave power – 100 W, argon flow rate – 1 l/min. The location within the flame – about 8 mm above the nozzle

Figs. 5 and 6 show the electron density n_e in the argon plasma flame (0.5 mm and 5 mm above the nozzle) as a function of microwave power for two argon flow rates. As it can be seen, the electron density increases with increasing microwave power delivered to the discharge. The electron density is slightly higher for the higher argon flow rate. This behaviour is in a good agreement with the observations of other researchers (e.g. [11]). The higher electron density at the higher argon flow rate is probably due to a decrease of MTP flame volume observed by us when increasing the gas flow rate. This causes that the microwave power delivered to the unit volume of the flame is higher, resulting in the higher electron density.

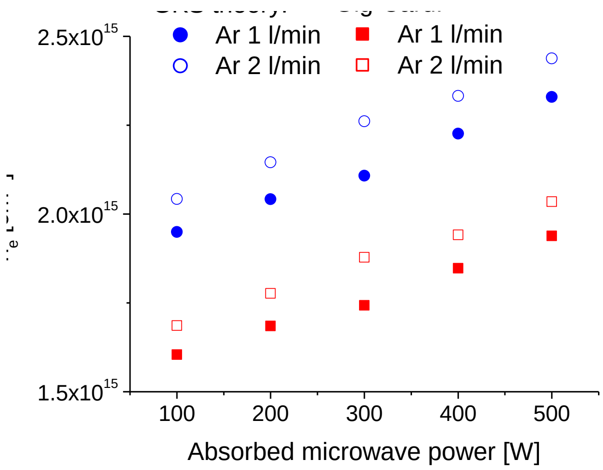

Fig. 5. Electron density n_e in the argon MTP flame (0.5 mm above the nozzle) as a function of microwave power for two argon flow rates.

The values of the electron densities are similar to those presented in [11-14].

Fig. 7 shows the electron density n_e in the argon plasma flame as a function of distance above the nozzle (AN). The microwave power and argon flow rate were 100 W and 1 l/min, respectively. For these parameters, the MTP flame was stable and it allowed us to measure the electron density along the MTP flame. The height of the MTP flame was about 50 mm and the flame mainly consisted of the plasma core (Fig. 3).

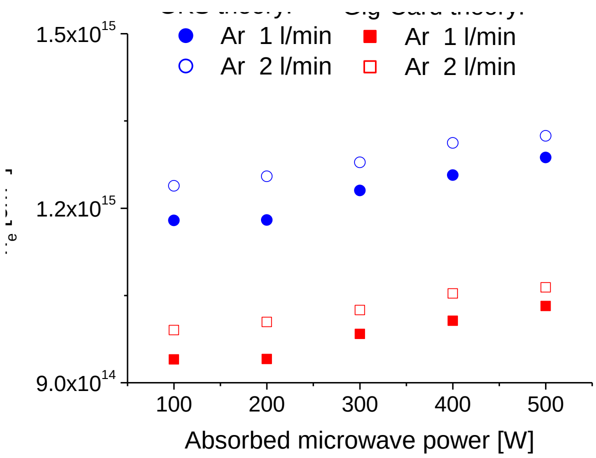

Fig. 6. Electron density n_e in the argon MTP flame (5 mm above the nozzle) as a function of microwave power for two argon flow rates

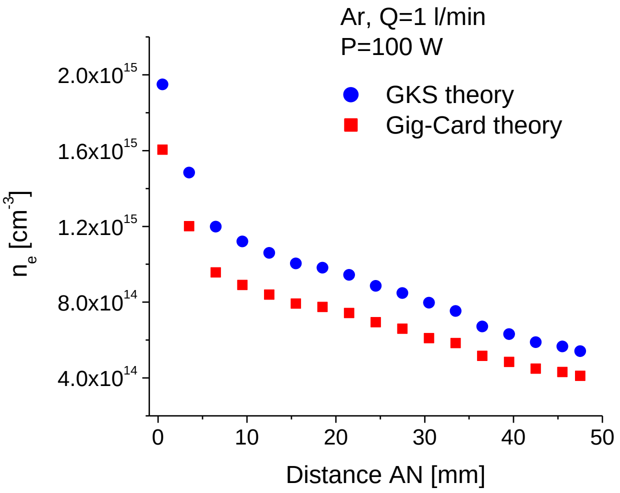

Fig. 7. Electron density n_e as a function of distance above the nozzle (AN) in the argon plasma flame. Microwave power P = 100 W, argon flow rate Q = 1 l/min

As shown in Fig. 7, the electron density decreases from about 2×10^{15} cm^{-3} to 5×10^{14} cm^{-3} with increasing distance AN from 0.5 mm to 47 mm. These results are similar to those reported in [13, 14]. The linear n_e decrease starts at 5 mm above the nozzle. We suppose that it is the outset point of the plasma sustained by a surface wave propagating along the flame core.

Generally, the Gig-Card theory gives lower (by about 20 %) values of electron densities than GKS theory. This behaviour is in a good agreement with the observations described in [5].

We found, that the detectable intensity of H_β emission spectral line for the electron density measurement by Stark broadening could be obtained only from the argon MTP flame core. The intensity of the light emission from the plasma shell was not sufficient for such a measurement.

SUMMARY AND CONCLUSIONS

We measured the electron density in the MTP generated at atmospheric-pressure argon flow using Stark broadening method. It ranged from $5 \times 10^{14}\ \mathrm{cm}^{-3}$ up to $2 \times 10^{15}\ \mathrm{cm}^{\ 3}$, depending on the discharge conditions and the location along the plasma flame. The obtained electron densities in the atmospheric-pressure Ar MTP flame are similar to those obtained in atmospheric-pressure Ar microwave torch discharges by other researchers.

Such a high electron density is sufficient for efficient microwave plasma decomposition of many gaseous pollutants.

The values of the electron densities obtained in this investigation can be used as input parameters for the modeling of processes in the MTP.

We suppose that the MTP in the region where the electron density decreases linearly along the MTP flame is sustained by a surface wave.

At present, our aim is to use the Stark broadening of H_β and H_γ lines for determining the electron temperature in the MTPs based on the procedure recently proposed by Torres et al [5]. This allows simultaneous determination of the electron temperature and electron density in the MTPs.

ACKNOWLEDGEMENT

This work was supported by the State Committee for Scientific Research (KBN) under programme PB 1124/T09/2003/24 and by the Institute of Fluid Flow Machinery, Polish Academy of Sciences under programme IMP PAN O3Z3T2 and O3Z1T1.

LITERATURE

[1] M. Jasiński, J. Mizeraczyk, Z. Zakrzewski, T. Ohkubo, J.S. Chang, *J. Phys. D: Appl. Phys.*, vol. 35, 2002, pp. 2274-2280

[2] M. Jasinski, J. Mizeraczyk, Z. Zakrzewski, *J. Adv. Oxid. Technol.*, vol. 40, 2004, pp. 51-58

[3] M. Jasiński, J. Mizeraczyk, Z. Zakrzewski, J.S. Chang, *Czech. J. Phys.*, vol. 52D, 2002, pp. 743-749

[4] M. Jasiński, J. Mizeraczyk, Z. Zakrzewski, *Journal of High Temperature Material Processes*, vol. 6, 2002, pp. 317-320

[5] J. Torres, J. Jonkers, M. J. van de Sande, J. J. A. M. van der Mullen, A. Gamero and A. Sola, *J. Phys. D: Appl. Phys.*, vol. 36, 2003, pp. L55-59

[6] Griem H. R., Kolb A. C., Shen K. Y., *Astrophys. J.*, vol. 135, 1962 p. 272

[7] H. R. Griem, “Spectral line broadening by plasmas”, *Academic Press*, New York, 1974, p. 316

[8] H. Goktas, A. Demir, E. Hajiyev, R. Turan, A. Seyhan, G. Oke, Int. Conf. Plasma 2003, Warsaw, Poland, 2003, p. 81

[9] M. A. Gigosos, V. Cardenoso, J. Phys. B: At. Mol. Opt. Phys., vol. 29, 1996, pp. 4795-4838

[10] M. Moisan, Z. Zakrzewski, J.C. Rostaing, *Plasma Sources Sci. Technol*., vol. 10, 2001, pp. 387-394.

[11] E.A.H. Timmermans, M.J. van de Sande, J.A.M. van der Mullen, *Plasma Sources Sci. Technol.*, vol. 12, 2003, p. 330.

[12] E. Timmermans, *PhD Thesis*, Eindhoven University of Technology, 1999, pp. 13-24

[13] J. Jonkers, J. M. de Regt, J. A. M. van der Mullen, H.P.C. Vos, F.P.J. de Groote, E. A. H. Timmermans, *Spectrochimica Acta*, Part B 51, 1996, pp. 1385-1392

[14] S. Jovicecic, M. Ivkovic, Z. Pavlovic, N. Konjevic, *Spectrochimica Acta*, Part B 55, 2000, pp. 1879-1893

PHENOL OXIDATION IN AQUEOUS SOLUTION BY GAS PHASE CORONA DISCHARGE

M. Dors and J. Mizeraczyk

Centre for Plasma and Laser Engineering
The Szewalski Institute of Fluid Flow Machinery, Polish Academy of Sciences
Fiszera 14, 80-231 Gdańsk, Poland
e-mail: mdors@imp.gda.pl

Abstract

In this paper, results of phenol degradation in water, induced by a DC positive corona discharge in an air-like gas mixture above the water surface are presented. A DC positive corona discharge was generated between a hollow needle, through which air with 1.5% CO_2 *flowed, and the water surface. The water was artificially contaminated wit phenol (0.027 mM). The results showed that ozone produced by the corona discharge in the gas phase dissolved in water and oxidized phenol into dihydroxyphenols. On the other hand, another phenol oxidant, i.e. hydrogen peroxide, was produced by the corona discharge in the aqueous phase. Increasing the corona discharge duration results in an increased phenol degradation rate as well as in a higher water conductivity and acidity. Due to the degradation of phenol into organic acids the pH of phenol solution after the corona discharge processing was lower and the conductivity was higher than in the pure water.*

Keywords: Corona Discharge, Phenol, Water Purification

INTRODUCTION

Providing access to clean water resources is one of the most important objectives of the United Nations Millenium Project [1]. Contamination of surface water is a big problem for many, mostly developing countries. The main sources of liquid polluted effluents are municipalities and industry. Effective wastewater technologies, mostly biological, for wastewater purification are available nowadays. However, they do not solve such problems as destruction of non-biodegradable organic compounds or biological contaminations (caused by viruses, bacteria, parasites, etc.) of sludge. Recently, the non-thermal plasma has recovered its position as a very effective form of energy, which can destroy organic or biological contaminants.

Actually, the plasma treatment of drinking and waste water is not new. For a number of years tap water has been treated by ozone generated by various electrical discharges. This type of water treatment is called “the remote plasma method” [2] since the active species, like ozone, are generated by plasma aside the water system and then introduced into water. “The direct plasma method” of water treatment is the next generation method which generates plasma directly inside water or above the water surface, simultaneously oxidizing the inorganic and organic compounds in water and destroying the biological contaminants [3-11].

This paper is focused on the direct non-thermal plasma method of water treatment based on a DC positive corona discharge generated above the water surface.

EXPERIMENTAL SET-UP

The experimental set-up and the reactor are presented in Fig. 1. The positive DC corona discharge was generated between a stainless steel hollow needle electrode and the surface of pure water or water contaminated with phenol, which filled the reactor so that a grounded flat mesh electrode was 10 mm below the water surface. The mesh electrode was made of stainless steel. The outer and inner diameter of the hollow needle was 2 mm and 1.6 mm, respectively. The hollow needle-water surface spacing was 20 mm.

The positive polarity DC high voltage (18-23 kV) was applied through a 10 MΩ resistor to the hollow needle electrode. The time-averaged discharge current was 75 μA. The discharge pulse repetition rate was 50 kHz.

A dry air with CO_2(1.5%), stabilizing the corona discharge, was supplied through the hollow needle with a flow rate of 1 l/min. The pure water or water containing 0.027 mM of phenol was mixed continuously with a magnetic stirrer.

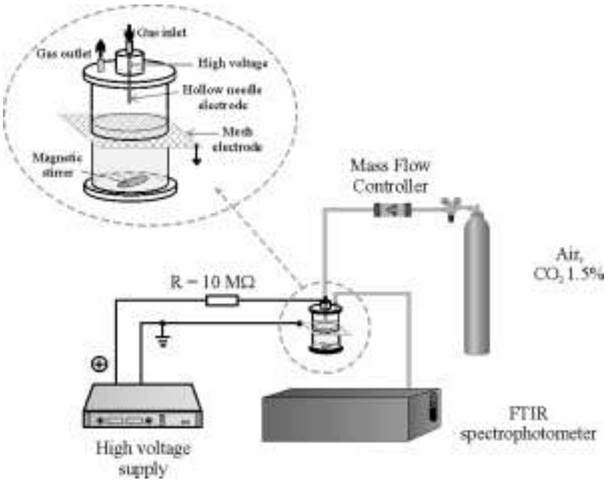

Fig. 1. Experimental set-up

The composition of the gas at the reactor outlet was analyzed by a FTIR spectrophotometer. The concentration of phenol in the water solution was measured by a gas chromatograph before and after the corona discharge processing. The water solution was analyzed also for the presence of ozone (iodometric method) and hydrogen peroxide (pertitanic acid formation method). The acidity (pH) and conductivity of water solution were measured as well.

RESULTS AND DISCUSSION

As a result of the DC corona discharge processing, the concentration of phenol in water solution decreased with processing time from 0.027 mM to 0.002 mM (Fig. 2). The decrease in the phenol concentration was accompanied with the production of dihydroxyphenols, the concentration of which was, however, much lower than expected. It probably means that the phenol was converted also to other products not measured in this experiment.

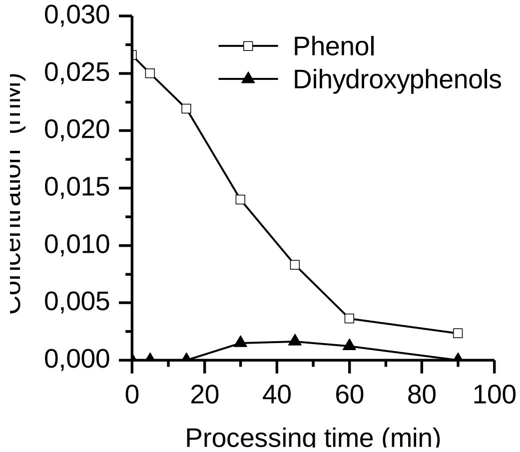

Fig. 2. Concentrations of phenol and dihydroxyphenols in the aqueous phase during the DC positive corona discharge processing. Discharge current 75 μA. Gas flow rate 1 l/min. Initial phenol concentration 0.027 mM

As it is seen in Fig. 2, after 45 minutes of the DC corona processing the concentration of dihydroxyphenols decreased. It is known that dihydoxyphenols are formed in oxidation reactions of phenol caused by ozone and OH radicals, which can also react with dihydroxyphenols, resulting in organic aliphatic compounds, in particular acids, such as muconic acid, oxalic acid etc. [5-8]. If in our experiment organic acids were really formed, then one would observe an increase in acidity and conductivity of the water solution. Indeed, the measurements of pH and conductivity showed the increase of the acidity and conductivity (Fig. 3). As it is seen in Fig. 3, the acidity and conductivity increased also in the case of pure water. The pH decreased from 5.1 to 3.4 and the conductivity increased from 9 μS up to 200 μS in pure water due to the carbonic acid formed from CO_2^- and CO_3^- ions generated in the gaseous phase by the corona discharge. Organic acids, produced from dihydroxyphenols, decreased pH of 0.2 and increase the conductivity of 10 μS only.

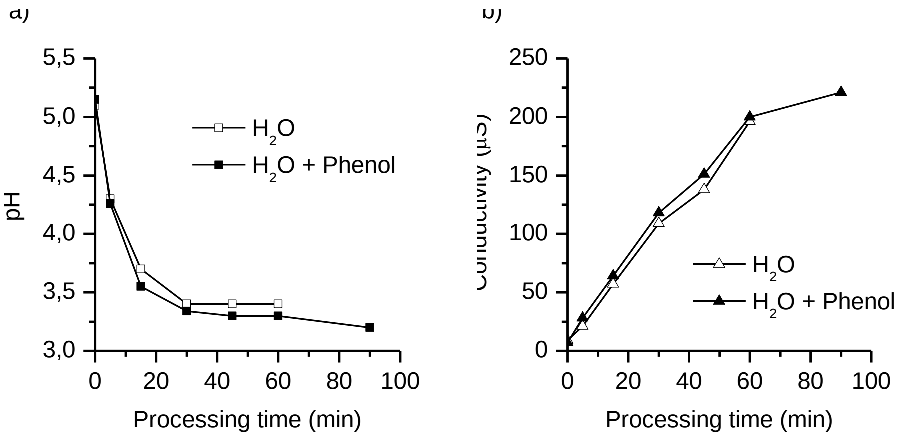

Fig. 3. The pH (a) and conductivity (b) of pure water and water contaminated with phenol during the DC positive corona discharge processing. Discharge current 75 µA. Gas flow rate 1 l/min. Initial phenol concentration 0.027 mM

As mentioned, phenol is converted to dihydroxyphenols and then to organic aliphatic acids in reactions with ozone and OH radicals. The analysis of the gaseous phase composition after the DC corona processing of the pure water (without phenol), showed that the concentration of ozone produced by the corona discharge was 247 ppm and did not change during the processing (Fig. 4a). The presence of phenol in the water caused a decrease in the concentration of gaseous ozone to 74 ppm.

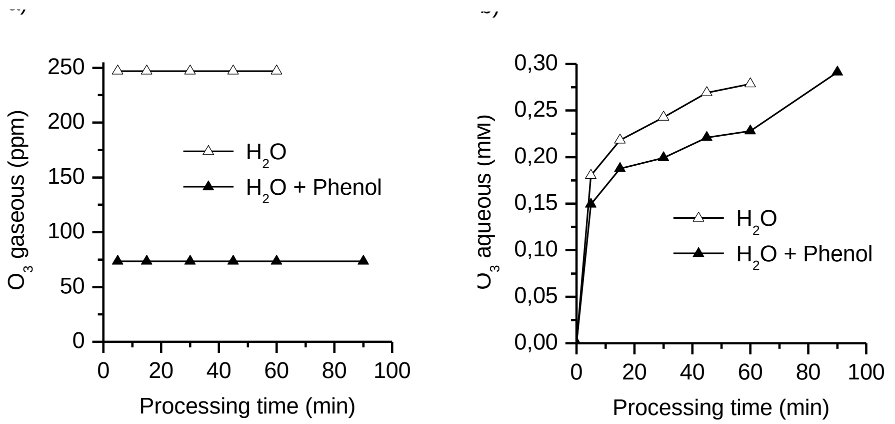

Fig. 4. Concentration of ozone in the gaseous phase (a) and aqueous phase (b) during the DC positive corona processing of pure water and water contaminated with phenol. Discharge current 75 µA. Gas flow rate 1 l/min. Initial phenol concentration 0.027 mM

The concentration of ozone in the aqueous phase increased when increasing processing time. Due to the reactions of ozone with phenols, the ozone concentration in the water containing phenol was lower of 0.03-0.06 mM than in the pure water (Fig. 4b).

Changes in the concentration of H_2O_2 in the pure water and water contaminated with phenol are similar to those concerning ozone, i.e. H_2O_2 concentration, always higher in the pure water, increased with processing time (Fig. 5). Since H_2O_2 molecules are produced from OH radicals in reaction:

$$OH + OH \rightarrow H_2O_2, \tag{1}$$

the increased consumption of OH radicals when phenol is present in the water results in lower production of H_2O_2 and, therefore, in lower H_2O_2 concentration in the phenol contaminated water.

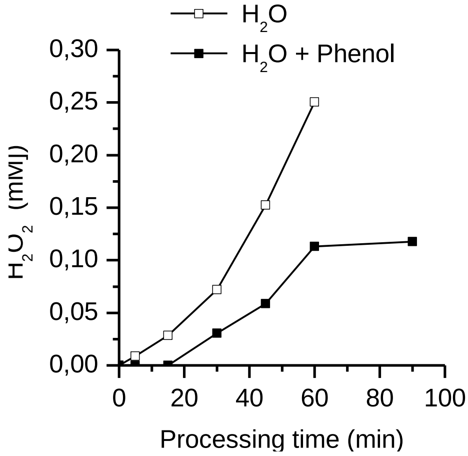

Fig. 5. Concentration of H_2O_2 in the aqueous phase during the DC positive corona discharge processing of pure water and water contaminated with phenol. Discharge current 75 μA. Gas flow rate 1 l/min. Initial phenol concentration 0.027 mM

Table 1 summarizes the results of the phenol degradation experiments carried out by us and presented in [3-5]. In order to compare the efficiency of all the experiments, a *G* yield value has been calculated, expressing the number of converted phenol molecules divided by the energy input required. The yield value at 50% phenol conversion is given by [5]:

$$G_{50} = \frac{0.5 \cdot C_0 \cdot Vol}{E_p \cdot f \cdot t_{50}}, \tag{2}$$

where C_0 is the phenol concentration at $t = 0$, *Vol* is the aqueous phase volume, E_p is the discharge pulse energy, f is the pulse repetition rate and t_{50} is the time required for 50% phenol conversion. *G* is expressed in mol/J. In all cases, it was observed that for the discharges over water (columns IV–VI) G_{50} is one to four orders of magnitude higher than for the discharges in water (columns I–III). Moreover, G_{50} obtained using the DC corona discharge to the water surface is close to that obtained during the pulsed corona inside water. Although the numbers are difficult to compare, it is estimated (column VII) that the ozonation of phenol in a remote plasma method has an efficiency which is in the same range as that for the discharge over water.

Taking into account that our results (column VI in Tab. 1) are only a first attempt using the DC positive discharge over the water surface, it is expected that the results can be improved by the optimisation of the reactor shape and other parameters.

Table 1. A comparison of phenol conversion using different corona discharge methods (except column VII)

	I	II	III	IV	V	VI	VII
Reference	[4]	[3]	[6]	[5]	[5]	this work	[5]
	pulsed corona in water	pulsed corona in water	pulsed corona in water	pulsed corona in air	pulsed corona in air	DC corona in air	ozonation
C_0 (mM)	0.03	0.53	0.53	1	0.1	0.027	0.5
Vol (cm^3)	550	1000	250	500	300	80	4000
E_p (mJ)	1750	800	880	10	7	0.03	-
f (Hz)	60	50	48	100	100	50 000	-
t_{50} (min)	180	260	7	237	25	30	8
G_{50} (mol/J)	$7.3x10^{-12}$	$4.2x10^{-10}$	$3.7x10^{-9}$	$1.8x10^{-8}$	$1.4x10^{-8}$	$3.5x10^{-10}$	$5.2x10^{-8}$

CONCLUSIONS

The results of gas phase DC positive corona discharge processing of water solution with phenol showed that:

- DC positive corona discharge produces OH radicals and ozone in gas phase. Both species dissolve in water and then oxidize phenol.
- Phenol is oxidized to dihydroxyphenols and aliphatic organic acids.
- The oxidants generated by DC positive corona discharge oxidize up to 91% of phenol during 90 min.
- The acidity and conductivity of the water increase with processing time mainly due to the presence of CO_2 in the gas phase (formation of CO_2^- and CO_3^- ions, which are precursors of carbonic acid). Organic acids formed from phenol slightly increase acidity.
- The energy efficiency of the phenol oxidation is up to $3.5x10^{-10}$ mol/J, and is comparable to the results obtained in pulsed corona discharge systems.

The main advantage of using DC corona discharge system is that it does not require matching the power supply to the corona discharge reactor, which is the problem in case of pulsed supply systems. Thus, energy loses and electromagnetic noise generated by the pulsed power supply can be avoided using DC corona discharge systems which are as efficient in phenol conversion as pulsed corona discharge installations.

ACKNOWLEDGEMENT

This work was supported by the Ministry of Science and Information Society Technologies under programme PB 1280/T10/2004/27 and by the Institute of Fluid Flow Machinery, Polish Academy of Sciences under programme IMP PAN O3Z3T2.

REFERENCES

[1] Introduction in “Status of industrial scale radiation treatment of wastewater and its future”, Proceedings of a consultants meeting held in Daejon, 13-16 October 2003, IAEA

[2] J. S. Chang, Pulsed arc electrohydraulic discharge water treatments: next generation direct plasma drinking and waste water treatment process, Proc. of 4th Int. Conf. on Electromagnetic Devices and Processes in Environment Protection ELMECO, Nałęczów, 2003, pp. 13-26

[3] P. Sunka, V. Babicky, M. Clupek, P. Lukes, M. Simek, J. Schmidt, M. Cernak, Generation of chemically active species by electrical discharges in water, Plasma Sources Sci. Technol., 8, 258–265, 1999

[4] A. A. Joshi, B. R. Locke, P. Arce, W. C. Finney, Formation of hydroxyl radicals, hydrogen peroxide and aqueous electrons by pulsed streamer corona discharge in aqueous solution, Journal of Hazardous Materials, 41, 3-30, 1995

[5] W. F. L. M. Hoeben, E. M. van Veldhuizen, W. R. Rutgers, G. M. W. Kroesen, Gas phase corona discharges for oxidation of phenol in an aqueous solution, J. Phys. D: Apl. Phys., 32, L133–L137, 1999

[6] B. Sun, M. Sato, J. S. Clements, Use of a pulsed high-voltage discharge for removal of organic compounds in aqueous solution, J. Phys. D: Appl. Phys., 32, 1908-1915, 1999

[7] A. T. Sugiarto, M. Sato, Pulsed plasma processing of organic compounds in aqueous solution, Thin Solid Films, 386, 295-299, 2001

[8] P. Lukes, A. T. Appleton, B. R. Locke, Hydrogen peroxide and ozone formation in hybrid gas–liquid electrical discharge reactors, IEEE Trans. Ind. Appl., 40, 1, 60-67, 2004

[9] J. S. Clements, M. Sato, R. H. Davis, Preliminary investigation of prebreakdown phenomena and chemical reactions using a pulsed high-voltage discharge in waterm IEEE Trans. Ind. Appl., 23, 2, 224-235, 1987

[10] M. Sato, T. Ohgiyama, J. S. Clements, Formation of chemical species and their effects on microorganisms using a pulsed high-voltage discharge in water, IEEE Trans. Ind. Appl., 32, 1, 106-112, 1996

[11] N. Sano, D. Yamamoto, M. Nakao, T. Kanki, Decomposition of aqueous phenol by direct contact of gas corona discharge with water: The influence of current density and applied voltage, J. Chem. Eng. Japan, 37, 11, 1319-1325, 2004

5^{th} International Conference **ELMECO**
Nałęczów, Poland
September 2005

ENERGETIC OF NO_x OXIDISING BY OZONE IN A COMPUTATIONAL CHEMISTRY SCHEME

J. Jaroszyńska-Wolińska

Department of Chemical Technology, Lublin University of Technology
Nadbystrzycka 40, 20-618 Lublin, Poland
e-mail: jwtchem@akropolis.pol.lublin.pl

Abstract

Several chemical methods have been designed for the removal of nitrogen oxide pollutants from gaseous waste streams. One of these is based on the oxidation of NO_X *using ozone. Developments in computational chemistry have delivered powerful tools for studying chemical problems. In this work we have applied computational chemistry methods to describe the energetic of reactions comprising steps in the ozone-based* NO_X *oxidation process. To determine the main factors responsible for overall oxidation process efficiency in the model presented the path and energetic of each reaction must be known. The number of such reactions is probably very large but we have selected certain of the most important reactions. We have used computational chemistry methods based on the Density Functional Theory (DFT) and the Complete Active Space Self Consistent Field (CASSCF) method, a special variant of the ab initio Multi-configurational Self Consistent Field (MCSCF) approach. The equilibrium geometries of the molecules taking into account in this work we are presented. All reactions considered turned out to be exothermic.*

Keywords: ozone, nitrogen oxides (**NO_x**), oxidation, energetic, DFT, CASSCF

INTRODUCTION

Ozone synthesis development can be understood as a research into the field of environmental technology.

There are a couple of chemical methods for a NO_x removal from industrial flue gases such as catalytic reduction or oxidation that lead to obtaining easily removable higher oxides. Presently used technologies of a selective catalytic reduction (SCR) and a selective non-catalytic reduction (SNCR) require an application of additional substances such as ammonia or urea. Catalytic reduction methods also require an application of high temperatures, which in industrial conditions with big quantities of gas can be costly. Oxidation methods, and especially the ones that apply ozone, are characterized by high efficiency and lack of wastes and therefore they are subject of extensive laboratory research. Actual significance of the problem can be proved by the latest reports in *Ozone News* [2] by an American environment protection agency (U.S.EPA) about an attempted commercialization of the NO_x removal process with the use of ozone within a program of evaluation of technologies in the environment protection (Environmental Technology Verification Program ETV). The process is so actual and attractive that American researchers (BOC Group, Inc., Murray Hill, N.J) obtained for their version of that method, recently implemented in Midland (USA), the prestigious 2001 Kirkpatrick Award for Chemical Engineering Achievements[2].

Simultaneous considerable development of ozone production technologies (reduced energy costs) contributed to the increased interest in that strong and ecological oxidizer. Some application tests have even been performed [2]. The author has been researching within the mentioned field for many years now and among other achievements co-authored 3 Polish patents related to the process. An application of non-thermal plasma to oxidize nitrogen oxides with ozone requires a determination of optimal parameters that decide over the process efficiency. To this end it is necessary to fathom and explain the mechanism of chemical and physical changes (chemical reactions and a process of mass exchange) occurring in the process. The process of nitrogen oxide oxidation with ozone runs towards the formation of N_2O_5. It is a quick process but it is composed of many-stages.

The key question there is to recognize mechanisms of individual reactions and to determine their competitiveness which will make a basis for elaborating a global description of the process and finding optimal conditions for its running. In this work we have applied computational chemistry methods to describe the energetic of reactions comprising steps in the ozone-based NO_X oxidation process. To determine the main factors responsible for overall oxidation process efficiency in the model presented the path and energetic of each reaction must be known. One way to determine major factors which govern the process is to perform exhaustive and expensive experimental studies. An attractive alternative seems to be molecular modeling based on quantum chemical methods. Quantum chemistry today delivers very powerful tools for studying varied chemical problems.

OBJECTIVE AND SCOPE

We have applied quantum chemistry methods to describe the energetic of elementary reactions comprising the oxidation process. The number of such oxidation reactions is probably very large but we have selected four of the most important ones. Assuming a quite simple mechanism of the NO_x oxidation process at the first approximation it can be described by the following reactions: (1-4)

$$NO + O_3 \rightarrow NO_2 + O_2 \tag{1}$$

$$NO_2 + O_3 \rightarrow NO_3 + O_2 \tag{2}$$

$$NO_2 + NO_3 \rightarrow N_2O_5 \tag{3}$$

$$2NO_2 + O_3 \rightarrow N_2O_5 + O_2 \tag{4}$$

The by-product N_20_5 is a key intermediate product enabling industrially useful conversion via water-based hydrolysis into nitric acid:

$$N_2O_5 + H_2O \rightarrow 2\,HNO_3 \qquad (5)$$

The above given reactions make the first step that is necessary to describe the process so that its first approximation could show its basic character which in reality is much more complex. The reactions run much quicker than it, is in the case of CO to CO_2 or SO_2 to SO_3 oxidation by means of ozone. The performed tests prove that the NO oxidation process runs in a much complex way. In the first reaction nitrogen monoxide gets oxidised to NO_2 with only one oxygen atom from ozone. Next, NO_2 gets oxidised to NO_3 and then a reaction between those two oxides takes place towards the formation of N_2O_5 which in turn by the action of water can be changed into nitric acid (N_2O_5 immediately reacts even with moisture contained in flue gases forming HNO_3). However, these mechanisms are complex and not well known. In addition, obtaining such information only from experimental data is complicated, time-consuming and expensive. Alternatively, theoretical investigation of these reactions and proposal of a model for the overall process may be more economical. Quantum chemical methods may turn out to be very useful in this respect. To determine the main factors responsible for the efficiency of the entire process modeled by the above series of equations, the path and energetic of each reaction must be known. Calculation of the energetic of each of these processes is of particular significance. Modern theoretical techniques involving the DFT and the *ab initio* multiconfigurational approach MCSCF are well suited for these kinds of calculations. Here we present our theoretical investigations of the structures of the oxygen molecule, the ozone molecule and certain nitrogen oxide molecules as well as their energies with the ZPE correction in each of the reactions (1) – (4). The equilibrium geometry found for each molecule has been confirmed by vibrational frequency calculations. Then, we have calculated relative energies of each reaction, i.e. $\Delta E = E_{products} - E_{substrates}$ (reaction heat). Finally, we have tried to determine the transition state for each model reaction.

COMPUTATIONAL METHODS

The primary goal of our theoretical investigations was determination of the relative energies, defined as $\Delta E = E_{products} - E_{substrates}$ for the reactions (1) – (4).

This can be accomplished by calculating the equilibrium geometries and electronic energies of substrates and products, the oxygen molecule, the ozone molecule and a few nitrogen oxide molecules NO_X, as well as their zero-point vibration energy (ZPE).

Firstly, the optimal structures of oxygen and ozone molecules and all nitrogen oxide molecules involved in the reactions (1) – (4) were calculated at the DFT theoretical level [4]. In particular the so-called B3LYP exchange-correlation potential [5,6] was used. This method, called DFT/B3LYP, is known to give accurate molecular geometries and (relative) electronic energies. Note, that in the case of the open-shell molecules (O_2, NO, NO_2, NO_3) the unrestricted DFT procedure has to be adopted. The DFT calculations were carried out using the 6-311G(d,p) basis set [7].

Secondly, correlated *ab initio* calculations of the optimal structures were carried out. We have chosen the CASSCF [8–10] method, a special case of the more general MCSCF [11] approach. This method is known to account for the major part of the so-called static (or non-dynamic) correlation effects, such effects being of particular importance in the description of systems containing the lone-pair electrons. However, it does not incorporate the very important dynamic correlation effects and, therefore, the final results may suffer from this deficiency. It should be emphasized that for the CASSCF calculations to be of reasonable quality an adequate choice of the so-called active space (the CAS space) is of particular importance. This is especially true with regard to the description of the phenomena involving different potential energy surfaces. The balanced and consistent (in a well defined way) inclusion of the molecular configurations into the wave functions of all species of interest is essential in obtaining reasonable values of the relative energies. For example the active space adequate for treatment of the static correlation in the case of the ozone molecule should consist of at least all *p*-derived orbitals, i.e. 6 orbitals from the σ space and 3 orbitals from the π space [12]. This active space may be referred to as the (6/3) active space. The distribution of 12 electrons among 9 orbitals leads to the configuration interaction (CI) expansion of the CASSCF wave function into approximately 670 configuration state functions (CSFs). Note that the size of the CI expansion has been reduced not only by the spatial symmetry but also by the spin symmetry of the configurations. However, choice of the active space on the same grounds for the biggest molecule considered in this paper, i.e. the N_2O_5 molecule, becomes impractical. We managed to carry out this kind of calculation, called CASSCF (σ- and π-derived), only for O_2, NO, O_3 and NO_3 molecules. This means, that CASSCF (σ- and π-derived) relative energies were computed only for the reactions (1) and (2). Thus, we decided to reduce the CI expansion of the MCSCF wave functions by including the excitations only within the π space for all systems. However, it is known [12,13] that, at least for the ozone molecule, any restriction of the active space below that of the (6/3) quality leads to substantial worsening of some of the calculated properties. Indeed, the π-derived active space turned out to be too small (*vide infra*). The CASSCF calculations were carried out using the smaller 6-31G(d,p) basis set [14]. In both DFT and CASSCF calculations the type of the stationary point was determined by frequency calculations. All calculated frequencies turned out to be real indicating that structures corresponding to local minima were found. It is also important to realize that dissociation/association processes may lead to a change in the number of the vibrational degrees of freedom when going from substrates to products. Thus, the harmonic frequencies were also used in the calculation of the zero-point energy (ZPE) correction for substrates and products.

All DFT calculations were carried out using the parallel version of the PQS [15] quantum chemistry software. All CASSCF calculations were carried out using the DALTON [16] quantum chemistry software.

RESULTS AND DISCUSSION

Equilibrium Geometries and Vibrational Frequencies

The equilibrium geometries of the molecules considered in this work are presented in Figure 1. Note that only a few selected parameters of the N_2O_5 molecule are reported. The total electronic energies as well as the harmonic frequencies are reported in Table 1. These values were used in the subsequent determination of the relative energies for the reactions (1) – (4). The equilibrium bond length of the ground state ($^3\Sigma_u^-$) oxygen molecule is in good agreement (within 1%) with the experimental value. Apparently the DFT method seems to slightly overestimate and the CASSCF method to slightly underestimate the attractive forces between atoms causing the bond length to be shorter/longer, respectively than that found experimentally. As a consequence, the harmonic frequency (cf. table 1) of the stretching mode is higher (1640 cm^{-1}, DFT) and lower (1545 cm^{-1}, CASSCF) than the corresponding experimental value of 1580 cm^{-1} [17]. The same trends regarding bond length are observed in the case of the NO molecule in its (open-shell, $^2\Pi$) ground state.

However, comparison of the theoretical frequencies with an experimental value cannot be done as only the fundamental experimental frequency is available [18].

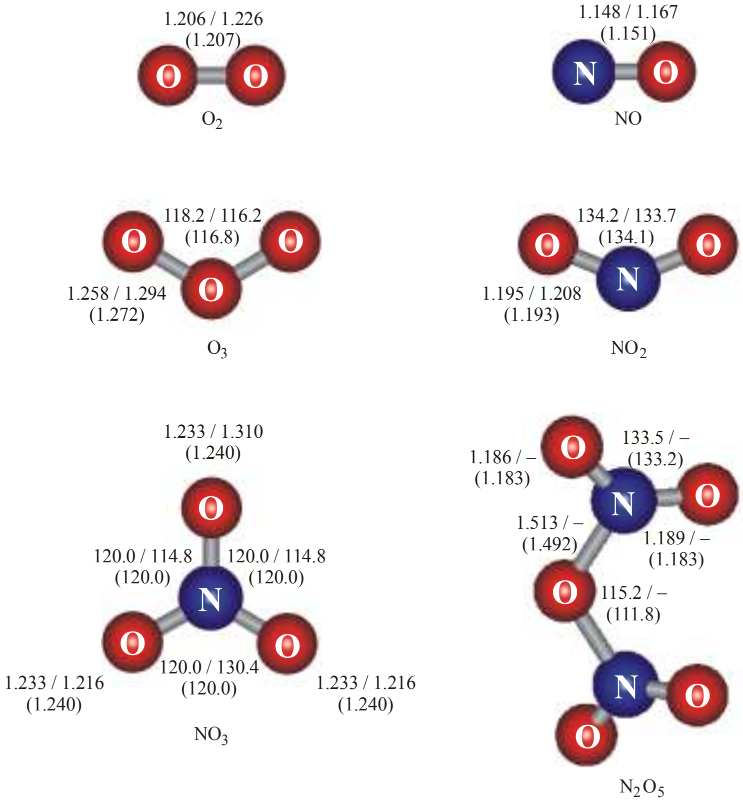

Figure 1. The geometrical parameters of the molecules considered in this work.
The upper (separated by "/") are the theoretical values reported in the following order:
DFT/B3LYP/6-311G(d,p) / CASSCF((σ- and π-derived) /6-31G(d,p).
The experimental values (O_2: ref. [17], NO: ref. [18], O_3: [19], NO_2: [20], NO_3: [21], N_2O_5: [22]) are given in parentheses (bond lengths in Å, valence angles in deg)

In the case of the ozone molecule (in the $^1A_1$ ground state) the theoretically predicted bond lengths behave similarly – they are too short at the DFT level and too long at the CASSCF level. However, it should be noted that much better agreement of the CASSCF results with experiment for both oxygen [23] and ozone [12] molecules was achieved using ANO-type basis set [24]. Consequently, the harmonic frequencies of two stretching modes (symmetric and anti-symmetric) are higher at the DFT level of theory. They are 1249 cm^{-1} and 1191 cm^{-1} at the DFT level and 1078 cm^{-1} and 1015 cm^{-1} at the CASSCF level, respectively. These values are to be compared with experimental harmonic frequencies of 1135 cm^{-1} and 1089 cm^{-1} [25]. The theoretical (DFT and CASSCF) valence angle reproduces well the experimental value and the frequency of the symmetric bending mode is well accounted for. The theoretical geometry of the ground state ($^2A_1$) nitrogen dioxide molecule is also in good agreement with experiment, although the DFT method seems to perform slightly better than the CASSCF method. The somewhat worse performance of the

CASSCF method may be due to the quality of the basis set – as was already pointed out the CASSCF calculations should be preferably carried out with a basis set of higher than 6-31G(d,p) quality. Again comparison of the theoretical frequencies with experimental values cannot be done – only the fundamental experimental frequencies are available [20].

Table 1. The calculated at the DFT/B3LYP/6-311G(d,p) and the CASSCF ((σ- and π-derived)/6-31G(d,p) levels of theory electronic energies and harmonic frequencies of oxygen, ozone and selected nitrogen oxide molecules used in the evaluation of the energy released during the reactions (1) – (4)

Molecule	Method	Energy [a.u.]	Harmonic frequencies[cm^{-1}]		
O_2	DFT/B3LYP	–150.364789	1640		
	CASSCF	–149.692351	1545		
	Exp. [17]	–	1580		
NO	DFT/B3LYP	–129.926701	1988		
	CASSCF	–129.351396	1919		
	Exp. [18]^a	–	1876		
O_3	DFT/B3LYP	–225.470791	748	1191	1249
	CASSCF	–224.475823	690	1015	1078
	Exp. [25]	–	716	1089	1135
NO_2	DFT/B3LYP	–205.132719	766	1398	1706
	CASSCF	–204.184820	746	1321	1663
	Exp. [20]^a	–	750	1318	1618
NO_3	DFT/B3LYP	–280.298553	258	258	802
			1121	1121	1135
	CASSCF	–278.993184	440	565	683
			946	1291	1695
N_2O_5	DFT/B3LYP	–485.465713	52	62	220
			344	384	570
			683	683	766
			812	894	1305
			1403	1797	1843
	CASSCF	–	–	–	–

^{a}Fundamental frequencies

The NO_3 molecule in its ground electronic state ($^2A_2$') is planar. Experimental investigations [21] clearly demonstrate that the molecule belongs to the D_{3v} symmetry point group. Thus, all N–O bond lengths should be the same and the O–N–O valence angles should be equal to 120°. Apparently the DFT/B3LYP approach is capable of predicting the proper structure of the molecule, both with regard to the symmetry of the ground state and the lengths of the N–O bonds. Oddly enough CASSCF is not! The structure predicted by the CASSCF method has C_{2v} symmetry (cf. figure 1). In addition the N–O bonds are substantially shorter than predicted experimentally. Although all the frequencies turned out to be real, indicating that the local minimum was found, the final result seems to be an artifact of the CASSCF approach. As can be seen (cf. figure 1) only the DFT/B3LYP geometrical parameters for the N_2O_5 molecule are available. Actually the DFT is a very efficient correlated method, which is used nowadays to carry out calculations on molecules containing hundreds of atoms. Molecules as small as those considered in this work should not present any kind of problem. Indeed, the DFT molecular geometry (note that only a few selected geometrical parameters for N_2O_5 are reported on figure 1) is in good agreement with the experimental one. It should be noted that the N_2O_5 molecule is not planar – the torsion O–N–O–N angle predicted by the DFT/B3LYP approach is equal to approximately 30° (or 150°).

Next, the CASSCF calculations were carried out. However, the CASSCF calculations are more complicated than the DFT calculations on account of the rapid growth of the CI expansion of the MCSCF wave function with the increasing size of the active space. As was already pointed out, the choice of the σ- and π-derived active space turned out to be impractical for this molecule. Thus, we decided to reduce the size of the active space. The choice of only π-derived active space for all the molecules led, however, to (*i*) substantial worsening of the results for other molecules and (*ii*) arriving at the saddle point (one complex frequency) rather than at the local minimum on the N_2O_5 potential energy surface. Many attempts to extend slightly the active space beyond that of the π-derived quality were made. A physically justifiable choice of the active space can be made on the basis of the MP2 natural orbital occupation numbers: (*i*) orbitals with occupation numbers above certain threshold remain inactive, (*ii*) orbitals with occupation numbers below certain threshold remain virtual and (*iii*) the remaining orbitals constitute the active space. However, we failed to find the local minimum of the CASSCF potential energy surface of N_2O_5 for all (chosen in this way) active spaces that could be handled in our laboratory.

Relative energies

The DFT/B3LYP/6-311G(d,p) and the CASSCF(σ- and π-derived)/6-31G(d,p) relative energies and the relative energies corrected for the zero point vibrational energy for the reactions (1) – (4) are presented in Table 2. The data necessary to calculate these energies can be found in Table 1.

For all reactions considered in the present work the DFT/B3LYP energy of products is lower than that of substrates. Apparently all reactions are exothermic. The relative energies are $\Delta E=-61.83$ kcal/mol for reaction No (1), $\Delta E=-39.62$ kcal/mol for reaction No (2), $\Delta E=-12.18$ kcal/mol for reaction No (3) and $\Delta E=-51.80$ kcal/mol for reaction No (4). Apparently, the most exothermic is the reaction of nitrogen oxide with ozone (reaction 1), the least being the reaction of nitrogen dioxide with nitrogen trioxide (reaction 3). It should be noted that for reaction (1) the number of vibrational degrees of freedom is the same for substrates and products. Obviously, therefore, the ΔE and $\Delta E^{(ZPE)}$ are close (cf. table 2)

Table 2. The DFT/B3LYP/6-311G(d,p) and the CASSCF(σ- and π-derived)/6-31G(d,p) relative energies and the relative energies corrected for the zero point vibrational energy for the reactions (1) – (4)

Reaction	Method	ΔE [kcal/mol]	$\Delta E^{(ZPE)}$ [kcal/mol]
$NO + O_3 \rightarrow NO_2 + O_2$	DFT/B3LYP	- 62.78	- 62.31
	CASSCF	- 31.36	-30.54
$NO_2 + O_3 \rightarrow NO_3 + O_2$	DFT/B3LYP	-37.56	-38.59
	CASSCF	-15.63	-14.69
$NO_2 + NO_3 \rightarrow N_2O_5$	DFT/B3LYP	-21.62	-16.90
	CASSCF	-	-
$2NO_2 + O_3 \rightarrow N_2O_5 + O_2$	DFT/B3LYP	-59.18	- 55.49
	CASSCF		

Somewhat bigger difference between these quantities is observed in the case of reaction (2) in which an extra vibrational degree of freedom appears for products. However, the two low-energy (degenerate, on account of symmetry) vibrational modes result in the ZPE correction for products being smaller than for substrates and consequently $\Delta E^{(ZPE)} > \Delta E$. Six and seven additional vibrational degrees of freedom are gained in the course of reactions (3) and (4) respectively. Thus, the ΔE and $\Delta E^{(ZPE)}$ values for these reactions differ by as much as 4.5 – 5 kcal/mol.

Although all reactions considered in the present work turned out to be exothermic (the total energy of products is lower than the total energy of substrates) they may not be spontaneous. In order to calculate the activation energy of the reactions (1) – (4) the search for the transition states was also carried out. No transition state was found for any of these processes even though numerous initial geometries were used and a few low-energy modes were followed in the iterative procedure. This is a strong indication of the spontaneous character of each of these reactions. The relative CASSCF energies of only the first two reactions (due to the lack of the reliable data for the N_2O_5 molecule, *vide supra*) were calculated. They are much (more than twice as much) lower than the corresponding DFT/B3LYP energies. However, we are inclined to trust more the DFT/B3LYP energies due to the lack of the dynamic correlation in the CASSCF wave function.

CONCLUSIONS

In this work the relative energies, defined as $\Delta E = E_{\text{products}} - E_{\text{substrates}}$, for a certain reactions involving nitrogen oxides and ozone were calculated at DFT/B3LYP/6-311G (d, p) and CASSCF (σ- and π-derived)/6-31G (d, p) levels of theory. It was demonstrated that the DFT/B3LYP is superior to the *ab initio* CASSCF approach. The DFT method provides an efficient way of estimating the (static and dynamic) correlation energy for strongly multiconfigurational species, such as these considered in the present work. Good agreement between the DFT/B3LYP and the experimental geometries as well as harmonic frequencies (if available experimentally) was achieved. On the other hand, in some cases the CASSCF approach either (*i*) gives the wrong structure of the molecule (as with the NO_3 molecule) or (*ii*) cannot be applied due to the computational problems (as in the case of the N_2O_5 molecule). The (ZPE corrected) relative energies for all reactions, i.e. reactions (1) – (4), were computed at the DFT level only. For all reactions considered in the present work the DFT/B3LYP energy of products is lower than that of substrates. Apparently all reactions are exothermic. The relative energies are $\Delta E = -61.83$ kcal/mol for reaction No (1), $\Delta E = -39.62$ kcal/mol for reaction No (2), $\Delta E = -12.18$ kcal/mol for reaction No (3) and $\Delta E = -51.80$ kcal/mol for reaction No (4). The negative values of the $\Delta E^{(ZPE)}$ (exothermicity) along with the lack of the transition states provides a strong indication of the spontaneous character of all reactions considered in the present work.

ACKNOWLEDGEMENTS

The research has been supported by *The Ministry of Scientific Research and Information Technology of Poland* within the frame of the Polish research project 4T 09B03425 covering the period 2003-2006.

LITERATURE

[1] Jaroszyńska-Wolińska J., Wroński M., Pol. J. Chem. Tech., 2002, 4, 8

[2] Jaroszyńska-Wolińska J., Wroński M., J. Ozonek, I. Pollo, Proc. Int. Symp. On High Pressure Low Temperature Plasma Chemistry, Hakone VIII, Estonia, 2002, 2, 210

[3] Jaroszyńska-Wolińska J., Proc. Int. Symp. On High Pressure Low Temperature Plasma Chemistry, Hakone IX, Padua, 7P-02 , 2004, (published as CD, 2004)

[4] See e.g. Parr R.G., Yang W., Density-Functional Theory of Atoms and Molecules, and Oxford University Press: New York 1989

[5] Becke A. D. J. Chem. Phys., 1993, 98, 5648

[6] Lee C., Yang W., Parr R G., Phys. Rev. B., 1993, 37, 785

[7] Krishnan R., Binkley J.S., Seeger R., Pople J.A., J. Chem. Phys., 1980, 72, 650

[8] Roos B. O., Taylor P.R., Siegbahn P.R.M., Chem. Phys., 1980, 48, 157

[9] Roos B. O., Int., J. Quantum Chem., 1980, S 14, 175

[10] Siegbahn P. E. M., Almlöf J.A., Heiberg A., Roos B. O., J. Chem. Phys., 1981,74, 2384

[11] Wah A. C, Das G., Adv. Quantum Chem., 1970, 261, 5

[12] Borowski P., Andersson K., Malmqvist P.-Å,. Roos B. O., J. Chem. Phys., 1992, 97, 5568

[13] Andersson K., Borowski P., Fowler P. W., Malmqvist P.-Å, Roos B. O., Sadlej A. J., Chem. Phys. Lett.,1992, 190, 367

[14] Hariharan P. C., Pople J. A., Theor. Chim. Acta, 1973, 28, 213

[15] PQS version 3.1, Parallel Quantum Solutions, 2013 Green Acres Road, Fayetteville, Arkansas 72703, USA

[16] Dalton, a molecular electronic structure program, Release 1.2, 2001, written by Helgaker T., Jensen H. J. A., Joergensen P., Olsen J., Ruud K., Aagren H., Auer A. A., Bak K. L., Bakken V., Christiansen O., Coriani S., Dahle P., Dalskov E. K., Enevoldsen T., Fernandez B., Haettig C., Hald K., Halkier A., Heiberg H., Hettema H., Jonsson D., Kirpekar S., Kobayashi R., Koch H., Mikkelsen K.V., Norman P., Packer M. J., Pedersen T. B., Ruden T. A., Sanchez A., Saue T., Sauer S. P. A., Schimmelpfennig B., Sylvester-Hvid K.O., Taylor P.R., and Vahtras O

[17] Slanger T. G., Cosby P. C., J. Phys. Chem., 1988, 92, 267

[18] Huber H. P, Herzberg G., Molecular Structure and Molecular Spectra. IV. Constants of Diatomic Molecules, Van Nostrand Reinhold: Toronto 1979

[19] Tanaka T., Morino Y., J. Mol. Spectr., 1970, 33, 538

[20] D. R. Lide, ed. CRC Handbook of Chemistry and Physics, CRC Press, Inc., Boca,Raton ,1995

[21] Stirling A., Pápai I., Mink J., Salahub D. R., J. Chem. Phys., 1994, 100, 2910

[22] McClelland B. W., Hedberg L., Hedberg K., Hagen K., J. Am. Chem. Soc., 1983, 105, 3789

[23] Borowski P., Füscher M., Malmqvist P.-Å.,Roos B.O,Chem. Phys.Lett.,1995,237,195

[24] Almlöf J. A., Taylor P. R., J. Chem. Phys., 1987, 86, 4070

[25] Barbe A., Secroun C., Jouve P., J. Mol. Spectr., 1974, 49, 171

[26] Jaroszyńska-Wolińska J., Wroński M., *Polish Journal of ChemicalTechnology*, 2002,4, 2**,** 8-11

5th International Conference **ELMECO**
Nałęczów, Poland
September 2005

DEPOSITS IN WATER - BASED COOLING SYSTEMS

Teresa Szymura

Institute of Building Engineering
Department of General Construction Engineering
Lublin University of Technology
e-mail: t.szymura@pollub.pl

Abstract

The paper discusses phenomena that cause scale and sludge formation in water based cooling systems. Results of experimental research into cooling water treatment in an industrial cooling installation with the application of ammonium salts of strong acids have been presented. It has been found that a stoichiometric dose causes carbonate hardness removal. Adequately higher doses bring about crumbling and insignificant dissolving of the scale. Simultaneous application of an inhibitor of corrosion and incrustation prevents corrosion losses and advantageously influences water treatment.

Keywords: cooling water, water treatment, scale, cooling system, inhibitors

INTRODUCTION

Cooling water systems operate practically in all sectors of the industry. In the year 2001 total consumption of water in Poland amounted to 7308 hm^3, out of which 55% has been used in the power engineering industry and most (about. 95%)of the water consumed by that sector has been applied for cooling purposes (Statistical Yearbook of 2003), (Spoz J., 2000). Situation illustrated by those data is typical for majority of industrialized countries (Veil J. A., 1999).

In Poland, cooling systems apply raw water that, due to the lack of treatment or inhibitor additives, exhibits aggressively corrosive and deposit-forming properties. It results from a considerable flow-capacity of those systems, which causes excessive consumption of the water and creates an economic barrier for its rational treatment. This unfavorable situation can be improved by replacing once-through systems by recirculating ones. At the same time it is possible to apply multi-functional inhibitor preparations that could protect the systems against such phenomena as corrosion, deposit formation and development of microorganisms, even at a high condensation degree of the recycled water.

It is important to reduce water consumption in Poland because fresh water resources are extremely poor there. In Europe an average fresh water amount per capita is 4560 m^3, while in Poland it is by three times less.

At late 90-ties of the 20th century fresh water consumption in Poland has been reduced by 25% owing to shutdowns of cooling systems. The mentioned water consumption reduction has unquestionably contributed to the improvement of water quality in Polish rivers (Spoz J.,2000).

COOLING SYSTEMS

Although in the pertinent literature many kinds of cooling systems are described all of them can be classified into three principal types: once-through systems, open recirculating and closed recirculating ones (Ahmed S., 2000).

CORROSIVE AND DEPOSIT-FORMING PROPERTIES OF WATER

Properties of water that is commonly used in industrial cooling installations cause corrosion and incrustation, which brings about many technical problems and considerably raises operation costs of those installations.

Depending on the water quality and construction materials the following weakly or firmly adherent deposits can form on heat exchange surfaces,

- corrosion products forming as a result of the reaction of water or its components with metal,
- incrustation products that form so called *scale* composed mostly of sparingly soluble calcium compounds,
- suspended solids in the form of *sludge* resulting from the sedimentation of mineral and biological particles that are present in cooling water.

The deposits impair operation of cooling water installations by bringing about such disadvantageous phenomena as:

- frequent and difficult repairs,
- costly overhauls and related system outages,
- induced use of oversized apparatus,
- increased water consumption,
- energy losses following from additional resistance to the water flow due to the formed deposit layers..

Corrosion of water coolers

Corrosion processes occurring in metals that heat exchangers are made of depend on a composition of the construction material as well as on the cooling water composition. Standard cooling water installations usually are made of carbon steel, zinc-coated steel, copper and brass. Oxygen in the cooling water makes the most frequent corrosive agent Metal elements corrode in oxygenated neutral water when the metal oxidation potential is more negative than the equilibrium potential of cathode depolarization

$$O_2 + 2H_2O + 4e = 4OH^-$$

Corrosion rate grows along with the increase of:

- temperature (value of the oxygen diffusion coefficient grows),
- oxygen concentration in water,
- water flow rate (decrease of the diffusion layer also called boundary layer).

In specific conditions carbon steel exchangers can undergo passivation, although an increase of oxygen concentration in water at higher temperatures and in the presence of chlorides can lead to the occurrence of strong pitting corrosion (Kubicki J., 1994).

Carbon dioxide makes another corrosion-accelerating agent in cooling systems.

The effect of various salts dissolved in water on corrosion depends on the kind of salts. Chlorides and sulfates considerably intensify corrosion processes, while phosphates, silicates, and carbonates cause passivation of carbon steel.

Significant share in the total of corrosion damages has the activity of various kinds of microorganisms that destroy the apparatus, armature, constructions, and protective coats on their surfaces.

Incrustation processes

In the case, when cooling water does not meet the chemical requirements it can cause precipitation of the following kinds of deposits:

- mineral crystalline,
- mineral amorphous.

The main reason for the mentioned precipitation is high carbonate hardness and excessive salinity of cooling water. Salts that are dissolved in the water get condensed as water evaporation proceeds and usually precipitate when the solubility product gets exceeded. The process runs in heat exchangers (and in cooling installations) that make an advantageous environment for the beginning of solid phase crystallization.

Scale deposits that form in cooling water systems are polycrystalline porous substances with amorphous inclusions. Their physical - chemical and mechanical properties are variable depending on many factors such as:

- the kind and concentration of substances contained in the recycled water - both pollutants and substances purposefully added to enhance properties of the water,
- local heat load,
- the kind of crystallization base,
- hydrodynamic conditions,
- contact with polluted atmospheric air,
- corrosive power of water against construction materials,
- development of biological life in water.

Depending on the prevailing content of carbonate, sulfate or silicate compounds three main types of scale can be distinguished (Stańda J., 1999):

- carbonate scale that contains mainly calcium and magnesium carbonates as well as magnesium hydroxide,
- sulfate scale (gypsum),that contains more than 50% of calcium sulfate,
- silicate scale whose basic components are calcium and magnesium silicates and aluminosilicates.

Considerable content of calcium bicarbonate in raw water that is used for cooling purposes, its low solubility and favorable conditions in recirculating cooling systems are the reason why carbonate scale occurs the most frequently and its basic component is calcium carbonate which can form as a result of:

- temperature increase in the system,
- pH changes,
- concentration increase following from the solution condensation.

COOLING SYSTEM PROTECTION AGAINST DEPOSIT PRECIPITATION

Methods for preventing scale formation can be developed in the two following directions:

- introduction of supplementary water with most of the scale-generating pollutants removed,
- treatment of the recycled water by adding inhibitors.

Inhibitor protection

An analysis of the pertinent literature reports of the recent 10 years and opinions based on practical experience leads to the conclusion that inhibitor protection, sometimes also coupled with biocide protection, makes the most effective and economical method for preventing scale formation and corrosion in industrial cooling water systems of the recirculating type.

The key to elaborate a good program for the cooling water treatment in recirculating systems is its chemical composition when it gets condensed.

The best regulator for the economics and reliability of the applied chemical treatment method is the recycled water reaction.

According to Ascolese Ch.It R., (1998) water treatment programs can be classified into two groups:

- a neutral program in the operation conditions of $6{,}8 < pH < 7{,}8$,
- an alkaline program when $7{,}8 < pH < 9{,}0$.

Till recent times many inorganic metallic compounds such as chromates, molybdates and zinc compounds as well as some non–metallic ones like phosphates (polyphosphates and orthophosphates), silicates, nitrites and also azoles that effectively protect copper alloys have been applied as corrosion inhibitors.

Disadvantages of inorganic inhibitors such as: toxicity (chromates), low stability (silicates and polyphosphates) or selective protective action (nitrites) as well as increasingly rigid ecological standards, have turned the interest of researchers to the application of organic compounds as potential inhibitors of multifunctional properties (Amjad Z., 1997).

Within the 10 recent years, many water treatment technologies based on phosphonate acid compounds have been elaborated. They exhibit relatively high efficiency both in inhibiting corrosion of ferrous metals as well as in water treatment and preventing scale formation.

REMOVAL OF DEPOSITS AND PREVENTING THEIR FORMATION IN AN INDUSTRIAL COOLING INSTALLATION

The testing has been performed in a recirculating cooling installation *Lacpol* in Gdynia. The installation has been composed of: four shell-and-tube ammonia condensers of the SRS type and fan coolers. All condenser and cooler elements that contact water have been made of ST3 steel. Surfaces of heat exchangers have been covered with scale layer of 3mm of average thickness.

Reference conditions

Chemical analysis of the scale has shown that it has contained 95% of $CaCO_3$, about 3% of iron compounds, and 2% of HCl-insoluble components (including organic ones).

Table 1 presents properties of the cooling water.

Table 1

No	Indicators	Makeup water	Recycled water	Condensation coefficient
1	pH	7	8,5	
3	general hardness mval/dm^3	6,6	7,92	1,2 (t)
3	carbonate hardness mval/dm^3	4,8	5,4	1,2
4	Cl^- content mg/dm^3	36,2	58,2	1,5 (n)
5	SO_4^{2-} content mg/dm^3	80,0	124,8	1,56

It follows from the analyses of the feeding and recycled waters that condensation coefficients have the values given in the last column of Table I. The condensation coefficient of chlorides (the best soluble salts) that by almost 2 times exceeds the condensation value of general and carbonate hardness proves the occurrence of precipitation of calcium and magnesium carbonates. As *t / n* is 0,75, it can be calculated that 25% of hardness introduced to the system precipitated in the form of scale.

The average water consumption prior to the treatment application:

in the summer season - 202 m^3/day,

in the winter season - 110 m^3/day.

In a one-year time, a scale deposit of 3 mm thickness has accumulated and has been mechanically removed every year.

Description of the cooling water treatment process and descaling

A water treatment method elaborated according to the Polish patent No. 102516 (Zagórski et al. 1978) has been applied. Ammonium salt of a strong acid (ammonium chloride and sulfate) has been used as the pH regulator. Sodium polyphosphate (the trade name - *polifos*) with the addition of zinc sulfate has been applied as the corrosion and incrustation inhibitor while sodium lignosulfonate (known in the market under name of *klutan*) has acted as a dispersion agent (Szymura et al. 2005).

Because of a great amount of scale in the installation a preliminary dose of ammonium salts of 1.7 of the stoichiometric dose with respect to carbonate hardness has been applied. The proportions of ammonium sulfate and chloride have been calculated in such a way for not to exceed the gypsum solubility product. Analyses of the feeding and recycled waters have been performed twice a week.

An additional system has been elaborated and applied to supply chemicals to the feeding water pipe and direct them together directly to the condenser. The system has been automated. When the salinity meter indication for the recycled water has exceeded by three times the value for the feeding water with chemicals a valve for supplementary water has been opened. It has made it possible to maintain an assumed level of the recycled water condensation. Fig. 1 presents a schematic diagram of the cooling installation together with the metering system.

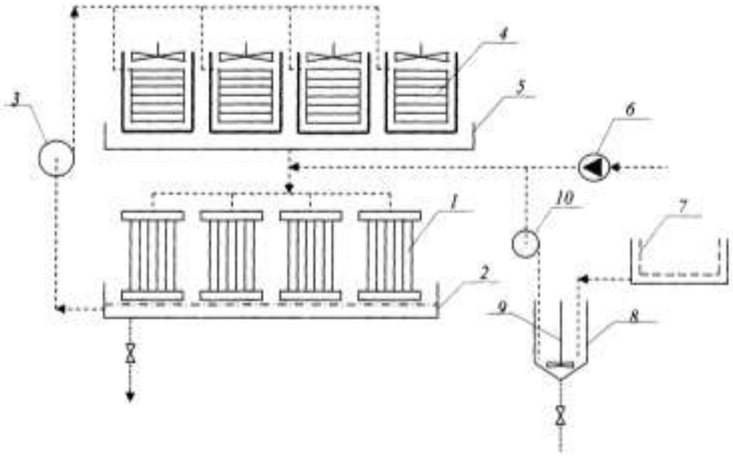

Fig. 1. Diagram of the cooling installation *Lacpol* in Gdynia
1 -shell-and-tube condenser, 2 - tank under condensers, 3 - recycled water pump, 4 - fan coolers, 5 - trays under coolers, 6 - water meter, 7 - tank with a screen for dissolving chemicals, 8 -mixer, 9 - stirrer, 10 - volumetric pump

Graph in the Fig. 2 presents a course of the cooling water treatment process realized in the discussed installation. Values of the *t/n* ratio illustrate the decarbonization reaction process (*t/n* =1). The *t/n* values of that are higher than unity indicate scale dissolution.

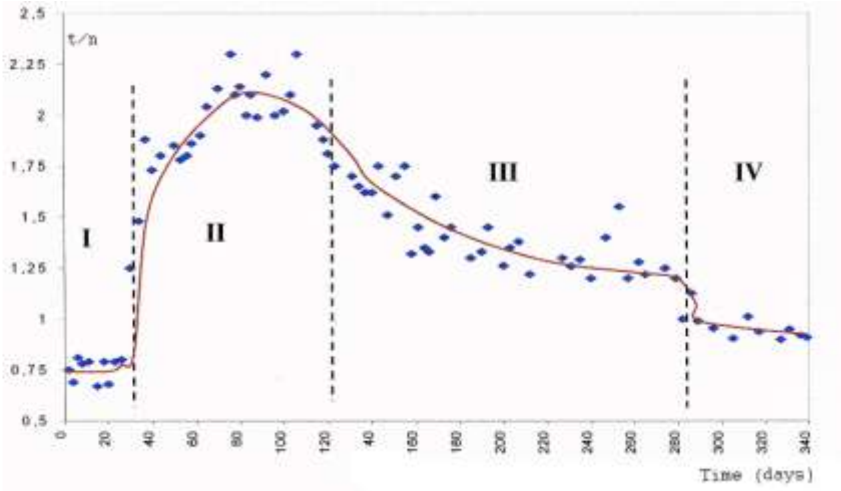

Fig. 2. Variations of the *t/n* ratio during the application of ammonium sulfate in the Cold Store *Lacpol* installation in Gdynia

DISCUSSION

In Fig. 2, a one-month period when the preparation has not been applied is denoted as I. The ratio $t / n \approx 0,75$ indicates scale deposition in the installation.

During the second two-month period (II) the preparation dose of 1.7 of the stoichiometric value has been applied. The *t/n* has increased even up to 2, but low pH (close to 6,2) has made authors reduce the preparation dose. Scale has kept softening and dropping off metal surfaces in great quantities.

Over the third period (III) a dose equal to 1.5 of the stoichiometric value has been applied and the recycled water pH has increased up to 6,5 ÷ 6,8. The mentioned procedures have been applied for four months and then it has been decided to stop the installation for a short time to remove sludge and pieces of dropped-off scale from trays under coolers and condensers.

After 330 days of the preparation application, in the fourth period (IV) it has been decided to reduce the preparation dose down to 1,2 of the stoichiometric value because the scale has practically been removed from the installation. The *t/n* ratio has been close to 1, and the carbonate hardness (alkalinity *m*) has been of fractional value, which confirmed decarbonization of the water.

The water treatment process in the discussed installation has been controlled for the next 10 years. By that time the recycled water pH has been maintained within the range of 6,5 ÷ 7,5. When the pH has been getting lower than 6,5 the dose of ammonium salts has been reduced by 10%, and when it has reached values higher than 7,5 - the dose has been increased by 10%. The installation has operated according to the expectations - scale deposit has not grown.

At the same time, a research into the corrosive effect of water on ST3 steel has been carried out as well as microbiological tests. Results of those investigations will be the subject of separate reports.

LITERETURE

[1] Ahmed S., Bayers J., 2000. *Design basics for cooling systems*: Chemical Engineering, 1, 78-83

[2] Amjad Z., Pugh J., Zibrida J., 1997. *Polymer performance in cooling water:* The Influence of Process Variables, Chemical Treatmant Materials Performances, 1, 32-38

[3] Ascolese Ch.R., Bain D.J., 1998. *Take advantage of effective cooling-water – treatment programs*: Chemical Engineering Progress, 3, 49-54

[4] Kubicki J., 1994. *Wybrane problemy korozyjne w instalacji wody chłodzącej*, Prace Nauk. I-26, 41, Wyd. Politechnika Wr., Wrocław, 46-57

[5] Rocznik Statystyczny R.P., 2003

[6] Spoz J., Gospodarka Wodna, 4, 2000

[7] Stańda J., 1999. *Woda do kotłów parowych i obiegów chłodzących siłowni cieplnych*, WNT, Warszawa

[8] Szymura T., Pomorska K., 2005. *Zastosowanie soli amonowych w układach wody chłodniczej*, Chłodnictwo, 1-2, 22-27

[9] Veil J.A., Puder M.G., Littleton D.J., Hoses D.O.: Cooling Water use Patterns at US Nonutility Electric Generation Facilitis, Environmental Science & Policy, 2, 1999

[10] Zagórski K., Warszawa Z., Szymura T., 1978. *Sposób usuwania węglanowego kamienia kotłowego i zapobieganie jego powstawaniu w wodno-chłodniczych instalacjach przemysłowych,* Patent Polski nr 102517

5th International Conference **ELMECO**
Nałęczów, Poland
September 2005

MICROWAVE REACTOR FOR NITROUS OXIDE PROCESSING

Krzysztof Krawczyk, Katarzyna Naperty, Michał Drozdowski

Warsaw University of Technology, Faculty of Chemistry
Noakowskiego 3, 00-664 Warszawa
kraw@ch.pw.edu.pl

Abstract

Processing of nitrous oxide in microwave discharge plasma coupled with gliding discharge were investigated. The studies were carried out in a quartz reactor with diameter of microwave discharge space 13mm or 6mm. The use of the smaller reaction space enabled to achieve a higher overall conversion rate of N_2O *(to oxygen, nitrogen, and nitric oxide), as well as higher conversion rate of the* N_2O *to NO. The conversion rate of nitrous oxide depended also considerably on the flow rate of gas mixture. The increase of gas flow rate from 200Nl/h to 400Nl/h resulted in a twice as high conversion rate of nitrous oxide. It refers to both the overall conversion rate of* N_2O *and conversion rate of* N_2O *to NO.*

Keywords: gliding discharge, microwave discharge, nitric oxide, nitrous oxide.

INTRODUCTION

The specific properties of non-equilibrium plasma, and particularly the presence of high-energy reactive species, have decided that is widely used in practice in many branches of technology. The plasma is used in the packaging industry, electronics, chemical analysis, surface treatment of materials, lightening technology, metallurgy, gas dedusting and water treatment [1].

In the non-equilibrium plasma the total energy of heavy particles is much lower than the mean energy of electrons. The plasma is obtained with the use of high voltage electric discharges (such as corona, glowing, or barrier discharges), or discharges resulted in high frequency electric currents, preferably under reduced pressures.

The non-equilibrium plasma can also be obtained in a gliding discharge. The gliding discharge is used in the studies on decomposition of chloro- and chlorofluoroorganic compounds, for manufacture of soot, for converting methane into a syngas, and for decomposition of nitrous oxide [2-8].

It was found that in the gliding discharge plasma, besides nitrogen and oxygen, NO is the main product of nitrous oxide processing. This way is the most favourable because NO can be used for nitric acid production. It should be added that when air was used as carrier gas, NO was produced also from nitrogen and oxygen. However, nitric oxide is unstable and it decomposes to nitrogen and oxygen. The scheme of plasma processing of nitrous oxide is as follows:

$$N_2O \rightarrow N_2 + O_2$$
$$\searrow NO \nearrow$$

High conversion of N_2O to NO (37%) was obtained in the studies on gliding discharge. Overall conversion of nitrous oxide amounted up to 80% [5]. Studies have also been carried out on the effect of reaction space on N_2O processing. The conversion of N_2O to NO exceeded 50% in a reactor with modified reaction space where much higher power densities were used. Maximum value of overall conversion of nitrous oxide was 82% [9]. The main problem is too small efficiency of the nitrous oxide conversion to NO in gliding discharge plasma. This may result from hydrodynamics of the gas flow through the reactor and from low values of the discharge energy.

The microwave plasma is a prosperous source of energy owing to the commercial production of microwave generators and low cost of plasma generation. The microwave plasma methods are suitable for conducting the reactions of high activation energy, for example for the decomposition of stable pollutants (gaseous, liquid or solid). The microwave plasma is characterised by a relatively high energy of electrons ranging from 1 to more than 10 electronovolts and high temperature up to several thousand Kelvin. The most substantial differences between the microwave discharge plasma and plasmas obtained from other kinds of electric discharges are high concentration of active particles and high density of energised electrons.

Two methods of carrying out chemical processes in gas phase in microwave discharges are known at present. The first one consists in the induction of electrode-less plasma by absorbing microwave energy concentrated within the volume of ionised gas, usually under reduced pressure. Another method consists in the induction of strong electric field in the reactor space by means of an additional electrode (discharge of the torch type).

The torch type discharges are employed in studying the decomposition of volatile organic compounds – methane, toluene, carbon tetrachloride and chloroform, fluorochloroorganic compounds and nitric oxide [10]. Since the chemical reactions occurring in plasma proceed, owing to the action of its active components, in relatively low temperature, the microwave plasma can be used for depositing thin layers on plastic substrates sensitive to the action of high temperatures. The microwave plasma is also used for coating optical materials (e.g. lenses) made of organic materials, such as polycarbonates, with a thin film of hard, transparent material, e.g. silicon dioxide or silicon oxynitride which can protect the surface against scratching. A similar technology is used for producing very hard carbon coatings from simple organic substances such as hydrocarbons, alcohol’s, etc. The process parameters are selected so as to obtain, by the decomposition of the organic substance, a thin film having a structure of diamond. A conversion of polyaromatic hydrocarbons carried out in a microwave discharge under low pressure in the presence of oxygen gave CO_2, CO, and some solid compounds as products of complete conversion of the starting materials [11].

For the acceptance of the method by the industry with the aim of eliminating harmful gases the plasma should be generated under atmospheric or similar pressure. It is very difficult to obtain microwave plasma under atmospheric pressure. The task was successfully realised only in a limited number of research centres.

The aim of the present study was to examine a new type of reactor combining two different plasma sources: gliding discharge and microwave discharge. The new reactor was used for the study of nitrous oxide conversion.

In the developed reactor [12], the preliminary gas ionisation by gliding discharge enables the initiation of microwave discharges under atmospheric pressure in different gases, e.g. air or oxygen. The reactor consists of two parts: a chamber for gliding discharge and a narrow tube for the microwave one. It was used for studying the conversion of nitrous oxide to NO at atmospheric pressure. The effect of the reactor diameter was also studied.

EXPERIMENTAL

The reactor designed and constructed in our laboratory consists of two parts: for gliding discharge generation and for microwave discharge. The reaction chamber (1) in which the gliding discharge and the microwave discharge proceed simultaneously is a substantial part of the reactor. Two electrodes (2) used for generating the gliding discharge for ionisation of the gas passing through a steel nozzle (3), mounted between the electrodes, are placed in the lower part of the reactor. The diameter of the reaction chamber for gliding discharge is 36 mm. The upper part of the reactor, in the direction of gas flow, comprises a chamber for microwave discharge generated by the radiation of frequency 2.45GHz from a magnetron (4) and supplied through a wave-guide (5). The initiation of microwave plasma is possible due to the initiating electrode (6) mounted in a ceramic sifter (7) in the quartz-glass tube 13mm or 6mm in diameter (8).

The processing of nitrous oxide was studied for the flow rate 200Nl/h or 400Nl/h of a gas containing 5% by vol. of nitrous oxide. Air was used as the carrier gas. The experiments were carried out under atmospheric pressure. The concentration of nitrous oxide was determined by gas chromatography using a column filled with Porapak Q. The amount of NO was determined by the volumetric-gravimetric method. The experiments were carried out in a reactor (Fig. 1), in which the reaction space of microwave discharge inside the quartz-glass tube had the diameter of 13mm or 6mm. The microwave plasma was initiated by means of a platinum-rhodium wire electrode of diameter 1mm mounted in a ceramic sifter. It was found that the microwave plasma could not be initiated in the mixture of N_2O and air as only after previous ionisation of the gas by gliding discharge in the lower part of the reactor.

After starting the gas flow and switching on the gliding discharge in the lower part of the reactor the content of N_2O was determined in the inlet gas and the content of NO was measured in the gas mixture at the outlet from the reactor. After having ended the study of N_2O processing in gliding discharge plasma the supply to the microwave part of the reactor was started. The power of gliding discharge was approximately equal as in the first point of earlier study (Table 1, Figs. 2 and 3, points denoted as 1).

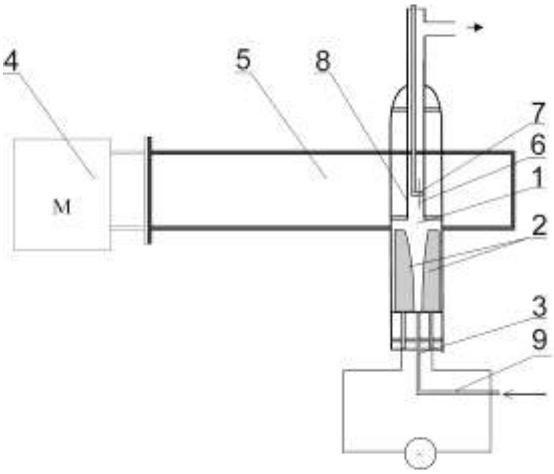

Fig.1. Reactors for nitrous oxide conversion:
1 – discharge zone, 2 – metal electrodes, 3 – gas inlet, 4 – generators of microwave,
5 – wave-guide cavity, 6 – microwave initiation electrode, 7 – ceramics, 8 – quartz-glass tube 13mm or 6mm in diameter, 9 – stainless steel nozzle

The overall conversion of nitrous oxide (X_1) was calculated from the formula:

$$X_1 = (A - B) / A$$

where:
A – number of moles of nitrous oxide in the inlet gas mixture,
B - number of moles of nitrous oxide in the outlet gas mixture.
The conversion of nitrous oxide to NO (X_2) was calculated as:

$$X_2 = C / 2A$$

where:
C – number of moles of NO in the outlet gas mixture.

On the basis of this results the calculation of the overall conversion rate of N_2O (r) and conversion rate of N_2O to NO (r_{NO}) was calculated from the following equation:

$$r = X_1 W [N_2O], \qquad [mol/h]$$

$$r_{NO} = X_2 W [N_2O], \qquad [mol/h],$$

in which
W [N_2O] - flow rate of N_2O [mol/h]

RESULTS AND CONCLUSIONS

It has been found that the organisation of the reaction space is substantial in the system where the action of gliding discharge is coupled with the action of microwave discharge. The hydrodynamics of gas flow through the space of gliding discharge and microwave discharge is of particular importance (Table 1).

Table 1. Conversion of nitrous oxide in gliding arc and microwave plasma. Electrode initiated of microwave discharge – rod from PtRh30

Gas flow rate, Nl/h	Gliding power, W	Microwave power, W	Overall power, W	Overall conversion of N_2O, %	Conversion of N_2O to NO, %
Diameter of microwave discharge 13mm.					
200	150	0	150	24	13
	158.7	80	238.7	40	18.1
	158.7	126	284.7	44	18.6
	176.1	155	331.1	48	21.1
	177.8	222	399.8	53	23.0
400	204.3	0	204.3	26	12.6
	197.9	102	299.9	33	17.6
	195.9	160	355.9	40	17.1
	200	221	421.0	39	18.4
Diameter of microwave discharge 6mm.					
200	184.6	0	184.6	46	17.8
	190.1	100	290.1	52	21.3
	192.0	140	332.0	54	23.2
	190.1	180	370.1	56	23.1
400	249.4	0	249.4	37.5	15.5
	228.6	139	367.6	43	18
	228.6	185	413.6	44	19.7
	228.6	205	433.6	46	19

The overall conversion rate of N_2O changed markedly when the diameter of the reaction space inside the quartz-glass tube was changed from 13mm to 6mm (Fig. 2). It was observed for gas flow rates 200 and 400Nl/h. It should be mentioned that slightly higher r_{NO} were observed for the smaller reaction space diameter (Fig. 3).

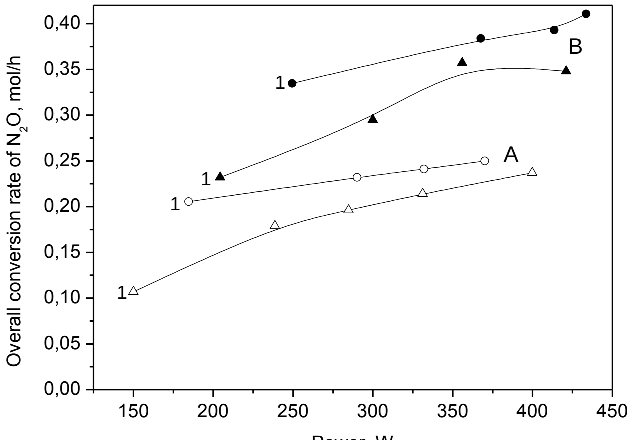

Fig. 2. Effect of electric power on overall conversion rate of nitrous oxide in gliding discharge (point denoted as 1) and coupled discharges. Initial concentration of nitrous oxide 5% by vol. Gas flow rate: A – 200Nl/h, B – 400Nl/h.
Diameter of microwave discharge space: 13mm – ▲, Δ ; 6mm – ●, ○

The gas flow rate influenced markedly the conversion rate of nitrous oxide and conversion rate of nitrous oxide to NO in the gliding discharge and in the coupled discharges (Figs. 2,3). The increase of gas flow rate from 200 Nl/h to 400N l/h gave almost twice increase of both the reaction rates.

The results obtained have shown that the modification of the reaction space consisting in reduction of the reaction space diameter enables to obtain a slightly higher conversion rate of N_2O to NO. It results probably from the change of hydrodynamics through the zone of coupled discharges. It should be pointed out that no electrode corrosion was observed and the working conditions were stable in the coupled discharges. No disturbance was observed during period of the 6 h.

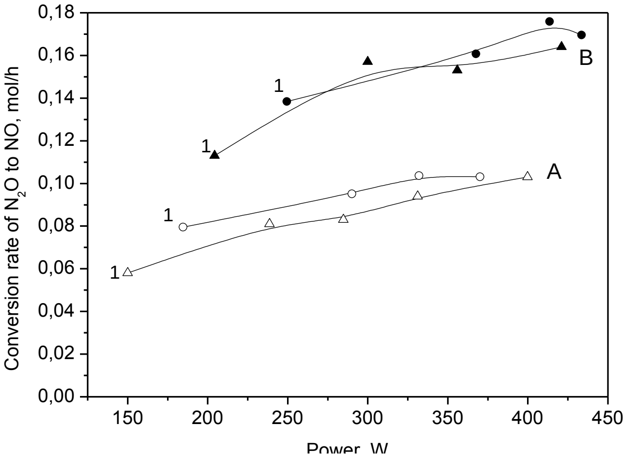

Fig. 3. Effect of electric power on conversion rate of nitrous oxide to NO in gliding discharge (point denoted as 1) and coupled discharges. Initial concentration of nitrous oxide 5% by vol. Gas flow rate: A – 200Nl/h, B – 400Nl/h.
Diameter of microwave discharge space: 13mm – ▲, Δ ; 6mm – ●, ○

ACKNOWLEDGEMENT

This work was supported by Polish State Committee for Scientific Research: grant No. 3 T09B 044 26.

REFERENCES

[1] Celiński Z., Plazma, PWN, Warszawa, 1980

[2] Czernichowski A., Gliding arc. Applications to engineering and environment control, Pure & Appl. Chem., Vol. 66, No. 6, 1994, pp. 1301-1310

[3] Schmidt-Szałowski K., Opalińska T., Sentek J., Krawczyk K., Ruszniak J., Zieliński T., Radomyska K., J., Methane conversion into C2 hydrocarbons and carbon black in dielectric-barrier and gliding discharges, Adv. Oxid. Technol., vol. 7, No.1, 2004, pp. 39-50

[4] Opalska A., Ph. D. Thesis, Warsaw University of Technology, Warszawa, 2004

[5] Krawczyk K., Młotek M., Combined plasma-catalytic processing of nitrous oxide, Appl. Catal. B: Environmental, 30, 2001, pp. 233-245

[6] Krawczyk K., Gapanowicz O., Catalytic and plasma-catalytic processing of nitrous oxide, Polish J. Chem., 78, 2004, pp. 873-877

[7] Krawczyk K., Ulejczyk B., Decomposition of chlomethanes in gliding discharges, Plasma Chem. Plasma Proc., vol. 23, No. 2, 2003, pp. 265-281

[8] Czernichowski A., Electrically assisted conversion of natural gas into syngas, Karbo-energochemia-ekologia, 11, 1998, pp. 359-369

[9] Krawczyk K., Młotek M., Rzepecka K., Conversion of N2O in gliding arc dirscharges, Przem. Chem. vol. 82, No. 10, 2003, pp. 1387- 1390

[10] Jasiński M., Ph. D. Thesis, Institute of Fluid Flow Machinery, Polish Academy of Science, Gdańsk, 2003

[11] Ballin L. J., Herzler B. L., Development of microwave plasma detoxication process for hazardous wastes, Environmental Science & Technology, vol. 12, No. 6, 1978, pp. 673-679

[12] Krawczyk K., Schmidt-Szałowski K., Reszke E., Pol. Patent Appl., P372039, 2004

5th International Conference **ELMECO**
Nałęczów, Poland
September 2005

THIN FILMS DEPOSITED FROM RIMETHYLMETHOXYSILANE

Zenobia Rżanek-Boroch, Krzysztof Jóźwik

Faculty of Chemistry, Warsaw University of Technology
00-664 Warszawa, Noakowskiego 3, Poland
rzanek@ch.pw.edu.pl

Abstract

The deposition and characterization of thin films of silicon oxide in Dielectric Barrier Discharge under atmospheric pressure from trimethylmethoxysilane as the precursor was carried out.

Keywords: thin films, silicon oxide, trimethylmethoxysilane

INTRODUCTION

Plasma deposited thin layers of silicon dioxide with the thickness from few to several hundred nanometers found application as reflective coatings in optics, anticorrosive layers in electronics and biocompatible coatings in the production of implants. On an industrial scale thin layers are plasma deposited, under reduced pressure, by means of silane or other silicon containing compounds, such as tetraethoxysilane. The precursors are introduced to the reactor in the form of gaseous mixtures. Currents of frequency 13.56 MHz are usually applied to excite the discharge.

In the Department of Inorganic Technology and Ceramics of Faculty of Chemistry, Warsaw University of Technology, a laboratory method of thin film deposition in dielectric barrier discharge (DBD) of frequency up to 5 kHz, under atmospheric pressure, has been developed. The silicon containing compounds such as tetramethoxysilane, tetraethoxysilane, hexamethyldisiloxane, hexamethyldisilazane served as procursors in the deposition process [1], [2], [3].

The purpose of the work was to study the effect of the gas mixture composition and substrate temperature on the properties of coatings deposited from a new, not used up to now, compound of formula, $CH_3OSi(CH_3)_3$ trimethylmethoxysilane (TMMOS). The coatings were characterized by thickness measurements with ellipsometric method, composition with FTIR spectroscopy and surface topography with atomic force microscope (AFM).

EXPERIMENTAL

The thin film deposition was carried out in a reactor equipped with a quartz dielectric barrier in a discharge of 3.5 kHz frequency under atmospheric pressure [1]. Plates of monocrystalline silicon of the surface parallel to the <111> plane were the substrate. The layers were deposited from gas mixtures: trimethylmethoxysilane (TMMOS) and helium, doped with oxygen. The TMMOS concentration was 0.18% at the gas flow through the reactor of 11 dm^3/h, whereas the oxygen concentration varied in the 0-0.36% range. The gases used in the process were pure or p.a. The deposition was carried out for 5 and 15 minutes at temperatures from ambient to 300°C.

The parameters of coatings are presented in Table 1.

Due to the fact that films deposited at room temperature were semi-liquid and viscous, further studies were carried out at above 100°C.

Table 1. Parameters of layers deposited for 15 minutes from the mixture TMMOS + He, TMMOS + 0.18% O_2+He and TMMOS + 0.36 O_2+He, at various temperatures of the support, a) weighing method, b) ellipsometric method

Notion	Oxygen concentration [%]	Temp.[^{o}C]	Thickness [nm]		TMMOS usage [%]	Roughness [nm]
			a	b		
K028	0	100	1340	-	14.20	-
K031	0	150	707	827	7.48	18.59
K033	0	200	463	445	4.92	86.83
K035	0	300	244	221	2.60	104.90
K017	0.18	100	804	851	8.52	2.34
K039	0.18	150	731	647	7.76	9.26
K019	0.18	200	608	572	6.44	10.84
K021	0.18	300	463	548	4.92	7.97
K041	0.36	100	1291	-	13.68	-
K040	0.36	150	439	537	4.64	42.17
K026	0.36	200	390	495	4.12	93.87
K024	0.36	300	731	797	7.76	2.02

In order to determine the effect of oxygen concentration in the mixture on the composition of deposited thin films at 150 °C, 200 °C and 300 °C, FTIR analysis was performed. From this analysis it appears that at 150 °C the oxygen concentration of 0.18% is most favorable, due to the intensity of absorption bands corresponding to Si–O–Si bonds (1037-1041 cm^{-1}) (Fig. 1). The intensity of the absorption band under these conditions is comparable with the absorption of silicon oxide deposited from mixtures without oxygen. The total share of the organic residues, i.e. Si–CH_3 and C–H bonds, with respect to Si–O–Si bonds is ca. 63% for films deposited without oxygen and 64% at oxygen concentration equal 0.18%. A large share of organic residues of as much as 83% at simultaneous low silicon oxide content is observed for films deposited from mixtures containing 0.36% of oxygen (Fig. 1).

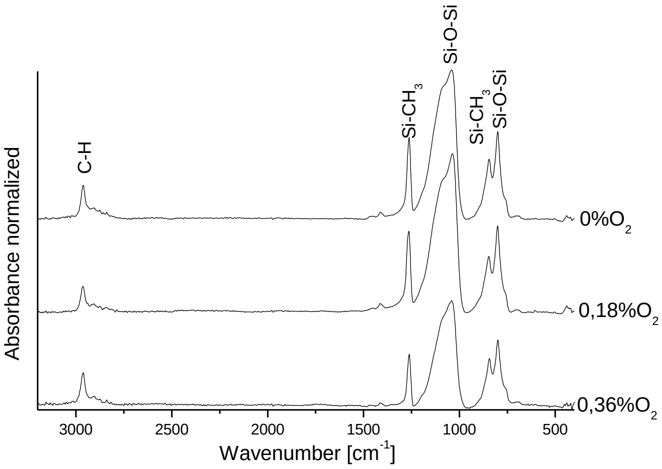

Fig. 1. FTIR spectra of films deposited, at 150 °C, from TMMOS+O_2+He mixtures at various oxygen concentration

After selecting the oxygen concentration of 0.18%, the effect of temperature on the composition of the films deposited was studied. As results from Fig. 2, the coatings deposited at from 100 to 300 °C contain quite considerable amounts of organic bondings such as Si–CH_3 of wavenumbers 1414, 1264, 846 cm^{-1} and C–H (2964 cm^{-1}). Their share in the film is 86% at 100°C and shows a decreasing tendency with an increase in temperature – 64% at 150°C, ca. 53% at 200 °C, whereas at 300°C this share slightly increases to 57%. The highest silicon oxide concentrations are observed in films deposited at 300 °C and 150 °C.

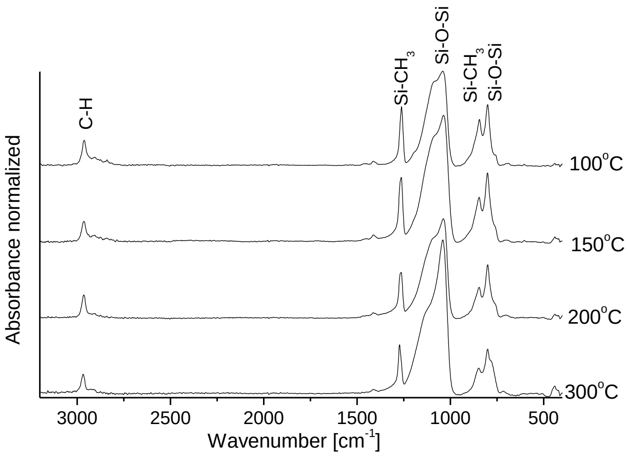

Fig. 2. Effect of the support temperature on the composition of films deposited from a TMMOS + 0.18% O_2+He mixture

In order to determine the effect of the oxygen content and substrate temperature during deposition on the topography of the coatings surface, studies have been carried out with atomic force microscope (AFM), the results of which are presented in Figs. 3a-f (Table 1).

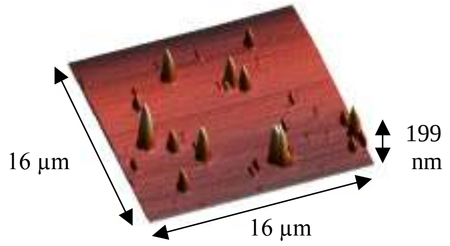

Fig. 3a. Topography of KO31 surface (without oxygen)

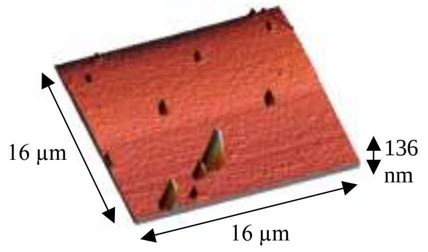

Fig. 3b. Topography of KO39 surface ($0.18\ O_2$)

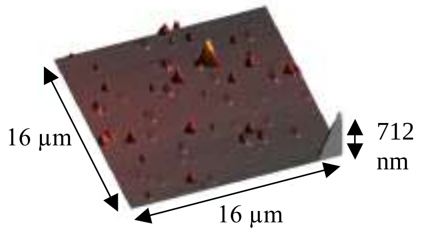

Fig. 3c. Topography of KO40 surface ($0.36\%\ O_2$)

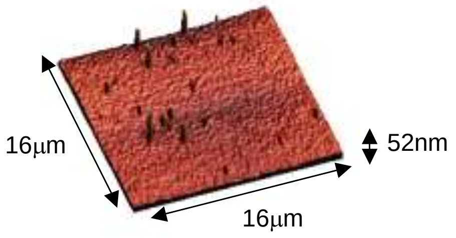

Fig. 3d. Topography of KO17 surface ($0.18\%\ O_2$)

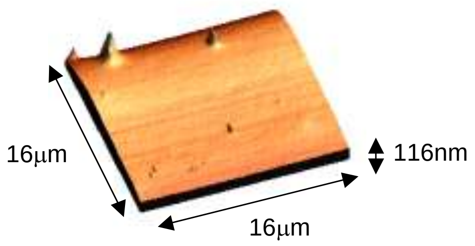

Fig. 3e. Topography of KO19 surface ($0.18\%\ O_2$)

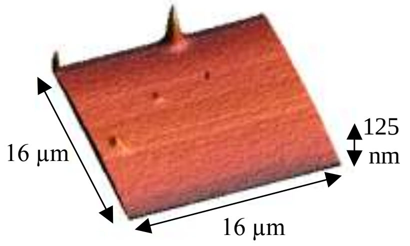

Fig. 3f. Topography of KO21 surface ($0.18\%\ O_2$)

As results from AFM studies, the films bearing higher oxygen concentration, i.e. 0.36%, at the same deposition temperature, e.g. 150 °C (3a-c) are characterized by a two-fold higher roughness in comparison with films deposited without oxygen (18.59 nm) and four-fold higher roughness at oxygen concentration of 0.18% (9.26 nm) (Table 1).

When analyzing the effect of the substrate temperature, at oxygen concentration of 0.18%, on the surface roughness, it can be noticed that the thinnest films are obtained at

300 °C, and their roughness is equal to 7.92 nm, whereas at 100 °C the films are the thickest (804 nm), but their roughness is equal to only 2.34 nm (Figs. 3b-f).

CONCLUSIONS

1. The thin layers in deposited in the plasma reactor in dielectric barrier discharge (DBD) under atmospheric pressure from trimethylmethoxysilane (TMMOS) in the temperature range from 100°C to 300°C are uniform and show high adhesion to the substrate.
2. The coatings deposited at 100-300 °C from TMMOS+O_2+He at oxygen concentration varying from 0 to 0.36% are characterized by the same qualitative composition, small differences are observed only in their quantitative composition.
3. The films deposited at 100 °C are semi-liquid independently from the composition of gas mixture.

ACKNOWLEDGMENTS

This work was support by Ministry of Science Research and Information Technology under grant no. 3 T09B 008 27.

LITERATURE

[1] Schmidt-Szałowski K., Rżanek-Boroch Z.,.Sentek J., Rymuza Z., Kusznierewicz Z., Misiak M., Thin films deposition from heksamethylodisiloxane i heksamethylodisilazane under dielectric-barrier discharge (DBD) continions Plasmas and Polymers, 5, No.3/4, 2000, pp.173 –190

[2] Rżanek-Boroch Z., Schmidt-Szałowski K., Janowska J., Dudziński K., Szymańska A., Misiak M., Thin films obtained by PE-CVD method from hexamethyldisiloxane under atmospheric pressure, *Hakone VIII Contributed papers vol.2 pp. 415-419, Estonia 2002*

[3] Rymuza Z., Misiak M., Rżanek-Boroch Z., Janowska J., The effects od deposition and test condition on nanomechanical behaviour of ultrathin films produced by PE-CVD process at atmospheric pressure, *Thin Solid Films **466**, 2004, pp.156-166*

5th International Conference **ELMECO**
Nałęczów, Poland
September 2005

PIEZOELECTRICAL PROPERTIES OF PLASMA LAYERS Zn-Bi-O

Daniel Dopierała, Jan Ziaja,

Institute of Electrical Engineering Fundamentals, Wrocław University of Technology
ul. Wybrzeże Wyspiańskiego 27
50-370 Wrocław, Poland
E-mail: jan.ziaja@pwr.wroc.pl

Abstract

The article is a presentation of specific piezoelectric properties of thin layers of zinc oxide modified with bismuth (Zn-Bi-O). The purpose of the above work has been to find the relation between the technological parameters of receiving thin films /density power deposited on target, reactive gas pressure, distance from the substrate to the target/ and the piezoelectric properties d_{33}. The thin layers of Zn-Bi-O were obtained in a reactive process of magnetron sputtering of the metallic target Zn-Bi. As a result of the technological processes involved, a coefficient value d_{33} received in the ranges 1-10 pC/N. The following step is to find the most suitable technological parameters in order to obtain optimum piezoelectric properties of the thin films Zn-Bi-O.

Keywords: piezoelectric detector EA, thin layer Zn-Bi-O, magnetron sputtering

INTRODUCTION

In recent years one can observe rapid development in the field of technics, and especially in the material production technology. The effect of the phenomenon has been fast progress in both fields of electrotechnique and electrotechnology. Not without significance is also ultrasonique technique whose integral part are piezoelectric transducers. The piezoelectric transducers are used in two ways: on one hand they serve as acoustic wave generators, whereas on the other hand they can serve as detectors used in acoustic emission technique (EA). The above technique has a wide range of applications in diagnostics of civil engineering, various devices, insulator high voltage, medicine as well as in testing of a correct realization of some chemical reactions [1].

Within modern technique EA there are two kinds of transducers applied as piezoelectric sensors: ceramic transducers PZT (lead-zirconian tytanian) and polymer PVDF. The presented technique is characterized by high fragility, narrow transmission band, and extremely high value of the piezoelectric coefficient d_{33} rising up to 500 pC/N, whereas the material PVDF shows much better mechanical properties and broader transmission band, however it must be mentioned here that the latter decreases the coefficient d_{33} down to 30 pC/N. [2].

Another field of technics developing in a spectacular way throughout several decades of the 20-tieth century and in the new age is electronics, and especially, microelectronics. Miniaturization of sizes to micro- and nanometers in control systems monitoring work of computer systems has generated a great number of problems deriving from excess charge deposition, both in volume and on its surface. It must be stressed here, that even small quantity of the charge might give an objectionable effect of excess heat emission which, in consequence might lead to damage or complete destruction of the device.

In order to protect micro- and nanosystems from their degradation it would be necessary to make use of suitable and effective protecting systems, reacting to deposition of such a charge on their surface. In such a case the best solution are acoustic sensors, due to their reaction to excessive charge deposit, and as such they could be used in this specific field. However their application would have to increase the size of an electronic device, and, as a result, slow down the work of the device and expose it to malfunctioning. The ideal sensor that would effectively take its task should be characterized by miniature size of an order of a few atoms. This is why it is important to make the most miniature sensor with properties as good as in polymer and ceramics. A proper direction of research on miniaturization of the sizes could be amorphic layers of Zn-O doped with Bi_2-O_3, with thickness of an order of nanometres. Research conducted on those materials has shown that they can be used as varistor material in both electric and telecommunication system protection, in view of optic properties in optoelectronics, i.e. optical waveguide and laser [3].

The purpose of this work has been analysis of representatively chosen piezoelectric properties of thin layers of bismuth and zinc (Zn-Bi-O) and defining their correlation to technological parameters needed to obtain them, such as: density power deposited on electrode, reactivation gas pressure, and distance from the base to the target, as well as stating possibilities of practical use of those materials in technics.

EXPERIMENTAL PART

Description of the method

The base for obtaining thin films of Zn-Bi-O was preparation of the target consisting of 96 % of Zn and 4 % of Bi weight. Secondly, the Zn-Bi-O films were obtained in magnetron sputtering reactivation process by means of impulse method. The most commonly used methods for obtaining varistor layers of Zn-Bi-O are: sol-gel, magnetron sputtering, direct and amplified currents / DC/AC /, screen process, flash evaporation and pyrolysis. [4, 5, 6]. The chosen method is thoroughly described in the literature, [7, 8] and numbered to plasma low – temperature methods because it makes use of plasma, where electron mean energy does not exceed 1 keV, and ion energy is of an order of singular eV. The deposited target was powered by the unit DPS (DORA POWER SYSTEM). The system is adjusted to powering plasma gun by Variable or impulse voltage with frequency f=200 kHz and voltage supply of 1,2 kV.

Duration of the sputtering process reached t=90-100 min. Wattage rating on target was placed in the range of 130-400 W. During the sputtering work gas pressure was constant, it was different for the samples: $9*10^{-3}$; $1,2*10^{-2}$; $3*10^{-2}$ Tr. The layers were deposited on the nickel surface and distance from target to the substrate was d=4-8 cm. By means of vacuum evaporation method the nickel or aluminum electrodes were deposited on layers.

All the obtained layers were then watched through a scanning electron microscope (SEM) equipped with roentgen microprobe. The measurements proved that the weight ratio Zn:Bi in the obtained layers was different from the weight ratio on the target. X-ray and microscope analysis have shown that the obtained piezoelectric thin layers are characterized by amorphous structure (Fig.1) but annealing of the layers in the temperatures higher than 750^o C causes their crystallization (Fig.2) Precise microsonde roentgen probe of the chemical constitution of heterogeneity obtained during the sputtering magnetron has proved the existence of granular site Bi on the area. See the granules of Bi in circles in Fig.1. With high power deposited on the target, the number of granules of Bi and their size is growing. Atomic consistence of some Bi sites almost reached the value of Zn/Bi 73/27. The results may be of great importance to a number of different properties of the tested material.

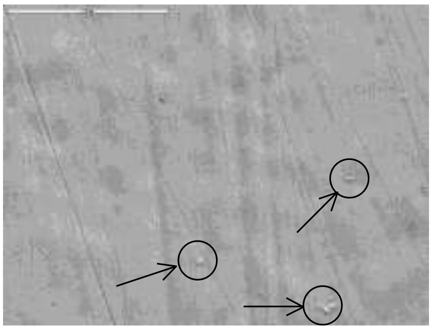

Fig. 1. Microscopic image of the fracture of Zn-Bi-O thin films deposited on glass substrate. The areas of metallic bismuth in circles were marked

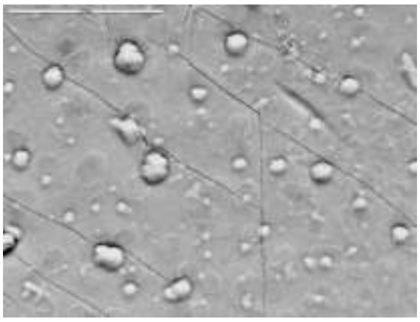

Fig. 2. Microscope image of fracture Zn-Bi-O deposited on Ni substrate an hold at a temperature of 750^o C

Measurement of piezoelectric properties in Zn-Bi-O layers

The parameter on the basis of which the value of the tested materials was measured was piezoelectric coefficient d_{33} defined as the relation between the value of induced charge Q on the surface of a layer and the value of applied force F. In the experiment we have used a measurement setup based on the method introduced by Łyszczejkin. The diagram of the measurement was shown in Fig.3. During the testing process the layer was exposed to external extensions with a variable force applied and it was being changed in the range of F=0,2-2 N. The induced electrical charge, by means of which the value d_{33} was defined, was measured with an electrometer, and its value was defined by means of quotation (1):

$$d_{33} = \frac{Q}{F} \quad [pC/N] \tag{1}$$

Where Q- induced electric charge, F- force applied perpendicularly to the layer surface

The electrical charge was measured in standart conditions, i.e. T=23 C, 65 % humidity and p= 1 atm. See examples of measurement results in Fig. 2.

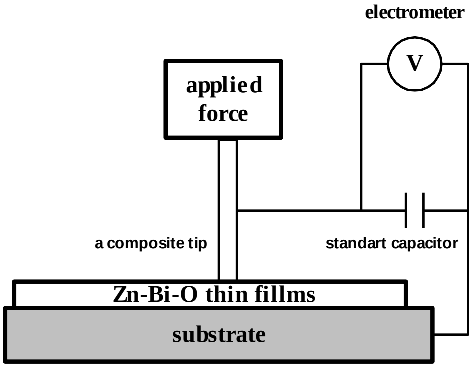

Fig. 3. Scheme of measurement setup for piezoelectric properties

In the modern technique EA there is tendency to apply ceramic transducers PZT and polymer PVDF as piezoelectric sensors. The above ceramics characterized by high fragility, narrow transmission band and extremely high value d_{33} up to 500 pC/N, whereas the material PVDF shows much better mechanical properties and much broader transmission band, however it takes place at the cost of lower coefficient d_{33} down to 30 pC/N. The value of the measured electric charge and the coefficient d_{33} greatly depends on the pressure under which the process took place (Fig.4) values of oxygen pressure.

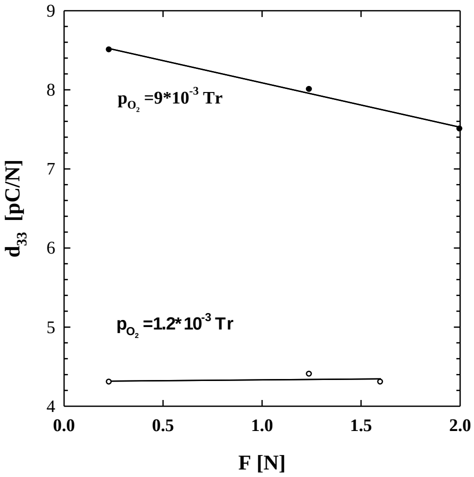

Fig. 4. Dependence of the coefficient d_{33} on the force applied for various

Other technological parameters having influence on the value of the discussed constant are: power deposited on the target and distance from the target to the substrate (Fig.5). Fig.6 shows the dependency between the phenomenal coefficient k- constant for a given process, defined in the units W/Pa, joining the parameters of power deposited on the target and reactive gas pressure and coefficient d_{33}. See the influence of the kind of deposited electrodes during the magnetron sputtering process by means of impulse method.

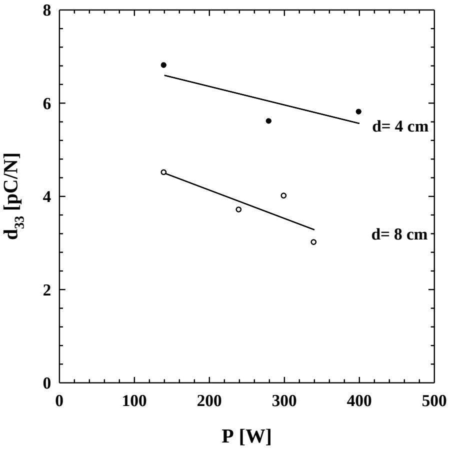

Fig. 5. Dependence of the coefficient d_{33} on the power for various values of distance target-substrate

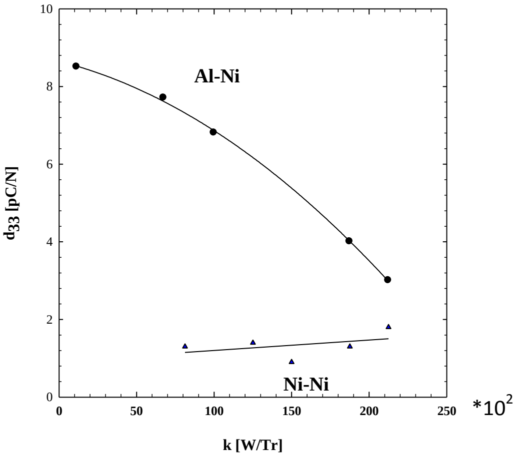

Fig. 6. Dependence of the coefficient d_{33} on the k for layers with various material electrodes

CONCLUSIONS

All the obtained layers of Zn-Bi-O were characterized by amorphous structure and piezoelectric properties. The value of piezoelectric coefficient d_{33} is comparable to piezoelectric coefficients for crystal layers of Zn-O.

There is influence of distance target – substrate on the value of the coefficient d_{33}.When the distance grows from 4 cms to 8 cms, the piezoelectric coefficient d_{33} decreases twice for the same powers deposited on the target.

Another relevant technological parameter is the value of the power deposited on the target. The deposition rate is proportional to the power, however the power higher than 400 W must not be used, otherwise forming of metallic sites of Bi will cause interelectrode discharge. For the powers lower than 400 W layer deposition rate is of the order of single nm/min.

Analyzing the highest values of the piezoelectric coefficients, the best results were achieved for small values of the power deposited on the target 130-140 W during the sputtering process up to 8,5 pC/N and for distance from the target to the substrate d=4 cms.

ACKNOWLEDGEMENTS

The project was supported by Polish State Committee for Scientific Research KBN, grant No 3 T10A 077 26

LITERATURE

[1] Pearton S., J., Norton D., P., Ip K., Heo Y., W., Steiner T., Recent progress in processing and properties of ZnO, Progress in Materials Science, 50 2005, 293-340

[2] Mazur K., Polimer ferroelectric ceramic copomsitis, Technical University, Zielona Góra

[3] BACHIR S., AZUMA K., KOSSANYI J VALAT., P., RONFARD-HARED J. C., *Photoluminescsence of polycrystalline zinc oxide co-activated with trivalent rare earth ions and lithium. Insertion of rare-earth ions into zinc oxide*, J. of Luminescsence 75, 1997, 35-49

[4] Miki-Yoshida M., Paraquay-Delgao F., Estrada-Lopez W., Andrade E., Structure and morphology of high quality indium-doped ZnO films obtained by spray pyrolysis, Thin Solid Films, 376, 200, 1699-109

[5] Ismail B., Abaab M., Rezig B., Structural and electrical properties of ZnO films prepard by screen techniqe, Thin Solid Films, 383, 2001, 92-94

[6] Jaroszewski M., Ziaja J., Juchim S., Properties of thin films obtained by metal evaporation, Przegląd Elektrotechniczny, APTADM`2001, 2001, 271-273

[7] Ziaja J., Magnetronowa metoda otrzymywania cienkich warstw Zn-Bi-O, Postępy w Elektrotechnologii, Jamrozowa Polana, 2003, 220-232

[8] Kacprzyk R., Ziaja J., Electrical properties of Zn-Bi-O thin films deposited by r.f. magnetron sputtering, APTADM`2004, 2004, 1153-157

[9] Tominaga K., Murayama T., Umezu N., Mori I., Ushiro T., Moriga T., Nakabayashi I., Properties of films of multilayer ZnO:Al and ZnO deposited by an alternating method, Thin Solid Films, 343-344, 1999, 160-163

5th International Conference **ELMECO**
Nałęczów, Poland
September 2005

DISCHARGE PLASMA CHARACTERISTICS IN PURE AR GAS AT MULTI-ATMOSPHERIC PRESSURE USING THE AUTOMATICALLY PRE-IONIZED PLASMA ELECTRODE

Chobei Yamabe, Sung-Ki Hong and Saburoh Satoh

Saga University, Department of Electrical and Electronic Engineering
1 Honjyo-machi, Saga 840-8502, Japan
E-mail: yamabec@cc.saga-u.ac.jp

Abstract

For the investigation of the possibility of the discharge-pumped Ar_2** *excimer laser oscillation whose wavelength is 126 nm, characteristics of the main-discharge in pure Ar at multi-atmospheric pressure (1~5 atm) have been investigated using the automatically pre-ionized (API) plasma electrode. It was demonstrated that the uniform pre-ionization formed the uniform main-discharge by the control effect of capacitance* C_{pr}*_connected with the trigger electrode for preionization and the maximum energy deposition into main-discharge increased. The control effect of capacitance* C_{pr} *was examined comparing with the light intensity of the main-discharge taken by integrated photograph and the two-dimensional simulation of the electric field distribution of the API plasma electrode discharge system.*

Keywords: discharge plasma, excimer laser, plasma electrode, pre-ionization

INTRODUCTION

Recently increasing attention is being paid to the short wavelength lasers in the vacuum ultraviolet (VUV) region as coherent light sources in the future optical lithography industry. The Ar_2* excimer laser whose center wavelength λ is 126 nm is one of a few emission sources in the VUV spectral region. However, Ar_2* excimer laser has been realized only by an electron beam pumping [1-3]. But the electron beam device is rather large and may not be appropriate for repetitive operation compared with self-sustained discharge pumping devices. Several interesting approaches have been attempted to oscillate Ar_2* excimer lasers by the self-sustained discharge-pumped scheme [4-6], but almost of these approaches have applied the API (automatically pre-ionized) plasma with unsuccessful results. The main unsuccessful reasons are the difficulties to form a uniform main-discharge and the fast high energy deposition (more than 10 MW/cm^3) in high argon pressure (more than 15 atm). Therefore, a new discharge electrode structure is required to solve these problems. The API transversely excited plasma electrode shown in Fig. 1 and Fig. 2(a) has been designed.

In this paper, to investigate the possibility of achieving discharge-pumped Ar_2* excimer laser action, the discharge characteristics of a system using the electrode are investigated experimentally under the condition at the multi-atmospheric (1~5atm) pressure in argon.

ELECTRICAL CIRCUIT CHRACTERRISTICS

The configuration of the discharge system of the API plasma electrode compared with the conventional charge transfer system is almost the same as shown in Fig.1. The driving parameters of the discharge system of the API plasma electrode discharge are shown in Table.1. The main capacitance C_m is charged by the required voltage V_0. As shown in Fig. 1, when the *S/W* is closed, the electric energy $E_p = (1/2)C_pV_{br}^2$ is transferred from C_m to C_p and, simultaneously, the electric energy $E_{pr} = (1/2)\ [(C_{pr}\ C_{di})/(C_{pr}+C_{di})]V_{br}^2$ is transferred from C_m to C_{pr}, where V_{br} is a breakdown voltage and C_{di} is the dielectric capacitance of the ceramic pipe.

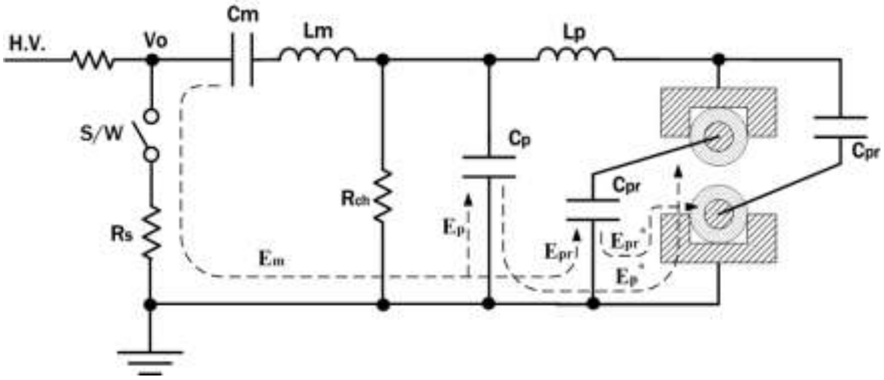

Fig. 1. Equivalent electrical circuit of the API plasma electrode discharge system

Table. 1. Parameters of the discharge system of the API plasma electrode

Parameter	
V_o	: Initial store voltage 20 kV
V_{br}	: The breakdown voltage
S/W	: Spark gap switch
Rs	: Resistance of the spark-gap S/W 0.5 Ω
Rch	: Charging bypass resistance 2.5 kΩ
C_m	: Main capacitance for energy store 36 nF
C_p	: Peaking capacitance 29.4 nF
C_{pr}	: Capacitance for pre-ionization and surface plasma 350 pF
Lm	: Circuit inductance for the current flow from $\boldsymbol{C_m}$ to $\boldsymbol{C_p}$ ~100 nH
Lp	: Self-inductance of the main-discharge ~10 nH
Electrode separation 0.3 cm	

The capacitance C_{pr} is used to control the equivalent capacitance of the pre-discharge circuit on the discharge system of the API plasma electrode. Before the main-discharge is formed, the electric energy E_{pr} produces surface-corona discharge on the cathode surface,and then an auxiliary plasma channel is generated. Consequently, the main-discharge of electric energy E_p forms in the discharge space by the auxiliary plasma channel.

EXPERIMENTAL SET-UP

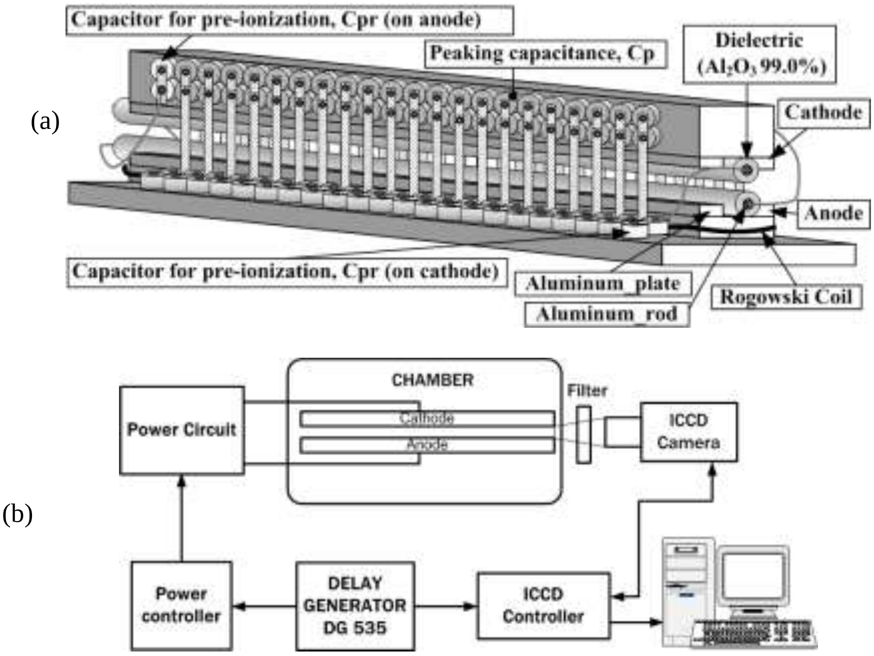

Fig. 2. Structure of the API plasma electrode (a) and a schematic describing the set up for observing the formation properties of the main-discharge (b)

Figure 2(a) shows the structure of the API plasma electrode. The surface discharge plasma that forms on the dielectric surface provides intense ultra-violet radiation which is suitable for the pre-ionization in the main-discharge space and able to sustain a surface conductivity high enough to serve as an electrode. The API plasma electrode can be used both for pre-ionization and as an electrode with plasma. Therefore, compared with the conventional flat-plate electrode, the API electrode can supply relatively high-energy in the main-discharge region and can persist for a long time operation. The discharge electrode consists of a 2-mm-thick ceramic (Al_2O_3: purity 99%) tube for which almost half of its outside is covered with aluminum plates. The surface discharge area of the API plasma electrode is about 2.2 cm × 74 cm. The main discharge gap is 0.3 cm.

The equivalent circuit was the conventional charge transfer type, but with two other points: the dielectric capacitance of the ceramic pipe was varied by using a special electrode structure, and the operation was performed with and without capacitance, C_{pr}, which controls the pre-ionization. Figure 2(b) shows a schematic describing observation of the formation properties of the main-discharge. An ICCD camera with high-speed electronic shutter (C5909, Hamamatsu, Japan) was used to observe the discharge of ~10 ns order. To observe the discharge form, quartz was used as the window material, but an optical resonator was not used. The gas used for these measurements was pure argon gas. The experiments were performed at a repetition rate of 1 Hz.

EXPERIMENTAL RESULTS AND DISCUSSIONS

Figure 3 shows the variation in the main-discharge with increasing argon gas pressure using the API plasma electrode. The main-discharge volume increases with increasing Ar gas pressure and is distributed very uniformly but is determined by the extent of the surface-corona discharge. This is limited by the voltage required for ignition of the surface-corona discharge. The breakdown voltage V_{br} increases with increasing Ar gas pressure. It can be considered that the impedance of the discharge space increases with increasing Ar gas pressure.

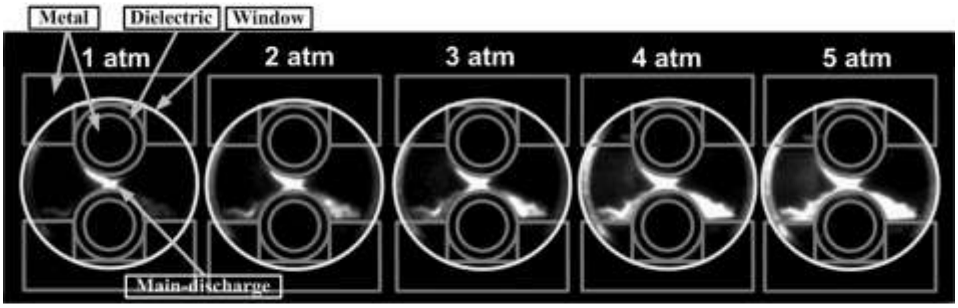

Fig. 3. Variation of the main-discharge with argon gas pressure in the API plasma electrode (about 150 ns ~ 250 ns, V_0 = 20 kV)

Figure 4(a) shows the variation in discharge power with argon gas pressure. The peak power put into the main discharge is about 90 MW (1.4 MW/cm^3). Figure 4(b) shows the time variation in the discharge voltage and current waveforms at 5 atm argon gas. An oscillation is observed in the discharge current waveform (dotted circle) before the main-discharge is formed. This oscillation seems to be due to the surface corona discharge that is the pre-ionization. In addition, the main-discharge forms according to the density and distribution of electric charges created by the surface corona discharge. Unfortunately, we are unable to observe the longitudinal uniformity of the main-discharge, because copper plates used to connect parallel capacitors of API plasma electrode discharge system shut off the side view as shown in Fig. 2(a). However, longitudinal uniformity of the surface-corona discharge for the pre-ionization has been reported [7], experimental results of the surface-corona discharge in this literature showed that the discharge spread uniformly along the longitudinal direction. Therefore, in the experimental results in Fig. 3, it is considered that a uniform main-discharge volume is formed because the surface-corona discharge itself is uniform. To investigate the influence of the surface-corona discharge, the capacitance C_{pr} was removed from the pre-discharge circuit . All experimental conditions except the capacitance C_{pr} were the same as those in Fig. 1.

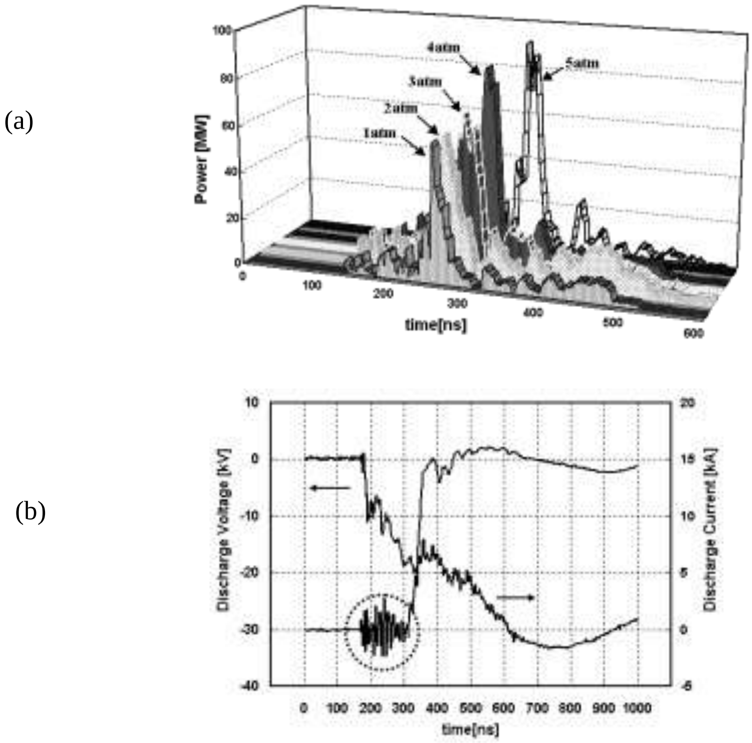

Fig. 4. Variation over time of the discharge power at various Ar gas pressures (a) and the discharge voltage and current at 5 atm (b)

Compared with Fig. 3, the observed main-discharge volume deflects perceptibly to the right side as shown in Fig. 5. In addition, oscillation of the discharge current (dotted circle in Fig. 6(a)) is not observed, though in former case the oscillation on the main-discharge waveform appers. In comparison with the results of the prior experiment, the main-discharge volume was increased and the breakdown voltage V_{br} was decreased. These changes are due to the surface-corona discharge not forming uniformly. Considering these results in terms of the equivalent circuit, when C_{pr} is operating, the voltage applied across the dielectric capacitor C_{di} (capacitance 380 pF) is approximately $V_{br}/2$, but without C_{pr} operating, the voltage applied across C_{di} is V_{br}. If a very high-voltage is applied at C_{di}, the cathode spots are formed at the edge of the metal. As a result of fluctuations in electron emission from the cathode, a highly conductive channel is formed near one of these spots, and the current from the entire cathode surface is drawn into this channel. This is the phenomenon that appears in Fig. 6. Consequently, when compared with Fig. 4(a), the maximum discharge power in Fig. 6(b) was decreased due to these cathode spots, which is the main factor limiting the maximum energy deposition. Therefore, from the above two experimental results, it is considered that the reduction of discharge power is caused by the non-uniform main-discharge. In addition, the non-uniform main-discharge exists over an expanded region. This can be clarified by measurement of the electric field distribution in the discharge region.

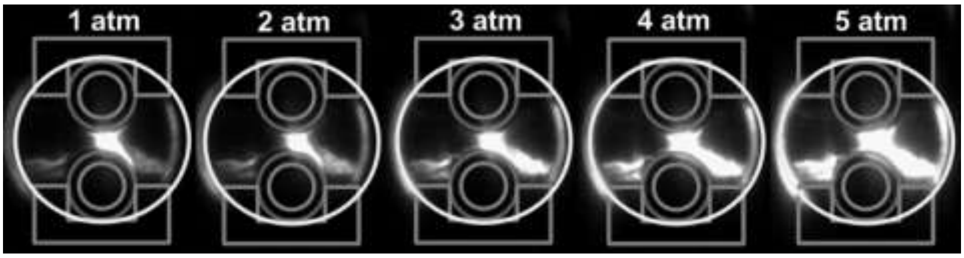

Fig. 5. Variation of the main-discharge with Ar gas pressure in the API plasma electrode without Cpr (about 150 ns ~ 250 ns, $V_0 = 20$ kV)

However, precise measurement of the electric field in the discharge region suffered from technical limitations. The calculation of the potential distribution was performed using the finite element method (FEM) in order to determine the electric field variation.

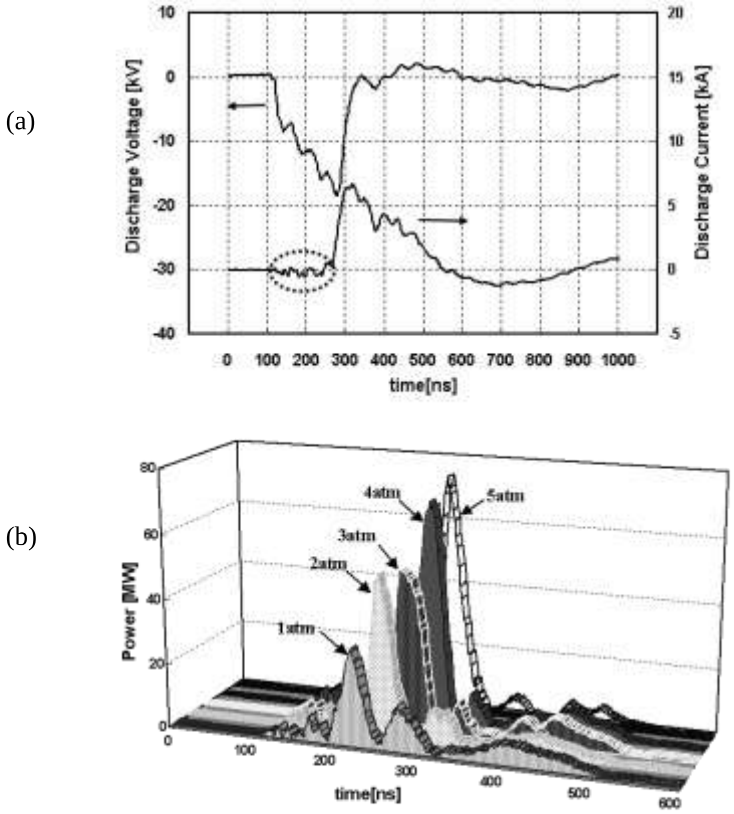

Fig. 6. Time variation of the discharge voltage and current at 5 atm (a) and the discharge power at various argon gas pressures without C_{pr} (b)

We used the general Galerkin finite-element software FlexPDETM [8], which provides great flexibility in boundary geometry and formulation of equations. Figure 7 shows the FEM modeling of the API plasma electrode. In order to determine the time dependent electrical field in the API plasma electrode, variable boundary conditions were obtained from actual experimental data (the discharge voltage data at 5 atm) for the electrode with C_{pr} and without C_{pr}, respectively. For example, variable boundary conditions in Fig. 7 are applied to a aluminum Al_*b*, Al_*t*, Al_*rod_b* and Al_*rod_t*. In the case with C_{pr}, actual experimental data (the time dependent breakdown voltage V_{br} at 5 atm with C_{pr}: sampling 2.0 GS/s) is applied to boundary condition Al_*b* and Al_*rod_t* is applied a half of V_{br}. Figures 8(a) and (b) show the calculated electric field distribution (log scale) at 150 ns after the initial discharge. To compare the previous two experimental results (obtained in Fig. 3 at 5 atm, with C_{pr}; and in Fig. 5 at 5 atm, without C_{pr}) we evaluate the simulation results (Fig. 8(a) and Fig. 8(b)). In the simulation results, the main discharge forms around the electric field region given by the distribution line n for the electrode with C_{pr} (Fig. 8(a)) and around the line m for the electrode without C_{pr} (Fig. 8(b)). Quantitatively, the electric field intensities of the distribution line n in Fig. 8(a) and line m in Fig. 8(b) are the same, representing values above 2×10^6 V/m. The area enclosed by the electric field distribution line m in Fig. 8(b) for the electrode without C_{pr} is more extensive than that enclosed by the line n in Fig. 8(a) for the electrode with C_{pr}. This result seems to indicate an increase in the discharge region. Therefore, in the case for the electrode without C_{pr}, it can be assumed that the probability of cathode spots forming at the metal edge is increased. For this reason, the main-discharge volume in Fig. 5 deflected to the right side and the maximum energy deposition was limited in the API plasma electrode discharge system without C_{pr}. However, for the electrode with C_{pr}, a uniform main-discharge was formed by controlling the effect of capacitance C_{pr}.

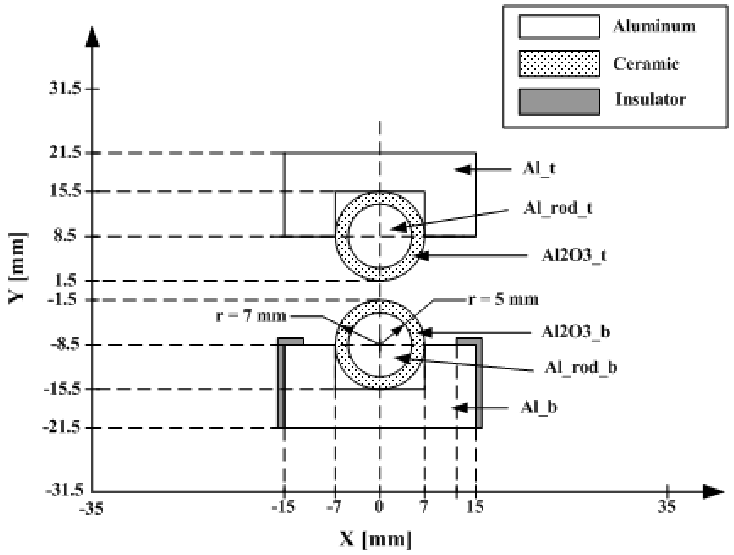

Fig. 7. Modeling of the FEM for the API plasma electrode

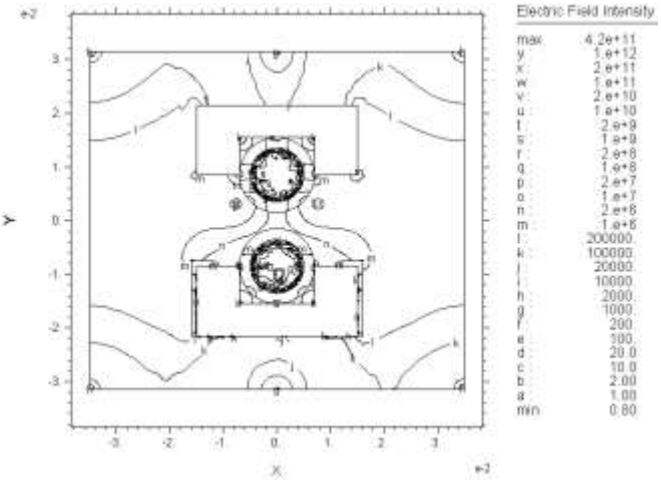

(a) The main discharge forms around the electric field region given by the distribution line n for the electrode with *C_{pr}*

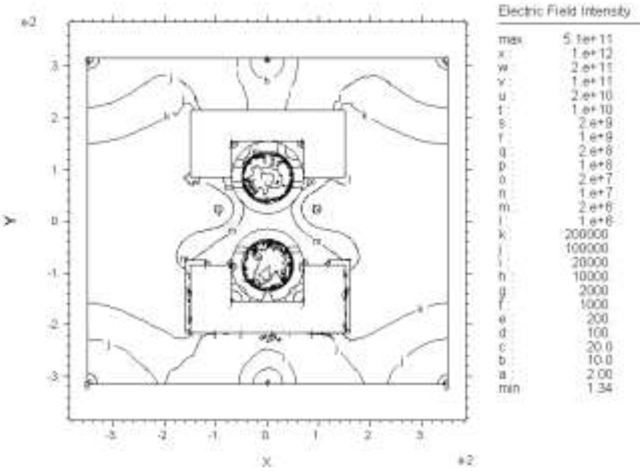

(b) The main discharge forms around the electric field region given by the distribution line m for the electrode without C_{pr}

Fig. 8. (a) (b) Electric field distribution (log scale) at 150 ns after initial discharge

CONCLUSIONS

A uniform main-discharge was formed by a API plasma electrode discharge system. The instantaneous maximum discharge electric power was 90 MW at 5 atm Ar gas and the maximum energy deposition was 1.4 MW/cm^3. It was demonstrated that the maximum energy deposition is increased by controlling the effect of the capacitance C_{pr}. Although these results are not enough to the discharge-pumped Ar_2* excimer laser action, it seems quite probable if a new chamber designed (more compact and can endure more high pressure 15 atm). Therefore, we will make a new chamber and also extend our research for different gas lasers such as Xe_2*, Kr_2* or F_2.

ACKNOWLEDGMENT

A part of this work was supported by a Grant-in-Aid for Scientific Research from the Ministry of Education, Science, Sports and Culture, Japan.

REFERENCES

[1] W. M. Hughes, J. Shannon and R. Hunter, Appl. Phys. Lett. 24, (1975) 488
[2] Y. Uehara, W. Sasaki, S. Saito, E. Fujiwara, Y. Kato, M. Yamanaka and K. Tsuchida, Opt Lett. 9, (1984) 539
[3] H. Tanaka, A. Takahashi, T. Okada, M. Maeda, K. Uchino, T. Nishisaka, A. Sumitani, and H. Mizoguchi, Appl. Phys. B 74, (2002) 323
[4] J. E. Tucker, M. F. Masters, B. L. Wexler, and S. K. Searles, Opt Lett, 17, (1992) 288
[5] S. K. Searles, J. E. Tucker, B. L. Wexler, and M. F. Masters, IEEE J. Quantum Electron. 30, (1994) 2141
[6] H. Ninomiya and K. Nakamura, Opt. Commun. 134, (1997) 521
[7] K. Fukuda, N. Hayashi, S. Satoh and C. Yamabe, Rep. Fac. Eng. Saga Univ., 29, (2000) 35 (Japanese)
[8] FlexPDE^{TM}, Finite element software, PDESolutions Inc
[9] Web page: http://www.pdesolutions.com

5th International Conference **ELMECO**
Nałęczów, Poland
September 2005

PLASMA-CATALYTIC CONVERSION OF METHANE BY DBD AND GLIDING DISCHARGES

Krzysztof Schmidt-Szałowski, Agnieszka Górska, Michał Młotek

Warsaw University of Technology, Faculty of Chemistry
ul. Noakowskiego 3, 00-664 Warszawa
kss@ch.pw.edu.pl

Abstract

The methane conversion into C_2 hydrocarbons was examined in atmospheric-pressure plasmas generated by dielectric barrier discharges (DBD) and gliding discharges (GD) using different mixtures of gases (CH_4 with Ar, CO_2, and H_2). Ethane was the main product of the methane conversion in filamentary DBD, whereas, mainly acetylene was generated by gliding discharge. It was found that one of the commercial catalysts (Cu/Zn/Al_2O_3) can be used for the methane conversion in DBD. A new type of the gliding discharge reactor was designed with a widening upwards working chamber, and two vertical electrodes. A spouted bed of alumina-ceramic particles (0.16 – 0.5 mm) was maintained in the inter-electrode volume by a stream of gaseous reactants passing upward. The presence of the spouted bed resulted in: 1) an increase in voltage and decrease in current, and 2) an increase of the overall methane conversion and selectivity into C_2 hydrocarbons.

***Keywords:** C_2 hydrocarbons, dielectric barrier discharges, gliding discharges, heterogeneous catalysis, methane conversion.*

INTRODUCTION

For the presented here, experimental study on plasma-catalytic methane conversion, two kinds of discharges were selected: dielectric barrier discharge (DBD) and gliding discharge (GD). The first one has been examined in a number of investigations on methane conversion up till now, because using this discharge, catalysts can be easy placed directly in the discharge zone [1-6]. DBD is characterised by a small energy of individual micro-discharges with a very short time of duration. Under those conditions, ethane, one of the primary products of methane transformation, is found the main gaseous product, however, due to the consecutive chain reactions, non-volatile products are also formed (polymeric substances and soot). They may be produced by the surface polymerisation involving free radicals and unsaturated hydrocarbons (C_2H_4 and C_2H_2).

On the other hand, as has been shown due to a number of studies, e.g. [7-13], GD can be effectively used for currying out different chemical processes. It is possible to conduct processes in homogeneous gas systems as well as in suspensions of powdered solids or liquid drops in gases. However, the problem arise when particles of the solid should be kept for longer time in the discharge zone. Those may be the cases when 1) the reaction involving the solid material proceeds slowly and 2) the solid plays a role of a catalyst in the reaction between gaseous reactants.

The majority of active species generated in the discharge plasmas (free radicals, excited molecules) can react immediately in the same plasma volume. A part of them, nevertheless, leave the discharge zone with the outlet gas stream. Thus, it seems to be possible increasing the yield (or selectivity) of plasma processes by placing a catalyst capable to accelerate the required reaction, downstream outside the discharge zone [13]. It has been found, however, that the effect of catalysts in such a system is generally unsatisfactory. The reason for that lays probably in the excessive time elapsing between the active species generation in the plasma volume and their contact with the catalyst's surface. Most of them, therefore, could react in gas phase before contacting the catalyst.

It has become clear now that the yield of the reactions in plasma-catalytic systems is strongly influenced by a distance between the active discharge zone and the catalyst's surface. This conclusion can be verified considering an example of the well known process of methane conversion under the plasma conditions when a substantial role is played by free radicals $CH_3^\bullet$ originated from the methane dissociation [14-16]. They may disappear quickly being consumed in different gas-phase reactions and one of them is

$$CH_3^\bullet + H^\bullet = CH_4$$

This is one of the most rapid reactions in the system [17], its rate constant at ambient temperature is about 10^{13} [$cm^3mol^{-1}s^{-1}$]. Adopting this value, it may be computed that if the $CH_3^\bullet$ participated only in this single reaction, the time needed to reduce their concentration by a factor of 10 would be about $2\cdot10^{-5}$ s. Assuming that under the conditions of GD the stream of reagents flows with a velocity of 10 m/s, the radicals formed in the discharge zone would be transferred with the gas stream at about 0.2 mm in this distance of time. Hence, if the catalyst is not located inside the discharge zone, only a small fraction of radicals $CH_3^\bullet$ can reach its surface, whereas most of them will react earlier in the gas volume. The conclusion is evident - the catalyst should be placed within the discharge zone.

EXPERIMENTAL

Dielectric barrier discharges

For the DBD investigation, a simple quartz-glass reactor was used, operated at the frequency of 4.7 - 5 kHz, with the inner high-voltage electrode made of aluminium (Fig. 1). The discharge gap between this electrode and the quartz tube, being the dielectric barrier, was about 3 mm wide. The coating made from silver-paste deposited on the outer surface of this tube, was the grounded electrode. The catalytic action was examined using one of the commercial catalysts ($Cu/Zn/Al_2O_3$) which was pre-treated with hydrogen at temperatures 200 - 220 ^OC for reducing metal oxides being the components of catalyst. Different gas mixtures were used: CH_4+Ar, CH_4+H_2, CH_4+CO_2, CH_4+H_2+Ar and CH_4+CO_2+Ar, with the overall gas flow rate 2 Ndm^3/h. The compositions of the inlet and outlet gases were determined by chromatographic methods. The temperature was measured with a thermocouple at the external surface of the reactor wall (inside the heater).

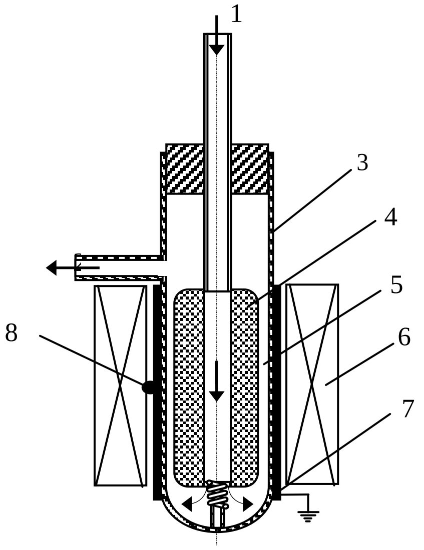

Fig. 1. Plasma-catalytic reactor with dielectric-barrier discharges:
1 - feed, 2 - products, 3 - quartz tube with catalyst, 4 - high voltage electrode,
5 - discharge gap, 6 - heater, 7 - grounded electrode, 8 - thermocouple

Gliding discharges

The GD reactor with spouted bed of granular material [18] being designed for the plasma methane conversion, is provided with a vertical reaction chamber, widening upwards to 50 mm in diameter. The chamber, lined with a ceramic material, holds two electrodes for the generation of gliding discharges (Fig. 2). Gaseous reactants, introduced through a nozzle in the bottom of the chamber, carries up the particles to keep them in a chaotic movement in the inter-electrode space. In this spouted bed, the particles, when passing across the reactor volume, can participate in the processes occurring within the plasma zone or at their boundaries. The methane conversion to C_2 hydrocarbons was studied using a spouted bed of alumina-ceramics particles (0.16 – 0.5 mm) with a single batch packed to the reactor of about 10 ml. The methane reactions were studied in different gas mixtures: CH_4+Ar, CH_4+H_2+Ar, and CH_4+CO_2+Ar, keeping the overall gas flow rate constant (300 dm^3/h) at atmospheric pressure. The reactor was powered by 50 Hz system (with controlled voltage) with the active power measured in primary circuit (by means of an energy meter Pafal MOD A5).

The inlet and outlet gases were analysed using Chrompak 9002 gas chromatograph with a Carboxen 1000 column and a FID detector. Methane, ethane, ethylene and acetylene concentrations were used for calculation of the overall conversion of methane and the conversion into C_2 hydrocarbons. The degree of methane conversion into soot (C_s) was estimated from the carbon balance.

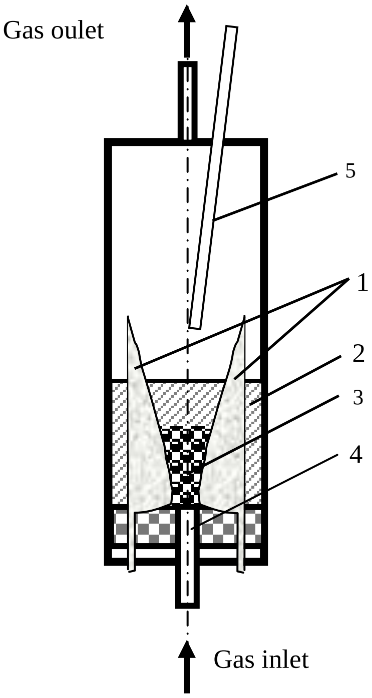

Fig. 2. Gliding discharge reactor with a spouted bed of alumina-ceramic particles (0.16 - 0.5 mm): 1 - electrodes, 2 - ceramic lining, 3 - spouted bed, 4 - nozzle, 5 - thermocouple

RESULTS

Dielectric barrier discharges

Ethane with small admixtures of ethylene and acetylene (besides hydrogen) were the main gaseous products of the methane conversion under DBD conditions. Moreover, some non-volatile products were deposited on the high-voltage electrode and the reactor wall. The overall methane conversion (X), the conversion into C_2 hydrocarbons (X_{C2}) and the selectivity into C_2 (X_{C2}/X) were examined at the temperature 240 ^{O}C, using the $Cu/Zn/Al_2O_3$ catalyst pre-treated with hydrogen (Table 1, Figs. 3 and 4). The effect of the gas-mixture composition was observed, especially, in the presence of carbon dioxide and hydrogen. It was found that an addition of CO_2 to the mixture CH_4+Ar results in the increased values of X and X_{C2}. On the other hand, when the mixture CH_4+CO_2 was used X_{C2} was lower than that with CH_4+Ar. One can conclude, therefore, that argon is an active component of the reactants mixture, being energised under the plasma action. When methane was converted in mixtures with H_2 the overall conversion was lower than that in other mixtures, although, the selectivity S into C_2 hydrocarbons was higher.

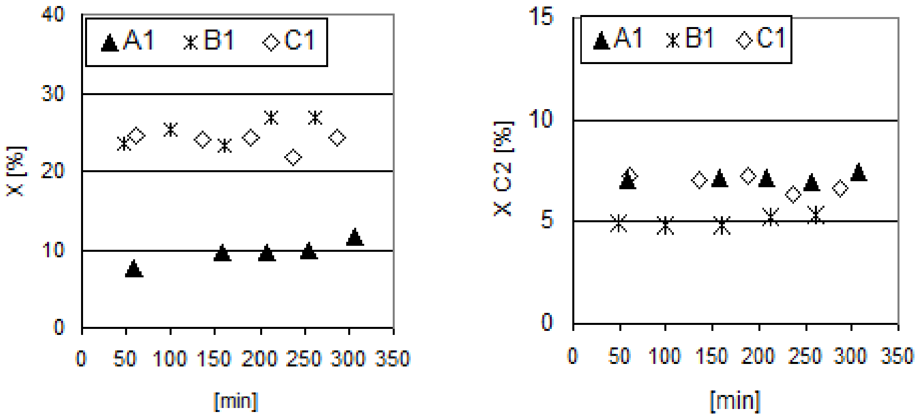

Fig. 3. The overall methane conversion X and conversion into C_2 hydrocarbons (X_{C2}) vs. time (Series A1, B1 and C1 - Table 1)

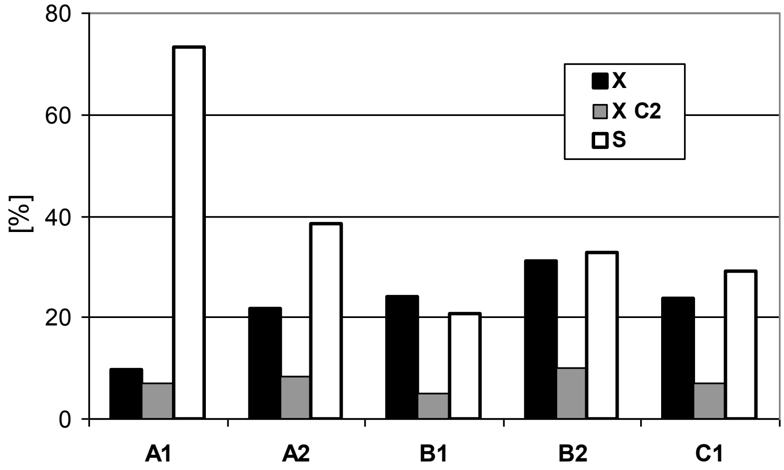

Fig. 4. The overall methane conversion X, conversion into C_2 hydrocarbons (X_{C2}) and selectivity (S) - mean values (Gas compositions given in Table 1)

Table 1. Gas compositions in the Series A – C

Series	Gas compositions
A1	$0.5\ CH_4 + 0.5\ H_2$
A2	$0.5\ CH_4 + 0.125\ H_2 + 0.375\ Ar$
B1	$0.5\ CH_4 + 0.5\ CO_2$
B2	$0.5\ CH_4 + 0.125\ CO_2 + 0.375\ Ar$
C1	$0.5\ CH_4 + 0.5\ Ar$

Gliding discharges

The reactant temperatures (measured at the axis of reactor at the level of the upper end of electrodes) depended on the discharge power and the gas composition. They changed within the range of 120 - 320 ^{O}C. So low temperature level resulted mainly from the high contribution of heat dissipated to the environment (70 - 80% of the energy supplied to the reactor). The discharge conditions underwent changes due to the presence of spouted bed. When keeping the constant value of discharge power, an increase in voltage and decrease in current were observed. The overall methane conversion increased with the increasing discharge power and depended also on the gas composition (Figs. 5 and 6). It was found that the presence of argon in the gas mixture results in the increase of the overall methane conversion (Series A0, A1, and A2).

From the experiment with the mixtures CH_4+H_2 and CH_4+H_2+Ar, one can conclude that the presence of spouted bed resulted in the increased productivity and selectivity of the methane conversion into C_2 hydrocarbons (Series A2, A3, and A5 - Fig. 7). On the other hand, taking into consideration Series A0, A1, and A5, a strong influence of hydrogen on the soot formation can be observed (Fig. 8). It is interesting that in Series A5, when using the gas mixture rich of methane (0.4 CH_4+0.6 H_2), the conversion into soot was reduced to nearly null due to the presence of the spouted bed.

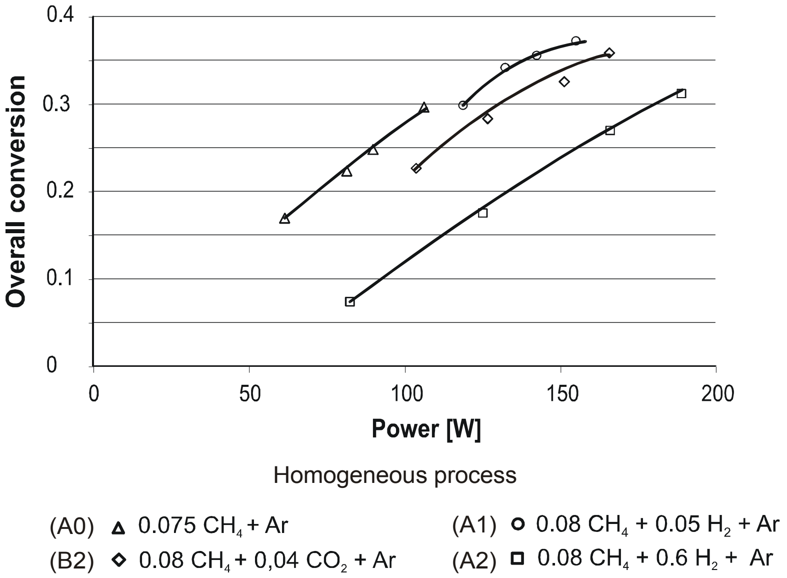

Fig. 5. Effect of the discharge power on the overall methane conversion for the homogeneous process in gliding discharges

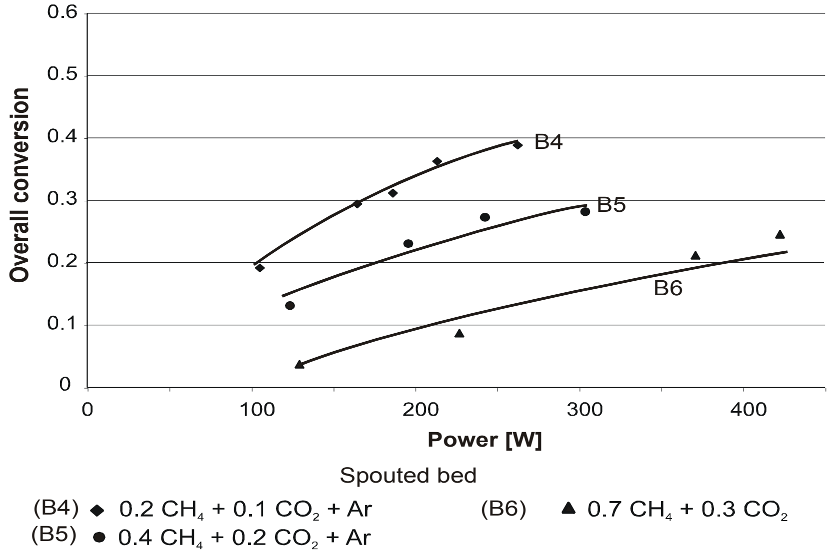

Fig. 6. Effect of the discharge power on the overall methane conversion in gliding discharges with spouted bed of alumina-ceramic particles (0.16 - 0.5 mm)

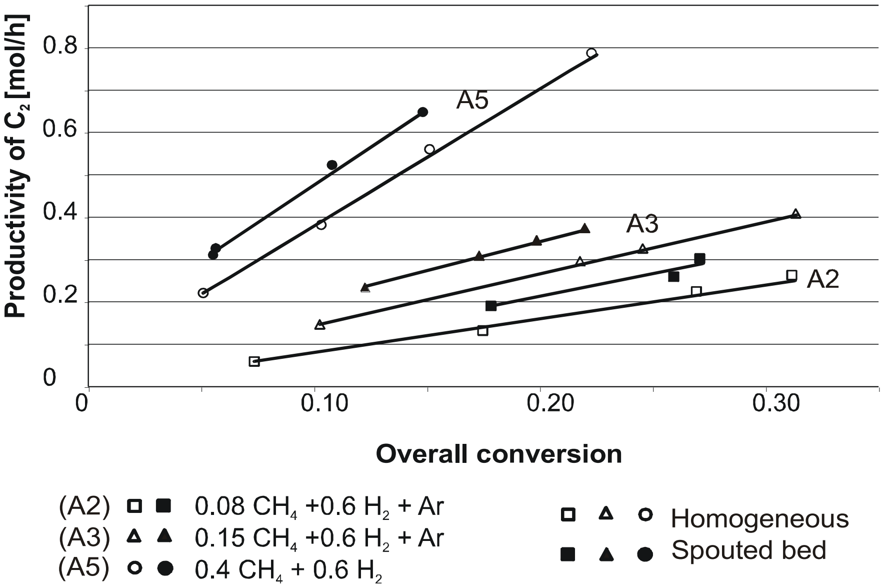

Fig. 7. Productivity of C_2 hydrocarbons vs. overall methane conversion in the homogeneous process and with the spouted bed of alumina-ceramic particles (0.16 - 0.5 mm)

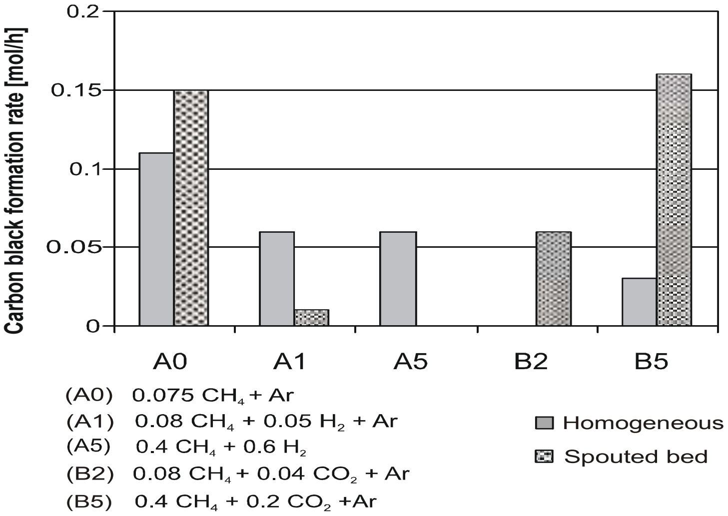

Fig. 8. Effect of the spouted bed of alumina-ceramic particles (0.16 - 0.5 mm) on the carbon black formation in different gas mixtures; power 110 - 150 W

CONCLUDING REMARKS

It has been shown that one of the commercial catalysts ($Cu/Zn/Al_2O_3$) can be used for the methane conversion under DBD conditions at elevated temperatures. Additions of carbon dioxide and hydrogen influence strongly the methane conversion in CH_4+Ar mixtures. Both components H_2 and CO_2 may inhibit the soot formation due to the equilibrium of the reactions

$$C + CO_2 = 2CO$$
$$C + 2H_2 = CH_4$$

It should be also taken into account that the soot generation may be an auto-catalytic reaction because the presence of solid carbon can accelerate the formation of aromatic hydrocarbons being the precursors of soot [19].

The laboratory gliding-discharge reactor, capable to operate with a spouted bed of solid particles, was used for currying out the methane conversion into C_2 hydrocarbons. The presence of spouted bed of alumina-ceramic particles resulted in an increase in voltage and decrease in current of the discharge. One of the reason for that may be the recombination of electrons and ions on the surfaces of solid particles.

When using the alumina-ceramic spouted bed in the mixtures CH_4+H_2 and CH_4+H_2+Ar, increased selectivity into C_2 hydrocarbons and lowered soot formation rate were observed. Considering the results of these experiments one can conclude that the presence of the spouted bed in the volume of the gliding discharge reactor influences the conditions of the process including the electrical discharge parameters (by recombination processes) and hydrodynamics of the gas stream. Moreover, the possible effects of the heterogeneous reactions, involving free radicals and excited molecules, occurring at the surfaces of ceramic particles, should be taken into account. The study on the catalytic properties of solid materials under discharge conditions will be continued.

ACKNOWLEDGEMENT

This work was financially supported by Warsaw University of Technology (no. 504/6/0287).

LITERATURE

[1] Pietruszka B., Anklam K., Heintze M., Plasma-assisted partial oxidation of methane to synthesis gas in a electrical barrier discharge, *Appl. Catalysis A: General,* 261, 2004, pp.19-24

[2] Song H. K., Choi J.-W., Yue S. H., Lee H., Na B.-K., Synthesis gas production via dielectric barrier discharge over Ni/γ-Al_2O_3 catalyst, *Catal. Today,* 89, 2004, pp.27-33

[3 Schmidt-Szałowski K., Opalińska T., Sentek J., Krawczyk K., Ruszniak J., Zieliński T., Radomyska K., Methane conversion into C_2 hydrocarbons and carbon black in dielectric-barrier and gliding discharges, *J. Adv. Oxid. Technol.,* 7/1, 2004, pp. 39-50

[4] Jiang T., Li Y., Liu C.-J., Xu G.-H., Eliasson B., Xue B., Plasma methane conversion using dielectric-barrier discharges with zeolite A, *Catal. Today*, 72, 2002, pp.229- 235

[5] Heintze M., Pietruszka B., Plasma catalytic conversion of methane into syngas: the combined effect of discharge activation and catalysis, *Catal. Today*, 89, 2004, pp. 21-25

[6] Chang C.-L., Lin T.-S., Decomposition of Toluene and Acetone in Packed Dielectric Barrier Discharge Reactors, *Plasma Chemistry and Plasma Processing,* vol. 25 No. 3, 2005, pp. 227-243

[7] Czernichowski A., Electrically assisted conversion of natural gas into syngas, *Karbo-energochemia-ekologia*, 11, 1998, pp. 359-369

[8] Fridman A., Nester S., Kennedy L.A., Saveliev A., Mutaf-Yardimci O., Gliding arc gas discharge, *Progr. Energy Comb. Sci.*, 25, 1999, pp. 211-231

[9] Czernichowski A., Gliding arc. Application to engineering and environment control, *Pure & Appl. Chem*., 66, 1994, pp. 1301-1310.

[10] Czernichowski A., Nassar H., Ranaivosoloarimanana A., Fridman A., Simek M., Musiol K., Pawelec E., Dittrichowa L., Spectral and electrical diagnostics of gliding arc, *Acta Phys. Polonica A*, vol. 89 No. 5-6, 1996, pp. 595-603

[11] Mustaf-Yardimci O., Fridman A., Saveliev A. V., Kennedy L. A., An investigation of non- equilibrium gliding plasma discharges, *14th International Symposium on Plasma Chemistry*, Praha 1999, pp. 997-1002

[12] Czernichowski A., *Oil Gas Sci. Technol.-Rev. IFP*, vol. 56 No. 2, 2001, pp. 181-198

[13] US Patent 6007742

[14] Deminsky M., Jivotov V., Potapkin B., Rusanov V., Plasma-assisted production of hydrogen from hydrocarbons, *Pure Appl. Chem.*, 74, 2002, pp. 413- 418.

[15] Spiess F.-J., Suib S. L., Irie K., Hayashi Y., Matsumoto H., Metal effect and flow rate effect in the hydrogen production from methane, *Catal. Today*, 89, 2004, pp. 35-45.

[16] Hammer Th., Kappes Th., Baldauf M., Plasma catalytic hybrid processes: gas discharge initiation and plasma activation of catalytic processes, *Catal. Today*, 89, 2004, pp. 5-14

[17] Kondratiev V. N., Konstanty skorosti gazofaznyh reakcii, *Izd. "Nauka"*, Moskva, 1970

[18] Schmidt-Szałowski K., Krawczyk K., Sentek J., Młotek M., Polish patent application P367122, 2004

[19] Heintze M., Magureanu M., Methane conversion into aromatics in a direct plasma-catalytic process, *J. Catalysis,* 206, 2002, pp. 91-97

5th International Conference **ELMECO**
Nałęczów, Poland
September 2005

RESEARCH ON WASTE WATER PURIFICATION BY OZONE TREATMENT AND PULSED DISCHARGE TREATMENT

Yoshiaki Suda, Hiroharu Kawasaki, Tamiko Ohshima

Department of Electrical and Electronics Engineering
Sasebo National College of Technology
1-1 Okishin, Sasebo, Nagasaki 857-1193, Japan
e-mail: y-suda@post.cc.sasebo.ac.jp

Abstract

The ozone treatment and high voltage pulsed discharge treatment have been performed to purify the waste water at several places of the sedimentation tanks in Sasebo city. Experimental results suggest that ozone treatment is effective for decreasing the number of colon bacillus and the bacteria count, however, ozone treatment is not so effective for chemical oxygen demand (COD). Pulsed discharge treatment is not so effective for both bacteria and COD. On the other hand, ozone treatment with pulsed discharge is effective for not only bacteria count, but also COD. This may be due to the effect of the hydroxyl radicals (OH radicals) which have stronger oxidizing and bleaching effect than ozone. These results suggest that advanced oxidation processes (AOPs) can be applied effectively in the ozone treatment with pulsed discharge.

Keywords: Waste Water Purification, Advanced Oxidation Processes, Ozone Treatment

INTRODUCTION

Recently, the environmental damage such as air pollution and water pollution becomes a serious problem. Especially, the water quality of river, lakes and marshes deteriorated by industrial waste water, domestic waste water and use of superfluous agricultural chemical [1]-[8]. Until now, the chlorine has been mainly used in the water purification. However, various problems have been indicated in this method as follows. The chlorine reacts with organic substance in the water, and generates the trihalomethane which is the carcinogen. The generation of the musty odor with the eutrophication of water source cannot be removed.

The ozone treatment attracts a great deal of attention as water purification. Ozone is one of the strongest oxidizing and bleaching agents without residues that could be harmful to the environment. For this chemical reaction, ozone has been used for a variety of applications such as bleaching, deodorization, and disinfection of water and atmospheric air. Recently, in the field of water purification, the use of ozonization is regarded as important in eliminating the precursor of trihalogenated urethanes which are generated in chlorination process and are carcinogenic organic chlorides.

On the other hand, high voltage pulsed discharge treatment was also used for the water purification. Pulsed discharge treatment leads to high energy voltage, a shock wave and high energy ultraviolet light. These physical effects may purify the waste water.

In this study, ozone treatment and pulsed discharge treatment for the waste water purification was applied at several places of the sedimentation tanks. In addition, ozone and pulsed discharge treatment was applied at the same time to lead the synergistic effect of both ozone treatment and discharge treatment.

EXPERIMENTAL

Figure 1 shows a part of flowchart of the water purification in the waste water treatment plant in Sasebo city. Generally, ozone treatment is carried out only in the final sedimentation tank exit, because the biochemical method with microorganisms, called activated sludge is most widely adopted. In this experiment, the ozone treatment was applied at the primary sedimentation tank entrance (PSTEN), the primary sedimentation tank exit (PSTEX) and the final sedimentation tank exit (FSTEX).

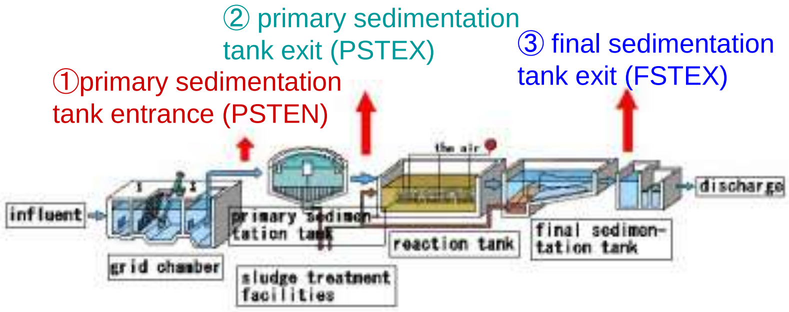
② primary sedimentation tank exit (PSTEX)

③ final sedimentation tank exit (FSTEX)

①primary sedimentation tank entrance (PSTEN)

Fig. 1. A part of flowchart of the water purification in the waste water treatment plant

A schematic diagram of the ozone treatment system is shown in Fig. 2. Oxygen (O_2:99.5 %) gas was used for the source gas. The source gas was controlled at 1.5 LM by the mass flow controller (STEC: SEC-400), and fed into the discharge area. Ozone was generated by the silent discharge between the electrode and the dielectric surface. The sinusoidal ac voltage of 8 kV (10 kHz) was applied between the electrodes to occur the silent discharge in the gap. The generated ozone density was measured by gas phase ozone monitor (Ebara: EG-4000) used by UV absorption method. The ozone density for water purification was 10 g/m^3. The waste water for treatment was 0.5 – 1.5 L, and it was kept at ~300 K. Treatment time was varied from 0 to 60 min.

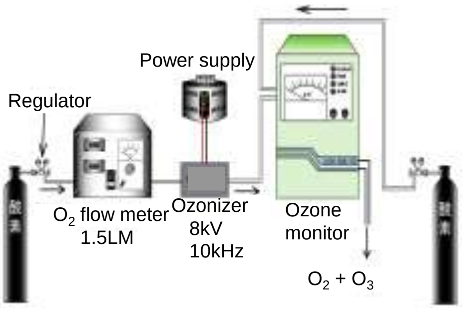

Fig. 2. A schematic diagram of the ozone treatment system

Conventional pulsed discharge system was used for pulsed discharge treatment of waste water. Tungsten rods (5mm in diameter) are fed into the waste water as electrodes. High power pulsed DC voltage was given to the electrodes using transformer, diode and condenser. Peak discharge voltage was about 15kVpp and peak discharge current was 7kA at the gap length of 3 mm.

The water quality was evaluated at turbidity, chemical oxygen demand (COD), and the number of colon bacillus and the bacteria count. The turbidity was measured by the light transmittance method. They were measured by the light absorption spectroscope (Shimadzu: 200V). The light of 660 nm in wavelength was used for the turbidity measurement.

RESULTS AND DISCUSSIONS

Ozone treatment

Figure 3 shows the temporal evolutions of the turbidity with ozone treatment. The turbidity before ozone treatment was about 73% at PSTEN, 38% at PSTEX and 7% at FSTEX. These values are much higher than those of the service water. The turbidity decreased to the half value after 30 min ozone treatment, that is, about 40% at PSTEN, 21% at PSTEX, and 4% at FSTEX. After 30 min ozone treatment the turbidity was saturated. This tendency is almost same for the color unit for waste water, not shown here.

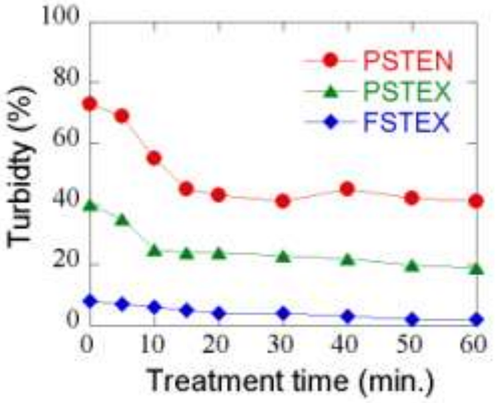

Fig. 3. Temporal evolutions of the turbidity with ozone treatment

Figure 4 shows temporal evolutions of the number of colon bacillus and the bacteria count at all places of the sedimentation tanks. Those values decrease drastically by ozone treatment, and the bacteria count decreases to almost zero after 10 min ozone treatment. These experimental results suggest that ozone treatment is effective for waste water purification of turbidity, color unit, the number of colon bacillus and the bacteria count.

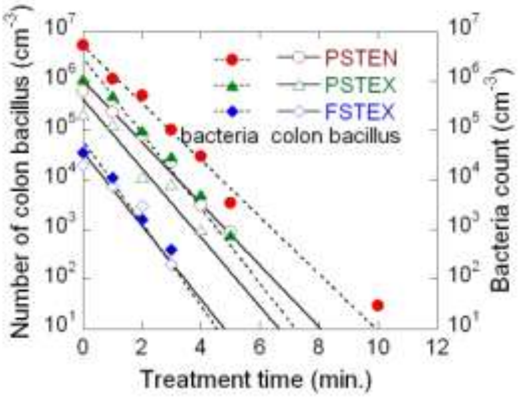

Fig. 4. Temporal evolutions of the number of colon bacillus and the bacteria count

Figure 5 shows the temporal evolutions of the chemical oxygen demand (COD) of the waste water before and after ozone treatment. The COD decreases slightly from 170 mg/1 to 130 mg/1 after 60 min ozone treatment at PSTEN. The COD also decreases from 120 mg/1 to 105 mg/1, and from 35 mg/1 to 20 mg/1 at PSTEX and FSTEX, respectively. These results suggest that ozone treatment is not so effective for COD.

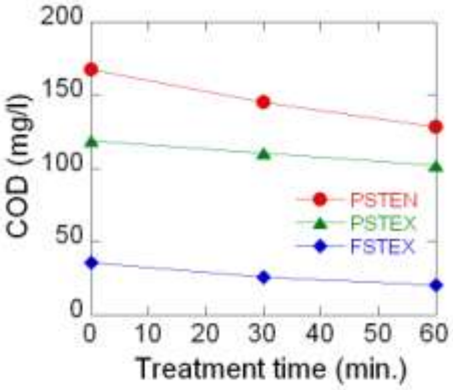

Fig. 5. Temporal evolutions of the COD of the waste water

Pulsed discharge treatment

Figure 6 shows the relation between the number of colon bacillus and the bacteria count, and the number of pulsed discharge times at PSTEN. As the results, the number of colon bacillus and the bacteria count decrease with the number of pulsed discharge times, however the decreasing rate is lower than that of ozone treatment.

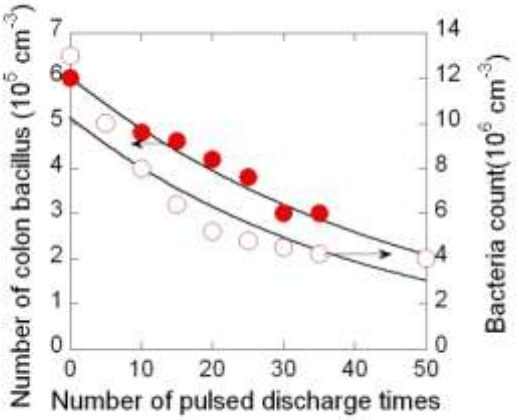

Fig. 6. Relationship between the number of colon bacillus and the bacteria count, and pulsed discharge time at PSTEN

Figure 7 shows the relation between the COD of the waste water and the number of pulsed discharge times at all places of sedimentation tanks. The COD at all places of the sedimentation tanks is independent of the number of pulsed discharge times. These experimental results suggest that pulsed discharge treatment is not so effective for the COD and the number of colon bacillus. Turbidity and color unit shows the almost the same tendency for pulsed discharge treatment, not shown here.

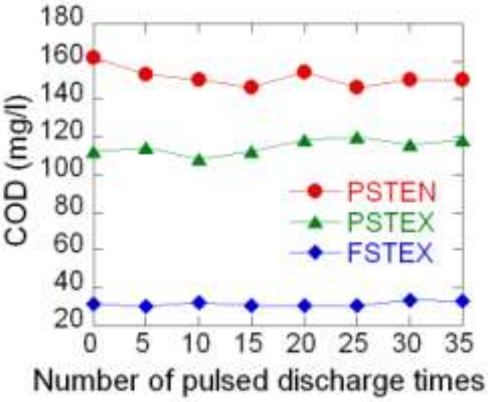

Fig.7. Relationship between the COD of the waste water and pulsed discharge times

Ozone treatment with pulsed discharge

Both of pulsed discharge treatment and ozone treatment cannot decrease the COD in the waste water. To decrease the COD, ozone treatment and pulsed discharge treatment are applied to the same waste water at the same time.

Figure 8 shows the temporal evolutions of the number of colon bacillus and the bacteria count. In this measurement, pulsed discharge was applied to 1 time per 1 minute. The number of colon bacillus and the bacteria count at all places of the sedimentation tanks decrease drastically by ozone treatment with pulsed discharge, and the number of colon bacillus and the bacteria count decreases to zero after about 7 min ozone treatment. As the results, the decreasing rate is higher than that of only ozone treatment.

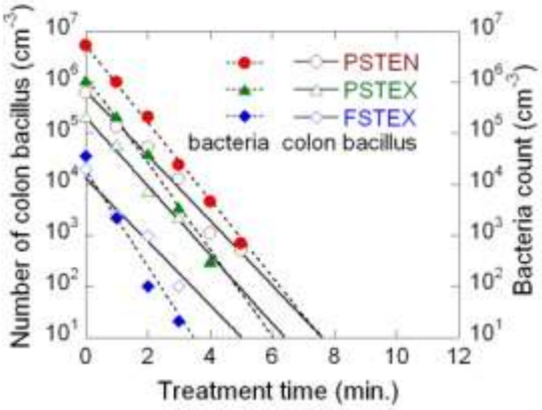

Fig. 8. Temporal evolutions of the number of colon bacillus and the bacteria count

Figure 9 shows the relation between the COD of the waste water and pulsed discharge time. The COD decreases from 170 mg/1 to 80 mg/1 after ozone treatment at PSTEN. The COD was also decreases from 120 mg/1 to 55 mg/1, and from 40 mg/1 to 20 mg/1 at PSTEX and FSTEX, respectively. These results suggest that only ozone treatment is not so effective for COD, but ozone treatment with pulsed discharge is effective for the waste water. The reason that ozone treatment with pulsed discharge is effective for not only bacteria count, but also COD is not clear yet, but it may be due to hydroxyl radicals (OH radicals). In our previous work, OH radical emission can be observed in the pulsed discharge between electrodes in water using emission spectroscopic method [8]. These results suggest that a kind of advanced oxidation processes (AOPs) can be applied effectively for the waste water treatment such as the ozone treatment with pulsed discharge.

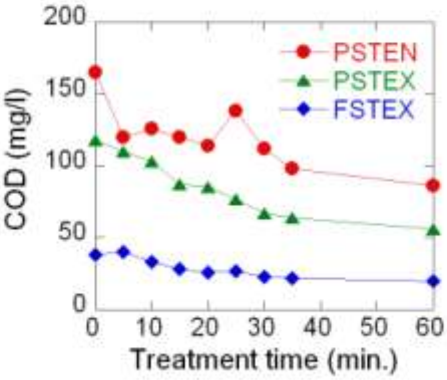

Fig. 9. Relationship between COD and pulsed discharge times

CONCLUSION

The ozone treatment for the waste water purification was applied at all places of the sedimentation tanks. Experimental results suggest that ozone treatment is effective for decreasing the number of colon bacillus and the bacteria count, however, ozone treatment is not so effective for COD. Pulsed discharge treatment is not so effective for both bacteria and COD. On the other hand, ozone treatment with pulsed discharge was effective for not only bacteria count, but also COD. This may be due to the effect of the hydroxyl radicals (OH radicals) that are one of the strongest oxidizing and bleaching agents. These results suggest that advanced oxidation processes (AOPs) can be applied effectively in the ozone treatment with pulsed discharge.

ACKNOWLEDGEMENT

This work was supported in part by the Grant-in Aid for Scientific Research (B), and Steel Industry Foundation for the Advancement of Environment Protection Technology. The authors wish to thank Prof. C. Yamabe of Saga University, Profs. K. Ebihara and T. Ikegami of Kumamoto University, and Dr. S. Aoqui of Sojo University for their helpful discussions. The authors also wish to thank Dr. H. Abe and Mr. H. Yoshida of the Ceramic Research Center of Nagasaki for their technical assistance with the experimental data.

REFERENCES

[1] Gosho M., Ihara S., Ishimine M., Satoh S., Yamabe C., J. Inst. Elec. Eng. of Japan, ED-98-102, 1998, pp. 49-52

[2] Fukagawa M., Harada T., Takeuchi M., Murakami S., Proc. of 5th Japan/Korea Symposium on Water Environmental Engineering, 1996, pp. 99-102

[3] Murakami S., Takeuclu M., Fukagawa M., Proc. of ENSEARCH-JAWE Post-Conference Seminar on Industrial Wastewater Management, 1996, pp. 37-42

[4] Zimin Yu., Tnikhanova N., Rafikava G., Nasyrov I. , Bazhenov Y., Morozova S., Gerchikov A., J. Water Chem. Technol. 19, 1997, pp. 31-35

[5] Ihara S., Miyachi T., Hayashi N., Satoh S., Yamabe C., Jpn. J. Appl. Phys. , 38, 2000, p. 4601-4605

[6] Fukagawa M., Harada T., Takeuchi M., Murakami S., Proc. of 5th Japan/Korea Symposium on Water Environmental Engineering, 1996, p. 99-104

[7] Zimin Yu., Trulhanava N., Rafikava G., Nasyrov I., Bazhenov Y., Morozova S., Gerchikov A., J. Water Chem. Technol. , 1997, 19, p. 31-37

[8] Ikeda Y., Kawasaki H., Fujita I., Suda Y., Proc. of the 3rd International Symposium of Non-Thermal Plasma Technology for Pollution Control, 3, 2000, pp. 5-9

5th International Conference **ELMECO**
Nałęczów, Poland
September 2005

LIF IMAGING OF OH RADICALS IN DC NOZZLE–TO-PLANE POSITIVE STREAMER CORONA

Marek Kocik(1), Jerzy Mizeraczyk(1), Seiji Kanazawa(2), Toshikazu Ohkubo(2)

[1] *Centre for Plasma and Laser Engineering*
The Szewalski Institute of Fluid Flow Machienery,Polish Academy of Sciences
ul. Fiszera 14, 80-231 Gdańsk, Poland
kocik@imp.gda.pl
[2] *Department of Electrical and Electronic Engineering, Oita University*
700 Dannoharu, Oita 870-1192, Japan

Abstract

In this study, the LIF detection of the hydroxyl (OH) radicals was performed in a nozzle-to-plane electrode system having an electrode gap of 30mm during the steady-state positive streamer corona discharge at atmospheric pressure. For monitoring the ground-state OH radicals, OH transition at 282nm was used. The time relationship between the regular streamer coronas, laser pulse, OH fluorescence and laser-induced streamer was measured. The time course of OH radicals between the successive streamers was measured for the evaluation of OH dynamics during the steady-state positive streamer corona discharge. The two-dimensional OH distribution in the DC corona discharge was observed. The obtained results showed that the ground-state OH radical were generated mainly in the filamentary part of the streamers. It was found that LIF detectable amount of ground-state OH radicals stayed in the region where streamers propagate during the steady-state DC positive streamer coronas.

Keywords: DC streamer corona discharge, Laser Induced Fluorescence, OH radical, Non-thermal plasma processing

INTRODUCTION

Streamer coronas at atmospheric pressure are widely used in the non-thermal plasma processing of harmful gases. The hydroxyl radical (OH) generated in the non-thermal plasma is considered to enhance the chemical reactions in the reactor. However, direct observation of the radical dynamics during the non-thermal plasma process is not yet performed experimentally. Therefore, the direct study of the streamer-induced plasma chemical processes in non-thermal plasma reactors is of great importance. Laser-induced fluorescence (LIF) is a useful diagnostic method for in-situ observation of the phenomena during the non-thermal plasma processing of gaseous pollutants. The LIF has been already employed by authors [1, 2] and other researchers [3-6] for studying NO removal process in various non-thermal plasma reactors.

Recently, several researchers succeeded in measuring the OH radicals using LIF technique in the pulsed corona discharges [7-9]. However, there are still no references for the measurement of OH radicals in the DC corona discharges. This is mainly due to difficulties in the synchronization of the DC corona streamers, LIF signals and observation time. The DC positive corona discharge consists of more of less regular self-repetitive current pulses (streamers) with pulse duration up to several hundred nanoseconds and repetition frequency in the range of 1 to 100 kHz. On the other hand, to generate OH radicals some dissociation process of H_2O or other chemical reactions are necessary and the lifetime is very short (up to 1ms). These complex phenomena make the measurement of OH radicals in the DC corona streamers difficult.

In this study, as a first step of the OH radical measurement, we tried to measure OH radicals generated in open air using a nozzle-to-plane electrode system having an electrode gap of 30mm. For monitoring the ground-state OH radicals, OH transition at 282nm (1-0 band) was used. One of the purposes of the present paper is to make clear whether DC streamer corona generate OH radicals or not. A second purpose is to observe the state of OH radicals during steady-state positive streamer corona discharge if OH radicals are generated.

EXPERIMENTAL SETUP

The schematic diagram of the experimental apparatus is shown in Fig.1. In order to observe the ground-state of OH radicals in the reactor using LIF technique, OH [$A^2\Sigma+(v'=1) \leftarrow X^2\Pi(v''=0)$] system at 282 nm was used. A frequency-doubled-dye laser system was used for the LIF measurement. The laser pulses from an XeF excimer laser (Lambda Physik, COMPex 150, tuned at 351 nm)-pumped a dye laser (Lambda Physik, SCANmate) with Coumarin 153 as a dye that generated a laser beam of a wavelength tuned around 564nm. A BBO crystal (BaB_2O_4) pumped by the tuned dye laser beam produced the second harmonic radiation of a wavelength correspondingly tuned around 282nm (energy: ~2.5 mJ, duration: 20 ns as FWHM). The 282nm laser beam with a diameter of 2mm passed between the electrodes as shown in Fig.2. Excitation of OH was achieved via the $Q_1(1)+Q_{21}(1)$ line(281.92nm). This transition was chosen due to the strongest fluorescence signal. LIF signal emitted at 90 degree to the laser beam was focused onto the entrance slit of a 25cm monochromator (Nikon, P-250) through a lens. The LIF signal at around 309nm [$A^2\Sigma+(v'=0) \rightarrow X^2\Pi(v''=0)$] was detected by a photomultiplier tube (PMT). The PMT signal was sent to a digital oscilloscope (Osc1, see Fig.1) through a preamplifier. In order to observe two-dimensional (2-D) OH profile, a gated ICCD camera (LaVision, Flame Star II) was used instead of the monochromator system. To remove the scattered laser light, the narrow optical filter centered at 310 nm was attached to the lens of the ICCD camera. For the 2-D observation of OH radicals between the electrodes with a 30-mm gap, a laser sheet (1 mm-width and 25 mm-height) was also used.

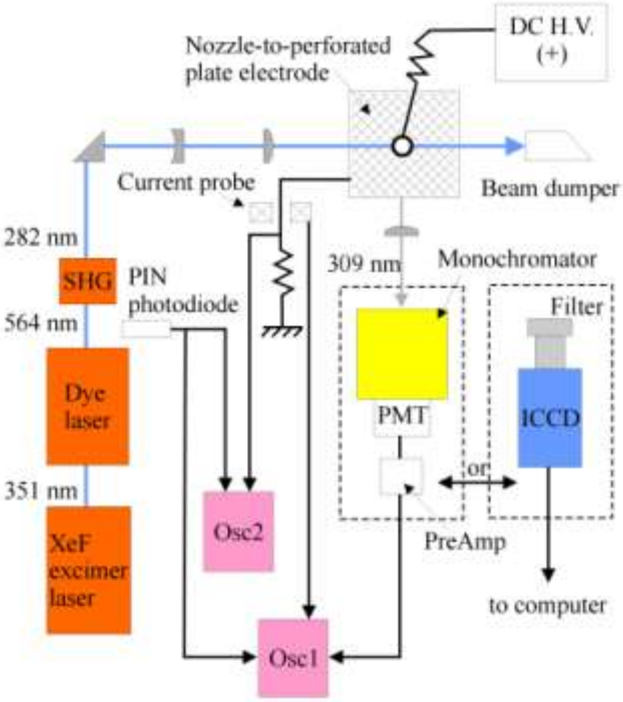

Fig. 1. Schematic diagram of the experimental apparatus (top view)

A stainless-steel pipe with a nozzle (1.0 mm in inner diameter, 1.5 mm in outer diameter) was used as the stressed electrode. An additional gas (argon) could be supplied to the discharge zone through the nozzle. The plane electrode (100 mm in square) was a brass plate with an array of holes (1.5 mm in diameter) perforated to allow the gas exhaust. Averaged air flow velocity due to this suction was 1.1m/s in the gap. DC high voltage with positive polarity was applied through a 10MW resistor to the nozzle electrode. The DC positive corona discharge was realized in open air with and without additional gas flow. The discharge current pulse was measured using a current probe (Pearson Electronics, 2877). Also the potential across a resistor connected between the plane electrode and the ground was measured. The laser shot was monitored using a PIN photodiode placed at 2.6m in advance of the discharge zone. A time relationship between discharge current and the laser shot was measured by another oscilloscope (Osc2) as shown in Fig.1. No time synchronization between the discharge and laser shot was made. This means that a laser pulse is irradiated at random between the discharge current pulses. The time relationship between the discharge current pulses, laser pulse, and LIF signal were described in detail elsewhere [10, 11]. The experiment was carried out at room temperature under atmospheric pressure. The concentration of water in the room was estimated to be in the range of 1-2 vol. %.

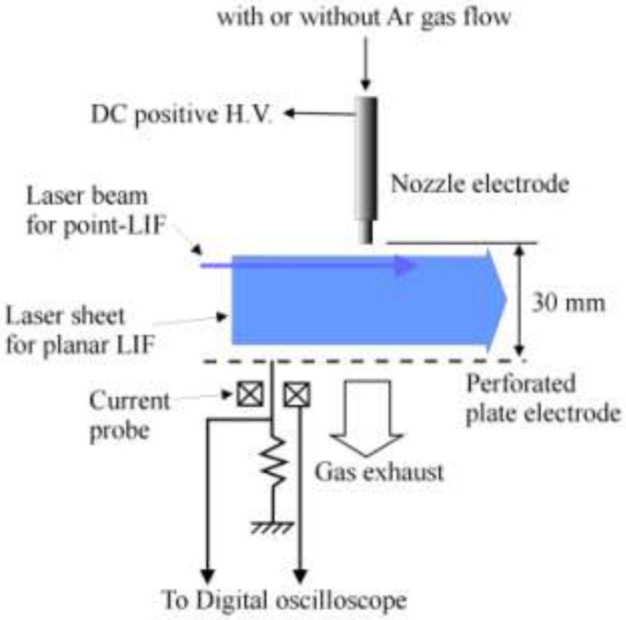

Fig. 2. Schematic diagram of the discharging region and incident laser for LIF measurement (side view)

RESULTS AND DISCUSSION

Fig. 3 shows the typical time dependence of laser incidence, OH LIF signal and laser induced streamer when the laser beam was irradiated during the steady-state positive streamer corona discharge in humid air. In this case, the incidence time of the probe laser beam was 140ms after the last current pulse of the discharge as shown in Fig.3(a). The distance between the center of the laser beam and the tip of the nozzle electrode was approximately 5mm. Taking into account the time delay between the laser pulse detected by the PIN photodiode and OH LIF signal by the PMT as well as the delay due to the circuits and cables, it is considered that the LIF signal appears immediately after the laser pulse. The lifetime of OH fluorescence is approximately 30-40ns as shown in Fig.3(b). When the wavelength of the probe laser was changed to off-resonance, OH LIF signal was disappeared. Consequently, it was confirmed that the ground-state OH radicals were present even in the steady-state DC streamer corona discharge. Additional streamer is induced due to the laser shot for LIF measurement because the photon energy of the probe laser is high enough to trigger the discharge. The emission from the laser-induced streamers is also observed. These peaks due to the laser-induced streamers are attributed to N2 second positive emission. In addition, no OH fluorescence was observed at the same position when the corona discharge was glow mode.

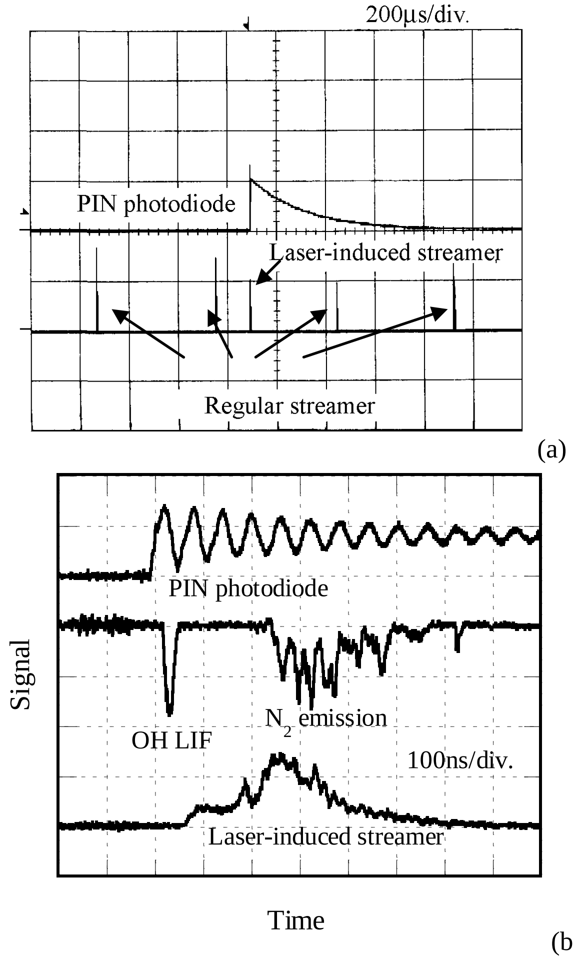

Fig. 3. Timing relationship between laser detected by a PIN photodiode, OH LIF signal and current waveform of laser-induced streamer. The applied voltage is 29kV and corona current is 185mA:
(a) Regular streamer current pulses and laser-induced current pulse;
(b) Typical waveforms of OH LIF signal and laser-induced current pulse. The peak current of laser-induced streamer is 90mA

Fig. 4 shows LIF intensity as a function of postdischarge time in respect to the last current pulse during the steady-state corona streamer discharge with and without Ar gas flow (0.3L/min). The time interval between the laser shot and the last current pulse of the discharge before the laser beam incidence was measured separately using another oscilloscope (Osc2). The LIF signal detected by fast oscilloscope (Osc1) was integrated over the lifetime of the fluorescence. Table 1 shows the corresponding discharge characteristics. As seen in Table 1, the current waveforms of DC corona discharge show that the averaged streamers repetition frequency for discharge in open air is 2.1 kHz at 29kV.

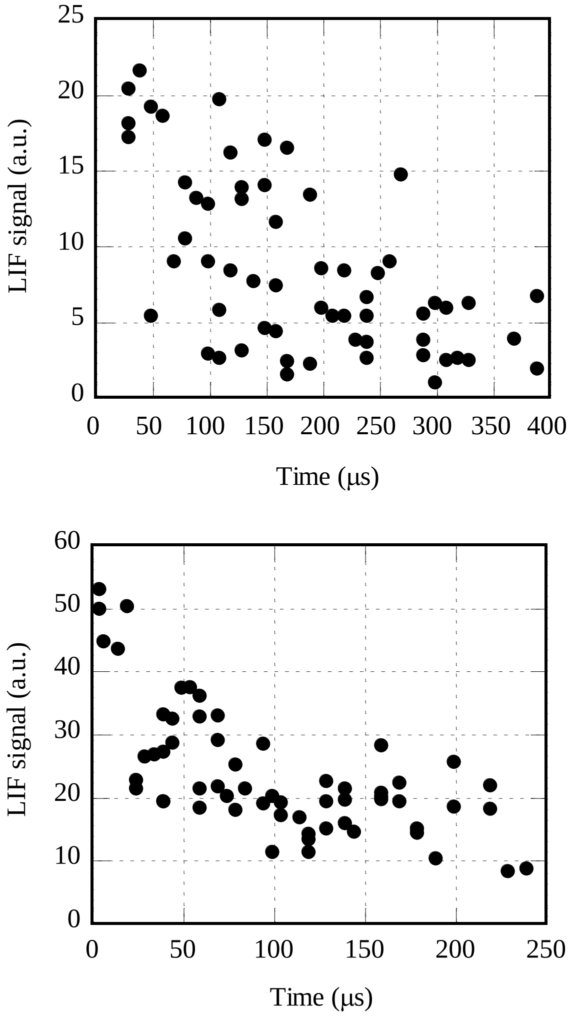

(a)

(b)

Fig. 4. Time evolution of OH LIF signal after the last streamer before the laser incidence:
(a) in open air without Ar gas flow (applied voltage 29kV, corona current 200mA);
(b) in open air with Ar gas flow (applied voltage 11kV, corona current 40mA)

When an additional gas (Ar) was supplied to the discharge zone through the nozzle electrode with the flow rate of 0.3L/min, the shape of the streamer discharge was changed drastically (see Figs. 5(a) and 6(a)) and LIF signal became more intensive. The streamer discharge in open air (i.e., humid air) is composed of many branches and occupies much more space, while filamentary type of discharge is generated if Ar is injected into the gap through the nozzle electrode. The averaged current densities underneath the nozzle electrode were about 0.6μA/mm^2 at 26kV for the discharge without Ar injection and about 4.7 μA/mm^2 at 13kV for the discharge with Ar injection, respectively. The averaged streamers repetition frequency increases up to 5.1kHz at 11kV when Ar is present in the discharge. The averaged time interval between two consecutive streamers is about 500 ms for the discharge without Ar gas flow and 200ms for the discharge with Ar gas flow. Therefore, the OH radicals produced in the one streamer may be still present in the discharge region when the next streamers occur. Moreover, OH LIF signal is highly dispersed in the case of the discharge without Ar gas flow through the nozzle. There are many factors which should be considered concerning to the fluctuation of LIF signals: fluctuation of laser energy, collisional quenching, discharge instability such as fluctuation of the current pulses respect to the time interval and amplitude, branching of the streamers, spatial relationship between the laser and streamers, and electrohydrodynamic (EHD) flow effect. Especially, the discharge characteristics are much different depending on the gas composition existed in the gap as shown in Table 1. In the case of Ar injection, it is considered that not only the energetic electrons but also metastable Ar atoms contribute to generate OH radicals through the dissociation of H_2O. From the results shown in Fig.4, the measurement method based on no time synchronization between the streamer and laser pulse can be applied to the evaluation of steady-state DC streamer coronas. If we average the signals, the steady-state measurement of OH LIF is possible. On the other hand, time synchronized measurement has been already performed and evaluated by authors [12].

Table 1. Discharge condition in the case of Fig. 4

	Discharge environment	
	in open air without Ar gas flow	in open air with Ar gas flow
DC applied voltage (kV)	29	11
Time averaged current (mA)	200	40
Averaged current pulse (mA)	122	52
S.D. of current pulse (mA)	44	16
Averaged repetition rate of current pulse (kHz)	2.1	5.1
S.D. of repetition rate (kHz)	1.2	0.9

S.D.: Standard deviation

Fig. 5 shows the 2-D discharge emission and OH profiles under steady-state DC streamer coronas in open air without Ar gas flow. The images of discharge emission were taken by the ICCD camera without the band pass filter. The discharge emission mainly consists of N_2 second positive band and no OH emission was observed [12]. This fact suggests that the concentration of excited OH is extremely low. In air the streamers are composed of many branches and occupy much more space than filamentary type of discharge in the case of Ar injection. When the discharge was realized in open air, the LIF signal is much weaker and it is insufficient for single-shot 2D imaging of OH radicals. Therefore, laser beam, which was not expanded to the sheet, was used. In order to increase SN ratio of the image, the image shown in Fig.5 (b) is an average of 50 captured images. Although the streamer emission and LIF images taken separately, it can be seen that OH LIF signal comes mainly from the streamer region as shown in Fig.5 (c).

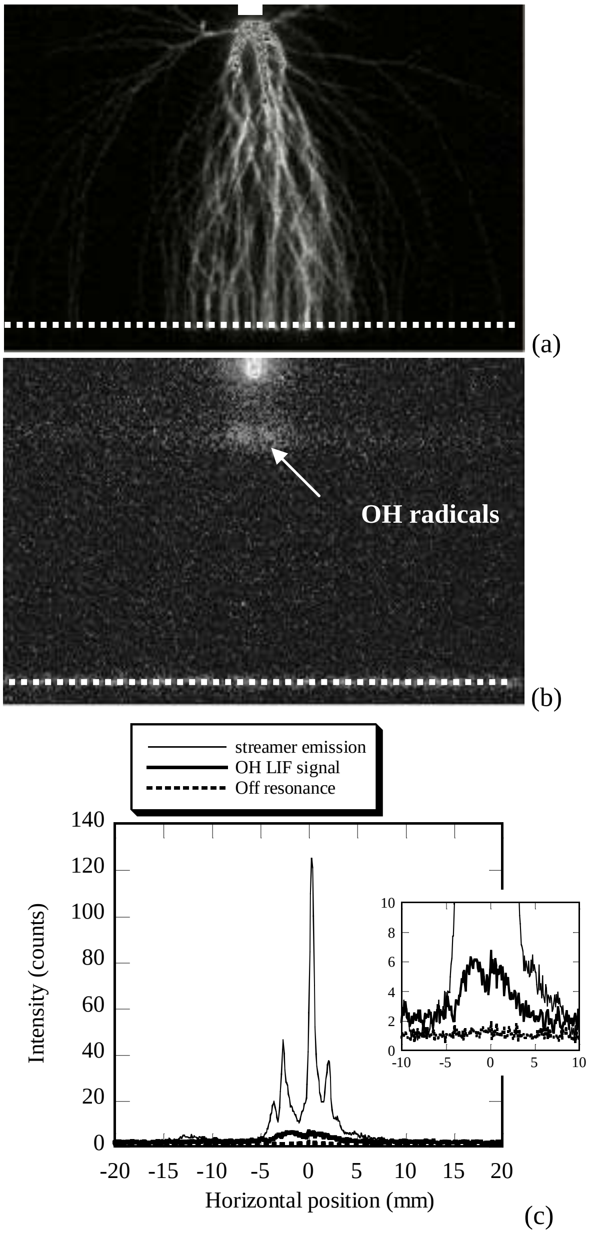

Fig. 5. Comparison of streamer and LIF images in open air. The applied voltage is 29kV and corona current is 190mA:

(a) streamer emission observed by the ICCD camera with gate time of 900ms;

(b) OH LIF near the tip of the stressed electrode (ICCD gate of 100ns);

(c) horizontal profile for both streamer emission and OH LIF. The profile obtained at the laser wavelength of off resonance is also shown

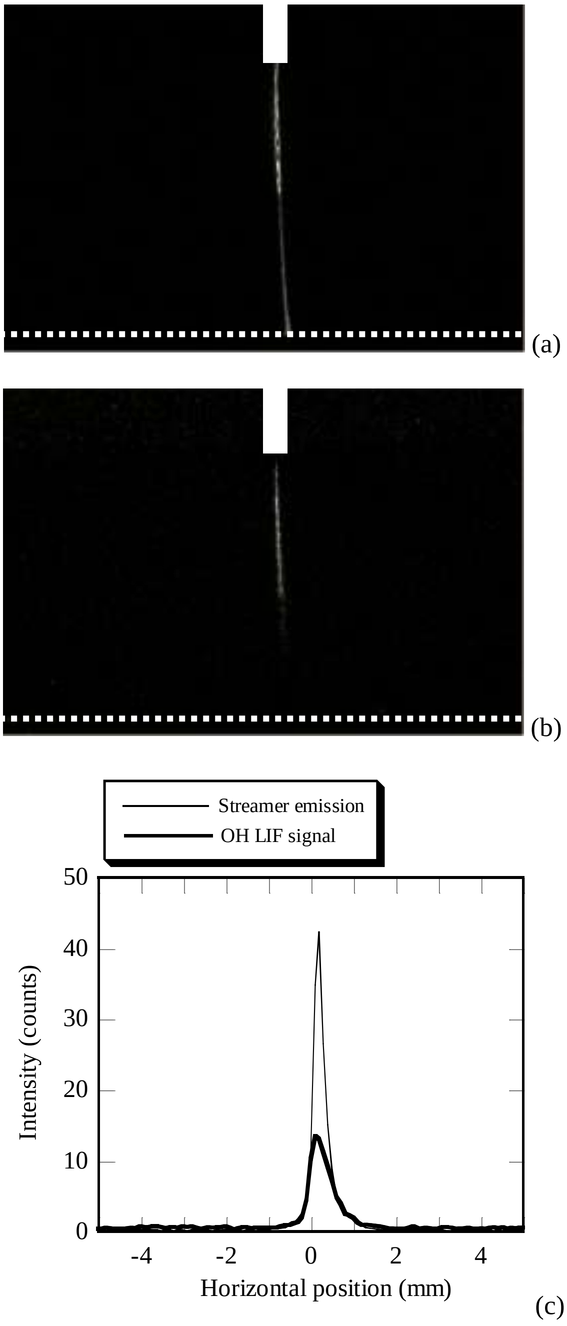

Fig. 6. Comparison of streamer and LIF images in open air. The applied voltage is 14kV and corona current is 60mA:
(a) streamer emission observed by the ICCD camera with gate time of 900ms;
(b) OH LIF between the electrodes (ICCD gate of 100ns);
(c) horizontal profile for both streamer emission and OH LIF

In contrast, the 2-D discharge emission and OH profiles under steady-state DC streamer coronas in open air with Ar gas flow (0.3L/min) is shown in Fig.6. In a spectroscopic analysis, the spontaneous emission of excited OH molecules was present as well as N_2 emission when the Ar was added to the discharge through the nozzle. When Ar is introduced through the nozzle electrode into the discharge region, the shape of the streamers changes to a filament without branches. The OH LIF signal was easily detected even in the case of single-shot LIF imaging. Similarly, OH LIF signal comes from within the streamer volume. These results suggest that OH radical generation occurred inside the streamer.

CONCLUSIONS

The OH radical generation in DC streamer corona discharge was examined using the LIF method with a frequency-doubled-dye laser system. It was found that the LIF could apply to the measurement of OH radicals stayed in the steady-state DC streamer coronas in open air. The influence of Ar injection on the discharging characteristics and the generation of OH radical was also examined. The streamer discharge in air is composed of many branches and occupies much more space than filamentary type of discharge in the case of Ar injection, resulting in the profiles of OH radicals between the electrodes. 2-D OH images show that OH radicals were generated in the streamers.

LITERATURE

[1] S. Kanazawa, T. Ito, Y.Shuto, T. Ohkubo, Y. Nomoto and J. Mizeraczyk, IEEE Trans. Ind. Applicat. 37 (2001) 1663

[2] S. Kanazawa, Y.Shuto, N. Sato, T. Ohkubo, Y. Nomoto, J. Mizeraczyk and J. S. Chang IEEE Trans. Ind. Applicat. 39 (2003) 333

[3] G. J. Roth and M. A. Gundersen, IEEE Trans. Plasma Sci. 27, (1999) 28

[4] H. Hazama, M. Fujiwara and M. Tanimoto, Chem. Phys. Lett. (2000) 542

[5] F. Fresnet, G. Baravian, S. Pasquiers, C. Postel, V. Puech, A. Rousseau and M. Rozoy, J. Phys. D: Appl. Phys. 33 (2000) 1315

[6] F. Tochikubo and T. Watanabe, in Inter. Symp. on High Pressure Low Temperature Plasma Chemistry, Hakone VII, 1, 2000, p.219

[7] A. Ershov and J. Borysow, J. Phys. D: Appl. Phys. 28 (1995) 68

[8] R. Ono and T. Oda, J. Electrostatic 55 (2002) 333

[9] F. Tochikubo, S. Uchida and T. Watanabe, Jpn. J. Appl. Phys., 43 (2004) 315

[10] S. Kanazawa, T. Ito, Y. Shuto, T. Ohkubo, Y. Nomoto, J. Mizeraczyk, J. Electorstatics 55 (2002) 33

[11] T. Ohkubo, T. Ito, Y. Shuto, S. Akamine, S. Kanazawa, Y. Nomoto, J. Mizeraczyk, J. Adv. Oxid. Technol. 5 (2002) 129

[12] M. Kocik, J. Mizeraczyk, S. Kanazawa, A. Kajiwara, J. Kumagai, T. Ohkubo, Y. Nomoto, J. S. Chang, Conference Record of the 2004 IEEE Industry Applications Conference, Seattle, U.S.A., October 3-7, 2004, in CD-ROM

5th International Conference **ELMECO**
Nałęczów, Poland
September 2005

STUDY OF A WIDE AREA CARBON NANOTUBES PREPARATION FOR AN ENVIRONMENTAL APPLICATION

Shin-ichi Aoqui, Yoshiyuki Suda (1), Kenji Ebihara (2), Takuhiko Uematsu (3)

Department of Electrical System & Computer Engineering, Sojo University,
4-22-1, Ikeda, Kumamoto 860-0082, Japan
[1] Graduate School of Information Science & Technology, Hokkaido University,
North 14, West 9, Sapporo 060-0814, Japan
[2] Department of Electrical & Computer Engineering, Kumamoto University,
2-39-1, Kurokami, Kumamoto 860-8555, Japan
[3] Elionix Inc., 3-7-6, Motoyokoyama-cho, Hachioji-shi, Tokyo 192-0063, Japan
e-mail: aoqui@cis.sojo-u.ac.jp

Abstract

The gas occlusion alloy that a metal atom was used for an application to the fuel cell and so on. However the price of rare metals and a few amounts of gas occlusion to the unit weight causes a problem. A gas occlusion of carbon-based material attracts attention recently. Especially, as for the carbon nanotubes (CNTs) it began to be known that sensitivity for gaseous such as NH_3 and NO_2, and also gaseous occlusion ability should be high. If large quantities of gaseous can occlude CNTs, atmosphere release of the hazardous material such as Dioxin may be able to be controlled. In this study, we used a way that we applied a catalysis organ-metal solution to a substrate, and then it was burned. This method is very unique. Not only the cost performance of this method is high in comparison with other method but also this can increase a wide area CNTs preparation.

Keywords: Carbon nanotubes, Carbon nanofibers, Organ-metal Solution, Thermal chemical vapor deposition, laser thermal CVD

INTRODUCTION

Ever since the discovery of carbon nanotubes (CNTs), a lot of efforts have been given to utilizing their unique electric, structural and chemical properties. That is to say, CNTs have been focus of considerable attention because of many possible applications in nanostructure, super strong materials, semiconductor, electron emitting device, hydrogen storage, gas sensor and gas occlusion materials. [1-3] Especially, as for the CNTs it began to be known that sensitivity for gaseous such as NH_3 and NO_2, and also gaseous occlusion ability should be high. [4-6] If large quantities of gaseous can occlude CNTs, atmosphere release of the hazardous material such as Dioxin may be able to be controlled. [7] And also when a electric device is used for environmental application, many conditions must be satisfied such as low preparation cost, wide aria, simple and safe preparation system and so on. Regarding to CNTs, several process methods such as arc discharge, chemical vapor deposition (CVD) and pulsed laser ablation (PLA) have been used to produce it. [8][9] However, as for which methods as well, it isn't easy to apply the catalyst metal, which is necessary for the CNTs growth. In this study, in order to prepare large surface aria on small substrate, the way that we applied a catalysis organ-metal solution to a substrate and then it was burned out was used. [10] This method is very unique, especially it has almost never used as the catalyst for the nanotubes. Nano size dots of catalytic metal such as platinum (Pt), and Nickel (Ni), on Silicon or quartz glass substrate preparation technique by burning of catalysis organ-metal solution had already been developed by pervious our work. Also two apparatus were used for the growth of CNTs by this study. One was a traditional thermal CVD system, the other hand was a laser thermal CVD (LT-CVD) system. This LT-CVD equipment is completely the same as a pulsed laser deposition (PLD) system, but growth mechanism of CNTs is different from a PLD remarkably. That is to say we used very high Ar ambient gaseous condition at 500 Torr, therefore laser plasma plume was very small and ejected particles from a graphite target are reduced its speed immediately. Almost ejected carbon particles reacts in a vapor phase, and then CNTs are formed on a substrate. Accordingly LT-CVD can correspond to wide aria CNTs preparation. Both simple systems realized catalyst supply and tubes growth in the same equipment together. However when a catalysis organ-metal solution was used, the thermal CVD could obtain the CNTs very easily but high process temperature (less than 1000 ºC.) was necessary. On the other hand, when the LT-CVD was used, we obtained CNTs in low temperature relatively. And also we carried out a selective growth of CNTs. In growth of CNTs, catalytic metal might be small quantity. When CNTs is used to a gaseous sensor, it should be had to add an electrode to CNTs, but device preparation might be allowed in one path process, if gold which has no catalytic effect and good electrode material, and catalytic metal are mixed.

In this paper, we investigated intensively about CVD and LT-CVD system for CNTs growth. The CNTs were deposited in the temperature range from 600 to 1100 ºC and laser fluences of 2 J/cm^2. The nano size metallic dot was characterized by an electron probe surface roughness analyzer, X-ray diffraction spectrometer (XRD), and scanning ion microscope (SIM), and deposited CNTs were characterized by a field-emission scanning secondary electron microscope (FE-SEM), transmission electron microscope (TEM) and a Raman spectrophotometer.

EXPERIMENTS

On CVD and LT-CVD, we used electric furnace which was work temperature range of upto 1600 ºC (CVD) and 1100 ºC (LT-CVD). Organ-metal solution was burned out atmospheric condition. After a reaction tube (Al_2O_3, ϕ = 50 mm) was exhausted by a vacuum pump to a base pressure of 1.0×10^{-2} Torr. As for LT-CVD, in the tube, a sintered pure graphite target (purity 99.99%) of 30 mm in diameter was mounted on the rocking holder. Pulsed ArF excimer laser (lambda Physik: λ = 193 nm) beam was introduced into the tube through lenses and a quartz window. The laser beam impinges on the target at an incident angle of ~90º. In order to prepare CNTs, n-type Si(100) wafers or quartz glass substrates, which an organ-metal solution was spread by using spin coater, were positioned lower inside the tube, it was almost parallel to the laser beam. The substrates were heated from room temperature to 1100 ºC or 1600 ºC. Substrate temperature (Ts) was measured by using a thermocouple. The gas pressure was varied from the base pressure to 10 Torr with 100sccm flow rate by feeding pure methane (CH_4) gas (in case of CVD) or 500 Torr with 750 sccm flow rate by feeding pure Ar gas (in case of LT-CVD) into the reaction tube.

RESULTS AND DISCUSSIONS

The surface morphology of Pt catalytic metal dots on the Si substrate which should be used for the CNTs growth was examined by 3D-SEM, as shown in Fig. 1(a) and (b). When the burning temperature was 300 ºC, it was a very smooth morphology with a silver mirror condition. When temperature rises up to 900 ºC, Pt makes a dot type island-shape structure. Moreover dot can be classified in three kinds of diameter, such as about 30 nm, 60nm and 120 nm. Now we consider that these dots have a different surface direction from the observation of XRD measurement, such as (111), (200) and (220) respectively. Fig.2 show a temperature dependence of XRD spectrum pattern of Pt. (2θ angle of (220) was not listed. It should be appear 65º.) Crystallite sizes were calculated by Scherrer equation using FWHM of each peak. In Pt dot case, crystallite size of (111) peak is 26.7 nm, (200) is 42.7 nm and (220) is109 nm. These values show good agreement at diameters of a Pt dot. Though generally, between crystallite size and grain size don't have direct relationship, this is a surprising thing.

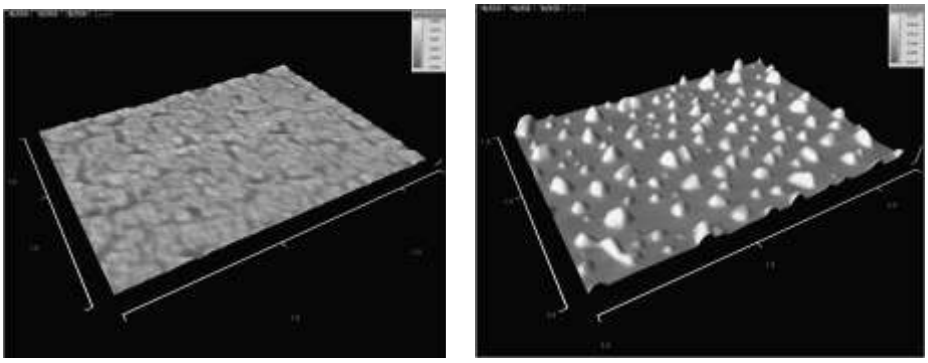

Fig.1 (a) Fig.1 (b)

Fig. 1(a). burning temperature 300 ºC at atmospheric ambient condition. Average roughness: 0.5 nm;

Fig. 1(b). burning temperature 900 ºC at atmospheric ambient condition. Height of dots: about 30nm;

Fig. 1. 3D-SEM images of Surface morphology of Pt nano dot on Si substrate (2.2 mm*1.8mm)

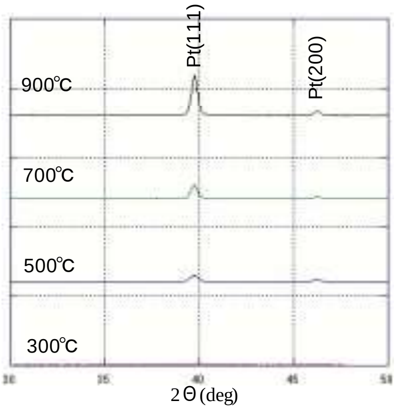

Fig. 2. Temperature dependence of XRD crystalline properties of Pt film on Si substrate

Fig. 3(a) and (b) show FE-SEM images of the CNTs prepared by simple CVD using Pt and Ni catalyst substrate at Ts = 1000 ºC, CH_4 ambient condition. CNTs growth can be confirmed. Tube diameters were 60 nm and 80 nm respectively. Although CNTs grows very long and flexibly with a Ni catalyst, it seems to be hard to grow with a Pt catalyst. This is based on the difference in effect on the catalyst, but in case of Pt, improvement of flexible growth should be possible for that by control of reaction temperature and ambient gas kinds and flow rates.

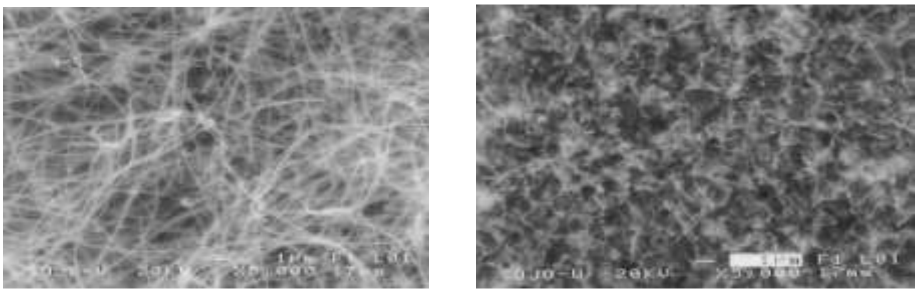

Fig. 3(a). CNTs on Ni catalyst
Fig. 3(b). CNTs on Pt catalyst
Fig. 3. FE-SEM images of CNTs (CH_4 ambient condition with Ts = 1000 ºC)

Accordingly we carried out completely another ambient condition of LT-CVD system. Extremely high Ar gas pressure of 500 Torr was introduced to a reaction tube on PLA graphite target ablation. The condition that CNTs were composed of the gaseous phase was considered. Because Ar pressure was very high, plasma plume hardly to spread out. On this condition, ejected carbon atoms and particles should be slowed down suddenly. Fig.4 shows EF-SEM images of CNTs on Pt catalyst (burning temperature of 900 ºC). (a) and (b) is same image but resolution is different. Average tube diameter was about 60 nm. Compare to the tube length, diameter and curvature property, LT-CVD was realized better conditions than CVD. In general, it's said with CVD that it is not easy to prepare CNTs only Pt catalyst. Because Pt hardly composes solid solution with carbon atoms and moreover Pt dot size of the substrate was not enough small regarding to a small diameter CNTs growth. Nevertheless CNTs growth of LT-CVD obtained good result, we considered that fullerences-like bonding could be combined by a high pressure Ar ambient gaseous phase by PLA.

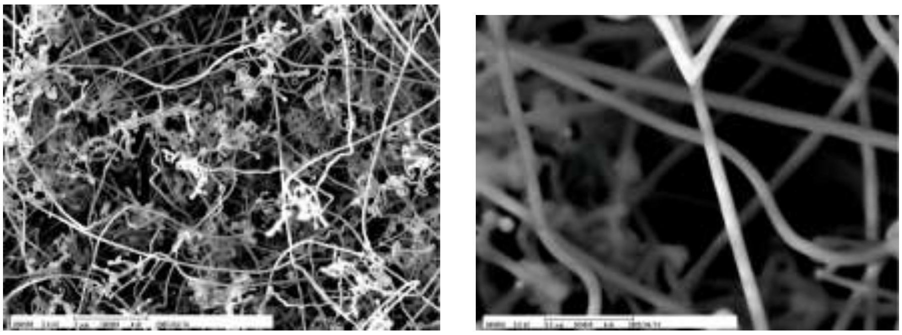

Fig. 4(a). CNTs on Pt catalyst
Fig. 4(b). CNTs on Pt catalyst
Fig. 4. FE-SEM image of CNTs by LT-CVD with ArF excimer laser (λ = 193 nm, Ar: 500 Torr)

Also we carried out the experiment of the selective growth of the CNTs. Because it doesn't have a effect of catalyst with Au, the substrate that the solution on which mixed a little (about 2 weight %) Ni or Pt to Au organ-metal solution was used for was burned out at 900 ºC on 100 Torr Ar ambient condition.

Fig.5 shows a SIM image of cross section of Au / Pt dots substrate. Au and Pt dots were buried in the silicone oxide that was growth in atmospheric burning conditions. (Refer to our report for details.) Fig.6 shows selective growth of the CNTs by using LT-CVD system on Ni/Au and Pt/Au substrate. Selective CNTs growth was confirmed in both Ni/Au and Pt/Au substrate. Both average tube diameters was 60 nm.

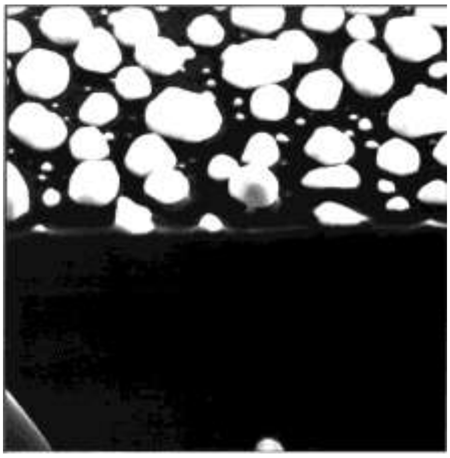

Fig. 5. FIM image of cross section of Au/Pt dots on Si substrate

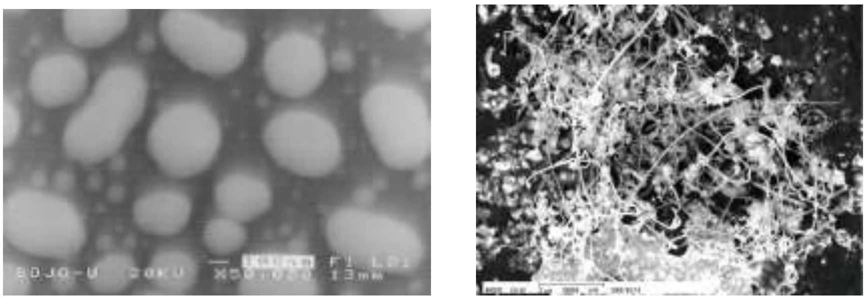

Fig. 6(a). Ni/Au catalyst nano dots on Si and CNTs on Ni/Au catalyst dot

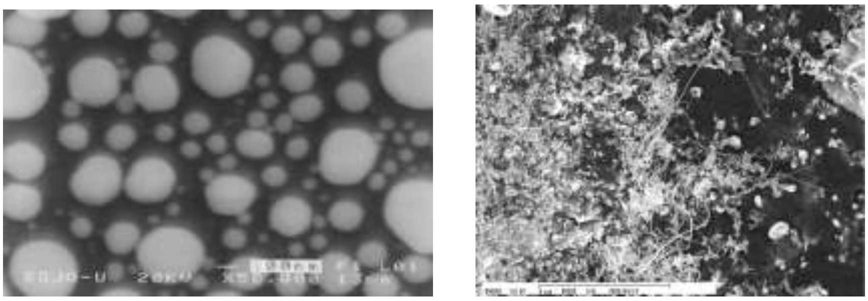

Fig. 6(b) .Pt/Au catalyst nano dots on Si and CNTs on Pt /Au catalyst dot

Fig. 6. FE-SEM image of CNTs by high Ar pressure LT-CVD

After CNTs growth, element composition of the black part was confirmed by EPMA/EDX (EDAX UDU leap detector) that part's component was almost graphite phase or diamond-like carbon in the FE-SEM images. When substrate will be refined chemically, Au dots and SiO_2 should be appear. CNTs grew only from top of the Ni or Pt catalyst dots.

Raman spectrometry was carried out to investigate a G/D ratio and RBM mode. Fig. 7 shows typical spectrum of CNTs on Pt and Ni dots using LT-CVD.

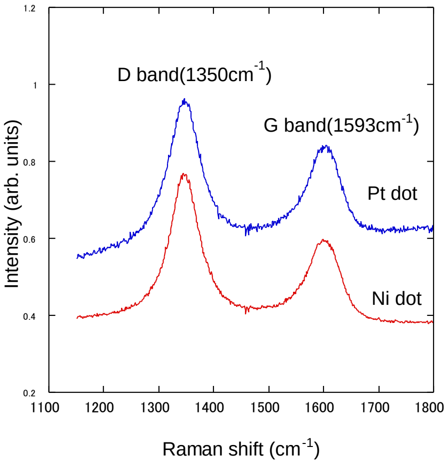

Fig. 7. Raman spectroscopy of CNTs films (Ni and Pt dots)

Very large peak of D band (1350 cm^{-1}) was detected. And RBM mode was not detected (it's not listed in the fig.5). From this result, we considered that the tubes were constructed by multi-wall system. It's almost carbon nano fiber. Also the D/G ratio designates that many carbon disorder bonding is contained. That means black part of the film should be DLC systems. This will be able to be controlled by optimizing a condition of PLA such as ambient gas, pressure, laser fluence and substrate temperature and so on.

CONCLUSIONS

In this study, CNTs were prepared using very new technique, which makes an organ-metal solution departure catalytic material. This technique is very simple therefore; it has a possibility of large-scale composition with lower cost. Also it has the possibility to have process temperature reduced by using LT-CVD system. This system had high yield rate of CNTs growth. Also we confirmed selective growth of CNTs.

ACKNOWLEDGMENT

This research was supported in part by RSP program of Kumamoto Technology and Industry Foundation.

REFERENCES

[1] S. Iijima, Nature 354 (1991) 56-59

[2] J. W. G. Wildoer, L. C. Venema, A. G. Rinzler, R. E. Smalley, C. Dekker, Nature 391 (1988) 59

[3] T. W. Odom, J. L. Huang, P. Kim, C. M. Lieber, Nature 391 (1988) 62

[4] T. Masciangioli, W. Zhang, Environ. Sci. Technol., 37 (2003) 102A

[5] J. Kong, N. R. Franklin, C. Zhou, M. G. Chapline, S. Peng, K. Cho, H. Dai Science, 287 (2000) 622

[6] A. Modi, N. Koratkar, E. Lass, B. Wei, P. M. Ajayan Nature 424 (2003) 171

[7] R. Q. Long, R. T. Yang J. Am. Chem. Soc., 123 (2001) 2058

[8] Y. Suda, et al, Appl. Phys. A, 79 (2004) 1331

[9] A. Thess, R. Lee, P. Nikolaev, H. Dai, P. Petit, J. Robert, C. Xu, Y. H. Lee, S. G. Kim, A. G. Rinzler, D. T. Colbert, Science 273 (1996) 483

[10] Naval avionics center, USA, Metallo-organic materials for impredection film reliability (1980)

5th International Conference **ELMECO**
Nałęczów, Poland
September 2005

INFLUENCE OF THE VORTEX PINNING ON THE CRITICAL CURRENT IN HTc SUPERCONDUCTORS

Jacek SOSNOWSKI

Instytut Elektrotechniki
04-703 Warszawa, Pozaryskiego 28
E-mail: sosnow@iel.waw.pl

Abstract

The vortex pinning is considered in the HTc layered superconductors. The importance of this effect for the critical current and therefore applications of these new materials is discussed, while analogy to the semiconducting superconductors mentioned. The mathematical modeling of vortices is presented. The capturing of the pancake type vortices in perpendicular magnetic field is considered, underlining the relevance of the pinning centers dimensions and anisotropy for critical current. In parallel magnetic field the capturing of the Josephson's like vortices in the buffer layer is dominant pinning effect.

Keywords: critical current, high Tc superconductivity, vortex pinning

INTRODUCTION

The superconductivity shall fill the particular function in the protection of the environment against the air pollution due to among other of the possibility of the electric energy saving and it's transportation in HTc superconducting cables in clean, lossless way. The proper work of the superconducting power devices is dependent on the critical current capabilities of the HTc materials [1]. In this subject the flux pinning of the vortices plays the essential function. The interaction of the pinning centers with characteristic vortices appearing in HTc superconductors is therefore very important subject from the point of view of the achievement the largest critical currents. Selected problems of the magnetic vortices pinning in the high temperature superconductors are discussed in the paper. The specific layered structure of these materials has been taken into account. Other peculiarity of the HTc superconductors lies in their low electric carrier concentration, which makes these materials similar to the semiconductors, materials indicating the superconducting properties sometimes too. There are few semiconducting compounds, in which the superconductivity phenomenon was detected. To this group belong: InTe, SnTe, GeTe, $SrTiO_3$, $La_{3-x}Se_4$. This latter compound, investigated in the past by the author indicates particularly strong influence of the carrier concentration on the critical temperature and magnetization, which experimental results are collected in Figs. 1-2.

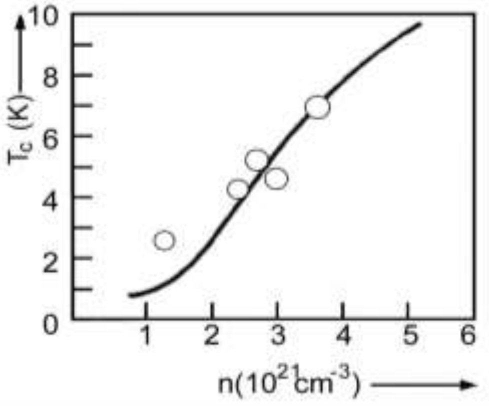

Fig. 1. Critical temperature dependence on the electron carrier concentration for lanthanum selenide $La_{3-x}Se_4$ samples. Solid line denotes the theoretical predictions

Previously the pinning phenomena were investigated mainly basing on the irreversibility of the magnetization curves analysis, shown for instance in the Fig. 2. In the present paper the other method of the pinning analysis based on the current-voltage characteristics investigations is developed.

THE VORTICES IN THE GINZBURG-LANDAU APPROACH

Mathematically the existence of vortices follows from the variational procedure of the Ginzburg-Landau [2] free energy leading to new two equations, which describe the space variation of the order parameter and the current flow in the type two superconductors. After appropriate modifications performed by Lawrence-Doniach these equations describe the high temperature superconductors too.

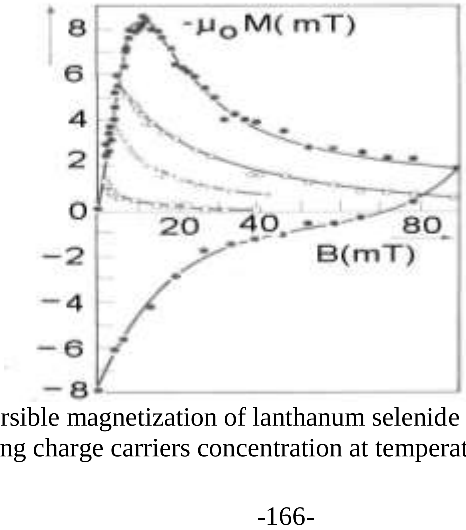

Fig. 2. The irreversible magnetization of lanthanum selenide $La_{3-x}Se_4$ samples with increasing charge carriers concentration at temperature of 1.8 K

In weak magnetic field the order parameter Ψ slowly varies around the Ψ_∞ value, then the second Ginzburg - Landau equation is reduced to the London form:

$$j = -\frac{4e^2}{mc}\left|\Psi_\infty\right|^2 A \tag{1}$$

where the London penetration depth λ is:

$$\lambda^2 = \frac{4\mu_0 e^2}{mc\left|\Psi_\infty\right|^2} \tag{2}$$

m is electron mass, while *e* it's charge.

Because the magnetic field vector potential A is defined as h = rot A, where ***h*** is the local microscopic magnetic field, Eq. 1 reduces to the following generalized expression, obtained in the approximation of the existence of an individual vortex at the point r:

$$\lambda^2 \mathrm{rot}\, j_S + h = \Phi_0 \delta(r) \tag{3}$$

The appearance of the vortex has been taken into account in Eq. 3 by inserting the δ Dirac function at the right hand side. Φ_0 is flux quantum equal to 2.07x10^{-15} Wb. Using additionally the Maxwell's equations Eq. 3 is transformed into new one describing the magnetic field distribution h(r) in the vortex by the Green's function:

$$\nabla^2 h - \frac{h}{\lambda^2} = \frac{-\Phi_0 \delta(r)}{\lambda^2} \tag{4}$$

Exact solution of Eq. 4 is expressed by the Hankel's function K_0 of zero order and imaginary argument for magnetic field and by first order function for the current description:

$$h(r) = \frac{\Phi_0}{2\pi\lambda^2} K_0\left(\frac{r}{\lambda}\right) \tag{5}$$

$$\mu_0 j(r) = \frac{\Phi_0}{2\pi\lambda^3} K_1\left(\frac{r}{\lambda}\right) \tag{6}$$

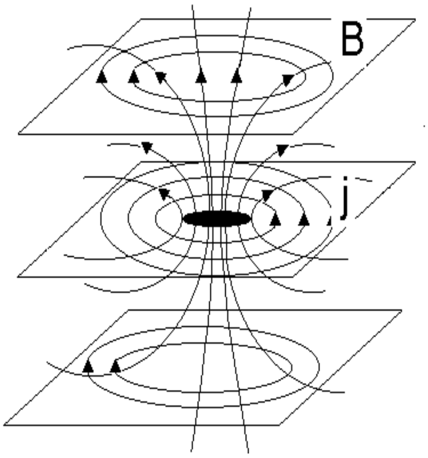

Fig. 3. The pancake magnetic vortex in the multi-layered structure of HTc superconductors

which for some limiting ranges $\xi << r << \lambda$ and large r are approximated by the logarithmic and exponential dependences. The interaction of the magnetic vortices with the pinning centers stabilizes the vortex lattice and allows for the resistance-less transport current flow.

THE INTERACTION OF THE PINNING CENTERS AND VORTICES IN HTC SUPERCONDUCTORS

In the present chapter we will consider the interaction of generated in perpendicular magnetic field vortices, localized in a-b plane of HTc superconductors structure with pinning centers of nanometric size, created for instance as the result of the heavy ions irradiation. The pinning effects for parallel magnetic field will be discussed too. These defects being the new important kind of the pinning centers in addition to the classical ones, such as grain boundaries or dislocations, arise during the work of HTc windings in nuclear reactors for instance, where they are exposed to heavy ions irradiation. Analysis of the defects interaction with vortices influencing the critical current plays therefore an important function from the point of view of proper work of near future superconducting power devices. The quantity of the normal phase and then free energy of the system increases during the flux line motion against the pinning center, what leads to the increase in the pinning potential and results in the creation of the pinning force. Because the coherence length in the high temperature superconductors describing the radius of the vortex core is of the order of several nanometers, similarly to the heavy ions dimensions, acting as the pinning centers, so the flux pinning takes place on the nanometer range scale. Influence on the critical current of the mutual relations between both these lengths is considered presently. The pancake type vortex generated in the high temperature oxide superconductors in the perpendicular magnetic field is shown in Fig 3. It is localized in single layer and interacts with individual pinning center. Due to the pinning interaction arises the potential barrier ΔU, which is a function of the current and pinning centers dimensions, frequently of the nano-scale range. The scheme of the investigated geometry of the interacting pinning center in the form of thin slab with a vortex is shown in Fig. 4. In the initial state the vortex captured at the depth equal to the coherence length ξ_0, describing the radius of the vortex core has been considered. Then the initial state normal energy is:

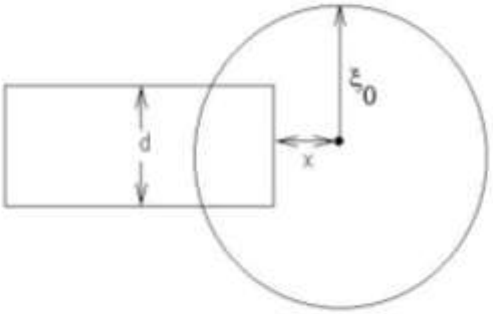

Fig. 4. View of the vortex core of the radius equal to the coherence length (ξ_0) captured on the pinning center of the width (d)

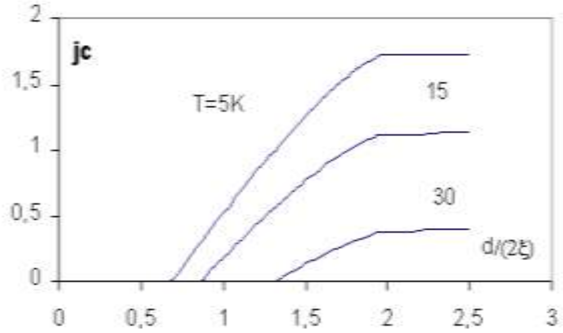

Fig 5. Dependence of the critical current density in arbitrary units on the pinning centers dimensions versus temperature

$$U_1(\xi)=\frac{\mu_o H_c^2 l}{2}\left[\pi\xi^2-\xi^2\arcsin\frac{d}{2\xi}-\frac{d\xi}{2}\sqrt{1-\left(\frac{d}{2\xi}\right)^2}\right] \qquad (7)$$

During the movement of the vortex on the distance x against the pinning center, as indicated in Fig. 4, the normal part energy of the superconductor with captured vortex increases according to the relation valid for $x > x_c$:

$$U_3(x)=\frac{\mu_o H_c^2 l\xi^2}{2}\left[\frac{\pi}{2}+\arcsin\frac{x}{\xi}+\frac{x}{\xi}\sqrt{1-\left(\frac{x}{\xi}\right)^2}\right] \qquad (8)$$

where $x_c=\xi\sqrt{1-(\frac{d}{2\xi})^2}$. The maximal pinning energy barrier height which should be jumped by the vortex during it's hoping movement to the next pinning center is given as follows:

$$\Delta U(i)=\frac{\mu_o H_c^2 l\xi^2}{2}\left[-\arcsin i+\arcsin\frac{d}{2\xi}+\frac{d}{2\xi}\sqrt{1-\left(\frac{d}{2\xi}\right)^2}-i\sqrt{1-i^2}\right]$$
$$+\alpha\xi^2\sqrt{1-i^2}\left(\sqrt{1-i^2}-2\right) \qquad (9)$$

The total potential energy barrier height $\Delta U(i)$ given by Eq. 9 is the function of the reduced current $i=j/j_{creep}$, where j_{creep} is critical current density for flux creep process, while the potential of the Lorentz force as well as the elastic energy of the vortex lattice described by elasticity constant α have been taken into account too. It allows us already to determine current - voltage characteristics applying the constitutive relation describing the generation of electric field E during the flux creep process both for forward and backward magnetic vortices hopping movement through the potential barrier:

$$E=-B\omega a\left[\exp\left[-\frac{\Delta U(0)}{k_B T}(1+i)\right]-\exp\left(-\frac{\Delta U(i)}{k_B T}\right)\right] \qquad (10)$$

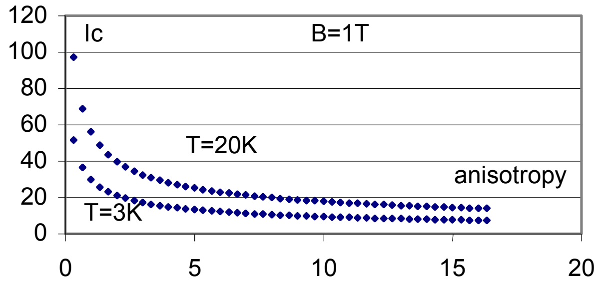

Fig. 6. The influence of material anisotropy ξ_a/ξ_b on the critical current

$\Delta U(0)$ is the potential barrier height without current, ω is characteristic frequency, which in the present paper has been assumed to be constant, T temperature and k_B is the Boltzmann's constant, *a* is the average distance between pinning centers. Results of calculations of the influence of the pinning centers dimensions and temperature on the critical current are shown in the Fig. 5. Analogous calculations were performed for taking into account the anisotropy of pinning interaction related to anisotropical shape of vortex core. Then potential barrier height by analogy to Eq. 9 is expressed by the relation:

$$\Delta U(i)=\xi_a\xi_b l\frac{\mu_0 H_c^2}{2}\left(-\arcsin i-i\sqrt{1-i^2}+\frac{\pi}{2}\right) \qquad (11)$$

while Fig. 6 presenting the influence of the coherence length anisotropy given by ratio ξ_a/ξ_b, on the critical current for two temperatures indicates the importance of this effect.

For parallel magnetic field geometry to the layer surface the capturing of the vortices in the buffer layer is dominant. The order parameter is modulated function along the z-axis while the existence of the single vortex in the system can be described by the function of the form: $\tanh(z-z_i)/\xi_c$, which possesses the singularity at point z_i being the origin of the vortex core position. The calculations performed basing on Ginzburg-Landau theory [2] show that the average change in the free energy density $\Delta f(z, z_i)$ connected with the vortex located in one from two basic positions, which is in the middle of the buffer layer (z_1) or in the middle of superconducting planes (z_2), is smaller just for that first case:

$$\Delta f\,(z, z_1, z_2) = (\sqrt{\Delta f\,(\overset{\frown}{z}, z_2)} - \sqrt{\Delta f\,(\overset{\frown}{z}, z_1)})^2 = \frac{\mu_0 H_c{}^2 \Psi_2{}^4}{2(\Psi_1^2 + \Psi^2{}_2)^2} > 0 \tag{12}$$

Present result denotes that buffer layer position is energetically more favorable to capture the vortices and explains the anisotropical critical current enhancement for parallel orientation of magnetic field in comparison to perpendicular one. H_C is thermodynamic critical magnetic field, while modulated with lattice constant a_z order parameter Ψ_0 is expressed as:

$$\Psi_0^2(z) = \Psi_1^2 + \Psi_2^2 \cos\left(\frac{2\pi z}{a_z}\right) \tag{13}$$

LITERATURE

[1] Sosnowski J., *Nadprzewodnictwo i zastosowania*, ed. Electrotechnical Institute, Warsaw, 2003

[2] Ginzburg V. L., Landau L. D., *Jour. Eksp. Theor. Phys*., vol. 20, 1950. p. 1064

5th International Conference **ELMECO**
Nałęczów, Poland
September 2005

HYDROGEN AS A FUEL AND AS A COOLANT - FROM THE SUPERCONDUCTIVITY PERSPECTIVE

B. A. Glowacki[1], A. P. Finlayson[1] W. J. Nuttall[2] and T. Janowski[3]

[1] Department of Materials Science and Metallurgy, University of Cambridge,
Pembroke Street, Cambridge CB2 3QZ
bag10@cam.ac.uk, apf23@cam.ac.uk
[2] Judge Business School (and Cambridge University Engineering Department)
Trumpington Street, Cambridge, CB2 1AG, UK
wjn21@cam.ac.uk
[3] Institute of Electrical Engineering and Electrotechnologies
Lublin University of Technology, 38a Nadbystrzycka, 20-618 Lublin, Poland
tadeuszj@eltecol.pol.lublin.pl

Abstract

Superconductors have a great potential in the future development of transportation and energy supply applications. Although MgB_2 superconductors that operate at liquid hydrogen temperatures are not yet commercially available, research indicates that these will be feasible in the future. Novel concepts for transportation and energy supply that would be possible using medium-temperature MgB_2 superconductors include the non-polluting 'cryoplane', a self-contained whole electric superconducting ship, and cheaper superconducting MgB_2 magnets for nuclear fusion, small energy storage and magnetic resonance imaging (MRI) systems. Development of rapid transport superconducting systems is already underway in Japan, with investment in MAGLEV trains that if placed in evacuated tunnels could travel at speeds of 2,800 mph. Superconducting conductors based on magnesium borides have been developed in Cambridge that can be fabricated into cables for power transport with minimal losses. With hydrogen being used as a coolant as well as an energy carrier. Hydrogen production from photocatalysis is particularly advocated. Research is on-going to investigate the optimisation of photo-catalysts for hydrogen generation.

Keywords: Hydrogen, Superconductivity, Fusion, Cryogen, Photocatalysis

INTRODUCTION

Crude oil prices are on the rise as stability in the Middle East erodes. There are fears that energy policy may be heading towards a situation not unlike the dark days of the early

1970s. Back then, nuclear power implied a more reliable and sustainable hope for the future. Recent thinking suggests making use of the unique combination of properties presented by hydrogen, allowing it to serve as both a source of energy and cryogenic medium, might provide a modern solution to demanding energy and environmental requirements. At present our main energy carriers are fossil fuels and electricity. Of these, the former is economically storable, while the latter is not an energy resource (or fuel) but merely a pure energy carrier. The hydrogen economy would rely on manufactured hydrogen (here there is a similarity to electricity) yielding a fluid energy product that could be transported and stored relatively straightforwardly (in a manner similar to petrol). Currently there is much discussion of global warming and the need to minimise the release of carbon dioxide from fossil fuel combustion into the atmosphere. Hydrogen on the other hand can release its energy by combustion (or more efficiently in an electrochemical fuel cell) without releasing any carbon dioxide. In order for hydrogen to be a truly environmentally benign energy carrier it will be important to produce the hydrogen in a clean way without the combustion of fossil fuels.

The concept "hydrogen as a fuel and hydrogen as a coolant" is fundamental to many feasible applications that fully exploit the complementary properties of hydrogen, including: nuclear fusion, the cryoplane, energy storage, the electric ship and even magnetic resonance imaging (MRI). Each of these technologies can operate independently of a widescale power distribution network and can be visualised as 'hydrogen-islands'. In this paper nuclear fusion and the cryoplane are highlighted as examples of the potential implementation of hydrogen technology. The cost-effective, reliable and environmentally benign generation of hydrogen is crucial to successful realisation of these applications. Photocatalytic water splitting offers one route to fulfilling these requirements.

One of the superconducting materials which can be used successfully in conjunction with hydrogen technology is magnesium diboride, MgB_2, in the form of the powder in tube conductors (see Fig. 1), as developed originally by the Applied Superconductivity and Cryoscience Group in Cambridge [1,2].

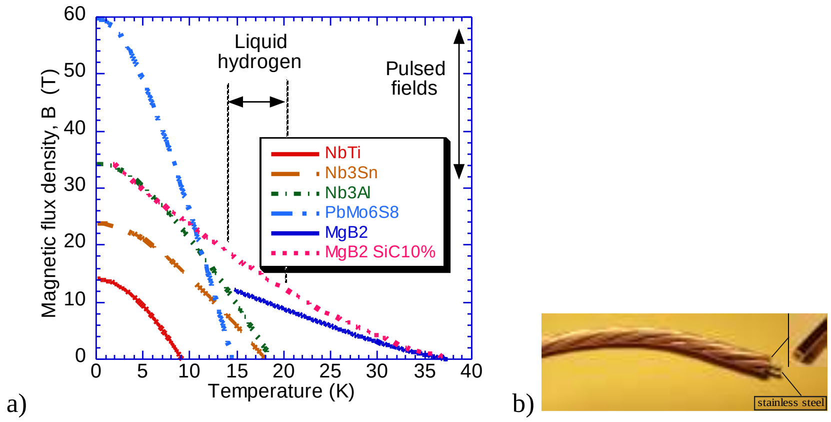

Fig. 1. MgB_2 conductors:
a) comparison upper critical flux density B_{c2} versus temperature of Nb-based conductors [3] and MgB_2;
b) Twisted multifilamentary $Cu/CuMgB_2$ with the internal reinforcement can be viable solution

HYDROGEN PRODUCTION TECHNOLOGIES

Steam Reforming

Steam reforming of natural gas is currently the most economical and widespread hydrogen production technology. Pressurised (3-5 bar) steam is fed into a methane gas reactor at 700-1000 ºC allowing the following endothermic reaction to take place.

$$CH_4 + H_2O \rightarrow CO + 3H_2 \qquad (1)$$

$$CO + H_2O \rightarrow CO_2 + H_2 \qquad (2)$$

Typically the thermal efficiency of the process is limited to 40-60% [4] by the need to heat the reaction to elevated temperatures. New methods, such as the Kvaerner Carbon Black & Hydrogen Process, a high temperature pyrolysis reaction, allow increased economic efficiency [5]. As a long term strategy for hydrogen production all natural gas based processes are dependant upon a continuous secure supply of hydrocarbon fuels and, if they are to become ‘carbon neutral’, the implementation of carbon or carbon dioxide sequestration.

Direct Electrolysis

A water electrolyser relies upon the application of electrical power to split water molecules into oxygen and hydrogen.

$$2H_2O + \text{energy} \Rightarrow 2H_2 + O_2 \quad :1.23V \qquad (3)$$

There are a number of different electrolytes that may be appropriate for electrolysers of different capacities and operating efficiencies. Alkaline electrolysers use 25% aqueous potassium hydroxide and can operate at up to 80% efficiency. They operate under moderate pressure and are most suited for large scale applications connected to the power grid. Polymer electrolyte membrane (PEM) electrolysers can theoretically reach higher efficiencies and are most suitable for small, variable output systems.

The cost and efficiency of hydrogen production via electrolysis is highly dependant upon the source of the electrical energy used to drive the cell. It is predicted that in the near future the cheapest sources of hydrogen supply will be natural gas, coal and gasoline at 6 to 11 $\$GJ^{-1}$ (17 to 31 US¢/kWh) with hydrogen from renewable, carbon neutral technologies such as wind generation and thermal solar power costing approximately 17 to 30 $\$GJ^{-1}$ (47 to 83 US¢/kWh)[6].

Thermal Decomposition

Concentrated solar thermal energy may be used to reach temperatures over 3000ºC allowing the thermal decomposition of water to occur. However this technology presents challenges in the separation of product gases at elevated temperatures and in the selection of construction materials.

Alternatively, thermochemical water splitting cycles have been developed to allow water pyrolysis at 900ºC, a temperature achievable by the proposed hydrogen fusion plant discussed later in this paper. The sulfur-iodine cycle developed by General Atomics is one of the most promising thermochemical cycles with an overall efficiency of 50% [7].

$$2HI \rightarrow H_2+I_2 \qquad (4)$$

$$H_2SO_4 \rightarrow H_2O + SO_2 + {}^{1}/_{2}\,O_2 \qquad (5)$$

$$SO_2 + I_2 + 2H_2O \rightarrow 2HI + H_2SO_4 \qquad (6)$$

Biogeneration

In 1896 it was discovered that some bacteria can produce hydrogen as a by product of photosynthesis. Theoretically efficiencies of up to 25% are possible, but in practice the simultaneous generation of oxygen inhibits the activity of the hydrogenase enzyme and reduces efficiencies to 10% [8]. Many different organisms including the green algae *chlamydomonas reinhardtii*, and the bacteria *rodobacter speriodes* and *clostridium acetobutylicum* are under investigation, however no one technology has been successfully scaled up for industrial production.

Photocatalysis

Photocatalysis is a mechanism whereby the energy from absorbed photons may be used to accelerate the rate of chemical reactions. The water-splitting reaction commonly used in hydrogen production proceeds via three steps:

Table 1. Common mechanism for the water-splitting reaction used in hydrogen production.

Photon Absorption:	$2hv \rightarrow 2e^- + 2h^+$
Anode:	$H_2O + 2h^+ \rightarrow {}^1/_2 O_2 + 2H^+$
Cathode:	$2H^+ + 2e^- \rightarrow H_2$
Overall:	$\mathbf{H_2O + 2hv \rightarrow H_2 + {}^1/_2O_2}$

Only those photons with sufficient energy to promote an electron across the band gap can contribute energy that may be used to drive the hydrogen production reaction. And, due to the rapid thermalisation of "hot" electrons, each photon only contributes the band gap energy to do useful work. For a standard solar spectrum the Shockley-Queisser limit calculated from these assumptions predicts that the band gap capable of extracting the maximum amount of useful work (30% efficiency) is 1.1 eV [9]. Consequently, much current research in the field focuses upon band gap minimisation without sacrificing chemical stability as a route to improving photocatalyst efficiency.

Photocatalysis is one of the most promising developing technologies for hydrogen production. Solar photocatalysis is particularly well suited to a distributed generation model or in remote applications where connection to the electricity grid is unfeasible. In contrast to steam reforming and direct electrolysis as they are commonly envisaged, it is a “carbon free” technology. In common with thermal decomposition technologies, it produces no CO_2 side product to attract potential environmental taxes and, perhaps more importantly for the proposed hydrogen fusion plant, it requires no post production cleaning processes to prevent the poisoning of fuel cell membranes.

The Tandem Cell™ developed by Hydrogen Solar ltd [10] uses a dye-sensitised solar cell to generate the biasing voltage necessary for optimised photoelectrode performance leading to increased solar energy conversion efficiency. Light absorption occurs in two steps. Firstly, UV and short wavelength visible light is absorbed by the photocatalyst layer. The longer wavelength photons at the red end of the spectrum pass through the photocatalytic cell to the underlying solar cell where they excite dye molecules to induce a voltage difference across the cell.

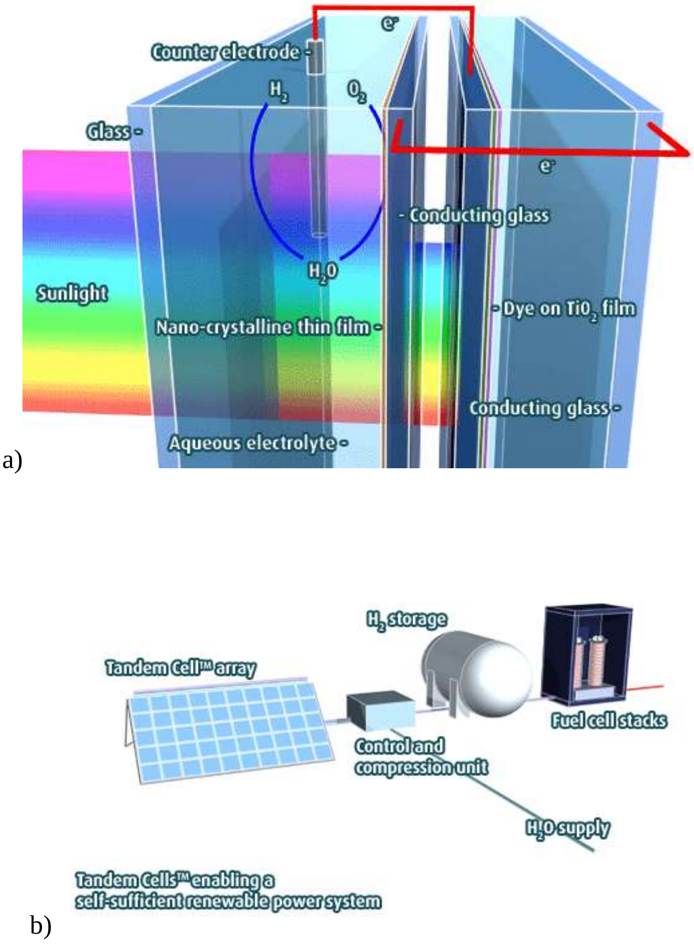

Fig. 2. Schematic representation of the Tandem Cell:
a) tandem cell;
b) self renewable hydrogen based power system [10]

Nanofine titanium dioxide is the most commonly used photocatalyst. It has a high surface area to volume ratio and exceptional chemical stability under typical reaction conditions. Unfortunately, its 3.2 eV band gap precludes the utilisation of visible light and drastically reduces the efficiency of solar energy conversion. Both anion or cation doping and alloying with other semiconductors can be used to allow some level of visible light response. Haematite (α-Fe_2O_3) has a much lower band gap at 2.1 eV but the difficulty of producing highly crystalline, stable samples which show acceptable quantum efficiencies has precluded its widespread adoption. Other more complex compound oxides such as $In_{1-x}Ni_xTaO_4$ and $In_{12}NiCr_2Ti_{10}O_{43}$ also show a promising combination of high stability and low band gap (2.3 eV and 2.14 eV respectively) [11, 12].

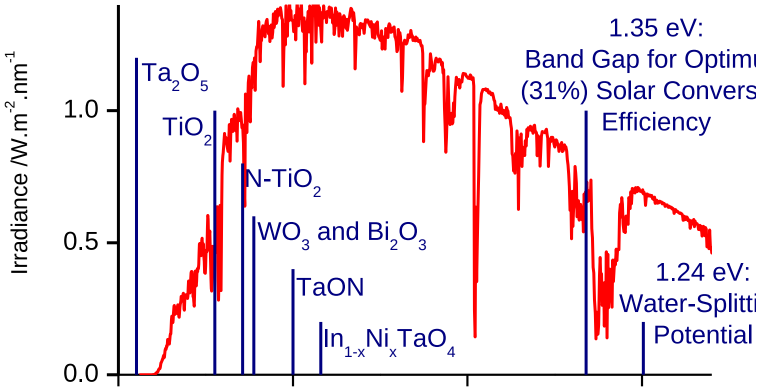

Fig. 3. Band gap of common photocatalyst compounds compared to a standard terrestrial solar spectrum [13, 14]

Tungsten oxide combines both chemical stability and good crystallinity with a band gap of 2.6 eV, significantly lower than that of TiO_2. Following the development of the effective sol-gel processing routes to nanofine WO_3 developed originally for electrochromic applications, doped WO_3 is an increasingly promising photocatalyst for the future.

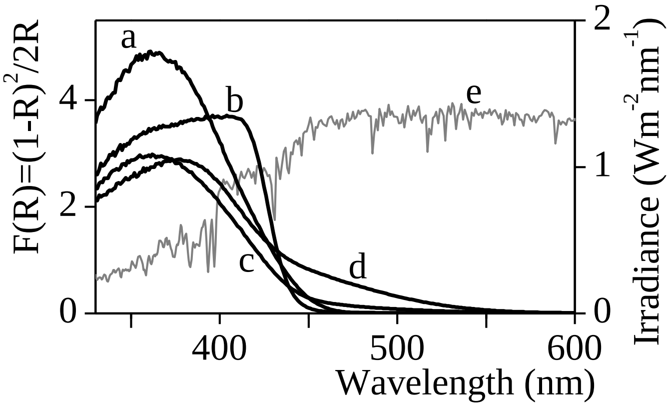

Fig. 4. UV-visible absorption spectra for a) WO_3, b) Bi_2O_3, c) Bi_2WO_6, d) Bi_6WO_{12} calculated from diffuse reflectance measurements [15] compared to e) standard terrestrial solar spectrum [13]

Photocatalysis of other chemical reactions including the production of hydrogen peroxide and the oxidations required for waste water treatment is also possible leading to a range of alternative applications in water purification, bactericidal and self-cleaning technologies.

FUSION AND THE HYDROGEN ECONOMY

General Atomics in San Diego have linked nuclear fusion to the possibility of hydrogen production for a 'hydrogen economy'. The term hydrogen economy refers to hydrogen as the dominant energy carrier in our future industrial and commercial economy. As discussed earlier several clean options are available for hydrogen production, but General Atomics has highlighted the efficiency benefits arising from the direct thermochemical production of hydrogen using high temperature catalytic reactions such as the sulfur-iodine cycle discussed in section 2. This method does not rely on wasteful intermediation using electricity for electrolysis, but does require high temperatures above 750°C. Conventional approaches to fusion dedicated to electricity production plan for fusion blanket temperatures (where steam or hot helium would be produced to drive thermal turbines) of around 500°C. If, however, the incentives were sufficient fusion designs could surely be shifted into the 750°-1000°C range.

Importantly environmental factors are not the only policy-driver for the hydrogen economy. Over the timescale of the development of fusion energy systems energy security issues are likely to motivate a shift towards both hydrogen and fusion. [16].

Hydrogen as a Cryogen for Fusion

The thermochemical fusion hydrogen generator described above would produce large amounts of hydrogen requiring safe storage ready for transport to regional and global markets. It seems likely that the energy density benefits of cryogenic hydrogen storage would outweigh the higher costs when compared to compressed gas storage. One possibility is that this existing cryogenic hydrogen reservoir might permit the operation of the superconducting magnets needed to maintain the magnetic 'Tokamak' confinement of the fusion plasma. Conventionally fusion systems are designed to use niobium titanium and niobium-tin superconducting magnet windings cooled, at great cost, with liquid helium. Our vision is for magnet windings of magnesium-diboride, MgB_2 cooled by liquid hydrogen. (Liquid hydrogen temperature is 20 K under normal pressure). Magnesium diboride has the pleasing property that despite being relatively high-temperature superconductor it is also straightforward (with the right know-how) to produce real flexible wires for magnet windings. It is expected that a full-scale fusion reactor will require fields of approximately 7 T in the heart of the plasma. It a conventional tokamak geometry this corresponds to a field of 13 T at the windings themselves. With a critical current density of 10^5-10^6 A/cm^2 in magnetic field of 20T, MgB_2 is well suited to the electromagnetic requirements of fusion containment. Current work (Purii et al) indicates that MgB_2 will actually benefit form neutron fluences (time integrated neutron doses) up to 10^{19} neutrons/cm^2. This is compatible with projected reactor lifetimes, provided some neutron shielding is employed as is currently envisaged.

Moving to hydrogen based fusion cryogenics may raise some moderate safety concerns and the need to ensure that flammable hydrogen is at all times safely isolated from any liquid oxygen or liquid air, such as might condense on exposed cold metal surfaces. But if there is to be a hydrogen economy using cryogenic systems these problems will surely already have been dealt with.

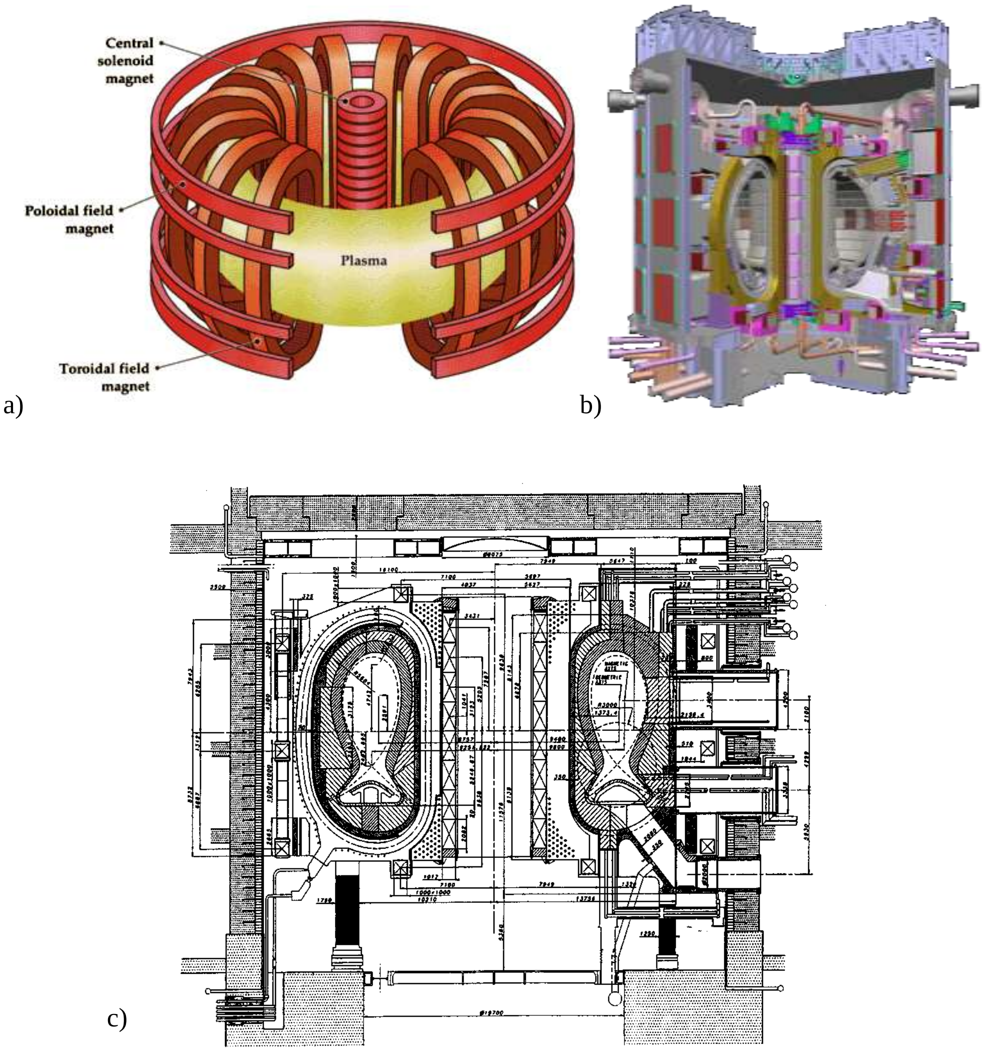

Fig. 5. a) Cross-Section of a Tokomak Reactor;
b) ITER (fusion power 500 MW, 400 s);
c) reactor (DEMO) (fusion power 2000 MW, continuous). The magnetic field generated by the superconducting coils is strongest towards the edges, causing the plasma to tend towards the outer wall. However, another magnetic field generated by a current going through the plasma itself combines with the coils' magnetic field to create magnetic lines that spiral around the torus. This spiralling counteracts the drifting effect on the plasma because of the strong inner field, and effectively traps the plasma. Images are courtesy of the Lawrence Livermore National Laboratory [17] and ITER website [18]

Table 2. Fusion Devices and Parameters (see also Fig. 5)

Parameters	ITER Fig b)	Power Reactor Fig c)
relative size	1	1…1.2
fusion power (MW)	500	2000
power to He-ions (MW)	100	400
total thermal power (MW)	500	2600
electric power (MW)		1000
efficiency (%)		38
neutron damage (dpa)	5	120 in 5y

Black-Starting the Fusion Energy System

Conventional plans for fusion energy involve electricity at two levels. First, and obviously, as the product produced for sale; second, however, one must not forget that a fusion power plant will require substantial electrical energy to fire up.

To first impression one might regard this reality as a major argument in favour of fusion's role in an integrated energy system, but upon further reflection this becomes far less clear. For instance a fusion power plant contributing 1.0 GWe to the English and Welsh electricity grid (with its overburdened interconnectors to other systems) could be providing several percentage points of total demand at a time of a very low capacity surplus in the system. If, for any reason, the fusion power station were to trip out, then the grid’s supply-demand balance could be very hard to maintain. The system operator would call upon various open cycle gas turbine systems and pumped water storage systems to cover the shortfall as the coal fired plant at the margin increased its contribution towards maximum levels. If the fusion power plant operators were to call the system operator asking for an extra 500MWe to restart their machine, it is far from clear that they would receive a positive response. Chances are that they would be asked to wait until the crisis (of their causing) had passed. We have named the integrated MgB_2 based scenario of hydrogen combined with fusion as: *Fusion Island.* The *Fusion Island* would be supported by its own dedicated large-scale hydrogen fuel cell park. The capacity of the park would be determined as part of an integrated black-start capacity for the machine involving fuel cells, energy storage flywheels (as used a present on the JET machine for roughly half its start-up power needs) and possibly supercapacitors for the peak of the big electrical push needed for start-up. In normal operations the *Fusion Island* has a range of on-site temperatures spanning from 20K to more than 1000K. As hydrogen fuel cells require elevated temperatures in order to operate, it is conceivable that there might be benefit in integrating the fuel cell system into the fusion heat extraction system or even the fusion blanket itself. Even if the system were truly cold and dark, the plant could combust stored hydrogen to warm the hydrogen fuel cells sufficient for their operation.

The Fusion Island and Big Business

After much negotiation an international consortium of governmental research organisations recently announced plans to build an experimental fusion reactor to be known as 'ITER' at Cadarache in Southern France. Previously one of us has argued that this experimental system should be the last large-scale tokamak fusion machine to be built with public money [19]. It seems unlikely however that a risk averse liberalised and competitive electricity industry will be keen to invest the large sums necessary to construct prototype and early commercial fusion power plants for electricity. Their nervousness would also include a fear that early fusion power plants might suffer from poor operational reliability and suffer from intermittency. As electricity is not an economically storable commodity and supply contracts involve stiff penalties for failure to generate, any such reliability failings could be very expensive indeed. If as we have argued here, however, the early fusion energy systems are dedicated to thermochemical hydrogen production serving the needs of the transport sector then intermittency is not a major concern as hydrogen storage is an integral part of the system and supply-chain. Furthermore hydrogen as an energy carrier has the possibility of becoming the dominant fluid energy product sold by the oil majors once oil becomes depleted or environmentally unacceptable later this century.

Three independent timescales are likely to coincide, much to the possible benefit of the *Fusion Island* concept:

- First, as we have already mentioned, over the coming decades oil resources and reserves will diminish and probably be sourced from fewer regions at ever increasing prices
- Second, and at a similar pace, climate change caused by fossil fuel emissions will increase and as environmental harm increases, pressure will increase to replace oil and natural gas with a clean alternative. Demand for hydrogen will grow.
- Third fusion energy systems will become ready for commercial deployment over the same period.

Such considerations lead one naturally to consider that the source of private capital for the development of *Fusion Island* systems should come from the oil majors. These companies must transition from being oil companies to become energy companies. Thermochemical hydrogen production from fusion requires many of the skills and competencies already possessed by the oil majors. Importantly these companies retain an adventurous culture of 'exploration' and risk taking well suited to developing a difficult high-stakes technology such as fusion.

CRYOPLANE

Air traffic is growing by ~5% every year – and there has never been a better time for a clean aircraft. If it gets off the ground, the Cryoplane will run on liquid hydrogen, leaving a vapour trail of pure water. The actual clean efficiency will be achieved by flying at altitudes of less than 10 km. Hydrogen is more power-packed than conventional aviation fuel, but on board, it must be stored at 20 K.

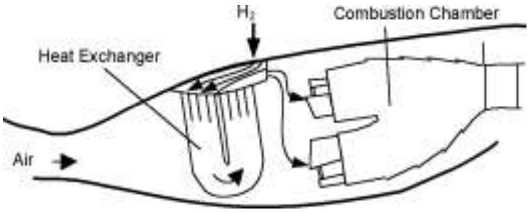

Fig. 6. The hydrogen engine. The heat exchange converts the liquid hydrogen to a gas before injection into the combustion chamber [20]

An optimised combustion chamber designed for hydrogen will have favourable properties in comparison to conventional engines. Because hydrogen will be used as evaporated gas, it mixes well with air during combustion (no ’hot spots’); combustion is possible with a large air surplus (low temperatures) and very high rate of combustion (short dwell times); the combustion chamber can be shortened considerably.

A separate issue is a noise pollution created by the aircraft during take off and landing. In a radical departure from current configurations, it has been decided between engine manufacturer Rolls-Royce and the Cambridge-MIT Institute that in their design for a silent aircraft, the engines will not hang below the wings [21]. Instead the project team has decided that the engines will be embedded into the body of the aircraft itself to help minimise the engine noise transmitted to the ground. By managing airflow over the wing and into the engine a much more efficient and quieter propulsion system will be produced. Such an integration would also be advantageous for the Cryoplane and its hydrogen delivery system. It was found that during take-off the total exhaust area must be about three times as large as that of today's conventional jet engines. During landing the engines of the airplane will throttled back to reduce speed of the aircraft delaying the use of airframe.

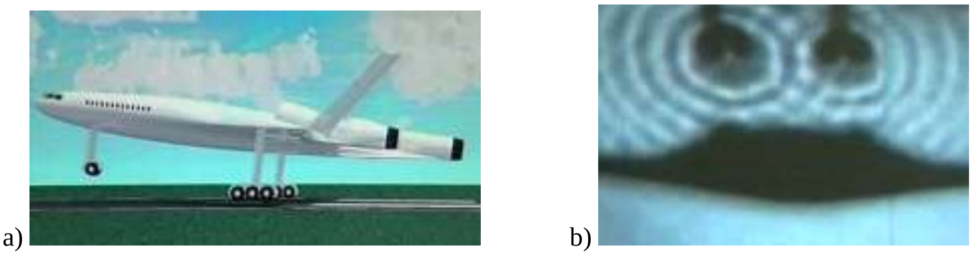
a) b)

Fig. 7. a) Artist impression of the 'silent plane during landing;
b) Simulation of the reduction of sound propagation from the engines mounted on the top of the plane. Pictures courtesy of the BBC: East Anglia News

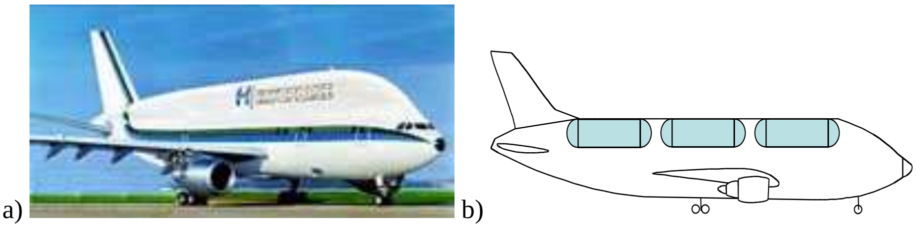
a) b)

Fig. 8. Cryoplane:
a) an artist impression of the Cryoplane;
b) schematic of the location of the H_2 cryotanks in the aicraft [20]

Table 3. Relative influence of gaseous combustion products on the greenhouse effect. (Normal cruising altitude for commercial jet traffic)

Altitude	kerosene	hydrogen
15km	175%	275%
12km	107%	84%
10km	88%	6%
5km	100%	1%

Burning 1kg of kerosene produces 3.16kg of CO_2 and 1.25kg H_2O. Since 0.36kg of hydrogen has the same energy content as 1kg of kerosene, the combustion of 0.36kg of kerosene will form 3.21kg of H_2O.

Carbon dioxide is a very long-lived greenhouse gas (residence time ~100 years). Its effect is independent of altitude. Water vapour is also a green-house gas. Its effect increases rapidly with altitude; the residence time also varies greatly with altitude (several days above ground; six months in the lower stratosphere).

At altitudes below 10km, the gaseous products of hydrogen combustion produce a much weaker long-term effect than those of kerosene, see table 3.

It can be expected that restrictions of the fossil fuel consumption will force rapid development of such cryoplanes including safety and crash tests. It has to be emphasised that liquid hydrogen offers the advantage of a high vaporization rate compared with liquid natural gas and kerosene. Hydrogen has a low flash point, and the detonation limit is reached only at much richer mixtures. In the case of a crash fire, no fire carpet will develop; the hydrogen will burn in an upward direction. The burn will progress very rapidly with very little radiation of heat. Thus, the aluminium airframe will not burn, but rather protect the passengers and help ensure their survival.

The new basic technologies for the production, liquefaction, storage and distribution of hydrogen have to be further developed and production of LH_2 would have to increase from less than currently 20 tons per day to 6000 tons. If the hydrogen were to be generated by electrolysis, it would require the electrical energy output of ten large power plants.

Consider the 20 K cryogen, and the current trend to move away from high frequency electric systems (400Hz) on the board of the aircraft and replace them with DC devices. These will naturally encourage a number of superconducting applications such as: DC conductors, ultra fast super computers, superconducting DC fault current limiters, also superconducting microwave communication and many other undeveloped superconducting applications. It is also possible that new designs of the superconducting bearings can be adopted in the combustion engines since heat exchangers converting liquid hydrogen to gas in the hydrogen engines will be required.

ACKNOWLEDGEMENTS

The authors would like to thank staff at the UKAEA Culham Science Centre for their advice towards the preparation of this document.

LITERATURE

[1] B. A. Glowacki, M. Majoros, M. Vickers, J. E. Evetts, Y. Shi and I. McDougall *Superconductor Science and Technology,* 14(2001)193

[2] Applied Superconductivity and Cryoscience Group, Cambridge University: http://www.msm.cam.ac.uk/ascg

[3] B. A. Glowacki 'Development of Nb-based Conductors' in: *Frontiers in Superconducting Materials*, ed. A. Narlikar, Springer Verlag (2005) 697

[4] Lutz A. E. et al., Thermodynamic anlaysis of hydrogen production by partial oxidation reforming. *International Journal of Hydrogen Energy*, 2004 (29) 809-816

[5] Gaudernack B. and Lynum S., Hydrogen from natural gas without release of CO_2 to the atmosphere. *International Journal of Hydrogen Energy* 1998 (23) *12* 1087-1093

[6] Winter C.-J., The hydrogen energy economy: an address to the World Economic Forum 2004, *International Journal of Hydrogen Energy*, 2004 (29) 1095-1097

[7] Raissi A. T., Analysis of solar thermochemical water-splitting cycles for hydrogen production. *FY Progress Report for Hydrogen, Fuel Cells and Infrastructure Technologies Program*. 2003

[8] Kaiser J., *Power From Pond Scum*. Science. 2000 (287) *5458* 1580-1583
[9] Shockley W. and Quiesser H. J., Detailed balance limit of efficiency of p-n junction solar cells. *Journal of Applied Physics*. 1961 32 (3) 510
[10] http://www.hydrogensolar.com
[11] Zou Z. et al., Direct splitting of water under light irradiation with an oxide semiconductor photocatalyst. *Nature*. 2001 (414) 625-627
[12] Wang D. et al., Photocatalytic H2 evolution over a new visibe-light-driven photocatalyst $In_{12}NiCr_2Ti_{10}O_{42}$. *Chemical Physics Letters*. 2005 (411) 285-290
[13] *ASTM G 170-03*, ASTM International. 2003
[14] Finlayson A. P. et al., Evaluation of Bi- W- Oxides for Visible Light Photocatalysis, *Physica Status Solidi A*, submitted for publication
[15] Finlayson A. P. et al., Optimisation of Narrow Band Gap Semiconductors for Photocatalytic Applications, *16th Workshop on Quantum Solar Energy Conversion*. 2005
[16] W. J. Nuttall *'Nuclear Renaissance - Technologies and Policies for the Future of Nuclear Power'*, IoP Publishing Bristol 2004 ISBN: 0750309369
[17] Lawrence Livermore National Laboratory: http://www.llnl.gov
[18] ITER: http://www.iter.org
[19] Nuttall W. J., Fusion should put its energy into oil. *The Engineer*. 28 May 2004, p. 18
[20] Russian-German Cooperative Venture Study Report, *Cryoplane* 1992
[21] Rolls-Royce and the Cambridge-MIT Institute: *The Silent Aircraft Initiative*. http://www.cambridge-mit.org

HYDROGEN AND SYNGAS PRODUCTION FROM METHANE BY MICROWAVE TORCH PLASMA

M. Dors, J. Mizeraczyk, M. Jasiński, Z. Zakrzewski

Centre for Plasma and Laser Engineering
The Szewalski Institute of Fluid Flow Machinery, Polish Academy of Sciences
Fiszera 14, 80-231 Gdańsk, Poland, e-mail: mdors@imp.gda.pl

Abstract

In this paper results of methane reforming using microwave torch plasma (MTP) at atmospheric pressure are presented. Methane (1-2%) together with argon (97-96%) and water vapor (2%) was introduced into the plasma. Microwave power delivered to the plasma was 200-750W. The largest concentrations of hydrogen and carbon monoxide in the outlet gas were 0.7% and 0.5%, respectively. The ratio of $CH_4:H_2O$ *influences the methane decomposition products. Increase in the* $CH_4:H_2O$ *ratio from 1:2 up to 1:1 decreases production of* H_2 *and increases* C_2H_2 *production. Higher ratio results in production of soot which is an undesirable by-product. Shorter residence time of the* $CH_4:Ar:H_2O$ *mixture in the plasma favors formation of acetylene. Increase in the residence time suppresses acetylene production and increases production of hydrogen.*

Keywords: Hydrogen, Microwaves, Plasma, Syngas

INTRODUCTION

Methane or natural gas reforming is widely used in industry to obtain hydrogen or synthesis gas (H_2+CO), which are utilized in industry, for example as source materials for the production of raw chemicals like methanol and ammonia, as hydrogenation agents in oil refinery or reducing gases in steel industry. Recently hydrogen gains in importance as fuel in fuel cell applications, combustion engines or gas turbines with the goal to achieve a more efficient exploitation of energy sources and to reduce noxious emissions.

Usual reforming of methane is carried out thermally with steam and oxygen. Since the reforming reaction with steam is endothermic, partial oxidation of methane takes place to provide reaction heat. The main reaction in steam reforming of methane is methane oxidation, yielding a mixture of hydrogen and carbon monoxide:

$$CH_4 + H_2O \leftrightarrow 3\,H_2 + CO. \qquad (1)$$

Noble metal catalysts are usually required to enhance the reaction rate. Hence, the reforming system is sensible to source impurities, which deactivate the catalysts.

An attracting method of reforming methane, or more generally, hydrocarbons is the use of plasma [1-16]. Plasma contains reactive radicals, ions and electrons. High reactivity shown by these species enhances the reaction rate and eliminates catalysts. These advantages as well as the plasma high energy density ensure the compactness of the plasma reformer. Moreover, the plasma system is versatile and can operate with various hydrocarbons including natural gas, gasoline, heavy oils and biofuels. Fast response time can be also achieved because the plasma is operated by electricity. When steam is added to the plasma supporting gas (a carrier gas), radicals such as H, OH, and O give both reductive and oxidative circumstances, and the plasma treatment becomes effective for various compounds.

Microwave discharge at atmospheric pressure is one of the techniques to obtain plasma in which the electron temperature is 4000 - 6000 K, while the heavy particle temperature is about 2000K [17]. Application of such plasma to hydrogen production by hexane reforming was studied by Sekiguchi et al. [6, 7].

In this paper results of methane reforming by microwave torch plasma (MTP) at atmospheric pressure are presented.

EXPERIMENTAL SET-UP

The main components of the experimental setup were a 2.45 GHz magnetron generator (operated in a continuous mode), waveguide-based MTP generator, plasma reactor with a heat exchanger, microwave power supplying and measuring systems, gas supplying and flow control systems, Fourier Transform Infrared (FTIR) spectrophotometer for gas analysis and GasHunter detector for hydrogen concentration measurement. The MTP generator is based on a TIAGO (Torche a Injection Axiale sur Guide d'Ondes) concept disclosed by Moisan et al. [17]. The essential design features of the MTP generator and reactor are shown in Fig. 1. The MTP reactor was a stainless-steel cylinder with a rectangular glass window in the sidewall. The height and the inner diameter of the reactor were 265 mm and 180 mm, respectively. A microwave torch nozzle was mounted vertically in the bottom of the reactor, with its outlet directed upward (the protruded from the waveguide directly into the reactor). A heat exchanger, cooling the gas mixture before leaving the reactor, was fixed 220 mm above the nozzle. The microwave power (200-750 W) was fed to the torch structure directly from a standard waveguide at its one end while its opposite end was terminated with a movable plunger. The plasma was generated in the form of a "plasma flame" at the end of the nozzle, and it.

The working gas [Ar(97-96%)+CH_4(1-2%)+H_2O(2%)] at atmospheric pressure flowed through the torch structure at a flow rate of 2-4 l/min and 25 l/min and exited through the nozzle at its conical tip forming the plasma flame. Composition of the gas before and after the plasma processing was analyzed using the FTIR spectrophotometer operating in the range of 4000-1000 cm^{-1}. Concentration of hydrogen in the gas exiting the MTP reactor was measured with the GasHunter detector.

RESULTS AND DISCUSSION

The analysis of gas composition after the MTP processing showed that methane is converted into hydrogen H_2, carbon monoxide CO, CO_2, H_2O and acetylene C_2H_2.

Concentrations of these products and conversion rate of CH_4 depend on microwave power, gas flow rate and initial concentration of CH_4.

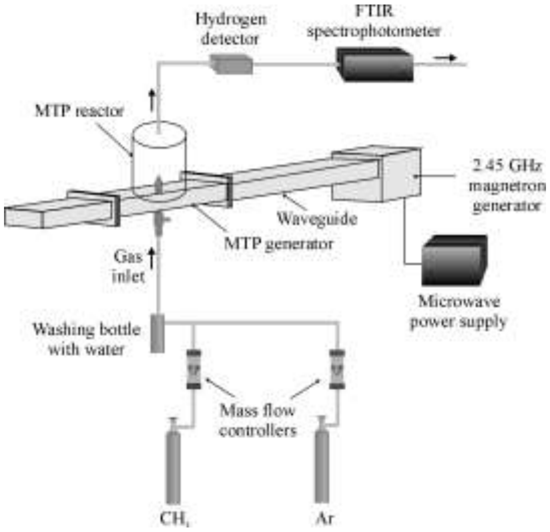

Fig. 1. Experimental set-up

Results of MTP processing of a gas mixture containing 1% of CH_4 (CH_4:H_2O = 1:2) are presented in Figs. 2 and 3.

Fig. 2a shows that CH_4 concentration decreases with increasing microwave power and decreasing gas flow rate (increasing residence time). At a high flow rate of 25 l/min, CH_4 conversion rate is low. CH_4 concentration decreases from 1% to 0.74% at 450 W and does not decrease with further power increase. Decrease in the gas flow rate results in longer residence time in the MTP and consequently CH_4 concentration decrease to 0.015% at 400 W at flow rate of 2 l/min.

Production of H_2 and CO corresponds to the CH_4 decomposition and increases with increasing microwave power and residence time in the MTP (Figs. 2b and 3a). The highest H_2 and CO concentrations of 1.8 % and 0.52%, respectively, were measured at 2 l/min and 400 W. At a high flow rate of 25 l/min, the highest H_2 and CO concentrations of 0.4% and 0.17%, respectively, were obtained at 450 W and they did not change with further power increase.

According to the reaction (1), the amount of CH_4 decomposed in the MTP should be equal to the concentration of CO and to one third of the H_2 concentration. However, our results show that concentrations of CO and H_2 are lower. One of the reason is production of acetylene C_2H_2 in the reaction:

$$2\ CH_4 \rightarrow C_2H_2 + 3\ H_2. \qquad (2)$$

In such a case CO concentration should correspond to the two third of decomposed CH_4. Indeed, concentration of CO obtained at the gas flow rate of 25 l/min proves this hypothesis. At a low gas flow rate, i.e. 2-4 l/min, concentrations of H_2 and CO are much lower than expected. Since no soot or other hydrocarbons were found after MTP processing, we assume that low concentrations of H_2 and CO result from their oxidation to

CO_2 and H_2O. Unfortunately, quantitative determination of CO_2 and H_2O could not be carried out in this experiment.

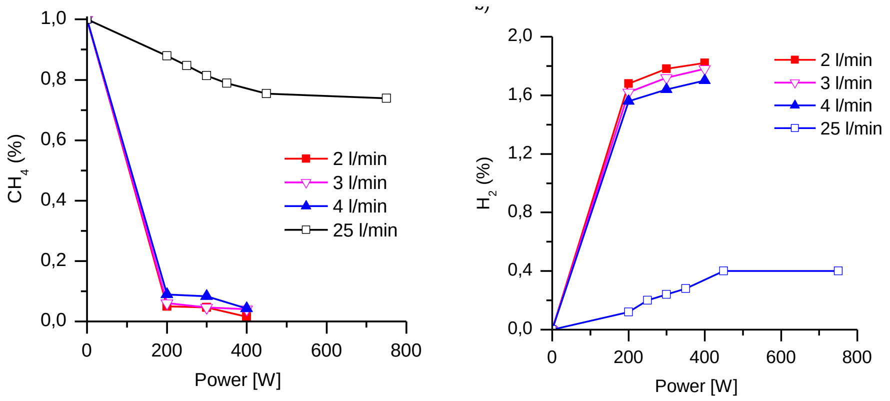

Fig. 2. Concentrations of methane (a) and hydrogen (b) in the outlet gas as a function of microwave power at gas flow rate 2-25 l/min. Initial methane concentration 1 %. Initial CH_4:H_2O ratio 1:2

Concentration of acetylene, produced during CH_4 decomposition, is presented in the Fig. 3b. At gas flow rates of 2 l/min and 3 l/min no C_2H_2 was found regardless of the microwave power delivered to the MTP. Detectable production of acetylene starts from 4 l/min and 300 W and increases with gas flow rate and microwave power. The highest C_2H_2 concentration of 0.038% was measured at a gas flow rate of 25 l/min and 450 W of microwave power and corresponds to the one third of CH_4, according to the reaction (2).

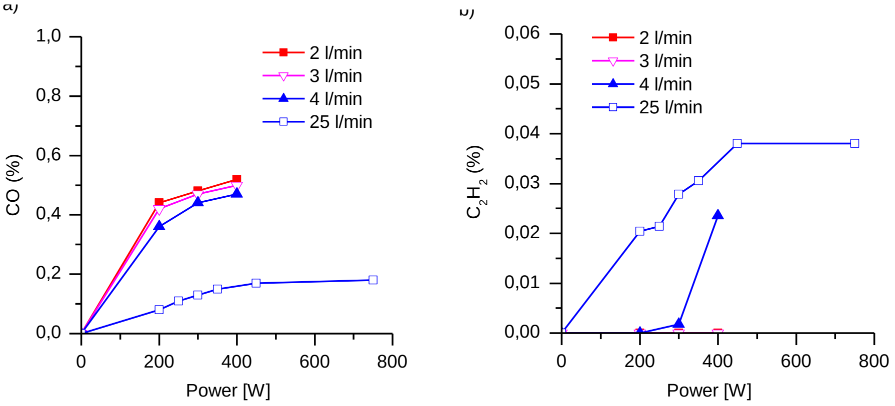

Fig. 3. Concentrations of carbon monoxide (a) and acetylene (b) in the outlet gas as a function of microwave power at gas flow rate 2-25 l/min. Initial methane concentration 1 %. Initial CH_4:H_2O ratio 1:2

When a gas mixture containing 2% of CH_4 (CH_4:H_2O = 1:1) was processed with the MTP, concentration of CH_4 in the outlet gas was 0.16% at 4 l/min and 200 W and decreased with increasing residence time and microwave power to 0.09% at 2 l/min and 400 W (Fig. 4a). This means that in this case the amount of CH_4 decomposed in the MTP was higher than in the mixture with 1% of CH_4. However, as it seen in Figs. 4b and 5a, the higher concentration is not accompanied with higher H_2 and CO production. The concentration of H_2 are even lower while CO is similar to that obtained at 1% of initial CH_4 concentration. Both concentrations increase with increasing microwave power and residence time from 0.36% and 0.41%, respectively, at 4 l/min and 200 W up to 1.48% and 0.66%, respectively, at 2 l/min and 400 W.

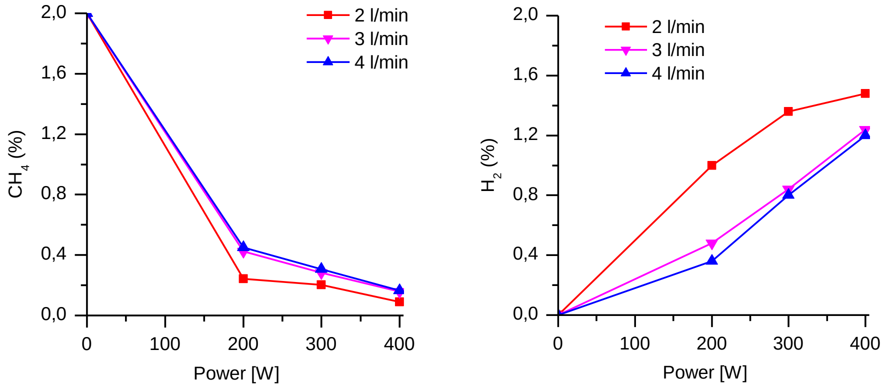

Fig. 4. Concentrations of methane (a) and hydrogen (b) in the outlet gas as a function of microwave power at gas flow rate 2-4 l/min. Initial methane concentration 1 %. Initial CH_4:H_2O ratio 1:1

The same concentrations of CO in two mixtures containing different CH_4 amount may be attributed to the same initial concentration of H_2O, which is the only source of oxygen in the reaction environment. As a result, increasing CH_4 initial concentration at constant H_2O concentration does not increase CO production. The observed lower H_2 concentration at higher CH_4 initial concentration is caused by higher production of C_2H_2. As it is seen in Fig. 5b, concentration of acetylene increases with increasing gas flow rate and microwave power from 0.02% at 2 l/min and 200 W up to 0.22% at 4 l/min and 400 W. These concentrations are over 10 times higher than those obtained with the gas mixture containing 1% of CH_4.

The results showed that at the ratio of CH_4:H_2O = 1:1 a small amount of soot, depositing on the reactor walls, was produced. It was noticeable only after several hours of processing. An attempt to increase CH_4:H_2O ratio resulted in much higher production of soot, so that the analysis of the effluent gas could not be carried out.

Energy efficiency of the hydrogen production during methane reforming in the MTP is presented in Fig. 6. In the gas mixture containing 1% CH4 (Fig. 6a) the energy efficiency decreases when microwave power and residence time increase. The highest production of H_2 of 1.56 g per 1 kWh was obtained at 4 l/min and 200 W. However, at a gas flow rate of 25 l/min the energy efficiency increases with microwave power reaching maximum value of 1.1 gH_2/kWh at 450 W. In the gas mixture with 2% CH_4 (Fig. 6b) the energy efficiency of hydrogen production is lower than that obtained in the mixture containing 1% of CH_4. This is due to the lower production of H_2.

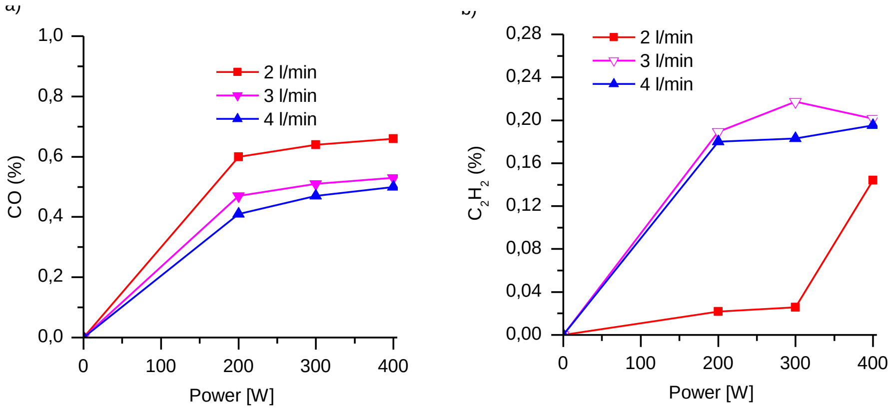

Fig. 5. Concentrations of carbon monoxide (a) and acetylene (b) in the outlet gas as a function of microwave power at gas flow rate 2-4 l/min. Initial methane concentration 2 %. Initial CH_4:H_2O ratio 1:1

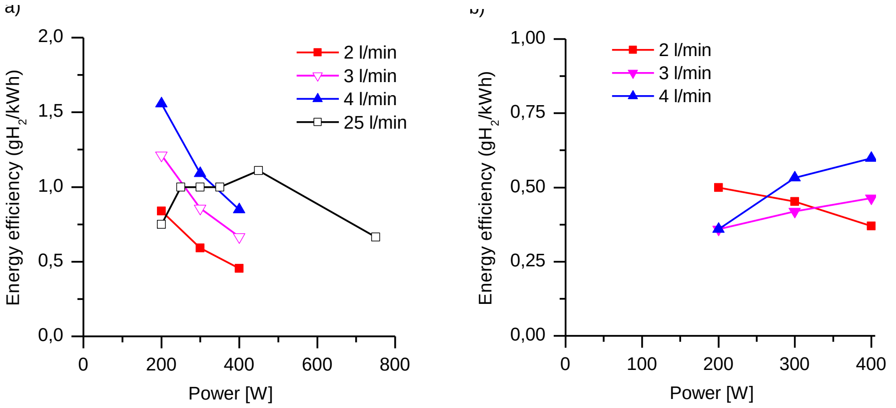

Fig. 6. Energy efficiency of hydrogen production during methane reforming in the gas mixture containing 1% CH_4 (a) and 2% CH_4 (b)

Tab. 1. Energy efficiency of hydrogen production using plasma methods

Plasma method	Initial gas composition	Energy efficiency [gH2/kWh]	Ref.
Plasmatron with a catalyst	CH4 + H2O + air	225	[1]
Gliding arc	petrol + air	545	[5]
Gliding arc	CH4 + H2O + air	40	[3]
MTP	hexane + H2O + air	23	[6]
Dielectric barrier discharge	CH4 + air	6.7	[11-13]
Electron beam	CH4 + H2O	3.6	[16]

All values of the energy efficiency obtained in this experiment are in the range of 0,36-0,59 gH_2/kWh. It means that energy efficiency of hydrogen production using MTP is much lower than that obtained in other plasma systems (Tab. 1). However, our experiment was carried out when the temperature of the influent gas mixture was only 25°C and, therefore, the water vapour concentration could not exceed 2%. Thus, we expect much higher hydrogen production and energy efficiency at higher water vapour concnetration and corresponding higher methane concentration.

CONCLUSIONS

The results of methane reforming in its mixture with water vapour and argon by MTP showed that:

- Decomposition of CH_4 and concentrations of all by-products increase up to 450 W and they do not change with further microwave power increase, when the CH_4 concentration was 1% or 2%, CH_4:H_2O ratio was 1:2 or 1:1 and gas flow rate up to 25 l/min.
- The ratio of CH_4:H_2O influences the methane decomposition products. Increase in the ratio from 1:2 up to 1:1 decreases production of H_2 and increases C_2H_2 production. Higher CH_4:H_2O ratio results in production of soot, which is an undesirable by-product.
- The composition of the post-processed gas depends also on the residence time of the working gas in the MTP reactor. Shorter residence time favours formation of acetylene. Increase of the residence time suppresses acetylene production and increases production of hydrogen.

The results presented in this work were obtained when the effluent gas mixture had room temperature. In contrast, however, most methane reforming systems using water vapour for production of synthesis gas, work with an effluent gas mixture having temperature at least 100°C. Thus, our next step in the studies of MTP application for methane reforming is to carry out experiment with much higher amount of water vapour, which would allow to increase methane concentration and improve the energy efficiency of hydrogen production.

ACKNOWLEDGEMENT

This work was supported by the State Committee for Scientific Research (KBN) under programme PB 1124/T09/2003/24 and by the Institute of Fluid Flow Machinery, Polish Academy of Sciences under programme IMP PAN O3Z3T2 and O3Z1T1.

REFERENCES

[1] L. Bromberg, D. R. Cohn, A. Rabinovich, N. Alexeev, A. Samokhin, R. Ramprasad, S. Tamhankar, System Optimization and Cost Analysis of Plasma Catalytic Reforming of Natural Gas, *Int. J. Hydrogen Energy*, 25, 1157-1161, 2000

[2] L. Bromberg, D. R. Cohn, A. Rabinovich, N. Alexeev, Plasma Catalytic Reforming of Methane, *Int. J. Hydrogen Energy*, 24, 1131-1137, 1999

[3] J. M. Cormie, I. Rusu, Syngas Production via Methane Steam Reforming with Oxygen: Plasma Reactors versus Chemical Reactors, *J. Phys. D: Appl. Phys*., 34, 2798–2803, 2001

[4] N. Reveau, M. Nikravech, O. Martinie, P. Lefaucheux, J. M. Cormier, Proc. HAKONE VII, Greifswald, Germany, 2000, pp. 252–256

[5] A. Czernichowski, M. Czernichowski, P. Czernichowski, GlidArc-assisted Reforming of Carbonaceous Feedstocks into Synthesis Gas. Detailed Study on Propane, Proc. 16th Int. Symp. on Plasma Chemistry, Taormina, Italy, 2003, p. 578

[6] H. Sekiguchi, Y. Mori, Steam plasma reforming using microwave discharge, *Thin Solid Films*, 435, 44-48, 2003

[7] H. Sekiguchi, S. Nakanishi, K. Fukuda, H. Inagaki, Hydrogen Production from Hydrocarbon Using Atmospheric Pure Steam Plasma Generated by Microwave Discharge, Proc. 16th Int. Symp. on Plasma Chemistry, Taormina, Italy, 2003, p. 598

[8] T. Kappes, W. Schiene, T. Hammer, Energy Balance of a Dielectric Barrier Discharge Reactor for Hydrocarbon Steam Reforming, Proc. 8th Int. Symp. on High Pressure Low Temperature Plasma Chemistry, Puhajarve, Estonia, 2002, pp. 196-200

[9] H. Kabashima, H. Einaga, S. Futamura, Hydrogen Generation From Water, Methane, and Methanol With Nonthermal Plasma, *IEEE Trans. Ind. Appl.*, 39, 2 ,340-345, 2003

[10] S. Futamura, H. Kabashima, L. Ma, Potential of Nonthermal Plasma in Fuel Reforming, Proc. 4th Int. Symp. on Non-thermal Plasma Technology for Pollution Control and Sustainable Energy Development, Panama City Beach, Florida, USA, 2004, pp. 211-215

[11] B. Pietruszka, K. Anklam, M. Heintze, Plasma-Assisted Partial Oxidation of Methane to Synthesis Gas in a Dielectric Barrier Discharge, *Appl. Catal. A: General*, 261, 19–24, 2004

[12] M. Heintze, B. Pietruszka, Plasma Catalytic Conversion of Methane Into Syngas: The Combined Effect of Discharge Activation and Catalysis, *Catal. Today*, 89, 21-25, 2004

[13] B. Pietruszka, K. Anklam, M. Heintze, Application of a DBD Reactor for the Partial Oxidation of Methane to Synthesis Gas in the Presence of a Nickel Catalyst, 16th Int. Symp. on Plasma Chemistry, Taormina, Italy, 2003, p. 582

[14] O. Mutaf-Yardimci, A. V. Saveliev, A. A. Fridman, L. A. Kennedy, Employing Plasma as Cagtalyst in Hydrogen Production, *Int. J. Hydrogen Energy*, 23, 12, 1109-1111, 1998

[15] J. S. Chang, Y. Uchida, M. Ara, J. T. Kim, K. Urashima, J. F. Kelly, M. Stanciulescu, R. Burisch, J. P. Charland, Soot Generation Free Non-thermal Plasma Reforming of Hydrocarbon Gas by Flow Stabilized Corona Discharges, Proc. 4th Int. Symp. on Non-thermal Plasma Technology for Pollution Control and Sustainable Energy Development, Panama City Beach, Florida, USA, 2004, pp. 216-220

[16] T. Kappes, T. Hammer, Methane Reforming using Non-thermal Plasma, Proc. 4th Int. Symp. on Non-thermal Plasma Technology for Pollution Control and Sustainable Energy Development, Panama City Beach, Florida, USA, 2004, pp. 206-210

[17] M. Moisan, Z. Zakrzewski, J. C. Rostaing, Waveguide-based single and multiple nozzle plasma torches: the TIAGO concept, *Plasma Sources Sci. Technol.*, 10, 387-394, 2001

5th International Conference **ELMECO**
Nałęczów, Poland
September 2005

A STUDY ON A DIODE-BRIDGE TYPE DIFFERENTIAL CAPACITANCE DETECTION CIRCUIT

Takahiro MATSUO*, Ken KUNITOMO** and Toshitsugu UEDA*

**Graduate School of Information, Production and Systems, Waseda University*
Address: 2-7 Hibikino, Wakamatsu-ku, Kitakyushu-shi, Fukuoka 808-0135 JAPAN
***Sakamoto Electric MFG. CO., LTD.*
Address: 3-27-55 Wajiro, Higashi-ku, Fukuoka-shi, Fukuoka 811-0202 JAPAN
E-mail: t.matsuo@ruri.waseda.jp, kunitomo@sem-sakamoto.co.jp, t-ueda@waseda.jp

Abstract

Differential capacitance sensor with movable electrodes is usually applied for accelerometers, pressure gauges, etc. because of its high sensitivity and resolution. Two axis inclination sensor with differential capacitance structure using MEMS (Micro Electro Mechanical Systems) technology was designed for industrial and environmental fields recently. The initial capacitance of the sensor should be very low as few pF, therefore, a C-V converter circuit, which is able to detect very small capacitance variations is required. In this study, the particular principle of a "diode-bridge type differential capacitance detection circuit" is analyzed. After the mathematical simulations performed using PSpice simulator, the detection of the capacitance variations in fF order resolution is considered.

Keywords: Two Axis Inclination Sensor, MEMS, Differential Capacitance, A Diode-bridge Type C-V Converter

INTRODUCTION

There are many applications of MEMS as sensor devices in various fields because of their small size, high reliability and low cost by mass production. One of MEMS, e. g. differential capacitance structure with movable electrode has a high common mode signal rejection ability and it is used for detecting variation of acceleration as a capacitance change. Generally, the initial capacitance of the differential capacitor is few pF thus the variation is very small because of micro size of unit. In order to measure such a little capacitance variation, some C-V converters were studied and announced [1], [2].

A inclination sensor using quartz micromechanical device is presently under the development [3]. The sensor detects variation of acceleration due to the gravity by inclination of the device. The unit was designed in such a way, that it had about 3 pF of initial capacitance and a movable electrode moving about 1 % of displacement ratio at 1 degree of inclination of the device. The purpose of this study is development of a circuit, which detects capacitance change at as high resolution as 1/10000 degree.

DIFFERENTIAL CAPACITANCE STRUCTURE

The basic structure of differential capacitors is shown in figure 1. A movable electrode is placed between two fixed electrodes and they compose differential capacitances C_+ and C_- as follows:

$$C_+ = \varepsilon \frac{S}{d - x} = C_0 \frac{1}{1 - x/d} \qquad (1)$$

$$C_- = \varepsilon \frac{S}{d + x} = C_0 \frac{1}{1 + x/d} \qquad (2)$$

where ε is dielectric constant between electrodes, S is area of the electrode, d is the initial gap length, x is displacement from the initial position of the movable electrode and C_0 is the initial capacitance when x = 0.

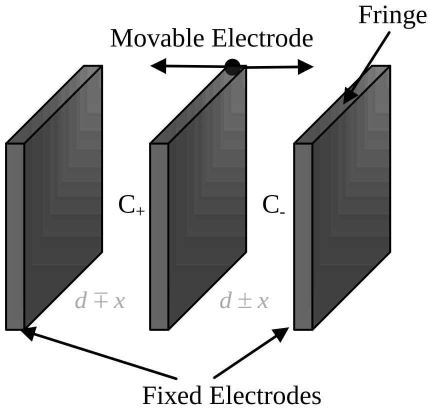

Fig. 1. The basic structure of differential capacitors

It is possible to remove common mode signal when the ratio of the sum $C_+ + C_-$ to difference $C_+ - C_-$ is taken. The ratio is as follows:

$$\frac{C_+ - C_-}{C_+ + C_-} = \frac{x}{d} \qquad (3)$$

Using a circuit, which detects the ratio, enables the measurement of the displacement ratio x/d without dependence on dielectric constant.

DIODE-BRIDGE TYPE DIFFERENTIAL CAPACITANCE C-V CONVERTER

Figure 2 shows a diode-bridge type differential capacitance detection circuit. This kind of circuit was known before, however, the particular principle of detection the ratio was not studied well. C_1 and C_2 are capacitors, which have sufficiently higher capacitance than the differential capacitors C_+ and C_-, R_1 and R_2 are bias resistances for operational amplifier in a differential amplification circuit. C_1R_1 and C_2R_2 are also high-pass filters to cut DC voltage of an unstable input signal.

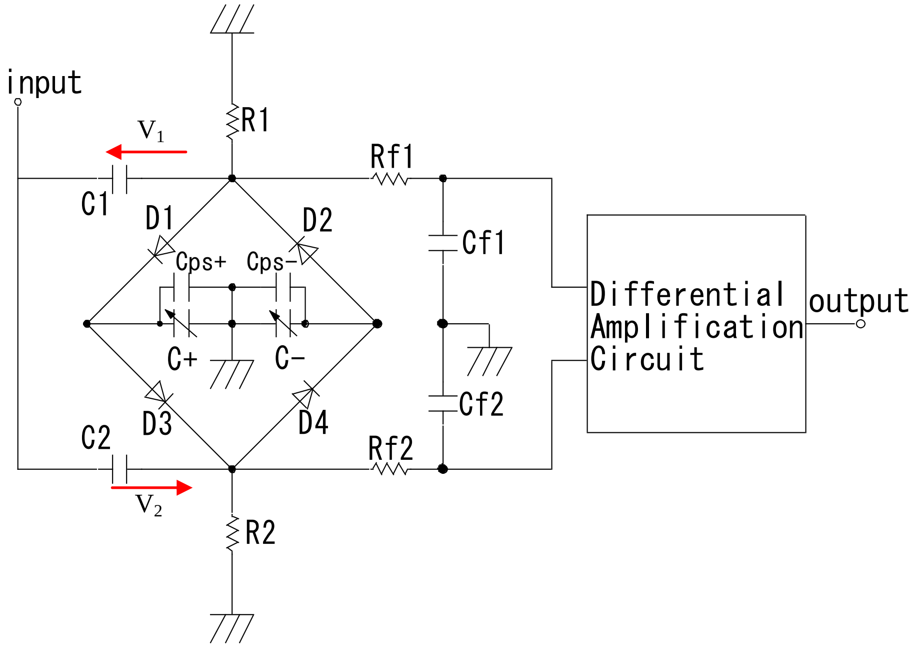

Fig. 2. A diode-bridge type differential detection circuit

When input signal V_{in} are supplied as $V_{in} = V_m \sin(\omega t)$ and there is displacement value x of movable electrode, amount of charge and discharge Q_{C+} and Q_{C-} of C_+ and C_- in every cycle are as follows:

$$Q_{C+} = \left(\frac{C_0}{1 - x/d} + C_{ps+} \right) \left(2V_m - V_1 - V_2 - V_{f1} - V_{f3} \right) \tag{4}$$

$$Q_{C-} = \left(\frac{C_0}{1 + x/d} + C_{ps-} \right) \left(2V_m + V_1 + V_2 - V_{f2} - V_{f4} \right) \tag{5}$$

where C_{ps+} and C_{ps-} are stray capacitances including fringe ones, which should be placed parallel to C_+ and C_-, V_{f1}, V_{f2}, V_{f3} and V_{f4} are forward voltages of diodes D_1, D_2, D_3 and D_4 respectively. The charge difference “Q_{C+} - Q_{C-}” is charged cycle by cycle at C_1 and C_2. Therefore DC voltages V_1 and V_2 appear as shown in figure 2. The convergence conditions of V_1 and V_2 are explained as follows:

$$V_1 = fR_1 \left(Q_{C+} - Q_{C-} \right) \tag{6}$$

$$V_2 = fR_2 \left(Q_{C+} - Q_{C-} \right) \tag{7}$$

The equations mean that the charge difference "Q_{C+} - Q_{C-}" and amount of charge, which flow to R_1 and R_2 by DC voltage V_1 and V_2 are balanced. DC voltage V_1 is solved using the equations (4) – (7) as follows:

$$V_1 = \frac{2\frac{x}{d}\left(V_m - \frac{1}{4}V_{f1+2+3+4}\right) + \left(1 - \frac{x^2}{d^2}\right)A - \frac{1}{2}V_{f1-2+3-4}}{1 + \frac{R_2}{R_1} + \left(1 - \frac{x^2}{d^2}\right)\left\{\frac{C_{ps+} + C_{ps-}}{2C_0}\left(1 + \frac{R_2}{R_1}\right) + \frac{1}{2fC_0R_1}\right\}}$$

$$\because A = \frac{C_{ps+} - C_{ps-}}{C_0}V_m - \frac{C_{ps+}\left(V_{f1} + V_{f3}\right) - C_{ps-}\left(V_{f2} + V_{f4}\right)}{2C_0} \tag{8}$$

$$\because V_{f1+2+3+4} = V_{f1} + V_{f2} + V_{f3} + V_{f4}$$

$$\because V_{f1-2+3-4} = V_{f1} - V_{f2} + V_{f3} - V_{f4}$$

When $V_{f1}=V_{f2}=V_{f3}=V_{f4}=V_f$, $C_{ps+}=C_{ps-}=C_{ps}$ in particular, and V_1 is described as follows:

$$V_1 = \frac{2\frac{x}{d}\left(V_m - V_f\right)}{1 + \frac{R_2}{R_1} + \left(1 - \frac{x^2}{d^2}\right)\left\{\frac{C_{ps}}{C_0}\left(1 + \frac{R_2}{R_1}\right) + \frac{1}{2fC_0R_1}\right\}} \tag{9}$$

DC voltage V_2 of C_2 is also solved as follows:

$$V_2 = \frac{2\frac{x}{d}\left(V_m - V_f\right)}{1 + \frac{R_1}{R_2} + \left(1 - \frac{x^2}{d^2}\right)\left\{\frac{C_{ps}}{C_0}\left(1 + \frac{R1}{R_2}\right) + \frac{1}{2fC_0R_2}\right\}} \tag{10}$$

Input signals for the differential amplification block are equal with $-V_1$ and V_2, because the low-pass filter of "$R_{f1}C_{f1}$" and "$R_{f2}C_f$" cuts high frequency components. When $R_1=R_2=R$, the output signal V_o of the differential amplification block is as follows:

$$V_o = A\left\{V_2 - \left(-V_1\right)\right\} = A\frac{2\frac{x}{d}\left(V_m - V_f\right)}{1 + \left(1 - \frac{x^2}{d^2}\right)\left(\frac{C_{ps}}{C_0} + \frac{1}{4fC_0R}\right)} \tag{11}$$

Where A is the amplification factor of the differential amplification block. According to the above equations, to decrease offset voltage, each forward voltages of four diodes should be established on the same level. The stray capacitances C_{ps+} and C_{ps-} also should be adjusted in the same way. In addition, the third term of the denominator of the equation is a non-linearity component, so frequency of input signal, C_0 and R should be larger. An advantage of the circuit is common-mode noise reduction capability because of the differential-mode input of the amplification circuit.

COMPARISON WITH PSPICE SIMULATION AND EVALUATION

In order to confirm the equity of the solution, the equation (9) was compared with PSpice simulation. Figure 3 shows DC Voltage V_1 characteristic of the detection circuit. Simulation and calculation conditions are V_m=5V, f=1MHz, C_0=3pF, C_1=C_2=1nF, R_1=1MΩ, R_2=22kΩ. Diodes are default models and each diode's V_f are 0.55V during the simulation and calculation respectively. Both of the results are in agreement, therefore, it is possible to recognize that the equations are correct.

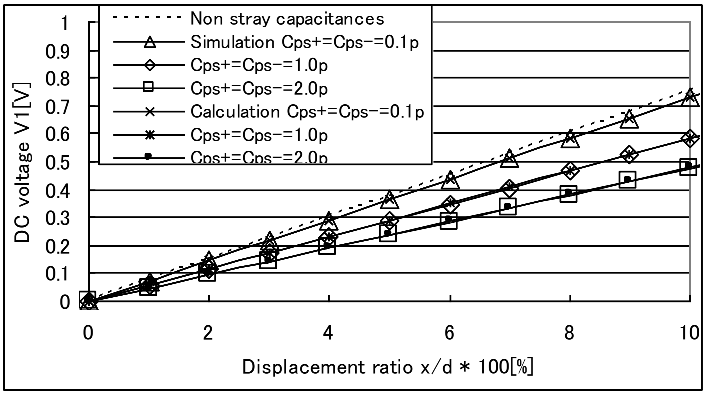

Fig. 3. Displacement ratio x/d to DC voltage V_1

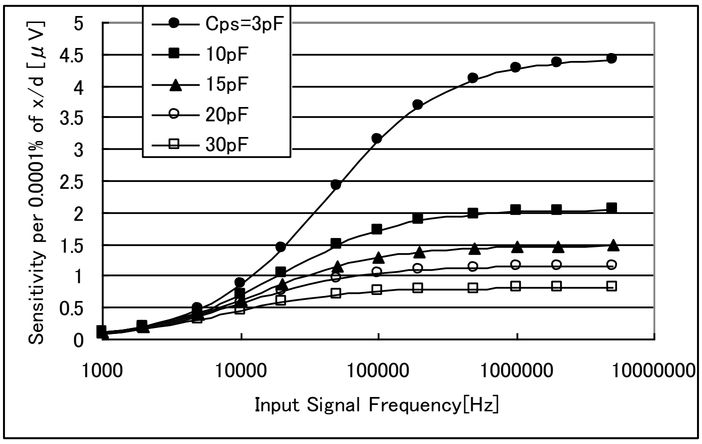

Fig. 4. Input signal frequency to sensitivity per 0.0001% of displacement ratio x/d

Using the equation (11), the sensitivity per 0.0001% of displacement ratio x/d and the non-linearity of the output were evaluated as shown in figure 4 and 5. The calculating conditions are V_m=5V, C_0=3pF, R_1=R_2=1MΩ and V_f=0.55V. As the stray capacitance is getting larger, the sensitivity increase over the rise of the frequency is getting smaller. Non-linearity at 1% of displacement ratio is less than 0.01%, at 1% of the displacement ratio is less than 1%.

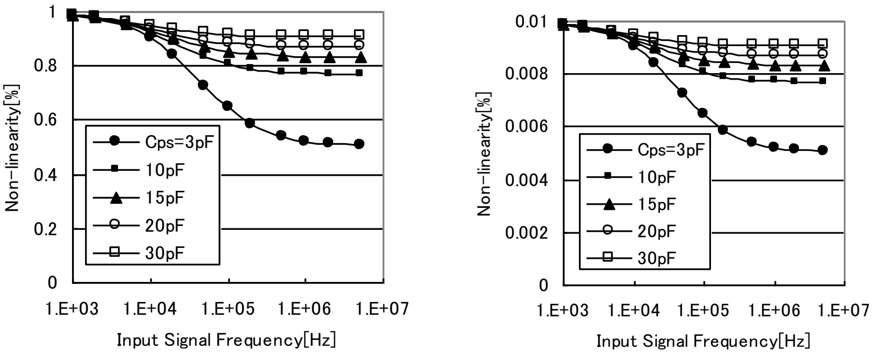

Fig. 5. Input signal frequency to non-linearity at displacement ratio x/d: 1% (left) and 10% (right)

EXPERIMENT

Using a Cu print basis and surface mount components, the detection circuit was manufactured. Parameters of each elements are C_1=C_2=1nF, R_1=1MΩ, R_2=22kΩ. Silicon PIN diode BAR64-04 (Infineon) and operational amplifier OP177G (Analog Devices) were selected for the circuit. The output of the circuit is 11 times as large as V_1. In order to evaluate the circuit, a differential capacitance device shown in figure 6 was manufactured. It consists of a parallel movable electrode, as a balance structure.

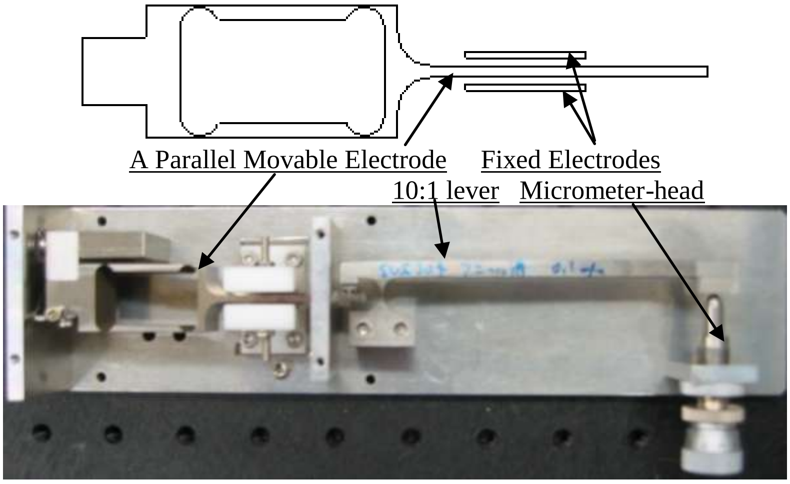

Fig. 6. Differential capacitance device

The initial gap length is 1.0mm and the initial capacitance is 3pF. With micrometer head and 10:1 lever, the movable electrode might be displaced by 0.1μm pitch.

The experimental results are shown in figure 7. Taking the input side of the amplifier onto consideration, the sensitivities of 14.9mV/% at f=1MHz was obtained when 10V of V_{p-p} was supplied. Theoretically the sensitivity increase with a rise in frequency theoretically, however, on the contrary, it decreased. Consumption of voltage by inductances of the circuit pattern and connection cables was considered as a reason. If smaller circuit and micro-size differential capacitance device are combined, the sensitivity should be improved.

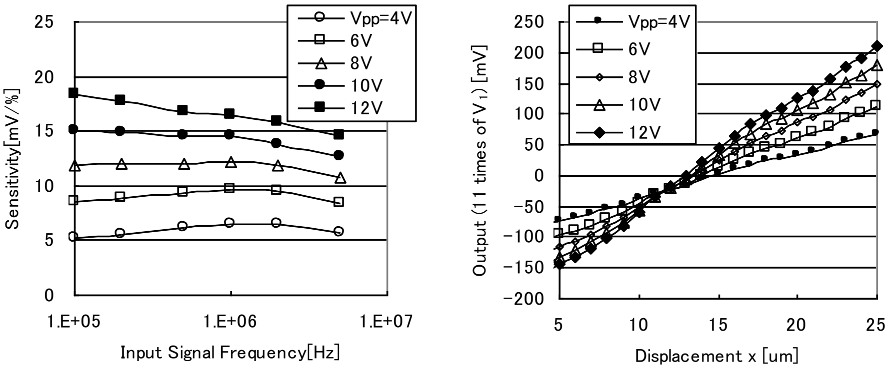

Fig. 7 Movable electrode displacement to output DC voltage at f=1MHz (left),
Input signal Frequency to Sensitivity per 1% of the displacement ratio (right)

CONCLUSION

The equation, which explains output of a diode-bridge type differential detection circuit was derived. When 10V (the practical value of input amplitude) is supplied, few 10mV/% is obtained, what was confirmed experimentally. Non-linearity of output characteristic is less than 0.01% under 1% ratio of the displacement and the initial gap length. On next stage, new constructed circuit with diodes replaced by CMOS switches will be evaluated. By taking off the diode forward voltage V_f, net voltage value, which is supplied to differential capacitance device will increase and the sensitivity will be improved.

ACKNOWLEDGMENT

This research is supported by the Grant-In-Aid of Fukuoka Industry, Science and Technology Foundation.

LITERATURE

[1] Y. MATSUMOTO, S. KAWAHITO and M. ISHIDA, “Development and Evaluation of Capacitance Detection ASIC for Three-axis Common Electrode Type Capacitive Accelerometer”, *Trans. IEE of Japan*, vol. 121-E, No. 3, 2001, pp. 135-141

[2] M. TSUGAI, Y. HIRATA, T. ARAKI and M. KIMATA, “A Charge Balanced C-V Converter for a Differential Capacitance Sensor”, *Trans. IEE of Japan*, vol. 123-E, No. 9, 2003, pp. 357-362

[3] F. KOHSAKA, J. LIANG and T. UEDA, “Mechanical Strength of Quartz Micromechanical Devices”, *Proc. of the 21st Sensor Symposium*, 2004, pp. 225-228

[4] T. UEDA, F. KOHSAKA, D. YAMAZAKI and H. HAYASHI, “High Sensitive Quartz Crystal Microphone using Micro-Machining Technology”, *Trans. IEE of Japan*, vol. 121-E, No. 12, 2001, pp. 629-635

5th International Conference **ELMECO**
Nałęczów, Poland
September 2005

INVESTIGATION OF HOT GAS MIXTURE FREE JET

Gregor J., Jakubová I., Mendl T., Šenk J.

Faculty of Electrical Engineering and Communication, Brno University of Technology
Address: Purkyňova 118, 612 00 Brno, Czech Republic
E-mail: jakubova@feec.vutbr.cz, gregor@feec.vutbr.cz

Abstract

The analysis of the distribution of individual species of a hot gas mixture in a free jet is based on the vector form of the continuity equation, including the diffusion member, and on the momentum equation. The measured distributions of temperature and axial velocity in cross-sections of the free jet, together with thermodynamic and transport properties of working gas are used in a designed process of calculation. By means of approximation of temperature and velocity radial profiles by Gaussian functions, the two-dimensional problem is transformed into the one-dimensional task. The designed method is applied on the cold region of the jet generated by a hybrid water stabilised plasma torch with argon gas added into the chamber. In this cold region (T<2500 K), rather precise measurement of temperature and velocity can be carried out using rather simple methods (thermocouples, cooled Pitot tube). By the derived mathematical-physical model, the distribution of mass fractions of individual species of the working gas mixture is computed, and the influence of velocity component and turbulence on this distribution is studied. During the calculation, axial dependencies of cross-section, axial velocity, and the turbulence coefficient in the free jet are obtained.

Keywords: gas mixture, free jet, concentration, mathematical-physical modelling

INTRODUCTION

In the paper the measurements on hot gas mixture free jet are analyzed. The main interest is oriented on the analysis of the distribution of the individual species in the jet based on the vector form of the continuity and momentum equation. In the continuity equation the diffusion member is involved. To simplify the problem, the temperature and velocity fields are approximated by suitable functions. The calculation process is applied on the jet generated by a hybrid water stabilized plasma torch with argon added into the chamber of a plasma heater. By the derived mathematical-physical model the distribution of the mass fractions of individual species of the working gas mixture can be computed and the influence of the axial and radial dependencies of velocity and temperature on the space distribution of individual species can be studied.

The jet is generated by a hybrid water-stabilized arc torch. An admixture of argon is added at the input of the arc heater. The hot mixture of argon and water vapour flows out of the output orifice into the surrounding air of normal pressure and subsequently mixes with it. The measurements were carried out just at the output of the arc heater and at the distance of z_k from the output. The calculation process issues from the vector form of the continuity equation including the diffusion member and from the momentum equation.

BASIC RELATIONS OF THE MODELL

If steady state can be supposed, the continuity equation for the k-th component of the gas mixture is

$$\nabla.\left(\rho x_k \vec{v}\right) + \nabla.\left(\rho D_{mk} \nabla x_k\right) = 0 \,. \tag{1}$$

The gas mixture consists of n components, the n^{th} of them is usually prevailing

$$x_n = 1 - \sum_{k=1}^{n} x_k \;. \tag{2}$$

For describing the velocity field in the jet we use the continuity equation

$$\frac{\partial v_z(r,z)}{\partial z} + \frac{\partial v_r(r,z)}{\partial r} + \frac{v_r(r,z)}{r} = 0 \tag{3}$$

and the axial component of the momentum equation

$$v_z(r,z)\frac{\partial v_z(r,z)}{\partial z} + v_r(r,z)\frac{\partial v_z(r,z)}{\partial r} = \upsilon(r,z)\frac{1}{r}\frac{\partial}{\partial r}\left[r\frac{\partial v_z(r,z)}{\partial r}\right] \tag{4}$$

at $\partial/\partial t = 0$, $\nabla p = 0$, $\vec{J} \times \vec{B} = 0$.

The measured radial dependencies of the temperature and axial velocity are approximated by Gaussian curves

$$\begin{aligned} T\,(r,z) - T_\infty &= T(0,z)\exp\left[-\ln 2\frac{r^2}{b_T^2(z)}\right], \\ v_z(r,z) &= v(0,z)\exp\left[-\ln 2\frac{r^2}{b_{vz}^2(z)}\right]. \end{aligned} \tag{5}$$

In the equations ρ [kg.m^{-3}] is the specific mass, v [m.s^{-1}] is the velocity, D_{mk} [m^2.s^{-1}] is the diffusion coefficient of the k^{th} component of the mixture with the mass fraction x_k, ν is the kinematic coefficient of viscosity, $b_T(z)$ and $b_{vz}(z)$ [m] are the half-widths of the temperature and axial velocity profiles, respectively.

Omitting the laminar component, the diffusion coefficient of the k^{th} component of the mixture

$$D_{mkt}(r,z) = c_t(r,z) b_{vz}(z) v(0,z) = \nu(r,z) \tag{6}$$

is the same as the kinematic turbulent component of the viscosity coefficient $\nu_t(r,z)$. By means of the Gauss-Ostrogradsky theorem the relations for the radial dependency of concentrations of the mixture's components can be obtained from the solution of the continuity equation (1) [3]

$$\frac{x_k(r,z)}{x_k(0,z)} = \exp\left[-\int_0^r \frac{1}{\nu(z)} \frac{v_r(r,z) + \frac{dr}{dz} v_z(r,z)}{1+\left(\frac{dr}{dz}\right)^2} dr \right] = \exp\left[-b_c(r,z)\right]. \tag{7}$$

Solving the equation (4) using the relation (5) we obtain for the radial component of velocity

$$v_r(r,z) = \frac{1}{r}\left\{ v_z(r,z)\left[\frac{b_{vz}^2(z)}{2\ln 2} \frac{1}{v(0,z)} \frac{\partial v(0,z)}{\partial z} + \frac{1}{b_{vz}(z)} \frac{\partial b_{vz}(z)}{\partial z} r^2 \right] - \upsilon(r,z)\left[\frac{2\ln 2}{b_{vz}^2(z)} r^2 - 2 \right] \right\} \tag{8}$$

The solution of the differential equation following from the condition $\lim_{r \to 0} v_r(r,z) = 0$ gives the expressions for axial dependencies of velocity

$$v(0,z) = \frac{B v(0,0)}{B+z}, \tag{9}$$

and the velocity half-width

$$b_{vz}(z) = 4\ln 2\, c_t(0,z)(B+z),\ c_t(0,z) = \frac{b_{vz}(z)}{4\ln 2 B}. \tag{10}$$

$v(0,z)$ and $b_{vz}(z)$ are the axial velocity and velocity half-width, and B is the integration constant.

The radial velocity $v_r(r,z)$ we obtain also from the solution of the continuity equation (3) using the relations (5), (6), (9), and (10).

$$v_r(r,z) = 3\frac{f(z)}{r(B+z)} v_z(r,z)\left\{ e^{-\ln 2 \frac{r^2}{b_{vz}^2(z)}}\left[1 - \frac{r^2}{2f(z)}\right] - 1 \right\} \tag{11}$$

where

$$f(z) = 8\ln 2 c_t^2 (B+z)^2. \tag{12}$$

From the equality of the both radial velocities $v_r(r,z)_{CONTINUITY} = v_r(r,z)_{MOMENTUM}$ the relation for the coefficient $c_t(r,z)$ and the diffusion coefficient $\nu(r,z)$ can be expressed as

$$c_t(r,z) = c_t(0,z) e^{-\ln 2 \frac{r^2}{b_{vz}^2(z)}}\left[3e^{-\ln 2 \frac{r^2}{b_{vz}^2(z)}} - 2 \right], \tag{13}$$

$$v(r,z)=\frac{f(z)}{2(B+z)}v_z(r,z)\left[3e^{-\ln 2\frac{r^2}{b_{vz}^2(z)}}-1\right]. \qquad (14)$$

INPUT DATA

The designed model has been applied for the evaluation of the jet parameters at the distance z_k=365 mm from the output of the arc heater with an arc stabilised and cooled by the steam evaporated from the surrounding water swirl. Water stabilised torch was modified by adding of argon into the chamber. The main parameters of the evaluated experiment are as follow: the output orifice diameter 5.7 mm, the input power 69 kW (the voltage 230 V, the current 300 A), the total loss 31 kW (the efficiency 0.55), Ar flow rate $0.346.10^{-3}$ kg/s.

To determine the initial parameters of the jet (the output temperature profile $T(0,z)$, the velocity $v(0,0)$, the flow rate of water vapour G_{WV}) the measurements on the arc heater output were carried out [4]. The measured output temperature profile was approximated by a parabolic function and the Mach number was assumed to be constant over the whole output cross-section. The calculation process was based on the energy and continuity equations [1]. During the calculation process the ratio of the flow rates $G_{WV}/G_{Ar} = x_{GS}=1.4$ was obtained. The total output flow-rate was $G_M = G_{Ar} + G_{WV} = G_{Ar}(1 + x_{GS}) = =0.346\cdot10^{-3}\cdot2.4=0.83\cdot10^{-3}$ kgs^{-1}. By means of approximation of the output parameters by the Gaussian curve we obtain the initial values of the axial velocity $v(0,0)$=3233 ms^{-1} and of the half-width $b_{vz}(0)=2.1\cdot10^{-3}$m.

MODEL COMPUTATION IN THE JET COLD ZONE

The temperature distribution in the cold part of the free jet (z_k=365 mm) was determined by Pt-Ir thermocouple inserted into the gas flow. This measured temperature may differ from the real gas temperature because of energy loss by radiation and by heat conduction through the leads. These differences were corrected using the energy balance equation for the thermocouple tip and the leads. The velocity profile was measured by a dynamic pressure sensor.

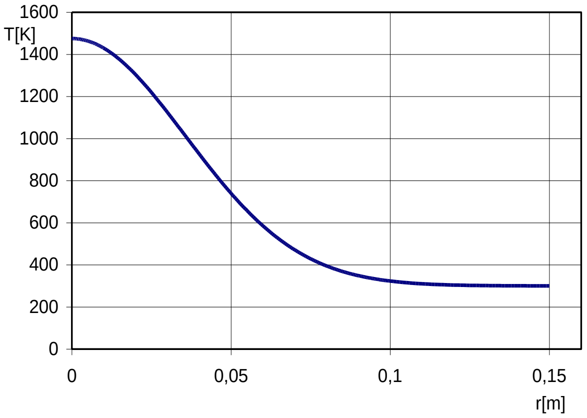

Fig. 1. The radial temperature profile at zk=365 mm

The measured temperature and axial velocity radial profiles at z_k=365 mm were approximated by Gaussian functions according to (5). The obtained parameters of the approximation functions were: $T(0,z_k)$=1475 K, T_∞=300 K, $b_T(z_k)$=2.25·10^{-2} m, $v(0,z_k)$=30.77 m/s, $b_{vz}(z_k)$=1,85·10^{-2} m, B=351·10^{-2} m. The radial dependencies of the approximated measured temperature and the axial velocity and of the computed radial velocity (11) at the distance z_k=365 mm are given in Figs. 1, 2. The radial component of the velocity is significantly lower than the axial velocity component (about ten times). In accordance with the physical presumptions the radial velocity is equal to zero in the axis r=0 and again at $r=\infty$. In fact it is practically zero for $r\geq 80$ mm and reaches its maximum value of 1.67 m/s at r=22 mm.

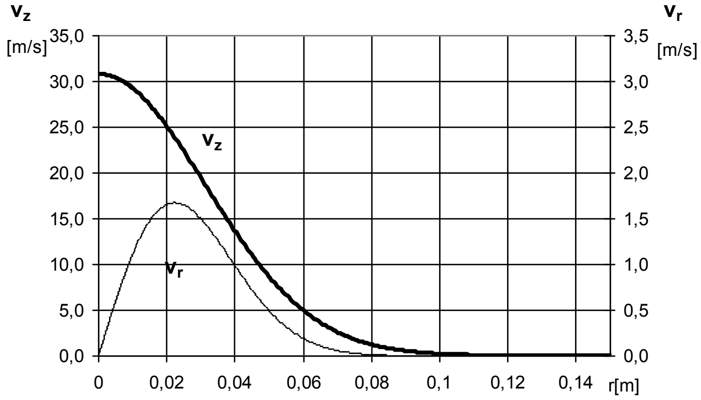

Fig. 2. The radial profiles of the axial and radial velocities at zk=365 mm

The radial dependency of the coefficient $c_t(r,z_k)$ in the relation (6) for the turbulent diffusion coefficient was computed by means of (13) and is depicted in Fig. 3. It was found out not to be constant if the velocity profiles are approximated by Gaussian functions. The course of the dependency $c_t(r,z_k)$ influences the course of the dependency of the diffusion coefficient ν (see eq. (14) and Fig. 4).

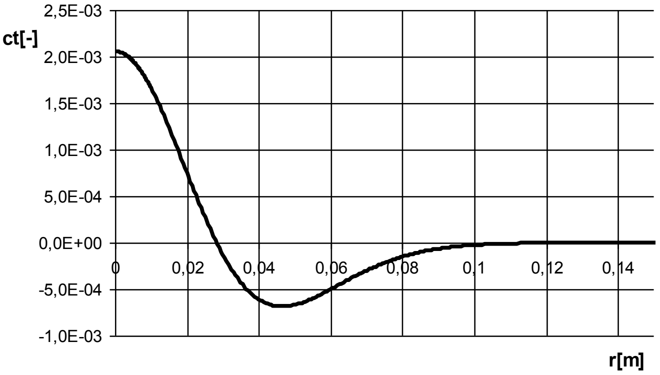

Fig. 3. The radial dependency of the computed coefficient ct(zk) – eq. (13)

RESULTS AND CONCLUSIONS

From the derived model it follows that while the half-width b_{vz} is proportional to the coordinate z (10), the velocity in the axis $v(0,z)$ is proportional to the inverse value of the coordinate z (9). This finding is in accordance with the conclusions of other authors [2] and corresponds to physical presumptions. Using equation (7), the described computations can be used for the determination of the radial profiles of the relative concentrations of individual components flowing out of the arc heater output. From the relation (7) it is obvious that these profiles are the same for all components and depend only on the velocity field of the flow. It results from the fact that the laminar component of the diffusion coefficient was omitted. This simplification can be applied in the cold region far from the arc heater output. In further research the suitability of the simplifying omissions will be tested and the modified model is intended to be applied for an evaluation of the data measured near the arc heater output.

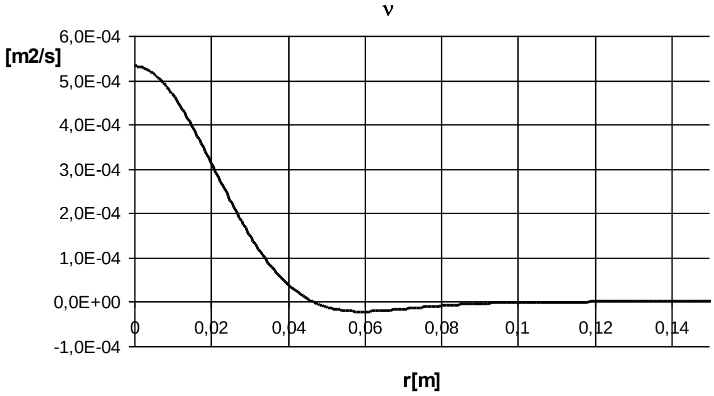

Fig. 4. The radial dependency of the computed coefficient ν(zk)

ACKNOWLEDGEMENT

This work was supported by the projects No. MSM 0021630516 and MSM 021630513 of the Ministry of Education of the Czech Republic.

LITERATURE

[1] Gregor J., Jakubova I., Mendl T., Šenk J., Sember V., The characteristics of the free jet generated by a hybrid water-argon torch, *Proc. of the 4thInt. Conf. Plasma Physics and Plasma Technology,* Minsk (Belarus), 2003, pp. 360-363

[2] Schlichting H., *Theory of Boundary Layer* (in German), Verlag G. Braun, Karlsruhe (Germany), 1965

[3] Gregor J., Jakubova I., Šenk J., *Czechoslovak Journal of Physics,* vol. 54-C, 2004, pp. 690-696

[4] Sember V., *Czechoslovak Journal of Physics,* vol. 52-D, 2002, pp. 643-650

5th International Conference **ELMECO**
Nałęczów, Poland
September 2005

AXIAL AND RADIAL ENERGY FLOWS IN THE ARC HEATER CHANNEL

Gregor J., Jakubová I., Mendl T., Šenk J.

Faculty of Electrical Engineering and Communication, Brno University of Technology
Address: Purkyňova 118, 612 00 Brno, Czech Republic
E-mail: jakubova@feec.vutbr.cz, gregor@feec.vutbr.cz

Abstract

The integral quantities measured on the arc heater with the electrical arc stabilized by flowing gas serve as input data of a mathematical-physical model of phenomena inside the arc heater channel. The model is based on the mass and energy conservation equations and Ohm law and uses the known material properties of the gas medium. The main simplifying assumptions are LTE, relatively small kinetic energy of plasma, and axial symmetry of the investigated area. The main measured values are the arc current I (50 to 220 A), the arc voltage U (approx. 100 V), the flow rate of the working gas G (argon, up to 22 g/s), energy loss of the arc heater channel P_z *determined from the warming of the cooling water. By means of the mentioned model, the energy flows in axial (enthalpy flow) and radial (conduction and radiation energy loss) directions are computed and presented in diagrams.*

Keywords: arc heater, energy exchange, mathematical-physical modelling

INTRODUCTION

The model is designed for the anode channel, which represents the main part of an arc heater (for details see [2]). The whole anode channel volume is divided in two zones - the area of the electric arc (so-called arc zone) and the remaining volume (heated zone and cold zone). This is because the energy equation for the arc differs from that for the heated gas. Thermodynamic properties of argon in the temperature interval up to 6000 K, at which ionization begins, are constant or can be simply mathematically expressed.

The model is based on mass and energy conservation equations and Ohm's law. The arc plasma is supposed to be in LTE and its kinetic energy to be small compared with its enthalpy. Mach number is assumed to be constant over the channel cross-section. Axial symmetry is assumed, and only the radial component of conductive and radiative energy flow and the axial component of enthalpy flow are considered.

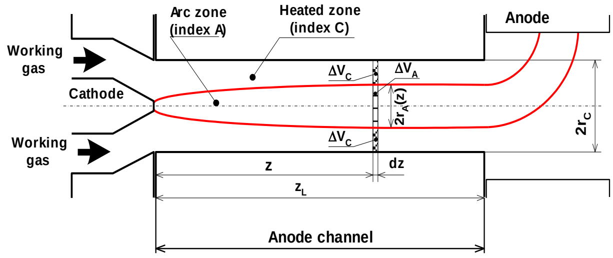

Fig 1. The investigated part of an arc heater

BASIC RELATIONS

The model for evaluation of measurements carried out of the arc heater anode channel consist of the continuity equation, energy equation, and Ohm’s law

$$\int_{\Delta V} \nabla(\rho\vec{v}).dV = 0\,, \tag{1}$$

$$\int_{\Delta V} \vec{j}\cdot\vec{E}.dV = \int_{\Delta V} \nabla\cdot\left(\vec{J}_q + \vec{J}_r + \rho\vec{v}h\right).dV\,, \tag{2}$$

$$\vec{j} = \sigma\cdot\vec{E} \tag{3}$$

where ρ [kg.m^{-3}] is the mass density, v [m.s^{-1}] the gas velocity, h [J.kg^{-1}] the enthalpy, $\vec{J}_q$ and $\vec{J}_r$ [W.m^{-2}] the terms of conductive and radiative energy flow, j [A.m^{-2}] the current density, σ [S.m^{-1}] the electrical conductivity of working gas, E [V.m^{-1}] the electrical field intensity, the volume $\Delta V=\pi r_C^2 dz$, r_C is the channel radius.

The dependency of the arc radius $r_A(z)$ on the axial position is taken from [4]:

$$r_A(z) = r_0\left[1+\left(\frac{z}{r_0}\right)^{1/n_r}\right] \tag{4}$$

where r_0 is the radius of the arc at the cathode, defined by the arc current and by the cathode current density (10^8 A.m^{-2} for current up to 2.16 kA [4]) and n_r is a calculation parameter which influences the axial shape of the arc.

To transform a two-dimensional problem into a one-dimensional task, the radial temperature profile in the arc zone was approximated by a parabolic function

$$\frac{T_A(r,z)^{1/n} - T_{AA}^{1/n}}{T_A(0,z)^{1/n} - T_{AA}^{1/n}} = 1-\left(\frac{r}{r_A(z)}\right)^2 \tag{5}$$

and in the heated zone by a Gaussian function

$$T_C(r,z) = T_{AA}.\exp\left(\frac{r_A^2(z)-r^2}{b_C^2(z)}\right),\; b_C^2(z) = r_A^2(z)\left\{n.\left[\left(\frac{T_A(0,z)}{T_{AA}}\right)^{1/n} -1\right]\right\}^{-1} \tag{6a,b}$$

where $T_{AA} = 6000$ K is the temperature at the arc boundary ($\sigma(T_{AA}) \approx 0$), the exponent n defines the shape of the radial temperature profile and represents further parameter of a calculation. The value of $b_C(z)$ is given by the condition of the equality of conductive heat flows from both sides of the arc boundary.

The boundary conditions of the model are given by measured integral quantities:

- the voltage U [V] on the analyzed part of the arc column $z \in \langle 0;z_L \rangle$

$$U = \int_0^{z_L} \frac{I}{2\pi \int_0^{r_A(z)} \sigma(T_A) r.dr} dz \tag{7}$$

- the electric power losses P_z [W] absorbed on the channel wall consist of the heat transfer from the heated gas to the wall and of the arc column transparent radiation, absorbed by the wall (expressed as a part of the input electrical power)

$$P_Z = 2\pi \int_0^{z_L} \left\{ r_C \lambda [T_C(r_C,z)] \left[\frac{\partial T_C(r,z)}{\partial r} \right]_{r=r_C} \right\} dz + \varepsilon.U.I \tag{8}$$

- the energy balance of the whole channel

$$\left[M(z) \int_0^{r_C} \rho(T) a(T) h(T) 2\pi r.dr \right]_0^{z_L} = U.I - P_Z . \tag{9}$$

The detailed description of the model is given in [2], [3].

RESULTS AND CONCLUSIONS

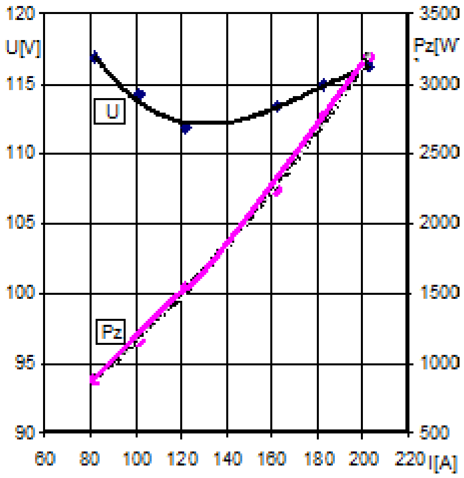

Fig. 2. The arc voltage U and the total radial loss of the arc Pz vs. the arc current I

The model was applied for the evaluation of the data sets measured on the arc heater in different points of the voltage-current characteristic of the arc. Fig. 2 summarizes the main measured integral quantities. During all the discussed experiments there was the flow rate G = 22.5 g.s^{-1}, the temperature of cold gas T_0 = 300 K, the radius of the anode channel r_C = 8 mm, and the length z_l = 80 mm. Comparing the results of the computations, we have found the exponent n (in the equation for the radial temperature profile of the arc) to decrease with the arc current from 1.5 down to 0.75, and the exponent n_r (in the equation for the arc radius) to be almost independent on the arc current with the most probable value of 3.2. The computed share of radiative energy ε on the Joule's energy loss UI is between 9.2 and 13.5 percent, which agrees with the data given by other authors, e. g. [4].

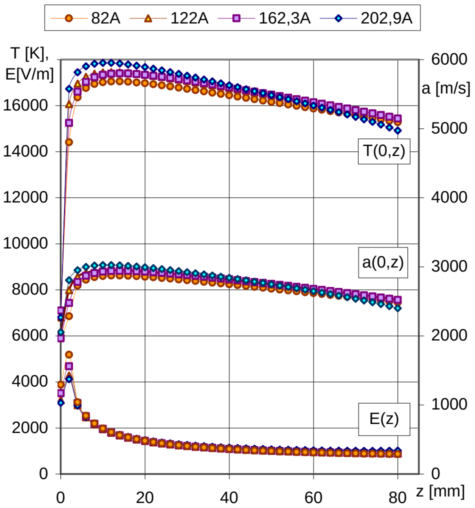

Fig. 3. The temperature and the sound velocity in the axis, and the electrical intensity along the anode channel

In Fig. 3 the dependency of the temperature $T_A(0,z)$ and the sound velocity $a(0,z)$ in the axis, and of the electrical intensity $E(z)$ on the coordinate z can be seen. The significant maximum of $E(z)$ near the cathode for z = 2 mm is partially caused by lower estimation of the electrical conductivity of plasma in the cathode region. This results in a very sharp increase of the axial temperature in this region. As assumed, the axial temperature slowly decreases in the prevailing part of the studied interval. The small differences in axial temperatures for the increasing arc currents (Fig. 3) show that the increasing power is carried off especially due to the increasing radii of the arc zone and heated zone (Fig. 5). It is obvious from the dependency of the radius of the heated zone $r_{jet}(z)$ in Fig. 5 that the region of heated gas does not reach the wall in none of studied examples; thus the wall is not heated by the hot gas even for the highest of measured currents. Consequently, all measured power loss P_z are due to transparent radiation. The distribution of the computed transparent radiation loss in individual computing intervals along the channel is depicted in Fig. 6. Its relation with the temperature dependency in Fig. 3 is obvious. The given dependencies allow computing only the mean coefficient of transparent radiation of the slice. The local transparent radiation coefficient is intended to be studied in further research. It can be seen in Figs. 3, 4 that while the sound velocity in the axis $a(0,z)$

decreases, the axial velocity of plasma *v*(0,*z*) increases with the coordinate *z* due to the increasing Mach number *M*.

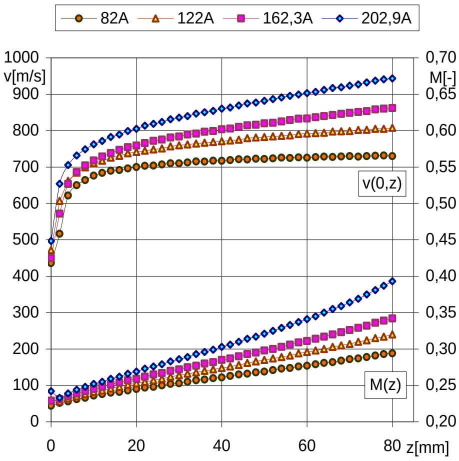

Fig. 4. The axial velocity and Mach number along the anode channel

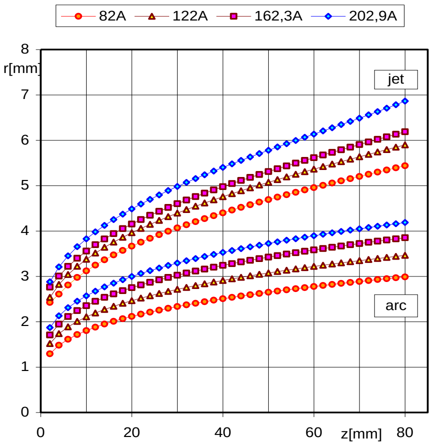

Fig. 5. The radii of the arc and of the heated zone along the anode channel

Fig. 7 shows relative values of power loss by transparent radiation P_z/UI, and by enthalpy flow both in the arc zone RAH_A/UI and in the heated zone RAH_C/UI vs. the arc current *I* at the end of the channel z_l=80 mm. Similarly, the right part of Fig. 7 shows the relative mass flows in the arc zone and the heated zone. From the comparison of the data in Fig. 7 it follows that the arc zone transfers 62 to 72 percent of power, but only 3 to 7 percent of mass. About 90 percent of the total power falls on the enthalpy flow through the arc and heated zones, while the mass flow of the heated gas in both mentioned zones is about 25 to 50 percent of the total flowing mass. The prevailing part of mass flow *GR/G* (75 to 50 per cent) is transferred in the cold zone.

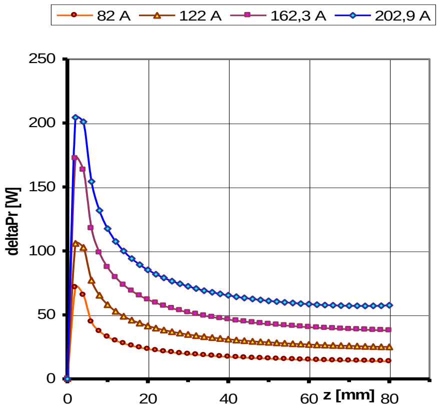

Fig. 6. The transparent radiation loss in the individual slices along the arc heater channel

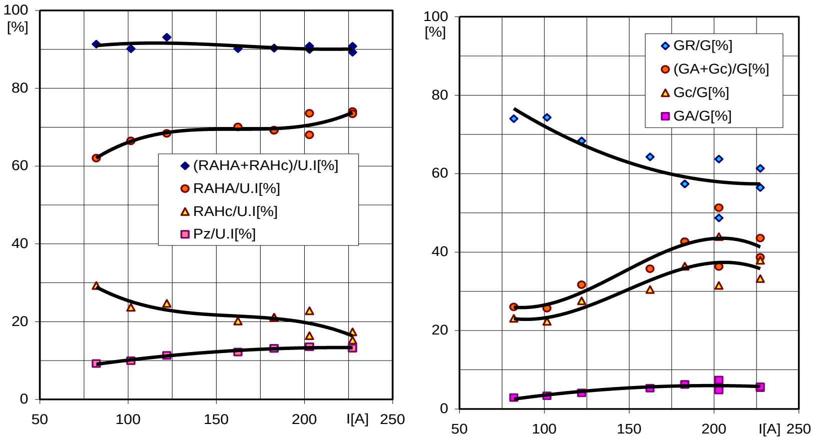

Fig. 7. The relative energy and mass flows in the arc heater channel vs. the arc current I

ACKNOWLEDGEMENT

This work was supported by the projects No. MSM 0021630516 and MSM 021630513 of the Ministry of Education of the Czech Republic.

LITERATURE

[1] Gregor J., Jakubová I., Kolářský J., Šenk J., Proc. of XIIIth Symp. on Physics of Switching Arc. Brno, Czech Republic, 1998, pp. 131-134

[2] Heinz J., Šenk J., Modelling of energy processes in intensively blasted electric arc, Czechoslovak J. Phys. 54-C, 2004, pp. 702-708

[3] Heinz J.: PhD Dissertation. Brno University of Technology, 2004

[4] Ramakrishnan S., Stokes A. D., Lowke J. J., An approximate model for high-current free-burning arcs, J. of Phys. D: Appl. Phys. 11, 1978, pp. 2267-2280

5th International Conference **ELMECO**
Nałęczów, Poland
September 2005

MODELLING THE INSERTION LOSS OF BEAD AND COMMON MODE CHOKE

Paweł A. Mazurek, Andrzej Wac-Włodarczyk

Institute of Electrical Engineering and Electrotechnologies
Lublin University of Technology, Poland
Address: Nadbystrzycka 38A, 20-618 LUBLIN
E-mail: pawelm@eltecol.pol.lublin.pl
andrzejw@eltecol.pol.lublin.pl

Abstract

The article presents the procedure of bead and common mode choke modeling. The insertion loss is the basic parameter which defines the effectiveness of electromagnetic interferences limitations. The article introduces the influence of magnetic and physical parameters of bead on insertion loss.

Keywords: electromagnetic compatibility, bead, common mode choke

INTRODUCTION

Electromagnetic compatibility (EMC) is connected with both, the process of unintentional electromagnetic energy emissions from electronic equipment and the ability of this equipment to function in the presence of interfering energy (immunity to the electromagnetic environment). Basically, the radiated interfering signals are classified as narrow and broad band. Narrow band signals occupy a small portion of the radio spectrum and have the energy concentrated in a single frequency wave. Broadband signals are those whose energy is spread over tens of hundreds of megahertz. That is why every frequency source could be a potential source of interference and all interference signals could be coupled to the power line and conducted to the power mains. One of the most used techniques for reducing EMI & RFI interference is the application of beads and chokes builded with soft magnetic materials. Beads provide a simple, economical method for attenuating high frequency noise or oscillations. The beads and chokes are seen as low impedance at low frequencies and relatively high impedance over a high frequency band. The effectiveness of bead's impedance depends on the relative magnitudes of choke, turn of winding number and permeability changes of used material.

INSERTION LOSS

The insertion loss is the basic parameter which defines the effectiveness of the electromagnetic interferences limitations. Insertion loss is relation between: voltage U'_Z measured on receiver when the beads are switch on, and the voltage U''_Z without the beads. The circuits are presented at Fig. 1.

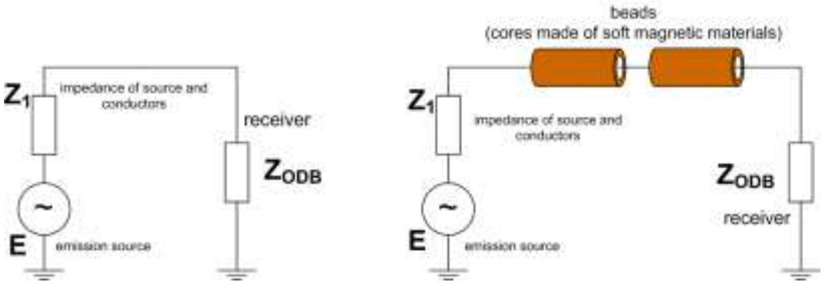

Fig. 1. EMI beads in electric circuit

Insertion loss a (1) maybe presented as relation between existing impedances in analyze circuit, where: Z_1 – impedance of power supply, Z_0 – receivers impedance and Z_D – core impedance. The analyze of insertion loss is reduced to the analyze of core's impedance.

$$a = 20\ \lg\left(\frac{U_1}{U_2}\right) = 20\ \lg\left|\frac{\underline{Z_1} + \underline{Z_D} + \underline{Z_O}}{\underline{Z_1} + \underline{Z_O}}\right| \quad \text{dB} \tag{1}$$

Two types of disturbances exist in the power supplies circuits of electric devices. Therefore, there exist two types of chokes, that limit the disturbances (interferences). The magnetic beads limit the asymmetrical disturbances, and the common mode chokes limit the common mode disturbances.

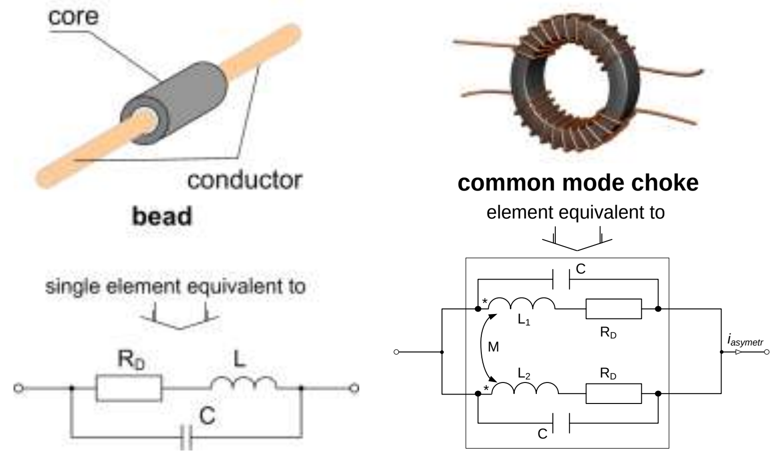

Fig. 2. The bead, common mode choke and their equivalent schematic diagrams

The impedance of cores (bead and common mode choke) are defined by such parameters as: *R*, *L*, *C*. Additionally, impedance depends on the range of frequency. These problems are present in equations (2) and (3).

BEADS	COMMON MODE CHOKE
$\underline{Z}_D(j\omega)=\frac{(R+\mathrm{j}\omega\cdot L)\cdot\left(-\mathrm{j}/\omega C\right)}{R+\mathrm{j}\left(\omega L-1/\omega C\right)}$ (2)	$\underline{Z}_D = j\omega M+\frac{\left(R_D+j\left(\omega L-\omega M\right)\right)\left(-jX_C\right)}{2\cdot\left[R_D+\left(j\omega L-j\omega M-jX_C\right)\right]}$ (3) where: $M=k\cdot\sqrt{L_1\cdot L_2},\ L_1=L_2=L, k\approx 0{,}8\div 0{,}99$

The inductance *L* of the core is defined as:

$$L=\frac{\mu_{core}\cdot\mu_0\cdot S\cdot N^2}{l}\quad \mathrm{H} \tag{4}$$

where: $\mu_0 = 4\cdot\pi\cdot 10^{-7}$ H/m, *l* – effective length, *S* – effective area, *N* – the turns of winding number.

The magnetic permeability value of magnetic core materials is not constant in the function of frequency. To calculate the characteristic of certain material permeability, the approximation of μ_{core} function should be applied. The value of permeability should be compared with catalogue curve estimated by producer. The following equation was applied to present model. The figure 3 presents modeling permeability.

$$\mu_{core}=\mu_i\cdot\frac{1}{\sqrt{f/f_w}}\left(\frac{\sinh(\sqrt{f/f_w})+\sin(\sqrt{f/f_w})}{\cosh(\sqrt{f/f_w})+\cos(\sqrt{f/f_w})}\right) \tag{5}$$

where: $f_w=(4\cdot\sigma)/(\pi\cdot\mu_i\cdot\mu_0\cdot d^2)$, μ_i – initial permeability, σ – resistivity of material, d – thickness of material.

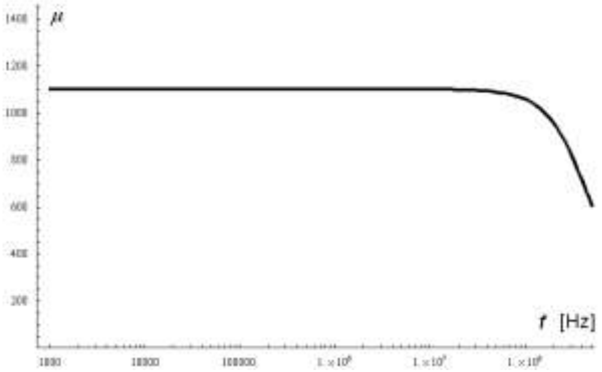

Fig. 3. Magnetic permeability – computer simulation

The resistance R, is equivalent to the total losses in the core, and can be reduced to a sum of three terms R_E, R_H and R_R with correspond respectively to the loss resistance caused by: eddy currents, hysteresis, residual losses (unimportant values).

Resistance R_H is defined as:

$$R_H = \frac{4\cdot\upsilon\cdot B_{\max}}{3\cdot\pi\cdot\mu_0\cdot\mu_i^2}\cdot\omega\cdot L \qquad (6)$$

Resistance R_E is defined as:

$$R_E = \frac{\mu_0\cdot\mu_i\cdot D^2\cdot\omega}{2\cdot\sigma\cdot\beta}\cdot\omega\cdot L \qquad (7)$$

where: ν – Rayleigh coefficient, B_{max}– flux density, β = 16 for a cylinder of diameter D

Capacity C is integrated with coil windings. The typical value of existing capacities between turns of windings and interlayers between theme average several to a few hundred micromicrofarads [1]. Dominating, parasitic capacitance is connected with configuration of coil winding. The capacity between two conductors is defined as:

$$C = 0,278\frac{\varepsilon\cdot l}{\text{arcosh}\left(a/d\right)} \quad \text{pF} \qquad (8)$$

where: d – conductor's diameter [cm]; a – distance between conductors [cm]; l – mutually lenght of conductors [cm]; ε - electric permeability of medium between conductors.

The mathematical model defined (which defined the impedance of core) if formed by putting together equations (2,4,5,6,7,8). To calculations the programme "MATHEMATICA 4.1" was used. The model defines the impedance in different configurations of core. The basic analysis concerns to: variable turns of winding number, different permeability and different geometry of core. The received values of core's impedance are defined in frequency function. Several simulations on Fig. 4, 5, 6 are present.

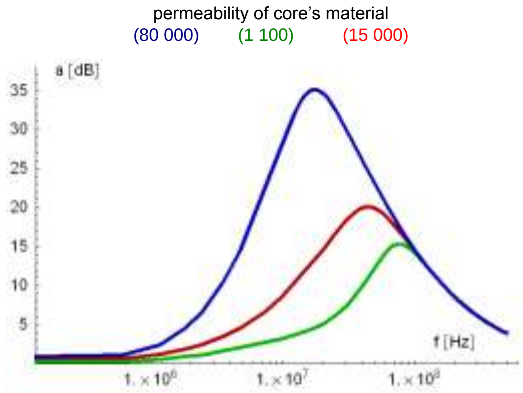

Fig. 4. Insertion loss of bead for different materials (permeabilities)

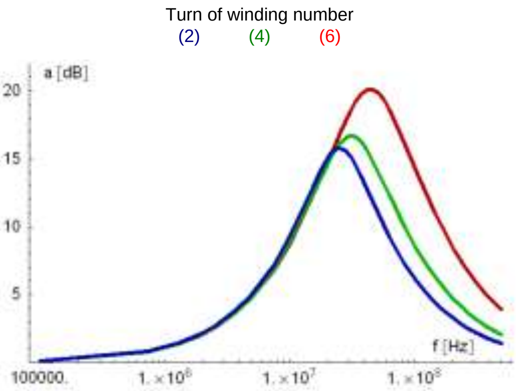

Fig. 5. Insertion loss of bead for different turns of winding number

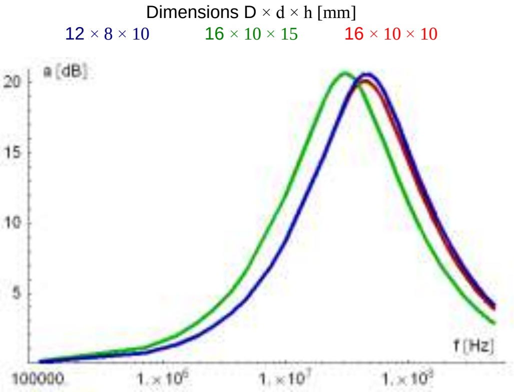

Fig. 6. The influence of overall core dimensions on frequency depends on the insertion loss of bead

CONCLUSION

The electromagnetic interference’s suppression core, dampen electric signals on the all range of frequency spectrum. Realization of these criteria does not mean that all problems connected with disturbances are dissolved. However, presented information enable to make a correct choice choke coils in filter.

Soft magnetic core materials for use in EMI filters must have high values of permeability in the wide frequency range (the higher, the better).

Computer simulations indicated that enlarging the core length, will lead to achieve the same values of insertion loss in lower frequencies.

The modifications in the turn of winding number fundamentally influence the interference’s suppression. The bigger amount of windings is, the higher the value of insertion loss ratio is.

The changes of magnetic permeability cause changes in insertion loss ratio. The bigger magnetic permeability is, the bigger electromagnetic interference’s suppressions are.

ACKNOWLEDGEMENT

This work was financially supported by the Polish State Committee for Scientific Research grant No KBN 3T10A06127.

LITERATURE

[1] P. A. Chattterton, M. A. Houlden, EMC Electromagnetic Theory to Practical Design, John Wiley & Sons, 1991

[2] V. Prasad Kodali, Engineering Electromagnetic Compatibility, IEE PRESS, 2001

[3] H. W. Ott, Metody redukcji zakłóceń i szumów w układach elektronicznych, WNT, 1979

[4] P. A. Mazurek, Model ferrytowego ogranicznika zakłóceń elektromagnetycznych, grant KBN, nr 8T10A01521

[5] P. A. Mazurek, A. Wac-Włodarczyk, Zastosowania materiałów magnetycznie miękkich w ograniczaniu zakłóceń przewodowych, II Krajowe Sympozjum, Kompatybilność elektromagnetyczna w elektrotechnice i elektronice, EMC’01, Łódź, 241-250

[6] J. Petzold, Applications of Nanocrystalline Softmagnetic Cores in Modern Electronics, Soft Magnetic Materials 16, Dusseldorf, Germany, September 9-12 2003, p. 97-106

[7] G. Herzer, Nanocrystalline Soft Magnetic Alloys, Handbook of Magnetic Materials, Vol. 10, Edited by K.H.J. Buschow, Elseview Science, 1997

[8] E. C. Snelling, A. D. Giles, Ferrites for Inductors and Transformers, John Wiley & Sons Inc 1983

5th International Conference **ELMECO**
Nałęczów, Poland
September 2005

EQUIVALENT CIRCUIT MODEL FOR HIGH TEMPERATURE SUPERCONDUCTORS

Dariusz Czerwiński, Leszek Jaroszyński

Institute of Electrical Engineering and Electrotechnologies
Lublin University of Technology
ul. Nadbystrzycka 38A, 20-618 Lublin, Poland
E-mail: darekc@weber.pol.lublin.pl, leszekj@weber.pol.lublin.pl

Abstract

Modern superconducting devices have many parts built of high temperature superconductors. An equivalent circuit model that describes the behaviour of a HTS superconductor viewed by an external user was proposed. From this point of view the most important quantities are voltage and current. The model is based on the physical structure and behaviour of HTS superconductors.

Keywords: AC power losses, high temperature superconductors, PSpice ABM model

INTRODUCTION

High temperature superconductors operates at various conditions depending on the application solution. HTS parts are cooled with cryocooler or using cryogenic liquid. The energy losses in practical superconductor are very small under suitable working conditions. However during the quench process the amount of energy in HTS parts rapidly increases. The circuit model of HTS superconductor will improve the processes analysis during the transient states.

For the purposes of model verification the transient analysis of HTS leads using PSpice environment was made. The simplicity of the model makes it fast and reliable. It is easy to obtain the results and compare them with the other ones based on finite element methods. Applied model is wide-ranging and may represent a HTS superconductor in different applications.

HIGH TEMPERATURE SUPERCONDUCTORS

The superconductors, because of their behaviour, can be divided into type I and type II. Type I superconductors have a clear border between superconducting state and resistivity state. Superconductors of type II have two values of critical magnetic flux density. High temperature superconductors are type II superconductors and the chemical structure of HTS are very specific (Fig. 1). All of HTS superconductors contain copper oxide walls, which act together with other elements as a active blocks conducting current. HTS superconductors contain also the defective regions. Forced current flow through defective regions may lead to a local quenching of superconductivity and the creation of so called hot spots. The deposited quench energy leads to a structural and chemical modification of the HTS material in the neighbourhood of these hot spots. Spreading of the quench zone may finally end up in the destruction of the superconductor.

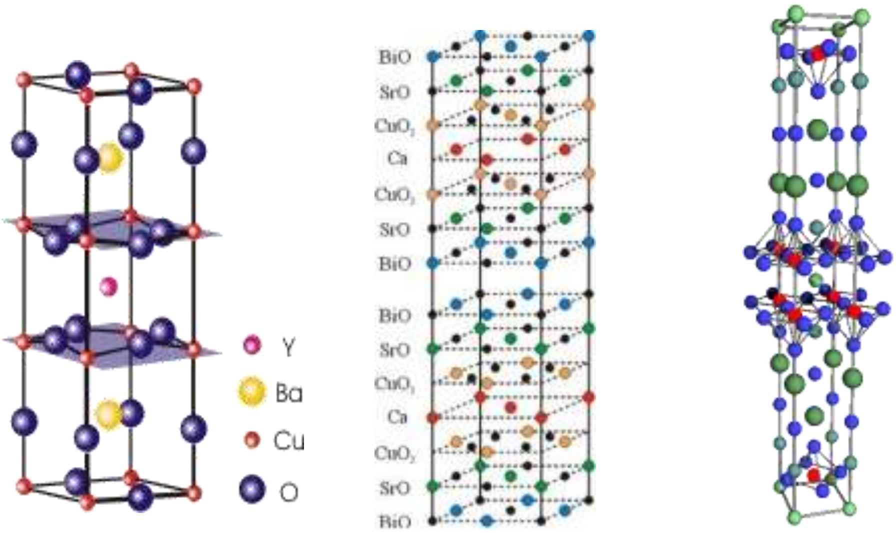

YBCO Bi 2212 Bi 2223

Fig. 1. Structures of HTS superconductors [1]

First purpose of this model was the numerical analysis of the superconducting current lead built of BSCCO. Most of HTS current leads are prepared as ceramic tubes made of YBCO or BSCCO superconductors (Fig. 2).

Fig. 2. Examples of HTS current leads

It is possible to build the current lead basing on HTS tape. This type current leads are designed in CERN laboratory and are working in LHC project. Electro-thermal model of HTS tape vas verified with behaviour of real Bi-2223/Ag tapes leads. [2]

ELECTRO-THERMAL HTS TAPE MODEL

Electric properties of HTS superconductor tape can be described in a simplified form as shown in Fig. 3.

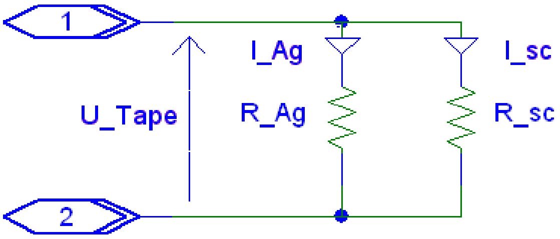

Fig. 3. Equivalent circuit of HTS tape

Silver alloy resistance can be calculated using equation (1):

$$R_{\mathrm{Ag}} = \frac{\rho_{\mathrm{Ag}}(T) \cdot L}{A_{\mathrm{Ag}}} \tag{1}$$

where: $\rho_{\mathrm{Ag}}(T) = \mathrm{a}T + \mathrm{b}$ – silver alloy resistivity; a, b – constants [2]; L – tape length; A_{Ag} – silver alloy cross-section area.

Superconductor resistance can be calculated using formula (2):

$$R_{\mathrm{Bi}} = R_{\mathrm{res}} + \frac{E_{\mathrm{C}} \cdot L}{I_{\mathrm{C}}^{n}} |i|^{n-1} \tag{2}$$

where: R_{res} – SC residual resistance; E_{C} = 10^{-4} V/m; $n = n_0 \frac{T_0}{T}$ – SC n-exponent; n_0 – n-exponent at temperature T_0; $I_{\mathrm{C}} = I_{\mathrm{C0}} \left(\frac{T_{\mathrm{C}} - T}{T_{\mathrm{C}} - T_0} \right)$ – SC critical current (at self field); I_{C0} – critical current at T_0; T_{C} – critical temperature.

Thermal properties of HTS tape in adiabatic condition can be described by the equivalent circuit shown in Fig. 4.

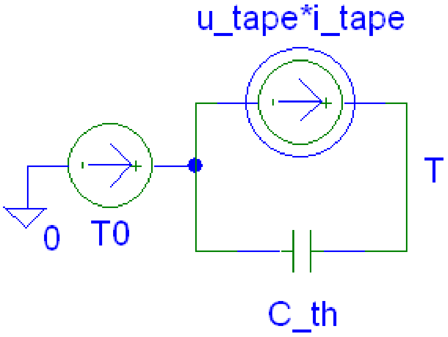

Fig. 4. Simplified thermal equivalent circuit of HTS tape

Uniform HTS tape temperature in adiabatic condition can be calculated using formula (3).

$$T = T_0 + \frac{1}{C_{\mathrm{TH}}} \int_{t_0}^{t_1} (u_{\mathrm{tape}} \cdot i_{\mathrm{tape}})\mathrm{d}t \qquad (3)$$

where: $C_{\mathrm{TH}} = m_{\mathrm{Bi}} C_{\mathrm{pBi}} + m_{\mathrm{Ag}} C_{\mathrm{pAg}}$ – thermal capacity; T_0 – ambient temperature;m_{Bi} – superconductor mass; C_{pBi} – superconductor specific heat; m_{Ag} – silver alloy mass; C_{pAg} – silver alloy specific heat; u_{tape}, i_{tape} – tape voltage and current.

HTS electro-thermal equivalent circuit made of analogue behavioural blocks is presented in Fig. 5.

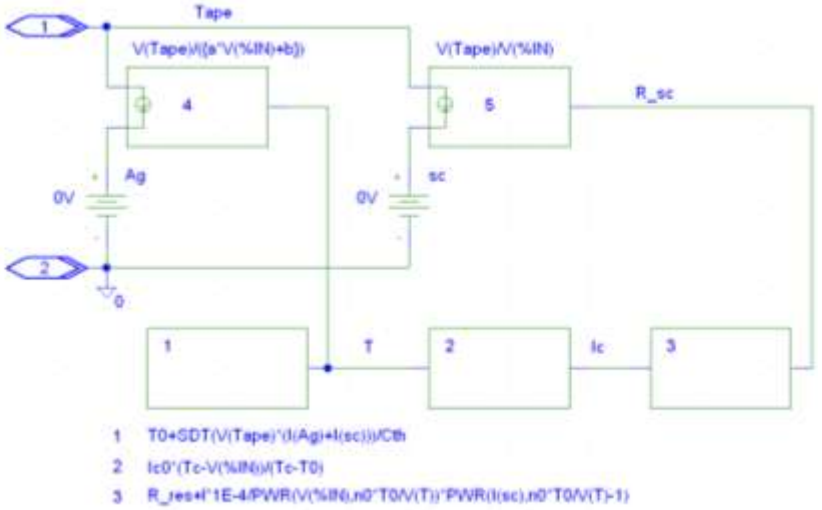

Fig. 5. Equivalent circuit for Bi2223/Ag tape and its simulation parameters
(PSpice ABM blocks: 1, 2, 3 voltage-controlled voltage sources;
4, 5 – voltage-controlled current sources)

Simulation parameters compiled from [2, 3, 4] are described in Table 1.

Table 1. Bi(Pb)-2223/AgAg tape simulation parameters

I_{C0} (77 K, self field)	57 A	R_{res}	10^{-15} Ω
T_C	106 K	a	$6.69 \cdot 10^{-11}$ Ωm/K
A_{TAPE}	3.81 x 0.193 mm^2	b	$-6.90 \cdot 10^{-10}$ Ωm
L	1 m	C_{pBi}	120 J/(kg K)
filling factor	30 %	C_{pAg}	170 J/(kg K)
E_C	10^{-4} V/m	γ_{Bi}	6000 kg/m^3
n_0 (77 K)	15	γ_{Ag}	10500 kg/m^3

NUMERICAL SIMULATION RESULTS

Transient analysis of electro-thermal HTS tape model has been carried out using PSpice. Selected results of the numerical analysis are presented in Fig. 6 and Fig. 7.

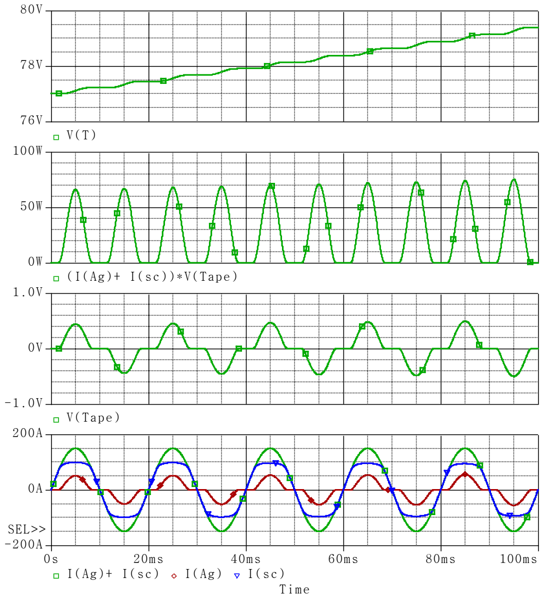

Fig. 6. Temperature, instantaneous power, voltage, current of HTS tape under sinusoidal over-current 150 A_{peak}

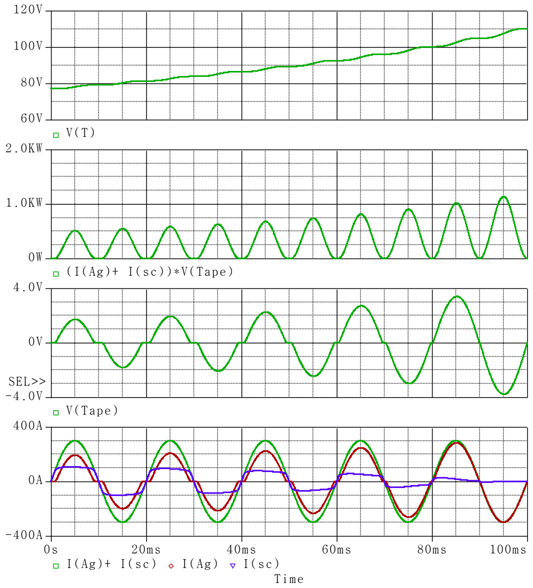

Fig. 7. Temperature, instantaneous power, voltage, current of HTS tape under sinusoidal over-current 300 A_{peak}

CONCLUSION

Physical properties of HTS superconductors vary in a wide ranges and their relation to the temperature, current and magnetic filed is very difficult for implementation in circuit model representation.

AC current overload of HTS superconductors is noticeable but normal resistance develops rapidly when the amplitude of over-current is over three times of the critical current.

Numerical model might be improved: it's necessary to use proper relation between HTS tape specific heat and temperature especially in low temperature range ($T < 20$ K).

Simulation results show good correlation with experimental results [2].

It's possible to use presented in this paper numerical model for simulation of electro-thermal properties of HTS materials in different applications.

REFERENCES

[1] Oomen, Marijn Pieter, *AC loss in superconducting tapes and cables*, Eerste Uitgave 2000, Universiteit Twente

[2] Seong-Woo Yim, Sung-Hun Lim, Hye-Rim Kim Si-Dole Hwang, Kohji Kishiro, Electrical Behavior of Bi-2223/Ag Tapes Under Applied Alternating Over-Currents, *IEEE Transactions on Applied Superconductivity*, vol. 15, No. 2, June 2005

[3] Y. S. Cha, Semi-Empirical Correlation for Quench Time of Inductively Coupled Fault Current Limiter, *IEEE Transactions on Applied Superconductivity*, vol. 15, No. 2, June 2005

[4] T. J. Arndt, A. Aubele, H. Krauth, M. Munz, B. Sailer, Progress in preparation of technical HTS tapes of type Bi-2223/Ag alloy of industrial lengths, *IEEE Transactions on Applied Superconductivity*, vol. 15, No. 2, June 2005

5th International Conference **ELMECO**
Nałęczów, Poland
September 2005

CIRCUIT MODEL FOR CURRENT LEADS MADE OF HTS TAPES

Dariusz Czerwiński, Leszek Jaroszyński

Institute of Electrical Engineering and Electrotechnologies
Lublin University of Technology
ul. Nadbystrzycka 38A, 20-618 Lublin, Poland
E-mail: darekc@weber.pol.lublin.pl, leszekj@weber.pol.lublin.pl

Abstract

Authors propose an equivalent circuit model that describes the behaviour of a current lead build of HTS tapes. Transient analysis of HTS leads using PSpice environment was made. The model is based on the physical structure and behaviour of HTS tapes. It was possible to calculate the temperature distribution in the lead as well as the transient current and power. The quench processes of HTS leads under sinusoidal current with different amplitudes were simulated. Obtained results can be very useful in the analysis of quench states of the superconducting current leads.

Keywords: ABM lumped model, current leads, HTS tapes, PSpice analysis

INTRODUCTION

The development of the HTS tape manufacturing technologies leads to evolution of many superconducting devices. It is possible to build the current lead based on the high temperature superconducting tapes (Fig. 1). For this kind of current leads it is very important to keep the heat sources on the very low level (even 1 Joule).

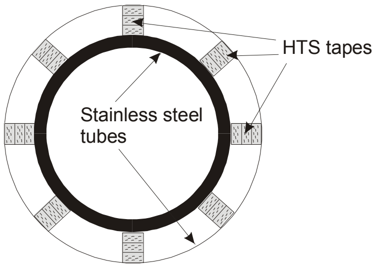

Fig. 1. Current lead build of HTS tapes

HTS TAPES

The discovery of superconductivity generated interest in practical applications, mainly because of its potential to save energy. Replacement of the copper or other normal conductors by superconductors avoids heat dissipation and energy losses due to finite resisitance. Discovery of the HTS materials was the first step in development of new generation superconducting applications. Many of HTS materials are superconductors and carry significant current above the boiling point of liquid nitrogen at 77.4 K.

High performance high temperature superconductor wire underlies the worldwide opportunity to revolutionize the electric power grid, transportation, materials processing and many other industries, with a new generation of high efficiency, compact and environmentally friendly electrical equipment. Rapid progress in commercializing these many applications has been enabled by an HTS wire known as first generation (1G) [1].

This wire is a composite structure consisting of number of filaments of HTS material embedded in a silver alloy matrix. First generation HTS wire is characterized usually by low critical current, therefore many companies are making researches on improved performance of HTS wires (Fig. 2).

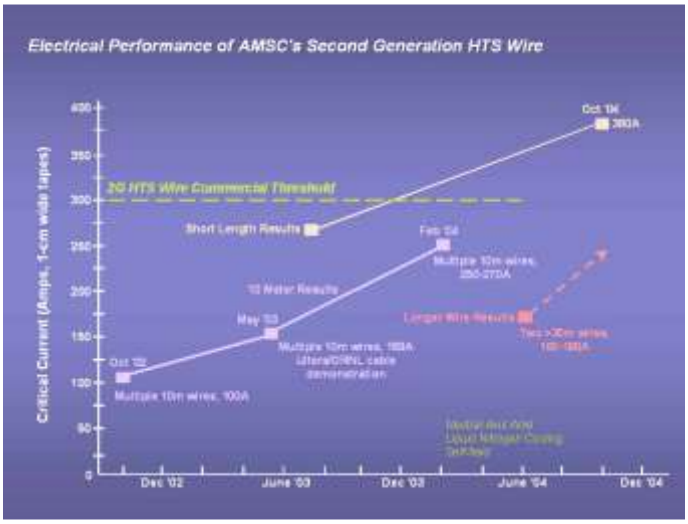

Fig. 2. Development of second generation HTS wire [1]

Second generation wire has quite different architecture compared with first generation wire. The 2G HTS wire comprises multiple coatings on a base material or substrate. This architecture is designed to achieve the highest degree of alignment of the atoms in the superconductor material. The reason of such construction is reaching the highest possible electrical current. The 2G wire architecture consists of slit 2G tape sandwiched between thin copper strips.

Second generation (2G) HTS wire consists of a tape-shaped base, or substrate, upon which a thin coating of superconductor compound, usually $YBa_2Cu_3O_7$ (“YBCO”) is deposited or grown such that the crystalline lattice of the YBCO in the final product is highly aligned, creating a coating that is virtually a single crystal. The superconductor coating in this coated conductor wire architecture typically has a thickness of the order of one micron (Fig. 3) [1].

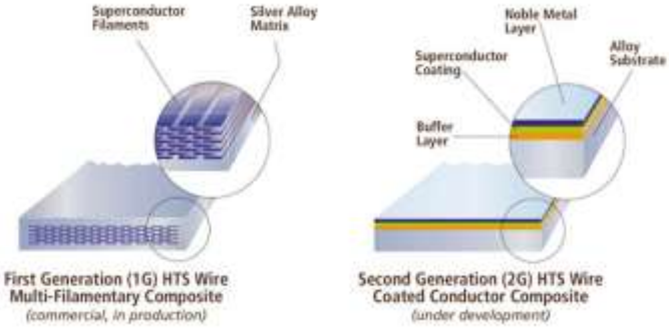

Fig. 3. First generation (1G) versus second generation (2G) HTS tape [1]

Another important aspect in HTS wire is the value of the critical current in external magnetic filed. When the magnetic flux increases the critical current decreases rapidly, even 10 times in some cases. To counteract this disadvantage the HTS wires are produced with special defects, so called pinning centres. Pinning can be achieved by introducing defects into the HTS material on a nanometer scale, comparable to the diameter of the flux lines passing through the HTS surface. While tubular defects can match the flux line geometry most optimally, a more practical approach is to find ways to introduce a high density of very fine particles called nanoparticles or nanodots.

The magnetic field angle dependence of the critical current density is another important aspect of the pinning phenomenon. Depending on the type and orientation of the pinning defects, the pinning can be different along different magnetic field directions (Fig. 4) [1].

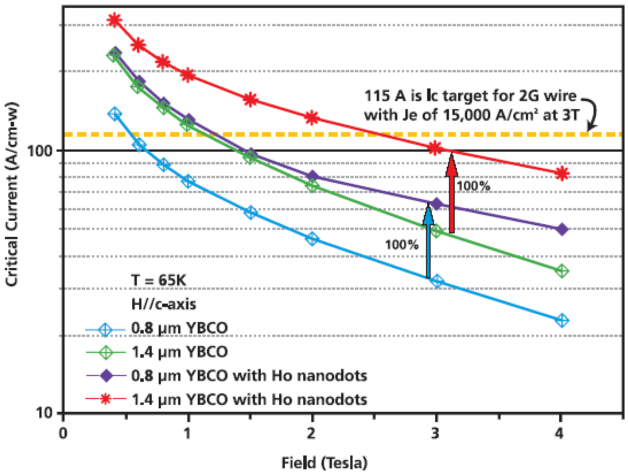

Fig. 4. Magnetic field dependence of HTS wire with and without holmium, 3 T (field perpendicular to sample plane) [1]

CURRENT LEADS

Current leads are used for energy transfer between superconducting devices and power supplying system. In such cryogenic application, it is necessary to pass electrical current from a power source at room temperature to a particular device at cryogenic temperatures. These current can range from a few milli-Amperes for instrumentation to 10 000 Amperes for high magnetic field superconducting magnets. The design of cryogenic power leads must attempt to minimize the refrigeration/liquefaction system capacity required for stable operation.

Fig. 5. Conventional current leads

Conventional current leads are usually made of conductor (copper) and cooled with liquid nitrogen or liquid helium (Fig. 5).

With HTS development current leads gain new compact design and better capabilities. HTS superconducting current leads architecture usually comprises of HTS tube with silver ends (for better connection) and/or shield made of metal or plastic (Fig. 6).

Fig. 6. Different types HTS current leads

The authors built the numerical model basing on existing HTS current lead design. [2] Current lead is made of HTS tapes connected together as shown in figure 7. HTS tape pieces are placed on tube support made of copper or stainless steel. The outer jacket performs a function of electrical insulation and mechanical protection.

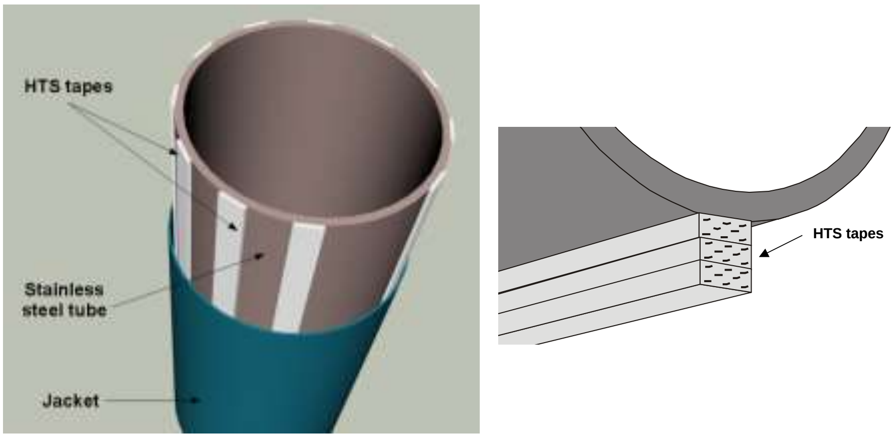

Fig. 7. Current lead made of HTS BSCCO tapes

ELECTRO-THERMAL LUMPED MODEL

Transient circuit analysis is performed in domain of time. To get basic distribution of an interesting physical quantity (for instance: temperature) along a slender object as a current lead it's necessary to make certain simplifying assumptions. In numerical experiment described below AC losses have been neglected.

Our ABM lumped model of the HTS current lead consists of series connection of 48 segments. Electrical properties of HTS tape can be described as a parallel connection of silver alloy and superconductor (Fig. 8). Resistivity of silver alloy can be expressed as a linear function of temperature [2]. Resistivity of a HTS can be described by power law $E \sim J^{n}$.

Uniform segment temperature of HTS current lead can be expressed as (1) and it is computed using equivalent circuit (Fig. 9).

$$T = T_0 + \frac{1}{C_{\mathrm{TH}}} \int_{t_0}^{t_1} \left(u_{\mathrm{tape}} \cdot i_{\mathrm{tape}} + \frac{T_{\mathrm{p}} + T_{\mathrm{n}} - 2T}{R_{\mathrm{cond}}} + \frac{T_0 - T}{R_{\mathrm{conv}}} \right) \mathrm{d}t \qquad (1)$$

where: $C_{\mathrm{TH}} = m_{\mathrm{Bi}} C_{\mathrm{pBi}} + m_{\mathrm{Ag}} C_{\mathrm{pAg}}$ – thermal capacity of current lead segment;

T_0 – ambient temperature;
m_{Bi}, m_{Ag} – superconductor and silver alloy masses per segment;
C_{pBi}, C_{pAg} – superconductor and silver alloy specific heats;
u_{tape}, i_{tape} – voltage and current of the current lead segment;
T_{p}, T_{n} – inter-segment boundary temperatures;
R_{cond}, R_{conv} – heat conduction and convection equivalent representations (heat radiation neglected).

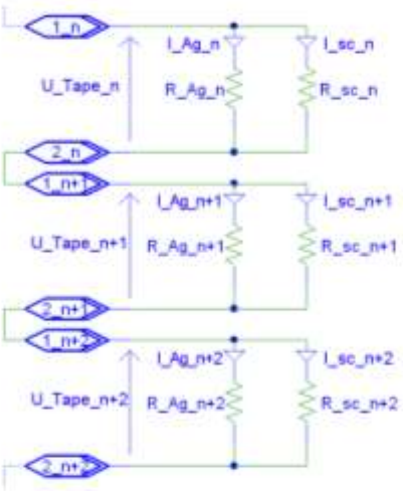

Fig. 8. Lumped circuit model of HTS current lead

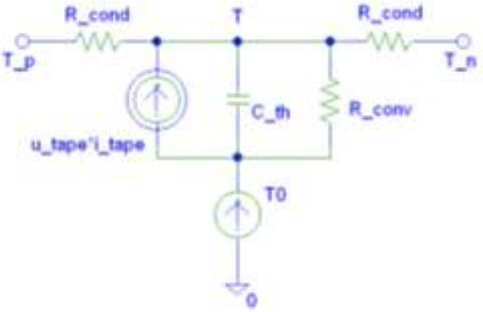

Fig. 9. Thermal equivalent circuit of HTS current lead segment

Electro-thermal lumped model of HTS current lead is depicted in Fig. 10. Each of 48 elementary segments has the same subcircuit diagram shown in Fig. 11.

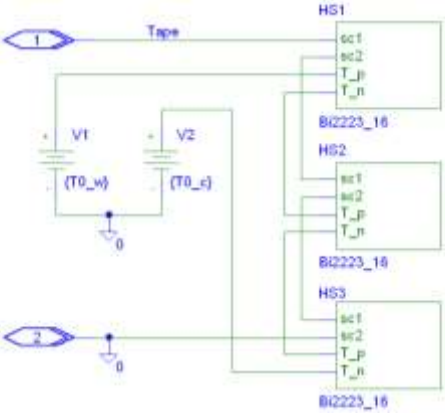

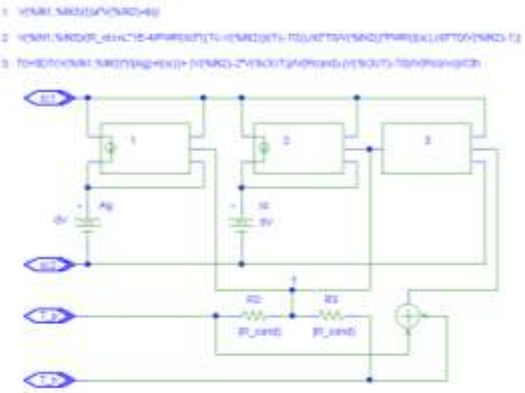

Fig. 10. HTS current lead simulation circuit containing three subcircuits (each of sixteen segments): T_{0_W}, T_{0_C} – warm and cold end temperatures

Fig. 11. Elementary lumped parameter segment of HTS current lead: 1, 2 – voltage_controlled current source, 3 – voltage-controlled voltage source

Numerical simulation parameters have been compiled using [2, 3, 4, 5]. They are presented in Table 1.

Table 1. Simulation parameters of HTS current lead
(33 x HTS tape; Bi(Pb)-2223/AgAu)

I_{C0} (77 K, self field)	16 A	a	$7.1\cdot10^{-11}$ Ωm/K
T_C	100 K	b	$-6.6\cdot10^{-10}$ Ωm
A_{TAPE}	4.30 x 0.25 mm^2	C_{pBi}	120 J/(kg K)
L	48 x 7.29 mm	C_{pAg}	170 J/(kg K)
tape filling factor	30 %	γ_{Bi}	6000 kg/m^3
E_C	10^{-4} V/m	γ_{Ag}	10500 kg/m^3
n_0 (77 K)	15	h_{conv}	1500 W/(m^2 K)
R_{res}	10^{-15} Ω	λ_{cond}	200 W/(m K)
T_{0W}	77 K	T_{0C}, T_0	20 K

NUMERICAL SIMULATION RESULTS

Transient analysis of the current lead has been performed using PSpice. Comparison of the current lead performance under its nominal current and short over-current is depicted in Fig. 12 and 13. Response to long lasting over-current is shown in Fig. 14 and 15.

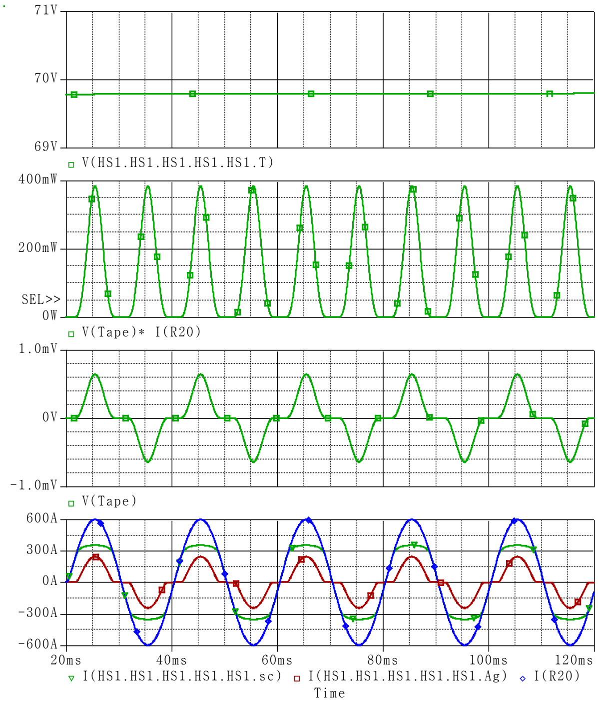

Fig. 12. Temperature (stated here in Volts) of the warmest segment, instantaneous power, voltage and currents of HTS current lead under nominal current I_N = 600 A$_{peak}$

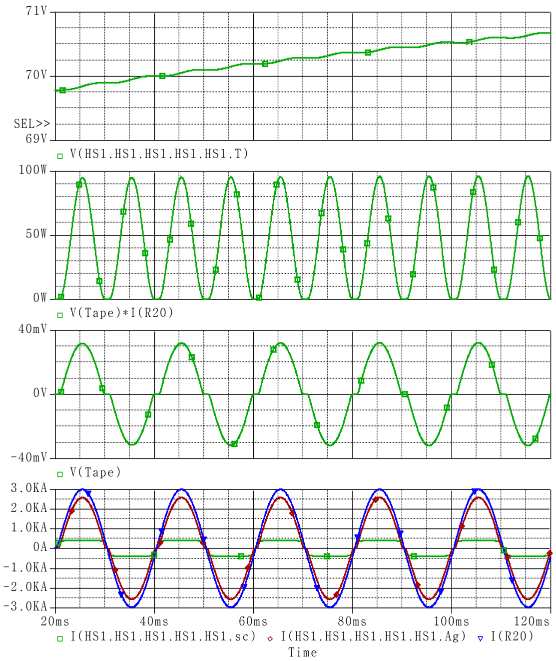

Fig. 13. Temperature of the warmest segment, instantaneous power, voltage and currents of HTS current lead under over-current I = 3000 A_{peak}

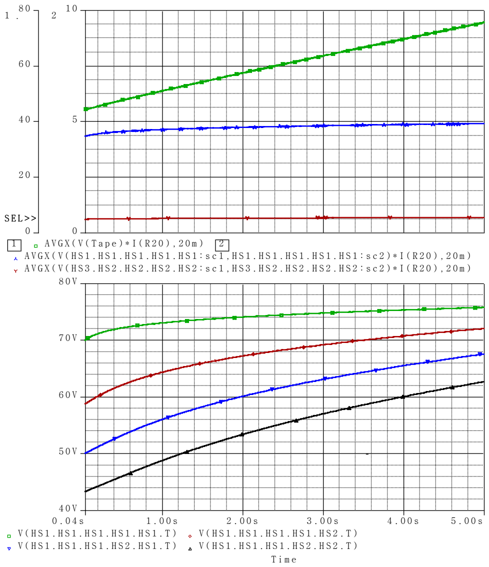

Fig. 14. Average power of the whole lead, average power of the warmest and the coldest segments (top); temperatures of first four segments (bottom) vs. time under over-current I = 3000 A_p

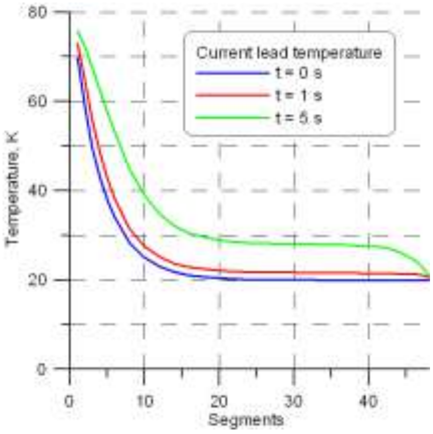

Fig. 15. Temperature distribution along HTS current lead under over-current I = 3000 A_p

CONCLUSION

Evolution in high temperature superconductor manufacturing allows to build modern and compact superconducting devices.

Circuit modeling of HTS tape is leading to complicated mathematical expressions which take into account geometric, thermal and electrical properties of the HTS.

It's possible to perform simplified electro-thermal analysis (coupled problems) using common circuit simulator like PSpice.

Nested sub-circuit simulation permits to perform numerical analysis of lumped-parameter systems. The maximum number of sub-circuits depends on computer resources.

Numerical simulation shows remarkable overload performance of HTS current lead. Short period AC over-currents doesn't pose a threat for system stability. Fastness to long lasting over-currents depends on cooling system efficiency.

REFERENCES

[1] American Superconductor Corporation, http://www.amsuper.com/, 2005

[2] Seong-Woo Yim, Sung-Hun Lim, Hye-Rim Kim Si-Dole Hwang, Kohji Kishiro, Electrical Behavior of Bi-2223/Ag Tapes Under Applied Alternating Over-Currents, *IEEE Transactions on Applied Superconductivity*, vol. 15, No. 2, June 2005

[3] Y. S. Cha, Semi-Empirical Correlation for Quench Time of Inductively Coupled Fault Current Limiter, *IEEE Transactions on Applied Superconductivity*, vol. 15, No. 2, June 2005

[4] T. J. Arndt, A. Aubele, H. Krauth, M. Munz, B. Sailer, Progress in preparation of technical HTS tapes of type Bi-2223/Ag alloy of industrial lengths, *IEEE Transactions on Applied Superconductivity*, vol. 15, No. 2, June 2005

[5] I. Bogdanov, S. Kozub, K. Myznikov, P. Slabodchikov, V. Sychev, V. Sytnik, L. Vassiliev, V. Zubko, I. Akimov, N. Gryaznov, D. Rakov, A. Shikov, Application of HTS Bi-2223 for current leads of superconducting magnets, *Proceedings of EPAC 2000*, Vienna, Austria

5th International Conference **ELMECO**
Nałęczów, Poland
September 2005

THE PROJECT OF TRANSFORMER TYPE OF SUPEROCONDUCTING FAULT CURRENT LIMITER

Joanna Kozieł, Tadeusz Janowski

Lublin University of Technology
Institute of Electrical Engineering and Electrotechnologies

Abstract

Experimental results of transformer type Superconducting Fault Current Limiter are described in this paper. The primary winding of the transformer is connected in series to the power line. Secondary winding is short-circuited through the HTS tape. We used to different tapes with critical current 60 A and 125 A as limiting devices cooled down in liquid nitrogen V-I characteristic and current courses are also presented.

Keywords: SFCL, superconducting element, superconducting fault current limiter.

INTRODUCTION

The short – circuits in power network are very important risks for transformers, generators, busbars and transmission lines as well as they decrease the energy supplies reliability to consumers of electric energy. The limitation of fault current with the use of impedance coil and adequately big reactance of transformer has an significant effect on the increase of the costs of building and operation electric power system, as well as the price of electric power. The biggest actual value of fault current (dynamic current) causes that the dynamic effects forces arised in electromagnetic devices flow through them during the short - circuits. The maximum value of the mechanic forces of fault current usually appears, when the current reaches the first maximum after the short- circuit, it is 0.005 second and the frequency 50Hz (Fig.1). If we break off the short circuit or we increase its impedance rapidly in much shorter time, than 0.005 second, then dynamic force do not reach first maximum and do not make excessive stretches as well as electromagnetic devices defects in short circuit [1].

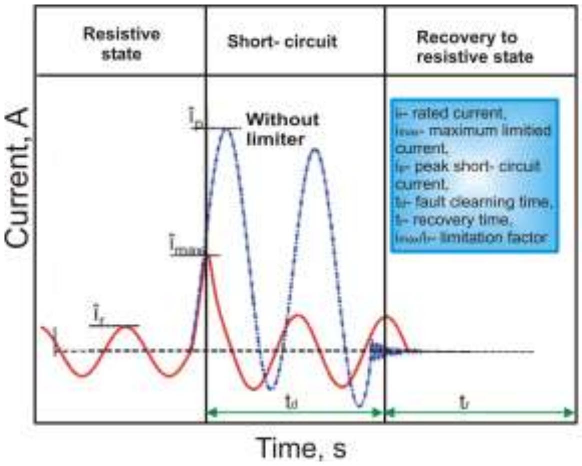

Fig.1. Idea the operation of superconducting fault current limiter [2]

Quick and infallible operation of electric power network may be assured by superconducting fault current limiters (Fig.2), because the time when superconductor transforms from superconductor to resistance state lasts tens microsecond, but their return to usual operation is almost immediate and do not require any human interference.

Superconductors reveals entire disappearance of resistivity only in conditions, when parameters like: temperature, current density, magnetic flux density do not exceed certain values, called critical values. Properties of the rapid resistance value increase in the superconducting limiting element enables to build superconducting fault current limiter in power network, only when superconducting limiting element exceed current critical value.

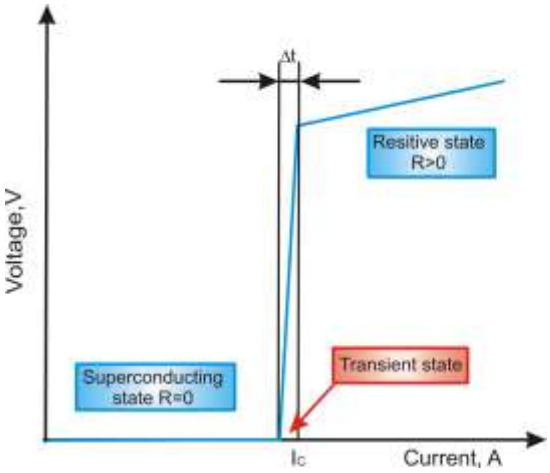

Fig. 2. Real value I-U of superconducting fault current limiting [1]

There exist two types of superconducting fault current limiters: resistance and inductance one. Resistance limiters are very simple in its structure, but they require working current being conduced to the superconducting limiting element by using current leads. Inductive fault current limiter are very similar in structure to current transformers, in which secondary winding is shorted by a superconducting wire, the most widely is used ring made of superconducting ceramics. Superconducting fault current limiting transformer type is a kind of inductive limiter, in which secondary winding is classically designed, but is shorted for a superconducting limiting element.

SUPERCONDUCTING FAULT CURRENT LIMITER TRANSFORMER TYPE

Superconducting fault current limiting transformer type is a kind of inductive limiter, in which secondary winding is classically designed, but is shorted for a superconducting limiting element. The primary winding of superconducting fault current limiting transformer type input in series in protect circuit similarly like current transformer, and limiting superconducting element we can connect to the clamps of secondary winding. This is presented on Fig.3.

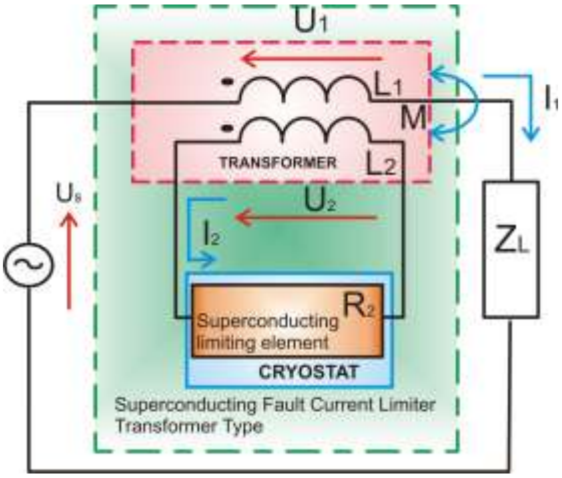

Designation on Fig.3: I_1- current on primary winding of transformer, I_2 -current on secondary winding of transformer, U_1 –voltage on primary winding of transformer, U_2- voltage on secondary winding of transformer, L_1 –self- inductance of primary winding, L_2- self-inductance of secondary winding, U_S - voltage source of energy, M –mutual inductance, Z_L – loading, R_2 – resistance of limiting superconducting element.

Fig. 3. Circuit configuration of superconducting fault current limiter transformer type

The one of advantages of superconducting fault current limiter transformer type is the possibility of using superconducting element of any shape in simple cryostat, without current transformers. The main defect of superconducting fault current limiter transformer type is the require of bigger resistance in non- superconducting state, in order to fill up desired level limited current.

The core and cooper winding, the primary and secondary winding are located on ferromagnetic core on ambient temperature, and superconducting element made of High Strength Conductor (HTS) is located in cryostat, which we can cooling liquid nitrogen. The idea of building is on Fig.4. The primary winding inputs in series in protect circuit of power network and the secondary winding is shorted by resistanceless superconducting limiting element, that its value of critical current is the same of value current – rise the protect circuit. When current of winding exceed the permissible value, that the value of critical current of superconducting limiting element will be exceed and is lossing the superconductivity.

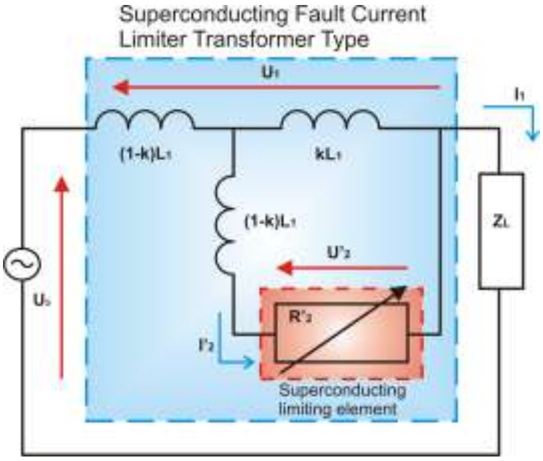

Fig. 4. The equivalent circuit of transformer type superconducting fault current limiter [3]

The transient superconducting limiting element is rapidly to resistive state. In several microsecond will be increase resistance of secondary winding in SFCL and current transformer changes in impedance coil, that limits current in protect circuit. Fault current do not reach first maximum during the quickly operation. It protects the electric devices like transformers from effects of mechanic forces. So far, it build SFCL inductive type has superconducting second winding single coil in form of HTS tube. The disadvantages of this solution are mechanic stresses and cracks. Superconducting fault current limiter of transformer type has not this disadvantage and is simply in building. The aim of experience on superconducting fault current limiter of transformer type is definition of influence the inductance in secondary copper winding for time , when SFCL is operated. In the aim to investigate the scientific research: the influence on parameters of second winding on work SFCL we build the model and carry out an experiment, in that determine parameters of model.

PHYSICAL MODEL OF THE TRANSFORMER TYPE SFCL

The physical model of transformer type superconducting fault current limiter with superconducting limiting element made of Bi-2223 High Strength Conductor tape with critical current 125 A, was designed and built in Laboratory of Superconducting Technologies [6]. Technical parameters of the model and superconducting limiting element are presented in table 1.

The bobbin of the superconducting limiting element was made of polyamide material ERTALON 6 S.A. This material is characterizes by high stiffness and mechanical strength, high stability of shape, good thermal endurance and abrasion resistance, very good electrical strength, high vibration damping and very high impact resistance. Figure 5 shows ready superconducting limiting element of transformer type SFCL made in Laboratory of Superconducting Technologies.

Table 1. Parameters of superconducting limiting element and winding of transformer type SFCL[6]

Parameter	Value
Tape Bi -2223	High Strength Conductor
Thickness of tape	0.29÷0.32 mm
Width of type	4.0÷4.4 mm
Critical current	125A/77K
Critical current density	9.8kA/cm^2
Maximal stress	296Mpa/77K
Maximal bending diameter	0.15%/77K
Minimal bending diameter	50mm
Winding	Cylindrical
Height of winding	260 mm
Diameter of winding	112 mm
Number of turns	40
Number of layers	1
Winding pitch	2.3 mm

Discuss model of SFCL was build on existing one phase test transformer which parameter are presented in table 2.

Fig. 5. Superconducting limiting element of transformer type SFCL

Table 2. Electrical parameters of transformer for model of transformer type SFCL [6]

Parameter	Value
Transformer type	TW1a
Primary voltage	220/230V
Frequency	50Hz
Power	1kVA
Testing voltage	2kV
Secondary current	80÷1000 A

Owing to change the value of transformers turn- ratio we may set the wide range of operating current of the limiter, depending on value critical current of superconducting winding.

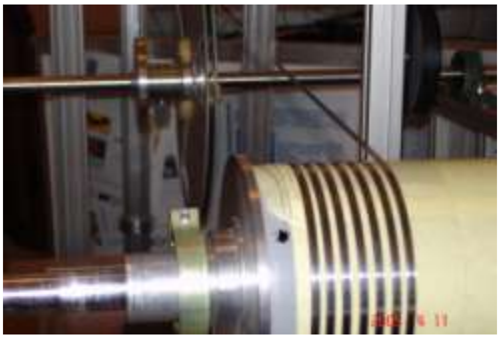

Fig.6. During winding of made superconducting limiting element (115A American Superconductor)

EXPERIMENTAL CIRCUIT WITH SUPERCONCUCTING COMPONENT

From the result of this experiment is U-I characteristic in ambient temperature, by cooling superconducting limiting element liquid nitrogen (77K). In this time we analyze the result of experiment of limiting current in SFCL transformer type and shape of U-I characteristic of SFCL.

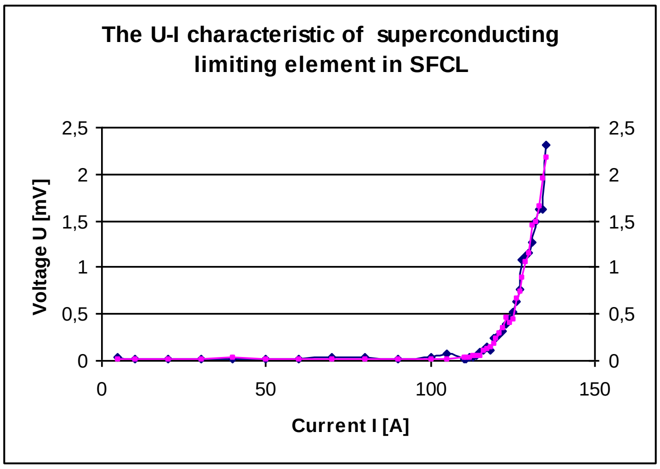

Fig.7. The U-I characteristic of superconducting limiting element in SFCL

With regard a various superconducting fault current limiter is not possible to elaborate universal mathematic model as well as the equivalent circuit of superconducting fault current limiter for all type. .During the creating mathematic equations we take into consideration so much aspect.

CONCLUSION

The main advantage of SFCL transformer type is possibility of using high resistivity superconductors in resistive state at 77K. in case of using superconductors tapes with silver matrix we have to build winding with high number of turns in order to obtain adequate value of windings resistance in resistive state.

REFERENCES

[1] Noe M., *Superconducting fault current limiters*, Summer School on Materials and Applications on Superconductivity, July 23-27, 2007 at Forschungszentrum, Karlsruhe, Germany

[2] Janowski at all, *Nadprzewodnikowe ograniczniki prądu*, Wydawnictwo Liber, Lublin 2002

[3] Yamaguchi H., Yoshikawa K., Nakamura M., Kataoka T., Kaiho K., Current Limiting Characteristics of Transformer Type Superconducting Fault Current Limiter, IEEE Transactions on Applied Superconductivity, Vol.15, No.2, June 2005, pp.2106-2109

[4] Janowski T., Kozak S., Kondratowicz-Kucewicz B.,Wojtasiewicz G., Kozak J., Analysis of Transformer Type Superconducting Fault Current Limiters, IEEE Transactions on Applied Superconductivity, Vol. 17, No. 2,June, 2007, pp. 65-72

[5] Kozak S., Janowski T., *Materiały nadprzewodnikowe dla nadprzewodnikowych ograniczniczów prądu,* Prace Naukowe IPEE Politechniki Wrocławskiej,nr 44, s. Konferencje nr 18 (Postepy w Elektrotechnologii), Wrocław – Jamrozowa Polana, 20-22 września 2006, str. 277-284

5th International Conference **ELMECO**
Nałęczów, Poland
September 2005

SUPERCONDUCTING HTS TAPES FOR TRANSFORMER WINDINGS

Grzegorz Wojtasiewicz

Electrotechnical Institute in Warsaw - Selfdependent Laboratory of Superconducting Technologies in Lublin
38a Nadbystrzycka Str., 20-618 Lublin, Poland
E-mail: grzegorz@eltecol.pol.lublin.pl

Abstract

One of the most interesting applications of superconducting technologies is using high-temperature superconductors for windings of superconducting transformers. The usage of superconducting transformers windings, instead of conventional ones, bring more benefits such as: low ac losses, smaller weight and volumes of magnetic core and windings as well as high efficiency and low cost of refrigeration.

The main aim of this presentation is the comparison of 1st and 2nd generation High-Tc superconducting tapes in consideration with their application in windings of superconducting transformers, taking mechanical strength of the tapes, their critical current, stresses and strains acting in the windings during their work at normal conditions, and maximal operating current of the windings into consideration.

Keywords:** **1st and 2nd generation HTS tapes, stresses and strains, superconducting windings, working current of winding

INTRODUCTION

One of the most important problems, connected with designing and using superconducting transformers is the influence of electromagnetic and dynamic forces, such as strains and stresses on the windings, because of brittle ceramic structure of HTS tape that was used to make the windings.

Electromagnetic forces acting on windings of superconducting transformers, that occur as a result of influence of alternating magnetic field on the conductors carrying current, are much bigger than forces acting in conventional transformers, even during operating at normal conditions. It is because the current density in superconducting windings is at least order of magnitude bigger than in copper ones [1].

The main aim of this paper is the comparison of 1st and 2nd generation High-Tc superconducting tapes in consideration with their application in windings of superconducting transformers, taking mechanical strength of the tapes, their critical current, stresses and strains acting in the windings during their work at normal condition, and maximal operating current of the windings into account.

Specially for the purpose of this comparison the windings made of 1st and 2nd generation High-Tc superconducting tapes have been designed, and the distribution of magnetic field density of the windings, and their components, have been obtained. According to obtained results the stresses and strains acting in that windings and their maximal operating current have been determined too.

1STAND 2ND GENERATION HIGH –TC SUPERCONDUCTORS

1st generation high-Tc superconductors are the bizmuth ceramic's tapes (Bi-2212 and Bi-2223). BISCCO tapes are composite materials consisted of superconducting fibers with high stiffness (tape core) and are surrounded by a metal matrix (pure silver) or alloy matrix (silver + metal) with considerably higher ductility. Because of anisotropic structure of the tape their stiffness and strength will be different in radial direction than in axial ones. Figure 1 shows the texture of 1st generation HTS tape. Table 1 describes parameters of 1st generation Bi-2223 tapes used for transformer's winding [2].

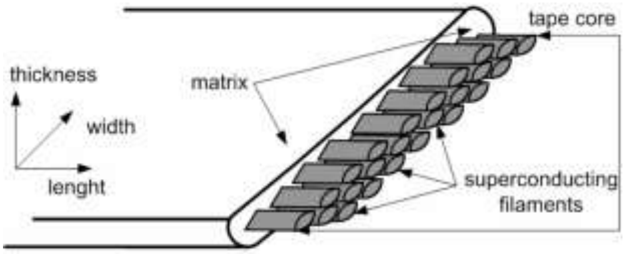

Fig. 1. Texture of 1st generation HTS tape [2]

Table 1. Parameters of 1st generation Bi-2223 tapes for transformer's windings

Width cm	Thickness cm	Maximal stress MPa	Critical current I_c, A	Critical current density J_c, A/cm^2
0.31	0.016	75	> 75	14,4
			> 80	15,4
			> 85	16,3
			> 90	18,1
0.41	0.021	75	> 125	14,5
			> 135	15,7
			> 155	18,1
0.31	0.025	265	> 75	9,7
			> 80	10,3
			> 85	10,7
0.41	0.0305	265	> 115	9,2
			> 125	10,0
0.2	0.015	100	30 - 60	10,0 – 20,0
0.4	0.035	150	30 - 60	2,1 – 4,3

2^{nd} generation high-Tc superconductors are YBCO coated conductor composites. YBCO wire bases on a flexible metal substrate, oxide layers, and YBCO superconducting layer. Positioning the superconductor layer between the metalic substrate and copper stabilizer layer results in a neutral axis configuration that enhance the mechanical, electrical and thermal properties of the tape [3], [4]. Figure 2 shows the texture of 2^{nd} generation HTS tape. Table 2 describes parameters of 2^{nd} generation YBCO tapes.

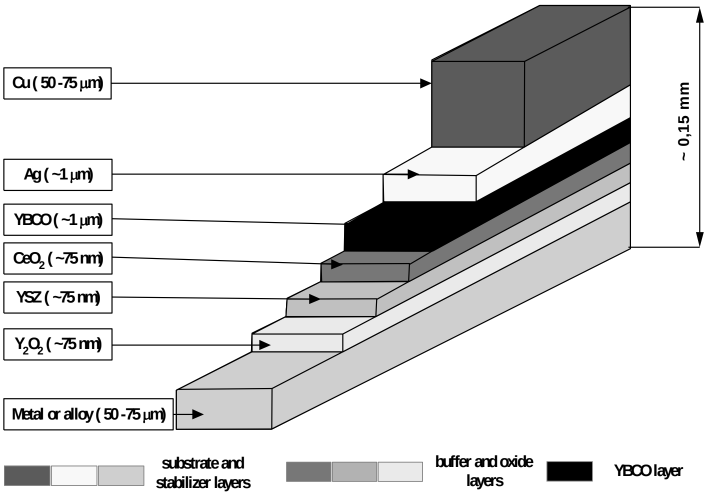

Fig. 2. Texture of 2^{nd} generation HTS tape

Table 2. Parameters of 2^{nd} generation YBCO tapes [3]

Engineering critical current density	10 000 – 20 000 A/cm^2 at temperature 30–65 K and magnetic field 3 T
Critical current – *I*C	1000 A/cm-width width at temperature 77 K and self-field
Operating current – *I*	100 – 200 A
Stabilizer design, stress	200 MPa (300 MPa) at temperature 77 K
Irreversible strain limit	tension – 0,6 % compression – 1 %
Minimal bend diameter	2 cm
Filament size	> 10 μm
Substrate thickness	25 – 75 μm
Tape width	< 1 cm
Piece length	~ 1000 m

Number of substrate and stabilizer layers, their parameters and composition decisively influence the mechanical strength of the 2^{nd} generation high-Tc superconducting tapes. By changing the thickness and width of both substrate and stabilizer layers or changing composition of substrate alloy, we can improve the mechanical and thermal parameters of the tapes and their mechanical strength [4] (see Table 3).

Table 3. Mechanical strength of 2nd generation HTS tapes versus composition of substrate alloy [4]

Composition of substrate alloy	Maximal stress of the tape [MPa]
Ni	34
Ni + 7% Cr	64
Ni + 9% Cr	87
Ni + 11% Cr	102
Ni + 10% Cr + 2% W	150
Ni + 5% W	165
Ni + 6% W	197
Ni + 8% Cr + 4% W	202
Ni +13% Cr + 4% Al.	228
Ni + 9% W	270
Hastelloy C-275 – 60% Ni + 5% Fe + 15% Cr + 16 % Mo	360
Inconel – 60,5% Ni + 15,1% Fe + 23% Cr + 1,4% Al	440
Inconel 625 – 66% Ni + 21,5% Cr + 9% Mo + 3,5% Al	520

MECHANICAL FORCES ACTING ON SUPERCONDUCTING WINDINGS DURING WORK AT NORMAL CONDITIONS

During superconducting transformer's work the stress and strains acting on superconducting windings may exceed their maximal value even if operating current is lower than critical current of the superconducting tape that was used to make the windings. Also electormagnetic forces acting on superconducting windings are much bigger than forces acting in conventional transformers, even during work at normal conditions, because the current density in superconducting windings is at least order of magnitude bigger than in copper ones.

One of the most important criterion of operating current selection is the maximal strength of the superconducting tape. The increase of operating current value up to the value of critical current of the superconducting tape, may induce the electromagnetic forces which exceed the maximal strength of the tape and may destroy them. The selection of operating current of the superconducting transformer may be accomplished by using the load graph of the winding which is a function of maximal stress and critical current of the superconducting tape that was used to make the winding [5], [6].

LOAD GRAPHS OF THE SUPERCONDUCTING TRANSFORMER'S WINDINGS MADE OF 1ST AND 2ND GENERATION HIGH -TC SUPERCONDUCTORS

To compare 1st and 2nd generation High-Tc superconducting tapes in consideration of their application in windings of superconducting transformers, these windings have been designed. The distribution of magnetic field density of the windings have been obtained and the electromagnetic forces acting on each of the windings have been calculated [5]. After analysing previous results the load graphs and operating current of the windings have been determined.

Each winding designed have the same number of windings, height, interlayer between primary nad secondary coil and inner radius of the coils. They have also been designed on the same nominal current and the same primary and secondary voltage. The only differences between windings are the type of superconducting tape, that was used to make them (BISCCO and YBCO tapes) and thickness of primary and secondary coil of each winding, what results from different dimension of that tapes. Figure 3 shows the draft of each winding. Table 4 describes parameters of the winding made of 1st generation superconducting tape (Bi-2223 tape).

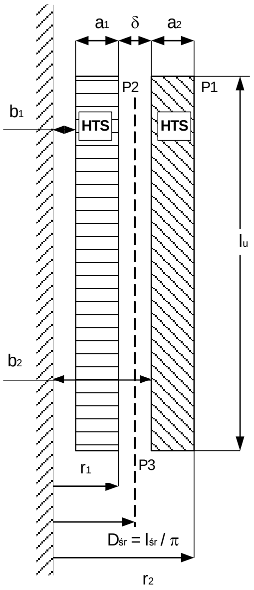

Fig. 3. Draft of superconducting transformer windings

Table 4. Parameter of winding made of 1st generation superconducting tape

Winding's parameters			
Superconductor	1st generation high-Tc superconductor Bi-2223		
Tape cross-section		mm²	0,496
Width / thickness of tape		mm	3,1 x 0,16
Critical current		A	60
Mechanical Strenght		MPa	75
Winding's dimension			
a_1	0,002 m	δ	0,008 m
a_2	0,002 m	l_u	0,093 m
b_1	0,043 m	$D_{śr}$	0,098 m
b_2	0,053 m	$l_{śr}$	0,308 m
r_1	0,045 m	No of turns $z_1 = z_2$	120
r_2	0,055 m	No of layers $m_1 = m_2$	4

Table 5 presents parameters of 6 various windings made of 2nd generation superconducting tape (YBCO tape). The only difference between these windings is the dimension of primary and secondary coil of each winding, that resulted from different width of tapes Tp1 – Tp6.

The distributions of magnetic flux density and electromagnetic forces were obtained in surfaces P1, P2 and P3 where the influence of the magnetic field on the value of electromagnetic stresses and strains was expected to be the highest. P1 is the outer surface of outer coil. P2 and P3 are surfaces between coils where the value of electromagnetic forces is the highest where P2 is the outer surface of inner coil and P3 is the inner surface of outer coil. The analyses were made for the current range 5 – 60 A as far as the Bi-2223 tape with critical current 60 A is concerned, and for the current 5 – 150 A as far as the YBCO tape with critical current 150 A is concerned.

Table 5. Parameters of windings made of 2nd generation superconducting tape

Winding’s parameters							
Superconductor		2nd generation high-Tc superconductor YBCO					
Tape		Tp 1	Tp 2	Tp 3	Tp 4	Tp 5	Tp 6
Tape cross-section	mm^2	0.75	0.9	1.05	1.2	1.35	1.5
Width / thickness of tape	mm	5 x 0.15	6 x 0.15	7 x 0.15	8 x 0.15	9 x 0.15	10 x 0.15
Critical current	A	150	150	150	150	150	150

Winding’s dimension						
Parameter	Tape					
	Tp 1	Tp 2	Tp 3	Tp 4	Tp 5	Tp 6
a_1 [m]	0.0042	0.0047	0.0057	0.0057	0.0067	0.0077
a_2 [m]	0.0042	0.0047	0.0057	0.0057	0.0067	0.0077
b_1 [m]	0.043	0.043	0.043	0.043	0.043	0.043
b_2 [m]	0.053	0.053	0.053	0.053	0.053	0.053
r_1 [m]	0.0472	0.0477	0.0487	0.0487	0.0497	0.0507
r_2 [m]	0.0572	0.0577	0.0587	0.0587	0.0597	0.0607
δ [m]	0.008	0.008	0.008	0.008	0.008	0.008
l_u [m]	0.093	0.093	0.093	0.093	0.093	0.093
$D_{\acute{s}r}$ [m]	0.1034	0.1054	0.1074	0.1074	0.1094	0.1094
$l_{\acute{s}r}$ [m]	0.310	0.331	0.337	0.337	0.343	0,343
turns $z_1 = z_2$	120	120	120	120	120	120
layers $m_1 = m_2$	7	8	10	10	12	14

LOAD GRAPHS FOR THE WINDING MADE OF Bi-2223 TAPE

Load graphs of the windings, obtained for magnetic flux density distribution in surfaces P1, P2 and P3, for operating current range 5 – 60 A, are presented in Figure 4 – Figure 6. Critical current of used Bi-2223 tape is 60 A, and its maximal stress is 75 MPa. Obtained graphs allow to calculate the maximal operating current of the winding

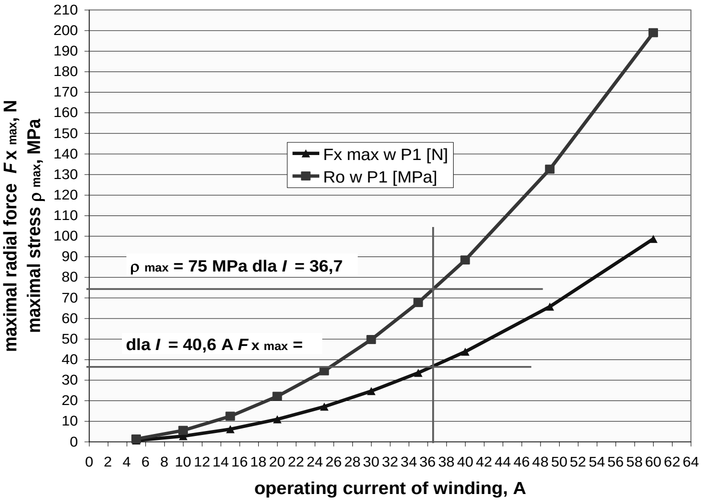

Fig. 4. Load graph in P1

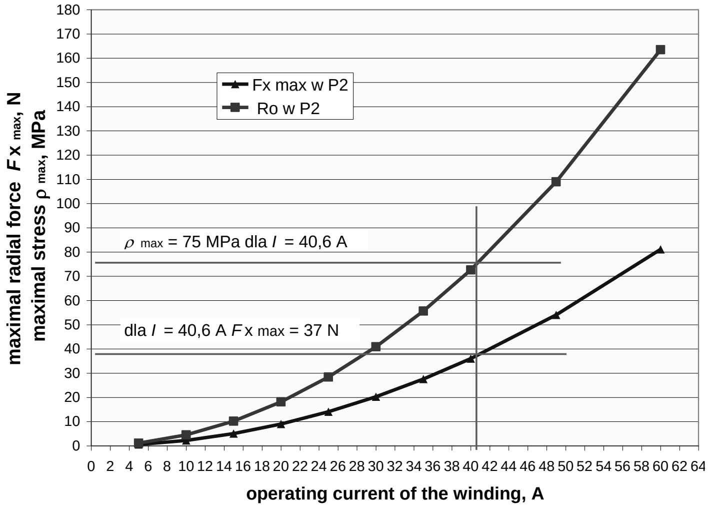

Fig. 5. Load graph in P2

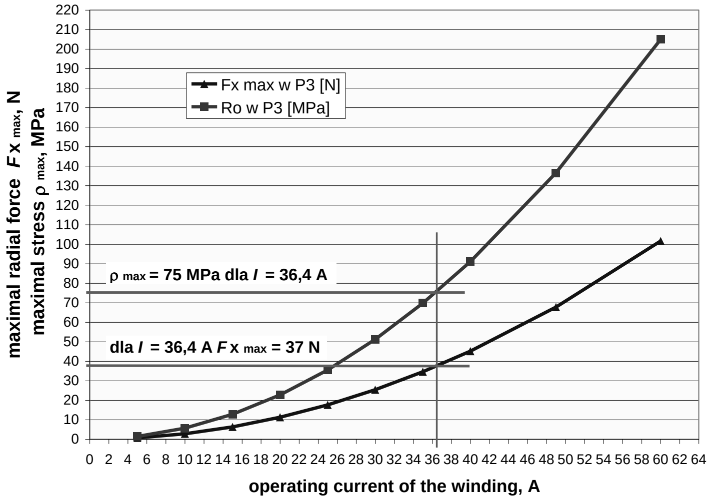

Fig. 6. Load graph in P3

The analyze of the results obtained, shows that the operating current vary between 36.4 and 40.6 A. Because the primary and secondary coils of the winding are understood as a one part, the maximal operating current of the analyzed winding is 36.4. It means that the influence of magnetic field on the value of electromagnetic stresses and strains is the highest for the current 36,4 A in surface P3.

Maximal calculated operating current covers only about 60.6 % of the critical current of the superconducting tape that has been used. The rest 39.4 % of critical current cannot be used because of mechanical strength of the tape.

LOAD GRAPHS FOR THE WINDING MADE OF YBCO TAPE

Load graphs of the windings families made of YBCO tapes, obtained for the magnetic flux density distribution in surface P3, for operating current range 5 – 150 A are presented at Figure 7 and Figure 8. Critical current of used YBCO tapes is 150 A. Maximal operating current of the windings was calculated for the value of 15 maximal stress of the tape, from range 34 – 520 MPa.

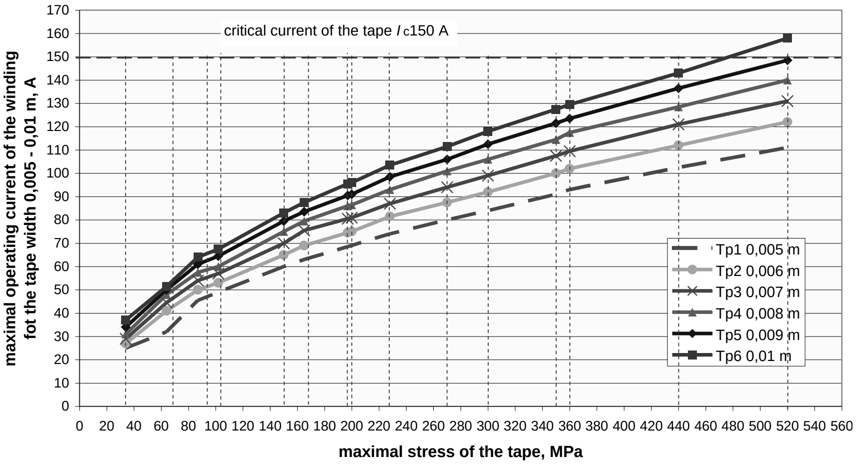

Fig. 7. Load graph for the YBCO Tapes in P3

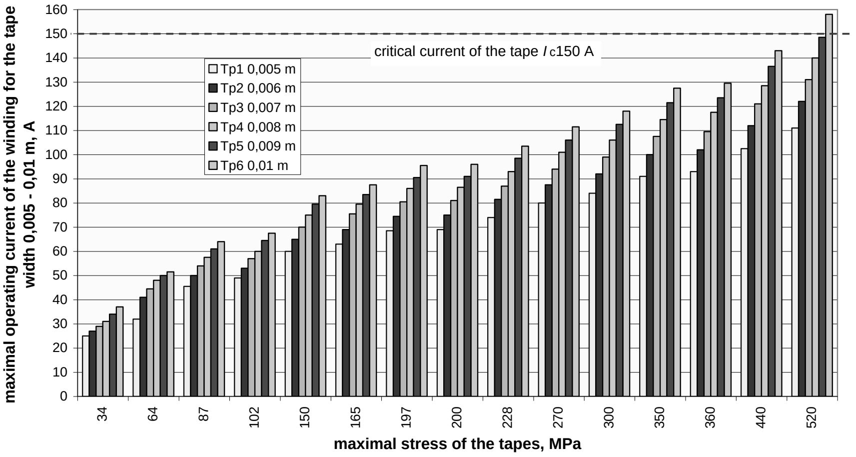

Fig. 8. Maximal operating current of the windings vs maximal stress of the tape for tapes Tp1 – Tp6

The analyze of obtained results shows that with the increase of the superconducting tape’s width and value of their maximal stress, the maximal operating current of the winding grows. For the tape’s width 9 and 10 mm and their maximal stress 520 MPa even at operating current of 150 A (that is equal to the tapes critical current), the maximal stress of the tapes will not be exceed. For the other tapes value of maximal operating current is lower and vary from 20 to 90 % of tapes critical current, according to their width and maximal stress.

COMPARISION OF 1st AND 2nd GENERATION HIGH-Tc SUPERCONDUCTING TAPES

Figure 9 shows the exemplary comparison of load graphs obtained for windings made of Bi-2223 and YBCO tapes. Load graphs, obtained for two windings with the same parameters but made of two types of superconducting tapes, located on common diagram, allow to choose the best superconducting tape for the realization of superconducting winding in consideration with maximal operating current of the windings and maximal stress of the tape.

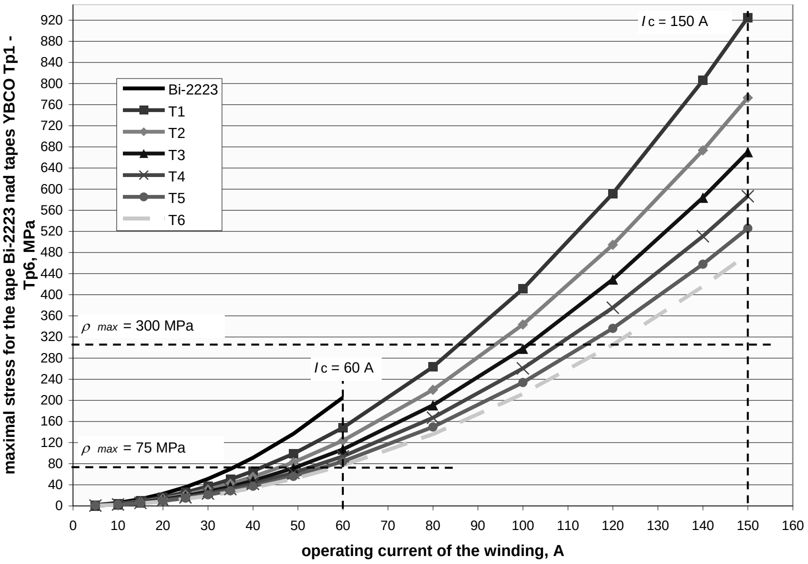

Fig. 9. Load graph for the tape Bi-2223 and tapes YBCO in P3

CONCLUSIONS

The 1st and 2nd generation high-Tc superconducting tapes have been compared, taking into consideration: mechanical strength of the tape, their critical current, stresses and strains acting in the windings during their work at normal condition, and maximal operating current of the winding

Specially for the purpose of this comparison the windings made of 1st and 2nd generation High-Tc superconducting tapes have been designed, and also the distribution of magnetic field density of the windings, and their components, have been obtained. According to results obtained the stresses and strains acting in that windings and their maximal operating current have been determined too.

The load graphs, for the windings made of 1st and 2nd generation high-Tc superconducting tapes, allow to choose the best tape for the realization of superconducting transformer's winding (in consideration of maximal operating current of the windings and maximal stress of the tape).

LITERATURE

[1] Janowski T., Transformatory nadprzewodnikowe, *Zeszyty Naukowe Elektryka*, Politechnika Poznańska (2000)

[2] Skov-Hansen P., Han Z., Bech J. I., Stresses nad Strains in Multi Filament HTS Tapes, http://www.nst.com/ASC98-PSH.PDF

[3] Parans Paranthaman M., Izumi T., High performance YBCO-coated superconductor wires, *MRS Bulletin,* August 2004, pp 533-537

[4] Goyal A., Parans Paranthaman M., Schoop U., The RABITS approach: Using rolling-assisted biaxially textured substrates for high performance YBCO superconductors, *MRS Bulletin,* August 2004, pp 553-559

[5] Wojtasiewicz G., Siły dynamiczne i rozkład indukcji magnetycznej w uzwojeniach transformatora nadprzewodnikowego, *IV Seminarium „Zastosowania Nadprzewodników”,* Lublin-Nałęczów 4-7.06 (2003), 60-72

[6] Wojtasiewicz G., Analysis of the operating current influence on magnetic flux density distribution in superconducting and copper winding of transformer, *Przegląd Elektrotechniczny 11’2004,* 1109-1112

5th International Conference **ELMECO**
Nałęczów, Poland
September 2005

RESISTANCE WELDING AT CRIOGENIC TEMPERATURES

Zygmunt Mikno

Institute of Welding, Gliwice, Poland
zygmunt.mikno@is.gliwice.pl
tel. (+48 32) 2310011 ext. 360, 0605360694

Keywords: resistance spot welding, criogenics, liquid nitrogen cooling, superconductors

Abstract

The paper presents results of computer simulation (MES) of the resistance welding process not only for standard (rated) conditions, i.e. industrial applications but also for modified procedures. The modification consists in application of increased electric current during welding in combination with intensive cooling of the electrodes whereas liquid nitrogen was used as a cooling agent. To improve welding conditions the author has suggested using a superconductor for the welder electrode design.

INTRODUCTION

Resistance welding is rated among the major methods for joining components of steel structures and is used in nearly all sectors of contemporary industry, but such branches as automotive technique, civil engineering, electrical engineering or aviation take the most benefits. Widespread application of the resistance welding technology is confirmed by the number of joints that are made during manufacturing e.g. a car chassis and that may range from 3 to 5 thousands spotwelds for a single chassis.

The resistance welding technology is used due to a number of advantages that include lack of any consumables, high rates of the process (parts of a second) and relatively low power consumption.

Permanently increasing requirements to quality of manufactured goods and competitiveness in the market impose the need of continuous technological improvements. That is why more advanced and efficient technological solutions for joining different parts are put into practice and more progressive technical equipment is involved. Hence, the welding process itself should offer high quality, affordable power consumption and assure top aesthetic properties of joints.

Basically, the resistance welding process can be described in the following way. The spot welding consists in joining two overlapping metal parts by means of two electrodes of a welding machine. The electrodes deliver electric current to the welded parts that results in heating them up to the melting temperature and eventually brings about to formation of a liquid metal spot. After reaching a sufficient size of the weldspot nugget the welding current is switched off but the welded parts are kept depressed one to the other for a period of time to assure that a durable joint is obtained. A very general and simplified diagram of the welding process is shown in Fig. 1.

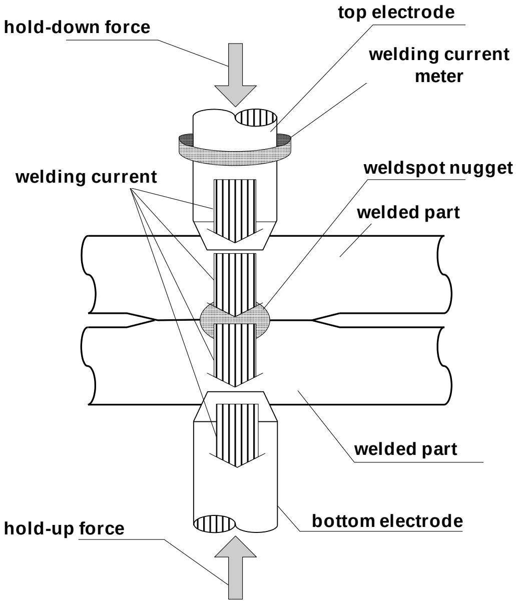

Fig. 1. Weldspot formation process

On the one hand, resistance spot welding involves the process of melting the material within the contact area of the welded parts and it is a desirable effect. On the other hand, a powerful electric current flows through electrodes and the welded material in that area, which results in excessive heating of electrodes and the welded material. Internal water cooling of electrodes is commonly used as a remedy but it is not a satisfactory solution as its efficiency is insufficient.

Application of new, alternative cooling methods within the welding area arises as an essential need in the aspect of improvements of thermal condition. These solutions should intensify transfer of heat in order to achieve adequate distribution of the applied power. Modifications in the electrode design, including implementation of new materials, e.g. superconductors, may also offer prospective opportunities.

THERMAL MODEL OF THE WELDING PROCESS

Simplified dissemination of heat within the welding area is shown in Fig. 2. The characteristic feature of a standard two-sided welding process consists in formation of a weldspot nugget on the contact surface between the two welded parts (usable heat Q_U). Temperature of the weldspot nugget reaches the melting point value for the welded metals. Temperature level of the weldspot nugget as well as the size of the nugget itself affect the temperature of the adjacent welded material (heat of losses Q_{SE}). The locations where the electrode comes into contact with the welded material and within the closest vicinity of electrodes are of extreme importance. For typical welding condition the temperature on the surface of the welded material is too high. Modification of the welding process that consists in decreasing the welding current with simultaneous prolongation of its flow time is unfavourable as it leads to excessive material overheating and eventual increasing of electric power consumption (I_{rated}=10kA, $t_{weld.}$ =200ms, I_2=8kA, t_{2_weld}=320ms, thickness of welded parts 2 x 1.5 mm, steel 08X).

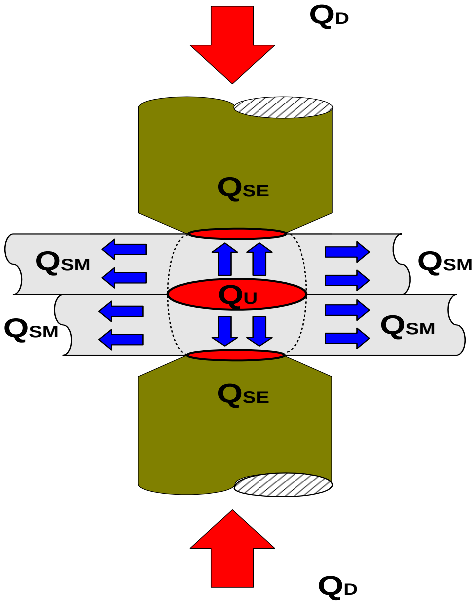

Fig. 2. Heat dissemination within the welding area
Q_U – usable heat, Q_{SM} – heat of losses – welded material, Q_{SE} – heat of losses – electrodes

ANALYSIS OF THE MODIFIED RESISTANCE WELDING PROCESS – COMPUTER SIMULATIONS (MES)

Spot welding with increased welding current may result in numerous benefits, with respect to both power consumption and lowering the temperature on the surface of the welded metal. Nevertheless, increasing of the welding current to exceed a specific rated value is practically impossible if cooling conditions remain unaltered. The reason is that a phenomenon of liquid metal splash occurs above the threshold limit. This effect was revealed as a result of computer simulations. Fig. 3 presents timing diagrams for temperature distribution within the welding area for classic electrodes and water cooling of the welding area. For standard welding conditions the weldspot nugget is formed from the centre (electrode axis) and expands outwards. If the welding current is increased the distribution of the current density changes, which results in the formation of the so-called circular weld. Therefore, a zone of highly plastic material is created whereas that material remains outside the area where the welded parts are pressed together and it is just the reason why the liquid metal splash occurs. Distribution of temperature within the welding area is presented in Fig. 3, which shows results of computations for the MES model (axial - symmetric model) for selected moments of the welding cycle.

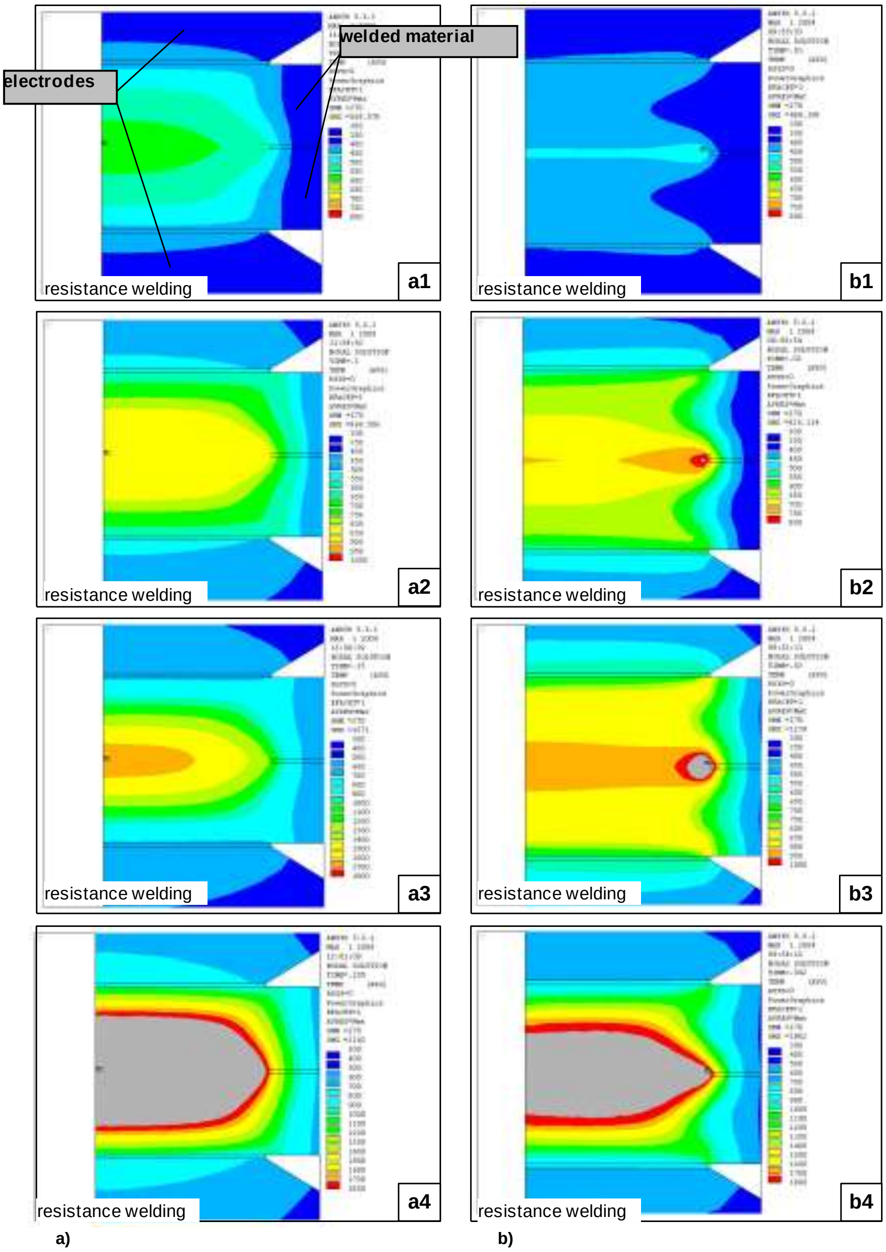

Fig. 3. Timing diagrams for distribution of temperature within the welding area when classic electrodes with water cooling are used for:
standard welding conditions (I = 10 kA) and respectively 1/4, 2/4, 3/4 and 4/4 of the electric current cycle,
increased welding current (I = 20 kA) and respectively 1/4, 2/4, 3/4 and 4/4 of the electric current cycle

Fig. 3 shows, besides diversities in distribution of temperature field for different technological conditions, that temperature decreases in the contact area in between the electrode and the welded material. The phenomenon of temperature decreasing for both the rated and increased values of electric current is also presented in Fig. 4.

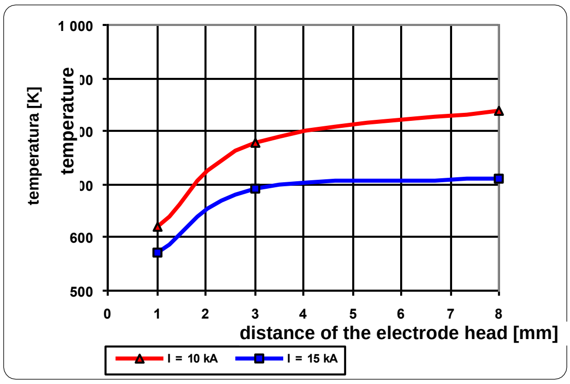

Fig. 4. Temperature of the contact between the welding electrode and the welded material vs. distance of the electrode head for the electric current values:
rated current (10 kA)
increased current (15 kA)

Increasing of the welding current is beneficial not only in terms of decreasing the temperature on the surface of the welded material but it also enables savings in power consumption. It results from a shorter time when the welding current flows through electrodes and thus a shorter time while the heat spreads out in the welding area. However there is also an adverse effect that consists in less favourable distribution of electric current density if the current value is increased. Due to the rise of electric current density near the outer edges of electrodes the so-called circular weld is eventually formed.

To alleviate effects of that phenomenon, the modified design of electrodes is proposed. The alteration consists in the application of an additional depressing ring that is dedicated to exert the additional holding force onto overheated areas that remain outside the zone where the two welded parts are pressed together by a typical electrode. However, it is only an indirect approach that prevents liquid metal splashes but is far from the elimination of increased concentration of the electric current density thus, the electric power dissipated around the electrode edges.

The average density of electric current during the process of welding steel sheets with the thickness of 2 x 1.5 mm and made of low-carbon steel of the 08X grade equals to 400 A/mm^2. The increase of the welding current results in the growth of current density, in particular around the outer edges of electrodes. It is visible as an effect of increased temperature in that zone – Fig. 3.b4 and **Błąd! Nie można odnaleźć źródła odwołania.**.a2. Hence, the intensification of cooling within the zone when the welding current is increased reduced the effect of heat concentration in the outer areas of electrodes – Fig. **Błąd! Nie można odnaleźć źródła odwołania.**.a3. The intensification of the cooling process was obtained by applying the liquid nitrogen as a cooling agent. Decreasing the temperature results in the resistance drop of the copper electrodes, which, in turn, reduces the effect of generating the Joule heat and increases the opportunity for more intensive dissipation of heat.

The implementation of intensified cooling process results in decreasing of temperatures around the contact area between the electrodes and the welded material as well as in the central zone of the welded materials **Błąd! Nie można odnaleźć źródła odwołania.**.a3. Although, any further increase of the welding current results in reappearing of unfavourable trends in spite of intense cooling (LN2). The electric current density around the contact area between the electrode and the welded material increases again, which leads to temperature increase within that area **Błąd! Nie można odnaleźć źródła odwołania.**.a5.

The use of a superconductor for the welder electrode design can offer a prospective solution of the problem as it would allow for the concentration of the current in the central part of the electrode. As the welder machine electrode is intensively cooled down to the temperature of liquid nitrogen, there are favourable conditions to provoke the effect of superconductivity provided the superconducting member is appropriately embedded into the electrode structure.

The application of a superconductor would enable the redistribution of the concentration of electric current. This is the solution that is extremely convenient for welding steel sheets with high electric and thermal conductivity coefficients, e.g. spot welding of aluminium and its alloys. Due to specific material characteristics the welding process of aluminium imposes tougher requirements onto energy delivering, i.e. high electric current value must act during a very short time interval. The application of an electrode with a superconducting concentrator of electric current would enable the increase of the welding current value with simultaneous reduction of welding time intervals.

CONCLUSION

The problem of welding with a superconducting electrode is a very interesting issue, both in the scientific aspect and with respect to engineering practice. This is a new approach that has never been presented as a solution of spot welding technologies. No information on liquid nitrogen cooling and applying superconductors to the welding process was found in the available literature references, and, in particular, no technical solution for resistance welding is known.

LITERATURE

[1] Mikno Z.: Badanie rozkładu przestrzennego mocy w procesie zgrzewania rezystancyjnego metali.(Research on spatial distribution of power in the welding process of metals). The grant form State Committee for Scientific Research (KBN), executed from April 2003 to April 2004.

[2] Mikno Z.: Analiza procesu sterowania przestrzennym rozkładem mocy zgrzewania rezystancyjnego. (Analysis of the control process for spatial distribution of power in the resistance welding process). PhD Thesis, Silesian University of Technology, Gliwice 2005.

5th International Conference **ELMECO**
Nałęczów, Poland
September 2005

VOLUME-SURFACE DISCHARGE AS AN ION SOURCE FOR PLASMA TECHNOLOGIES

M. V. Sokolova, S. A. Krivov

Moscow Power Engineering Institute
Moscow, 111250, Krasnokazarmennaya 14, Russia
sokolova@fee.mpei.ac.ru

Abstract

Experimental characteristics of discharge in a three-electrode system are presented. The system consists of a stripped electrode placed on upper side of a dielectric plate, while its reverse side has a metallic layer. With a high ac voltage (frequency f=14 kHz) applied to this layer, the stripped electrode being grounded, a surface discharge appears at the edges of the strips. If a high dc voltage is applied additionally to a plane electrode placed at a distance 1 cm above the strips (parallel to them) a direct current appears in the circuit including the gas gap and the stripped electrode. With dc voltage > 9 kV waves of glow discharge appear in the gas gap. Discrete channels can be seen inside the glow forming a volume-surface discharge. Influence of different factors on current and structure of such discharge is analyzed.

Keywords: ion source, plasma technology, surface discharge, volume-surface discharge

INTRODUCTION

The so-called “surface discharge” is a type of discharge from sharp edges of a thin strip electrode (of one or several strips) placed on one side of a dielectric plate whereas the reverse side of this plate has a metallic layer. If a high voltage is applied to this layer, the other electrode being grounded, discharge processes appear at the edges of the strip in a form of individual micro discharges. It has been experimentally proved that micro discharges have a discrete structure at each half cycle of an ac voltage or at every polarity of an impulse voltage [1-3]. If a third plane electrode is placed above and parallel to the stripped electrode (Fig. 1), at some distance from it (at least several millimeters), and a dc high voltage is applied to this plane electrode together with ac voltage applied to bottom metal layer, the strips being grounded, complex discharge processes appear. We called the discharge in the gas in a three-electrode system a “volume-surface discharge”.

One of the main processes of such complex discharge is an appearance of direct current through the electric circuit formed by the upper plane electrode, gas gap and grounded stripped electrode. The source of this current is the plasma of surface discharges while the applied dc voltage defines the movement of charged particles. If a flow of air is achieved through the gap between the electrodes, the gas during such complex discharge becomes filled by charged particles (ions of different structure) that can be used for charging of aerosol particles or modification of surfaces.

The aim of the present investigation was to review different factors that can influence the volume part of the discharge in three-electrode system and evaluate experimentally the intensity of ion formation in different conditions.

EXPERIMENTAL ARRANGEMENT

All experiments were carried out with an electrode system placed in a dielectric or a metallic cell. The last one was used to investigate the discharge in heated ambient air. Dry air was used if there was no special heating of the gas.

The experimental set-up (Fig. 1) consists of an upper conducting plane electrode (for the application of the DC voltage) and two lower electrodes placed at both sides of a dielectric plate (SD arrangement).

On upper side of the dielectric plate grounded metallic strips are used as an electrode, while a metallic foil attached to the reverse side of the plate acts as high voltage electrode. The width of the strips of the stripped electrode (Fig. 2) is about 1 mm, the distance between the strips was optimised for ozone production and is 4 mm. The thickness of the stripped electrode is 25 µm, the radius of the strip edge is about 20 µm.

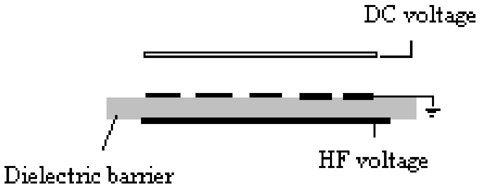

Fig. 1. Electrode arrangement

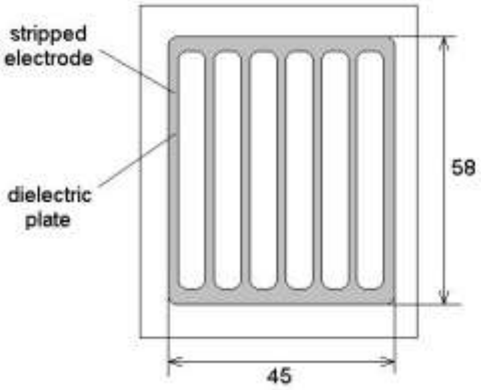

Fig. 2. Configuration of the stripped electrode (gray) on the upper side of dielectric barrier

The dielectric barrier is of polycor (relative permittivity ε=9.9) or alumina (ε=9.1) plates 1.1 mm of thickness. The dimensions of the plate are given in Fig. 2.

The upper transparent dc electrode, made of a glass plate 1 mm thick with a transparent metallic layer at its bottom side, can be replaced by a metallic plate. The area of the dc electrode is 23 cm^2 in all cases. The distance between this electrode and the surface of the dielectric plate can be 8-10 mm.

Main part of experiments with ac and dc voltages applied together was carried out with cooled dielectric barrier. It is a result of previous experiments when the influence of bias voltage on ozone formation was investigated [3]. It has been shown that a three-electrode system does not give much to improve ozone formation. So it is not necessary to cool the electrodes and the gas in case when the three-electrode system is used as an ion source. In this case the barrier with the stripped electrode and the gas above it are heated by the discharge. The gas temperature at the exit end of the cell was measured to be about 40^oC. If a special heating of the gas at the entrance of the cell is used, the cell being thermally isolated from its being cooled by the room air, the output gas temperature was increased up to 135^oC. This value corresponds to ac voltage U_{ac}= 2.1 kV and the flow rate of air through the cell about 3 l/min. With lower values of air flow the temperature at the exit end of the cell is about 110^oC.

A weak stream of dry air is flowing through the gap in between the plates. Most experiments were carried out with 1 l/min flow and only those that were aimed to see the influence of the gas flow rate on the characteristics of the discharge were done with different flow rates (0.5 to 3 l/min).

An ac high frequency voltage (14 kHz) is applied to metallic layer of the dielectric plate (Fig. 3), while the strips are earthed through a resistance R=191 Ohm and a capacitor C= 1μF put in parallel. Such scheme is used to measure the active power of the surface discharge by Lissajous figure method and at the same time constitute a circuit for the direct current through the gas gap. It was checked that the resistance 191 Ohm does not influence practically the current value and the value of the measured active power as well. An example of Lissajous figure that permits to evaluate the active power is presented in Fig. 4.

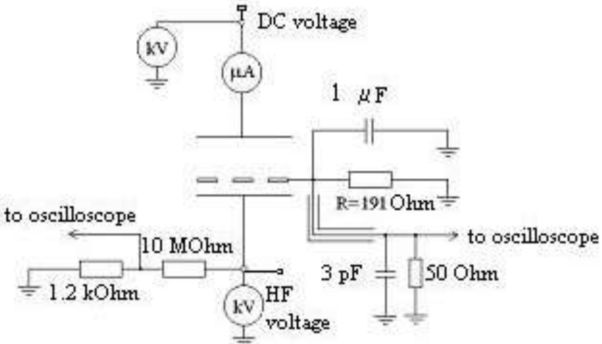

Fig. 3. Electric circuit

Direct current and active power of the surface discharge have been measured for dc voltages up to 20 kV at both polarities and ac voltages in a range between 2 and 3.4 kV (r.m.s. values). The high dc and ac voltages were measured with voltmeters and a Tectronix oscilloscope (TDS 754D) was used to determine the active power.

To measure the direct current there was a microampermeter installed into the dc high voltage circuit. Each value of the direct current presented in figures given further is a mean value of at least 5 measurements that were fulfilled several times when the dc voltage was increased or decreased. The accuracy of measurements is about 10%. The output voltage of the HF voltage source depends on the resistance of its load, which in our case is the surface discharge itself, so with a change of the SD intensity it was necessary to regulate the output ac voltage value. It was especially important when the dc voltage was applied, and the character of the SD began to change for the same ac voltage value.

The volume discharge structure was analysed with an intensified CCD-camera from PCO (DiCam Pro) through transparent side window of the cell.

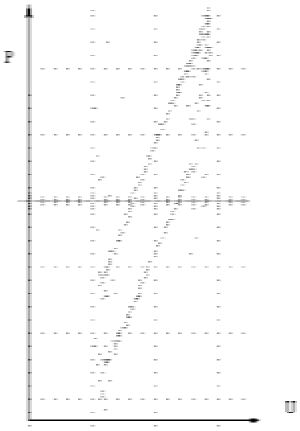

Fig. 4. An example of Lissajous figure of volume-surface discharge

The side view images were taken for a certain middle point in the gas gap for which the distance to the objective of the camera was 61 mm. The time exposure of the CCD-camera was 10 μs and all parameters of the camera were the same for all cases. The camera was synchronised with the ac power source, so it was possible to see the discharge at different polarity of the ac voltage applied to the strips.

EXPERIMENTAL PROCEDURE AND RESULTS

If an ac voltage is applied to the bottom electrode of the dielectric plate, surface discharge (SD) appears at the edges of the strip electrodes. A fully developed SD that covers all edges of the strips at normal conditions (without additional heating) is seen at ac voltages U_{HF} exceeding 2.2 kV (r.m.s.) and values up to 3.4 kV were achieved. Higher values are limited by the electric strength of the dielectric plate.

With an additional application of a dc voltage to the upper electrode of the electrode system a direct current appears in the circuit including the gas gap and the grounded strip electrodes (Fig. 3). The measurements indicate that this current depends on several parameters, such as: a) the value of the applied ac voltage, b) the value of the dc voltage and its polarity, c) the material of the dielectric plate, d) the value of the air flow rate in the gap and e) the intensity of additional heating of the gas.

The main parameter that determines the direct current values is the ac voltage (Fig. 5). For instance, with a polycor plate and U_{DC}= 8 kV a 30 % increase of the ac voltage leads to more than a twofold increase of the direct current. If an alumina plate is used (a single square dot in Fig. 5) the current is much higher, and it was even possible to increase the current up to 1.1 mA (the corresponding current density at the upper electrode was more than 50 μA/cm^2). This value was achieved with positive U_{DC} = 20 kV and U_{HF} = 2.5 kV (Fig. 6). Such high dc voltage is difficult to reach as any local increase of the electric field in the gap near the walls or at outer edges of the stripped electrode can lead to breakdown. For the same value of the ac voltage the increase of the direct current with U_{DC} is more pronounced with negative polarity (Fig. 7). As it is seen, the difference in the direct current values for different polarities grows with the value of the ac voltage.

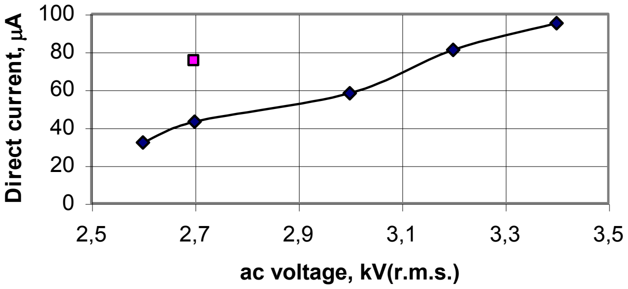

Fig. 5. Influence of the ac voltage value on the direct current for U_{DC}= +8 kV. The curve is for polycor plate, the square dot at 2.7

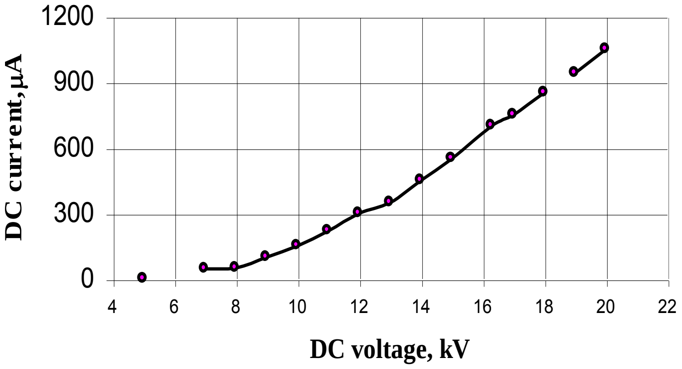

Fig. 6. Direct currents for extremely high positive DC voltage:
Dielectric – alumina, dry air flow 1 l/min, water cooling. Electrode spacing 8.5 mm

At higher air flow rates a notable increase of the direct current is detected with all other conditions remaining unchanged (Figure 8). This current increase is more pronounced for higher values of U_{DC}, but in all cases a saturation value appears.

All foregoing results were achieved with dry air and water cooling of the dielectric barrier. To estimate the influence of gas density on direct current and discharge processes special heating of air at the entrance of the cell was added. In this case ambient air was used. Heating of the air at the entrance of the cell up to 450°C does not give a uniform heating of all elements of the cell and the temperature of the gas at the exit is not more than 100°C if there is no surface discharge. With surface discharge an additional heating arises and the gas temperature at the exit can be increased up to 140°C.

The main result of the gas heating is a decrease of the initial voltage of the surface discharge as a result of a decrease of gas density. If there is no special heating of the gas, the discharge in conditions of our experiments and in case of alumina dielectric barrier appears at 1.8 – 1.9 kV. With initial heating of the gas up to 450°C the discharge near the gas entrance appears already at 1.3 kV, and covers all edges of the stripped electrode when the voltage is 1.4 kV.

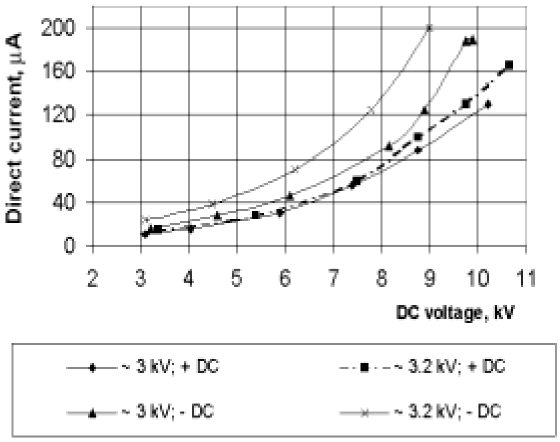

Fig. 7. Influence of the polarity of DC voltage on direct current

An influence of gas temperature on direct current and active power of surface discharge is shown in Fig. 9 and 10. Middle heating corresponds to temperatures at the cell entrance about 250°C, and intense heating - about 450°C. The results demonstrate practically two folds increase of direct current if the temperature is increased up to 450°C for all other conditions, while active power of the surface discharge is increased only by 15%.

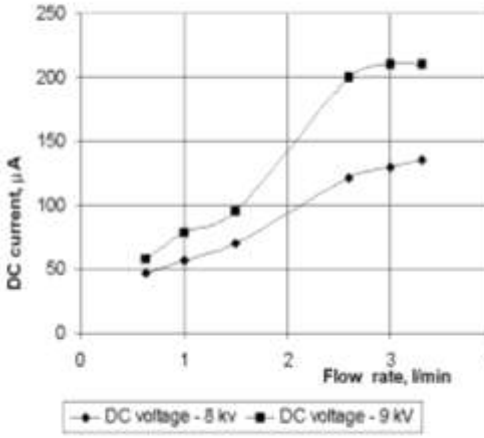

Fig. 8. Influence of dry air flow rate on direct current. Dielectric – polycor, U_{AC}= 3 kV; Negative dc voltage

DISCUSSION

The experimental results achieved in the present work permit to conclude that the three-electrode system in which a complex volume-surface discharge appears can be a source of charged particles in a flow of air. The movement of these particles in the applied dc field constitute the current, which is influenced by a range of external conditions, such as

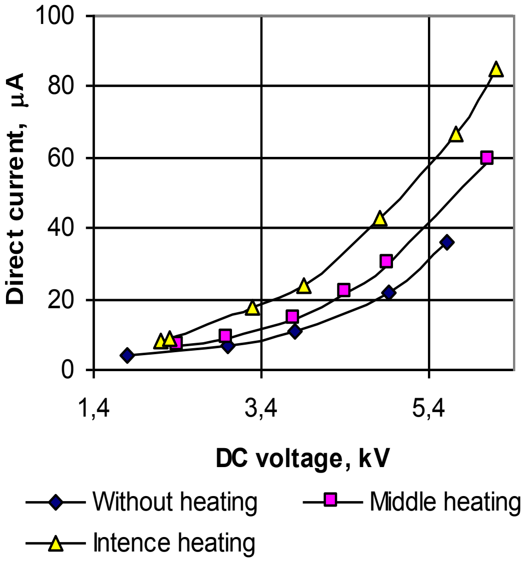

Fig. 9. Influence of gas temperature on direct current.. U_{HF} = 2.1 kV, Dielectric alumina, air flow 1.5 l/min

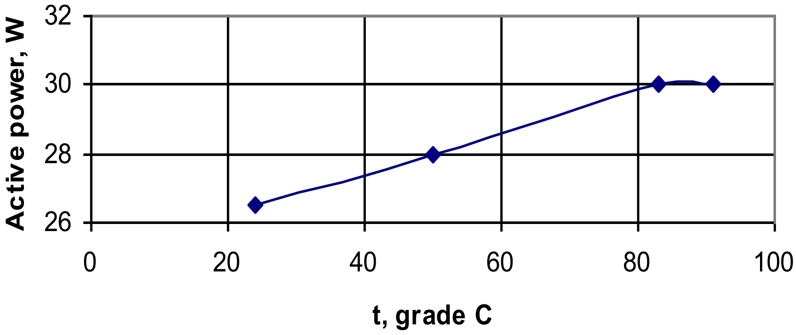

Fig. 10. Influence of gas temperature on active power of surface discharge. . U_{HF} = 2.1 kV, Dielectric alumina, air flow 1.5 l/min

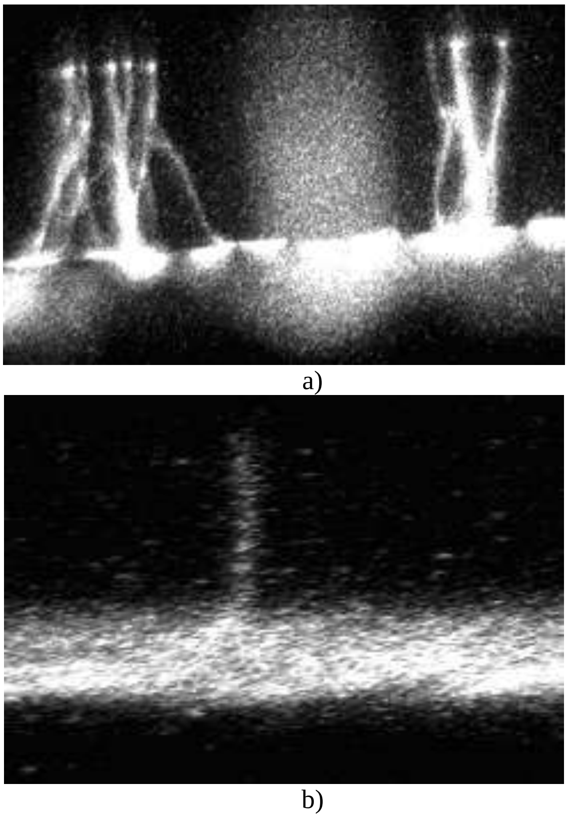

Fig. 11. Images of volume discharges in a three-electrode system. Dry air, air flow 1 l/min;
Negative dc voltage $U_{DC} = -8.5$ kV, $U_{ac} = 2.1$ kV, positive half-cycle:
a) With a surface discharge over polycor barrier,
b) With a surface discharge over alumina surface

the value and polarity of dc voltage, air density and air flow rate. But the main factor that defines the production of charged particles is the surface discharge that in its turn is defined by the characteristics of the dielectric barrier, the configuration of stripped electrode and the value of applied ac voltage.

It can be easily shown that any change in the current values is a result of a change in the electric field in different parts of the gap [3]. Near the stripped electrode the field is mostly defined by the ac voltage applied to electrodes with small radius of curvature and this field defines the surface discharge. The electric field in the gas gap is defined by the applied dc voltage and the volume charge of charged particles that move in the gap and constitute the direct current. With positive dc voltage the negative particles (electrons and negative ions created by surface discharge) form the direct current. As the electric field in the main part of the gas gap is not high enough to cause ionization, the main reaction is an attachment of electrons to neutral molecules. So the current is formed by negative ions that move to a positive upper dc electrode.

With negative dc voltage the movement of positive ions must take place. It was shown in [3] that surface discharge at positive half-cycle of the ac voltage is much more intense, than at negative one. So with negative dc voltage and positive half-cycle the direct current density must be the highest and it is confirmed by the experiment (Fig. 7).

The experiments with high dc voltage demonstrate the influence of the volume charge in the gas gap created by the moving ions. The field of this volume charge prevents breakdown of the gas even with so high values of the dc voltage as 20 kV. The gap length in this case was 8.5 mm, so the mean applied dc field in the gas gap could be 23.5 kV/cm and such value is practically equal to the breakdown field for dry air in normal conditions. Nevertheless there was no breakdown as the field of volume charge decreases the applied field.

The images of volume discharge processes presented in Fig. 11 [3] permit to see that the initial stages of the volume breakdown are being formed. With less current the volume channels are more probable and more powerful. The cause of different intensity of volume channels lies in different intensity of surface discharge over alumina and polycor ceramics. So it can be said that high direct currents prevent the breakdown.

An analysis of the surface state of the metallic upper dc electrode after the experiments with volume-surface discharge has shown that there is practically no diffusion (or it is very weak) of the flow of ions perpendicular to the flow direction. There appear clear traces of the ions that hit the electrode surface. The pattern of the traces fully repeats the pattern of the stripped electrode: dark traces on the dc electrode that correspond the zone with surface discharge from the edges of the strips and light traces that correspond the strips themselves. Only in case of high direct currents the traces at the metallic electrode become near to uniform ones. This result permits to evaluate the current density at the upper dc electrode. The maximal value achieved in present experiments without additional heating of the gas and without cooling of the electrodes can be as high as 50 $\mu A/cm^2$.

With an additional heating of the gas at the entrance of the experimental metallic cell the temperature at the exit of this cell can be as high as 120-130 ^oC. In this case the increase of the current is fully governed by the decreased air density because lower gas density leads to a decrease of the surface discharge initial voltage. The discharge exists for a longer period during each half-cycle with the same ac voltage value and besides each surface micro discharge becomes more powerful. Experiments with a transparent upper electrode confirm it. With an increase of the entrance gas temperature the heated gas begins to envelope all volume of the gap along the gas flow. At first at low values of ac voltage the surface discharge appears near the gas entrance. With an increase of the gas temperature the zone with discharge spreads over stripped electrode, enveloping new parts of it and finally filling all its surface of the stripped electrode.

The measured values of active power of the surface discharge do not demonstrate a significant change with gas temperature. It has been previously stated [3] that with a dc voltage the measured active power of surface discharge practically does not change, although the structure of the discharge itself shows a marked change especially in the positive half-cycle of the ac voltage. The same absence of marked change of active power values with a bias voltage has been registered using an advanced measuring circuit (Fig.3). We think it reasonable to conclude that so called “active power” does not characterize real processes of surface discharge. To our belief such conception may be useful to characterize the traditional barrier discharge, but is not physically true when a surface discharge is involved.

CONCLUSIONS

The results achieved in present investigation demonstrate a tendency and amount of the influence of different factors on the characteristics of volume-surface discharge and its ability as an ion source. The optimization of regime in any other device must be done taking into account a certain technology. For instance a possibility to charge aerosols for gas treatment depends on the necessary ion density which can be less than the highest values achieved in the present investigation.

One other consideration must be mentioned. To optimize any regime it is reasonable to pass to simulation of the processes in the three-electrode system. To do so a special theoretical analysis of the experimental results must be done. Such problem will be the task of a future paper.

LITERATURE

[1] Kozlov M. V., Sokolova M. V. et al. Nanosecond Surface corona discharge for different types of strip electrodes and ceramic or polymer dielectrics, *Plasma and Polymers*, vol. 8. No.3, 2003, pp. 179-197

[2] Saveliev A. B., Pietsch G. J. On the structure of dielectric barrier surface discharge, *Contr. papers of Int.Symp. on High Pressure, Low Temperature Plasma Chemistry*, vol. 2. 2002, pp. 229-233

[3] Sokolova M., Hulka L., Pietsch G. J. Influence of a bias voltage on the characteristics of surface discharge in dry air, *Plasma Processes and Polymers*, vol. 2. 2005, pp. 162-169

5th International Conference **ELMECO**
Nałęczów, Poland
September 2005

A NEW TYPE OF REACTOR WITH A COMBINATION OF SURFACE DISCHARGE AND ADVANCED OXIDATION PROCESS IN AIR AND ITS APPLICATIONS

Mitsuaki Shimosaki and Chobei Yamabe

Saga University, Department of Electrical and Electronic Engineering
1 Honjyo-machi, Saga 840-8502, Japan
E-mail: yamabec@cc.saga-u.ac.jp

Abstract

A new type of reactor which has a combination of surface discharge and UV radiation emitted by a lamp discharge is studied for the treatment of volatile organic compounds (VOCs). The surface discharge occurs along the wire electrode surrounded on the outer tube of reactor and generates ozone in air. It seems that the UV emission effects on the initiation and uniformity of the surface discharge appears. The toluene treatment in oxygen or argon mixture gas was carried out and the decomposition of almost 100 % was established at the applied voltage of 4 kV (peak to peak). The toluene was converted into CO_2 *(about 90%),* H_2O*, CO and HCOOH. In the case of mixture gas which is diluted with air,* CO_2 *(about 95%),* H_2O*, CO, HCOOH and NOx were detected by a FTIR measurements as byproducts under decomposition rate of 98% at 4.5 kV (peak to peak). It is very difficult to decompose the acetic acid (*CH_3COOH*) and formic acid .(HCOOH) by ozone itself, but it is possible to decompose by atomic oxygen (O) / hydroxy radicals (OH).*

Keywords: surface discharge, advanced oxidation process, ozone discharge

INTRODUCTION

The volatile organic compounds (VOCs) are used in the various industrial fields such as semiconductor production, automotive industry, coating with paint. It has been obvious that some of the VOCs are bad for the human health causing allergic and cancerous illness. Recently, these phenomena are given attention as the sick -house symptoms. Only the ozone used for the treatment of these VOCs is difficult and one of the methods for the decomposition has been proposed to use the advanced oxidation processes (AOPs). [1] - [3]

In this study, both the surface discharge and UV emission are used for the AOP and this method is applied for the decomposition of toluene ($C_6H_5CH_3$) and it is confirmed that the treatment of the formic acid as a by-product is also possible even though at higher concentration.

EXPERIMENTL APPARATUS AND PROCEDURE

The configuration of a reactor A is shown in Fig.1. A UV lamp (emitted wavelength is 253.7 nm) whose diameter is about 25mm is winded by a tungsten wire of 0.4 mmφ. This winded wire is the electrode for the surface discharge.

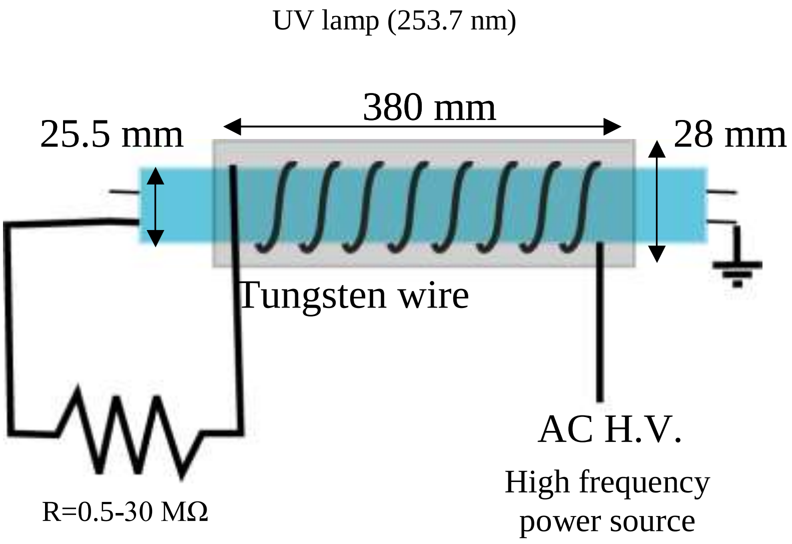

Fig. 1. A new surface discharge reactor A

One side of the wire electrode is connected with the lamp electrode through the high resistance (0.5 ~ 30 MΩ). to avoid the vaporization of lamp electrode. The other lamp electrode is earthed. To improve the discharge conditions of the lamp, both side of lamp electrode are earthed and high resistance R shown in Fig.1 is removed and this is called here the reactor B as shown in Fig.3. In these reactors, discharge plasma in the UV lamp is generated between the wire electrode applied high voltage and the earthed lamp electrode. The surface discharge on the lamp is generated by the high voltage applied on the wire electrode with the UV emission from the lamp.

The ozone generation with reactor B shown in Fig.3 is better than that with reactor A shown in Fig. 1. But due to the problem for the lifetime of UV lamp operated at higher applied voltage, the use of reactor B has to be operated very carefully.

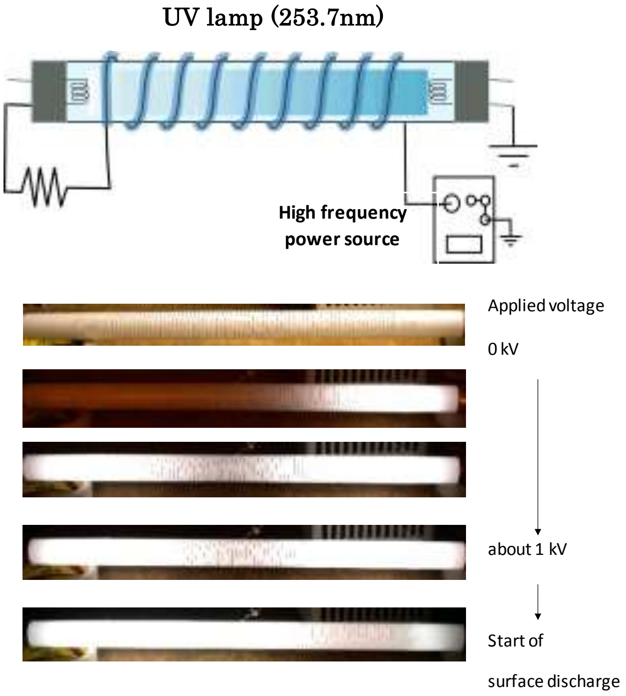

Fig. 2. Reactor A (upper) and various discharge conditions of the lamp (lower)

Schematic diagram of the experimental set up is shown in Fig.5. The frequency of discharge power source is 8~9 kHz. The mixture gas of toluene (100ppm)/N_2 and O_2 was used as the raw gas. The flow rate is 0.8 L/min for toluene/N2 mixtures and 0.2 L/min for oxygen respectively (i.e. totally 1.0 L/min). The applied voltage was 3~4.5 kV (peak to peak). The applied voltage and discharge current were measured by a high voltage probe (Tektronix, P6015A) and Rogowski coil with the oscilloscope (Sony, Tektronix TDS350). The electrical input power was measured by the voltage-charge Lissajous's figure. The decomposition of toluene and its by-product are analyzed by the FTIR (JASCO, FT/IR-430).

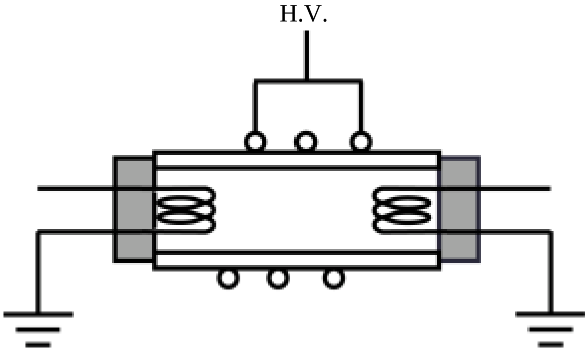

Fig. 3. Reactor B

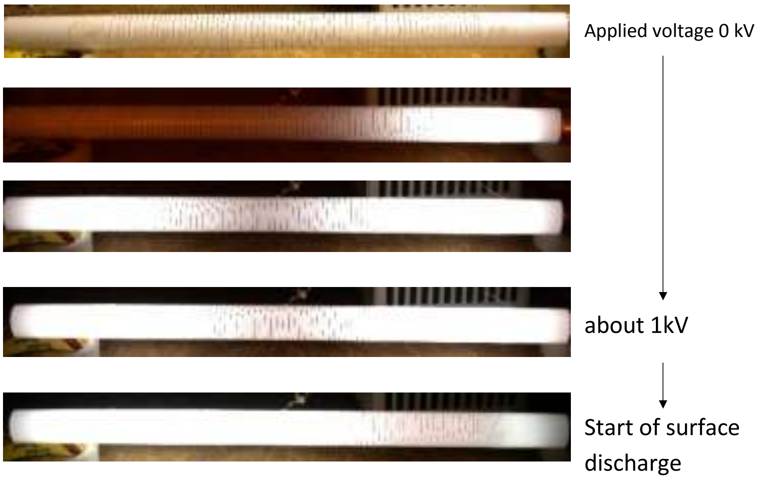

Fig. 4. Various discharge conditions with applied voltage (taken by reactor B)

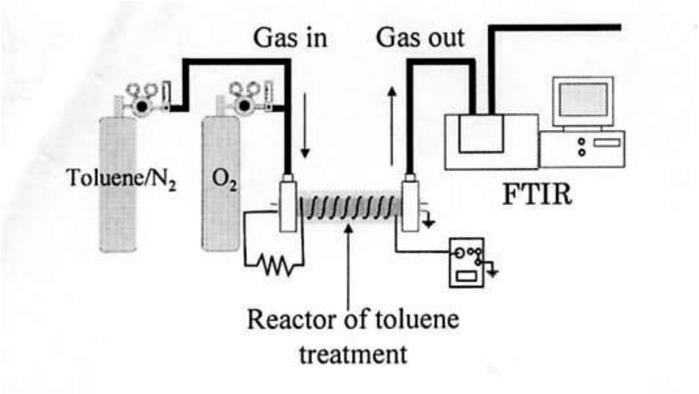

Fig. 5. Schematic diagram of the experimental setup

EXPERIMENTAL RESULTS

The discharge conditions of the lamp used for the reactor A and B with the applied voltage are shown in Fig.2 and Fig.3. When the low voltage is applied, at first the discharge plasma appeared at right side of the lamp due to the potential difference between the wire electrode and the earthed electrode. Increasing the applied voltage, the discharge plasma region spread from the side of earthed electrode to the other side of electrode. The discharge plasma was filled in the whole region of the lamp at about 1 kV (peak to peak). This plasma plays a important rule as an induced electrode of the surface discharge on the lamp and the high electric field appears between the wire electrode and the plasma in the lamp, and the surface discharge occurs along the wire electrode on the lamp.

The ozone is produced by this surface discharge and simultaneously the UV light from the lamp is radiated the produced ozone which dissociated into the atomic oxygen radicals. This surface discharge is very useful not only for the ozone generation but also for the decomposition of toluene due to the synergism of the surface discharge and atomic oxygen radicals.

To improve the discharge plasma region inside the lamp, both electrodes of the lamp were earthed as shown in Fig.3 and the discharge condition was observed with the applied voltage on the wire electrode. When the high voltage was applied, at first in the right side of the lamp, the discharge plasma was produced at the right side due to the different position of wire electrode in right and left. In creasing the applied voltage, the discharge plasma region spread from right to the center and whole region in the lamp was filled with discharge plasma at 1 kV (peak to peak) and the surface discharge on the lamp started.

Before the measurements, the water attached on the apparatus was carried out to remove by the discharge conditioning in the dry air and this discharge treatment was continued until both H_2O and CO_2 were not detected by the FTIR. The FTIR absorption spectra of the toluene before and after treatment is shown in Figs.6 and 7. The applied voltage used for the treatment is 4.25 kV (peak to peak).

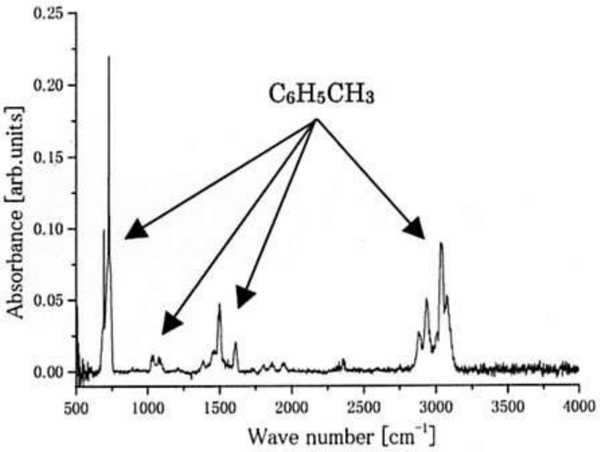

Fig.6 FTIR absorption spectra before treatment of toluene

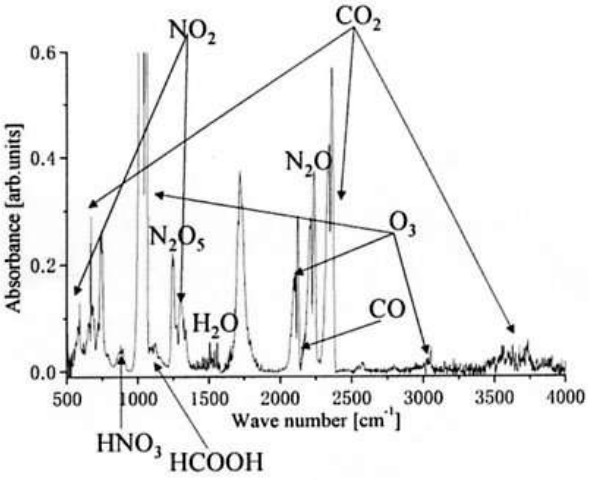

Fig.7 FTIR absorption spectra after treatment of toluene

It was found that many kinds of products such as H_2O, CO_2, CO, HCOOH, HNO_3, O_3, N_2O, NO_2, N_2O_5 were generated. The by-products due to the decomposition of toluene are H_2O, CO_2, CO, HCOOH and HNO_3. For the by-products of H_2O, CO_2, CO, HNO_3, they increase with the applied voltage. On the other hand, in toluene/argon and oxygen mixture gas, H_2O, CO_2, CO and HCOOH are generated as by-products. For the generation of HNO_3, the following reactions are proposed [4].

$$NO_2 + NO_3 \rightarrow N_2O_5 \tag{1}$$

$$N_2O_5 + H_2O \rightarrow 2HNO_3 \tag{2}$$

The N_2O_5 is solved easily into water and water is produced in the toluene composition and HNO_3 is produced. In this study, the treatment has been done in air and this produces the NOx which increases with the applied voltage.

The decomposition rate of toluene as a function of discharge power is shown in Fig.8.

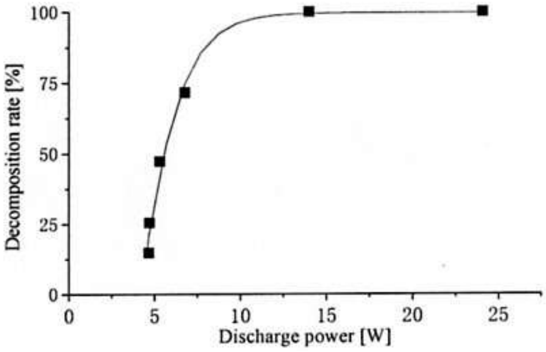

Fig. 8. Decomposition rate of toluene as a function of discharge power

The decomposition rate increases with the discharge power and it saturates to be about 98% at larger than 15 watt. Even though the high decomposition rate was established, the low molecule acid (i.e. formic acid, HCOOH) which was difficult to be treated by only ozone appeared..

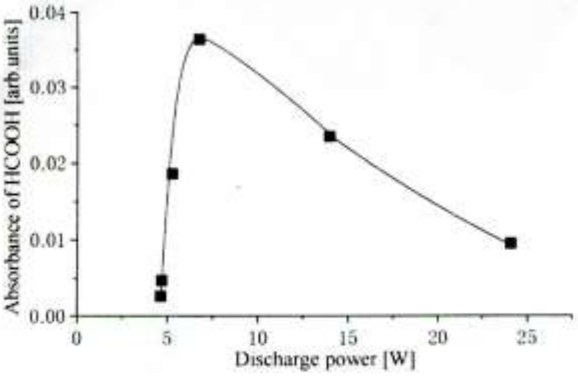

Fig. 9. Absorbance of formic acid (HCOOH) as a function of discharge power

The absorbance of formic acid (HCOOH) with the discharge power is shown in Fig.9. The formic acid increases with the discharge power up to about 7 watt and decreases with the discharge power at larger than 7 watt. The toluene is possible to be decomposed by the atomic oxygen, but the formic acid (HCOOH) is impossible to be decomposed by it. Both apply voltage and discharge current waveforms with time are shown in Fig.10. According to the measured waveforms, at the lower applied voltage at which the surface discharge is relatively weak (upper case) and at the higher applied voltage, the surface discharge along the wire occurs strongly (lower case). In this method, not only the reaction with the atomic oxygen and toluene but also the electrons produced by the surface discharge along the wire electrode play an important rule to decompose the toluene and formic acid with their collision.

(a) 3.25 kV

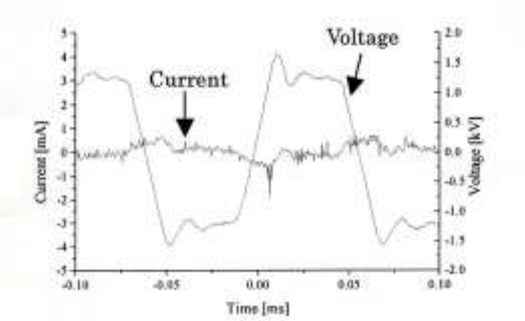

(b) 4.5 kV

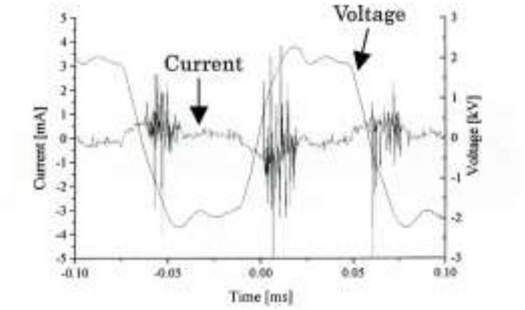

Fig. 10. Waveforms of applied voltage and discharge current operated at (a)3.25 kV (upper) and at (b)4.5 kV (lower) in toluene/nitrogen/oxygen mixtures

According to the emission spectra in the mixtures of toluene/N_2/O_2 measured by the PMA (Photonic multi-channel analyzer), mainly the emission lines of mercury and nitrogen were observed, but the nitride such as CN was not detected. Although there are some reports that the nitrogen radicals and oxygen radicals produced by the discharge plasma are useful for the VOC decomposition, the nitride except NOx was not detected by both FTIR and PMA. At the large discharge power, the toluene is decomposed by the synergism of the atomic oxygen generated by the O_3/UV (i.e. AOP) and electrons generated by the surface discharge and the formic acid (HCOOH) is decomposed by the electrons and it decreases with discharge power as shown in Fig. 9.

The conversion ratio of the carbon in CO_2 produced as by-product to the carbon included in the composed toluene as a function of discharge power is shown in Fig.11. This means that how much treated toluene was converted into CO_2 which was one of the by-products.

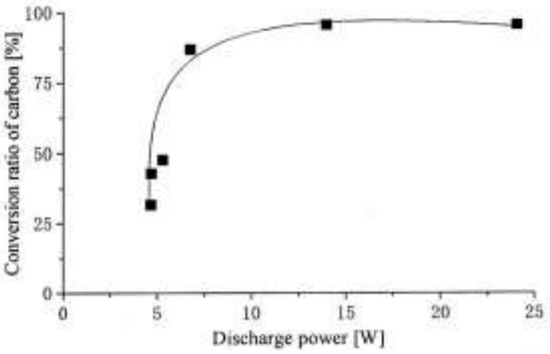

Fig. 11. Conversion ratio of carbon in CO_2 produced as by-product to the carbon included in the decomposed toluene as a function of discharge power in toluene(100 ppm)/N_2/O_2 mixtures

CONCLUSIONS

(1) Simple configuration of reactors for the VOC treatment were proposed to use not only useful radicals such as ozone and atomic oxygen but also using the electrons generated by the surface discharge. The latter is influenced very much by the operating voltage and these phenomena are confirmed by the decomposition of toluene and formic acid as for its application.

(2) The formic acid which is one of the by-products was easily composed by the new reactors with relatively large discharge power.

(3) The decomposed rate of about 98% was established at larger than 15 watt.

RFERENCES

[1] Zhang Pengyi, Lian Fuyan, Yu Gang, Chen Qing, Zhu Wanpeng: "A comparative study on decomposition of gaseous toluene by O3/UV, TiO2/UV and O3/TiO2/UV", Journal of Photochemistry and Photobiology A, Chemistry 156, 189-194 (2003)

[2] Mitsuaki Shimosaki, Koichi Miyazaki, Chobei Yamabe: "Treatment of toluene using combination method of AOP and surface discharge", Extended Abstracts (The 51st Spring Meeting, 2004), The Japan Society of Applied Physics and Related Societies, No.1, p.170. (in Japanese)

[3] Mitsuaki Shimosaki, Chobei Yamabe: "Treatment of Toluene Using Surface Discharge and Advanced Oxidation Processes", International COE Forum on Plasma Science and Technology, Technical Session Proceedings, p.267 (2004)

[4] J.F.Doussin, B. Picquet-Varrault, R. Durand-Jolibois, H. Loirat, P. Carlier: "A visible and FTIR spectrometric study of the nighttime chemistry of acetaldehyde and PAN under simulated atmospheric conditions", Journal of Photochemistry and Photobiology A: Chemistry 157, 283-293 (2003)

5th International Conference **ELMECO**
Nałęczów, Poland
September 2005

FUSION REACTORS FOR FUTURE POWER GENERATION

Paweł Surdacki

Lublin University of Technology
Institute of Electrical Engineering and Electrotechnologies,
Nadbystrzycka 38a, 20-618 Lublin,
E-mail: p.surdacki@pollub.pl

Abstract

This paper describes the reasons for developing magnetic confinement fusion, principles of fusion power generation, fusion reactor and power plant components, the strategy for fusion development and how the experimental reactor ITER fits in.

Keywords: thermonuclear energy, fusion reaction, magnetic confinement, power generation

INTRODUCTION

In 2050 energy consumption could reach two or three times current consumption of energy sources. The fact that fossil fuels are running out, and that it is difficult to adapt renewable energy sources to centralized energy production that is capable of providing for densely populated areas or countries, make the development of new energy sources indispensable. These new forms of energy should obviously meet economic requirements but also take into account environment, operational safety and resource availability requirements. Energy from fusion meets all these requirements [4,5,6,7].

This paper describes the reasons for developing magnetic confinement fusion, principles of fusion power generation, fusion reactor and power plant components, the strategy for fusion development, and how the experimental reactor ITER fits in.

PRINCIPLES OF FUSION ENERGY

Fusion reactions

To obtain a fusion reaction, we must bring two nuclei sufficiently close together for them to repel each other, as they are both charged positively. A certain amount of energy is therefore vital to cross this barrier and arrive in the zone, extremely close to the nucleus, where there are the nuclear forces capable of getting the better of electrostatic repulsion [1].

In fusion, nuclei of light atoms are fused together (Fig. 1) to form a new element of slightly less mass. The “missing” mass is converted into energy, as predicted by Einstein’s famous formula, E=mc^2. The most attractive reaction involves the fusion of deuterium (D) and tritium (T) (which is obtained from lithium Li – see chemical equation 1) ions which releases 17.6 MeV in the form of a neutron at 14.1 MeV and a helium ion (alpha particle) at 3.5 MeV, with an energy gain ~ 500.

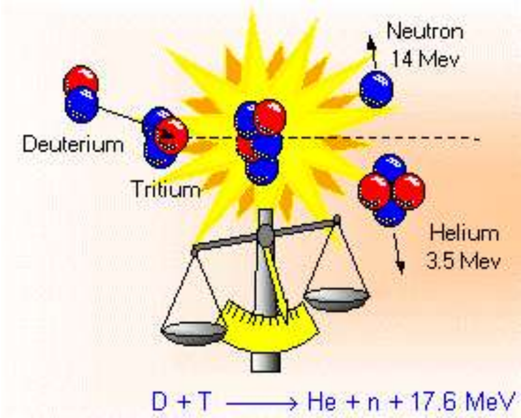

Fig. 1. Fusion of two light nuclei [9]

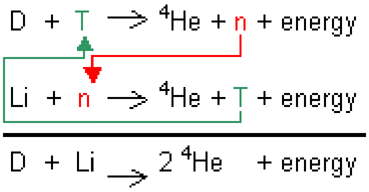

(1)

The temperatures required for thermonuclear fusion are greater than a hundred million degrees. At such temperatures, electrons are completely detached from the nucleus. The atom ionises and enters the fourth state of matter called a plasma.

For power production, the challenge is to produce a “burning plasma” where enough ions are confined at sufficient density and temperature such that the heat from the alpha particles can maintain the plasma without significant auxiliary heating power.

Magnetic confinement

In order for the fuel in the form of plasma to produce enough thermonuclear reaction, it must be maintained (or confined) in a limited volume and kept away from any structural material in order to maintain its high temperature. In the free state of plasma, the particles’ trajectory is random and the particles escape. As the plasma is made up of charged particles, the magnetic fields may act on them. If this same plasma is bathed in a rectilinear magnetic field, the particles wind around the field lines and will no longer touch the side walls. So as to avoid losses from the edges, we close off the magnetic bottle by creating a torus. The magnetic field thus created by a series of toroidal magnets surrounding the plasma is called a toroidal magnetic field (Fig. 2) [1,2,8].

However, confinement is not quite enough and to minimise particle leakage even more, the field lines must be helical. This is achieved by adding another magnetic field to the toroidal field, called a poloidal field, which is perpendicular to it. In a tokamak magnet configuration, the magnetic field created by an intense axial current flowing in the plasma itself, is added to the fields created by the assembly of coils.

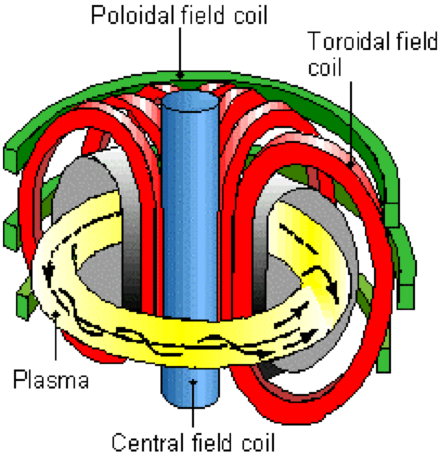

Fig. 2. Tokamak sssembly of coils producing three types of magnetic field [4,8]

Heating the plasma

In magnetically confined plasmas there are three main ways of heating the plasma (Fig. 3) [4,7,9]. The first is to use the strong electric current that is generated in the plasma (to help its stability and control) - this heats the plasma just like the current in a wire heats the wire. This current is very large (order of MA) and can heat the plasma to very high temperatures. However, to access the temperatures required for fusion to occur other methods are required. Powerful microwaves, injected in different frequency ranges (MHZ to GHz) can (under the right plasma conditions) give up their energy to the electrons or ions in the plasma and heat it up. Another method is to use very powerful neutral beams - these are beams of highly accelerated neutral atoms which are injected into the plasma and give up their energy as they undergo collisions with the background plasma ions.

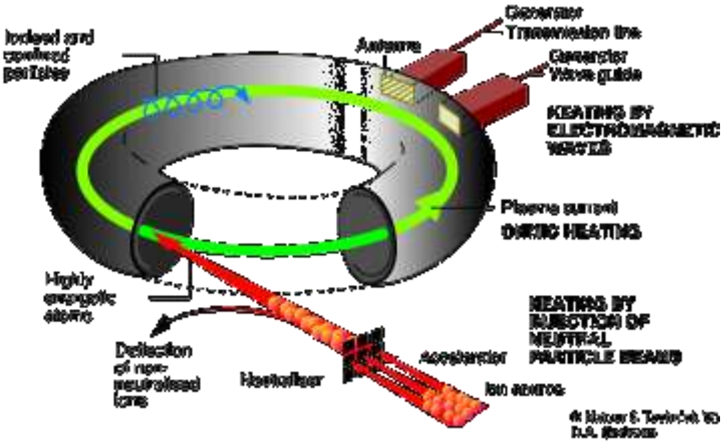

Fig. 3. Three main ways of heating the plasma [7,9]

The helium nuclei (alpha-particles) produced when deuterium and tritium fuse remain within the plasma's magnetic trap. Their energy continues to heat the plasma to keep the fusion reaction going. When the power from the alpha-particles is sufficient to maintain the plasma temperature, the reaction becomes self-heating (self-maintained) - a condition referred to as *ignition*. To obtain high performance plasma, it must meet three criteria: density, temperature and energy confinement time. They have been obtained independently in the various current experimental installations, like JT-60 (Japan), TFTR (Pronceton, USA), JET (Culham, UK) or Tore Supra (Cadarache, France). The main goal for the next international experimental machine (ITER) will be to demonstrate control of sustaned combustion of plasma over long periods [2,3,6].

FUSION REACTOR AND POWER PLANT

The components of the fusion reactor and power plant are shown in Fig. 4. The deuterium-tritium fuel mixture is injected (1) into a chamber, where, thanks to a system of confinement it goes into a plasma state and burns (2). In doing so, the reactor produces ash (helium atoms) and energy in the form of fast particles or radiation (3). The energy produced in the form of charged particles and radiation, is absorbed in a special component, the "first wall" which, as its name illustrates, is the first material element encountered by the plasma. The energy, which appears in the form of kinetic energy in neutrons, is, for its part, converted into heat in the breeding blanket (4), which is the element beyond the first wall, but nevertheless inside the vacuum chamber. The vacuum chamber itself is the component enclosing the area where the fusion reaction takes place. The first wall, blanket and vacuum chamber are obviously cooled down by a heat extraction system. The heat is used to produce steam and supply a conventional turbine and alternator electricity producing system (5).

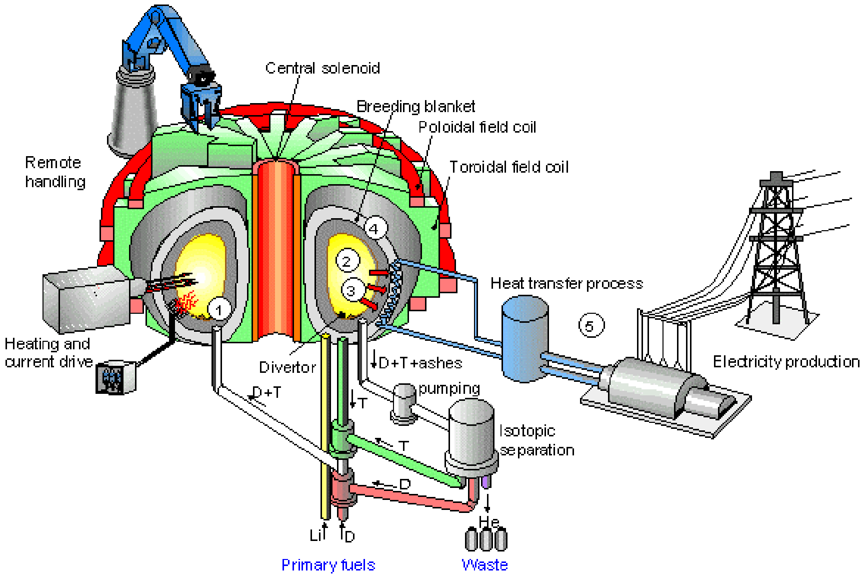

Fig. 4. Conceptual diagram of the thermonuclear power plant [7]

MAIN EXPERIMENTAL RESULTS AND CHALLENGES

One measure of the performance of a plasma is the ratio “Q” of fusion output power produced to auxiliary heating power input. A major step was achieved in the early 1990’s when fusion devices achieved Q ~ 1 conditions referred to as “breakeven”, where the fusion power production reached the level of heating power input. Three devices entered this domain, namely the Tokamak Fusion Test Reactor (TFTR) in Princeton, the Joint European Torus (JET) in England, and the Japanese Tokamak 60 m3 (JT-60) in Japan. For example, the TFTR succeeded in producing controlled D-T reactions yielding pulses of ~ 10 MW of fusion power lasting for a few seconds at a time. The TFTR, JET, and JT-60 machines were the result of ~ $0.5B investments made by each of the host countries in the late 70’s, as public interest in energy R&D reached a peak [2,3,6].

The next major step in the program is to enter the burning plasma domain where the alpha particle power begins to surpass the auxiliary power. Since the alpha energy is roughly 1/5 of the energy released per D-T reaction, and since Q is defined as the ratio of fusion power to heating power, the alpha particle heating becomes dominant when Q>5.

The design and construction of a burning plasma fusion machine is a major scientific and engineering challenge. The device itself will be of the same scale as a large electric power generating station with a cost ~ $5.0B. The scale of such an endeavor, the tradition of collaboration between nations in fusion research, along with the vital implications for the future of mankind all suggest an international project – ITER.

ITER – THE NEXT STEP IN FUSION RESEARCH

The International Thermonuclear Experimental Reactor (ITER) is designed to demonstrate the scientific and technological feasibility of fusion energy for peaceful purposes. Following on from today's largest fusion experiments worldwide, ITER aims to provide the know-how to build subsequently the first electricity-generating power station based on magnetic confinement of high temperature plasma - in other words, to capture and use the power of the sun on earth [4,7,9].

ITER will test all the main new features needed for that device - high-temperature-tolerant components, large-scale reliable superconducting magnets, fuel-breeding blankets using high temperature coolants suitable for efficient electricity generation, and safe remote handling and disposal of all irradiated components. ITER's operating conditions are close to those that will be experienced in a power reactor, and will show how they can be optimized, and how hardware design margins can be reduced to control cost.

The next major fusion project is the International Thermonuclear Experimental Reactor (ITER). The idea of ITER was born as an initiative at the 1985 Geneva Summit between the US and the USSR. President Reagan and General Secretary Gorbachev began a process that led to a collaboration among the European Union, Japan, Russia (initially the Soviet Union) and the US, to design and carry out the supporting research and development for ITER, whose programmatic objective is “to demonstrate the scientific and technological feasibility of fusion energy for peaceful purposes”.

The project of ITER began in 1985 and now it is as a collaboration between the USA, Europe (through EURATOM), Japan, the Russian Federation, the People's Republic of China and the Republic of Korea and India. Conceptual and engineering design phases led to an acceptable detailed design in 2001, underpinned by $650 M worth of research and development by the "ITER Parties" to establish its practical feasibility. The project is expected to cost ~$10 billion over its complete life. Recently (in June 2005), Tore Supra

Centre in Cadarache (France) has been selected as the site of the ITER experiment, which operation is expected to begin 10 years later and will last over the following 20 years.

ADVANTAGES AND DRAWBACKS OF FUSION ENERGY

Fusion is quite another form of nuclear energy. It includes all the advantages of "conventional" nuclear power (energy density and no operating pollution) while at the same time aiming at the reduction and even the elimination of its drawbacks (no long term waste, intrinsic safety and abundant fuel) – see Table 1.

Table 1. Advantages and drawbacks opf fusion energy [4,5,6,7]

Advantages	Drawbacks
• Suitable for large scale energy production • Intrinsic safety (no risk of runaway reaction) • Fuel abundant (available worldwide) - deuterium and lithium (to produce tritium) available for thousands or millions of years • No pollution nor release of greenhouse gases (CO, CO2) and no acid rain (SO2, NO2) • Short life radioactivity (associated with plant activation) • Fuel cycle inside the reactor, no need for transport of activated materials	• Feasibility remains to be proven • Concerns the long term (2050) • High investment cost · • Complex technology

CONCLUSIONS

Controlled thermonuclear fusion has the potential to open a new primary energy source to mankind. It has many advantages that has no other energy source. Fusion power engineering is a powerful contribution to a peaceful world.

Constructing and operating ITER is the essential step to determining whether magnetic confinement of plasma can be usefully employed by humankind for centralised electricity generation in the latter half of this century.

REFERENCES

[1] Wesson J., *The Science of JET*, Culham Science Centre, Abingdon, UK 2000

[2] Green B. J., Huguet M., The ITER Project: Status and Prospects, *IEEE Trans. on Magnetics*, vol. 32, no. 4, 1996, 2224-2229

[3] Baker Ch. C., Montgomery B., ITER - A World Class Challenge and Opportunity, *IEEE Trans. on Applied Superconductivity*, vol. 5, no. 2, June 1995, 61-68

[4] ITER website: www.iter.org

[5] Iternational Atomic Energy Agency website: www.iaea.org

[6] International Energy Agency website: www.iea.org

[7] European Fusion Development Agreement website: www.efda.org

[8] European Fusion Development Agreement (EFDA-JET) http://www.jet.efda.org/

[9] Fusion – power for future generations, CD-ROM, EFDA, Association EURATOM – FOM 2004

5th International Conference **ELMECO**
Nałęczów, Poland
September 2005

MECHANICAL CONNECTIONS OF SUPERCONDUCTING SYSTEM OF ELEMENTS IN CRYOGENIC TEMPERATURES

H.Malinowski, V.M.Drobin, V.V.Seleznev, G.P.Tsvineva, Yu.A.Shishov, V.I.Datskov,

Electrotechnical Institute, Warsaw, POLAND
malin@eltecol.pol.lublin.pl
JINR, LHE, Dubna, RUSSIA

Keywords: superconducting magnet;

INTRODUCTION

In centers of superconducting cooling of electromagnets that have contact cooling of winding, heat-conducting parts made of cooper or aluminum are used. Those connections enable easy separation of cooling system's elements.

The most important tasks are to:

- - provide infallibility of work
- - provide proper force of contact in conditions of multiplying cooling and heating provide good heat contact of elements which exchange energy

CONSTRUCTION OF BOLTED JOINT

The construction of bolted joint that are placed in electromagnetic system Decris-SC is showed on the pictures below.

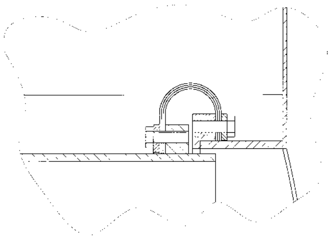

Fig. 1. Center of heat bridge of 40K screen with elastic connection of parts with usage of pure aluminum tapes

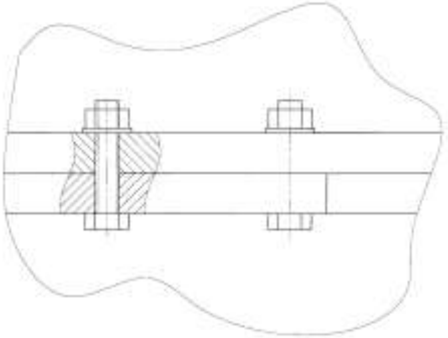

Fig. 2. Bolted connection of heat screen collars

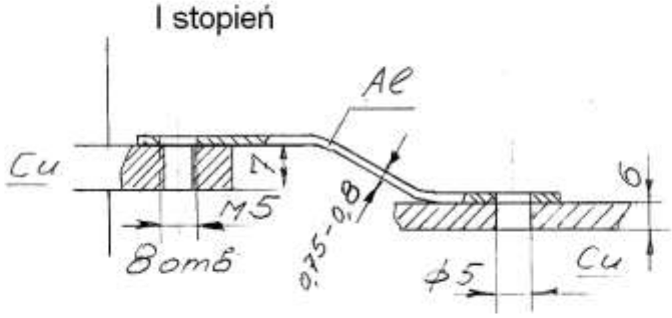

Fig.3. Center of connections in experimental cryostat of heat screen with collar of 1-st degree cryocooler.

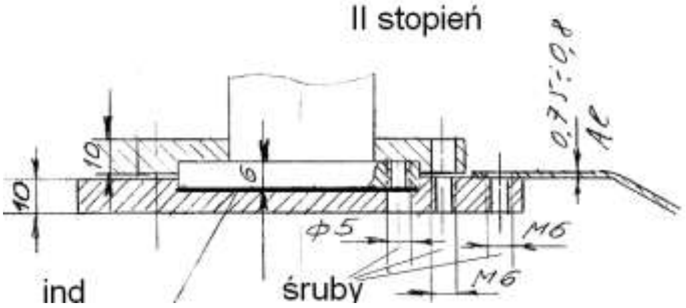

Fig. 4. Center of connections of 2-nd degree of cryocooler with solenoid in experimental cryostat.

INFLUENCE OF TEMPERATURE ON MECHANICAL AND HEAT PARAMETERS OF CONNECTIONS IN HEAT CENTER

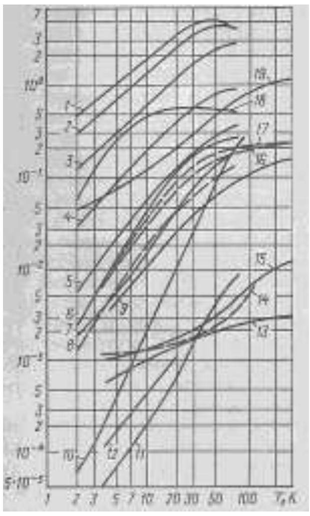

Fig.5. Temperature of dependences of heat conductivity for different materials

Difference in thermal expansion of materials used in heat center oblige to describe:

1) how shall the contact stress after cooling decrease

2) how to keep pressure by using compensation of thermal contraction differences of materials with application of washer made of material with small contraction for example invar

- it is needed to value thickness of the washer
- it is needed to value heat conductivity of such a connections contact

3) value of heat conductivity of the connections contacts

Those three issues have been examined

1;2-inner and outer cryostat vessel; 3-holder; 4-pipe

1-deoxidized cooper; 2-technical cooper; 4-duraluminum D16; 9-stainless steel; 18-solder 50%Pb50%Sn; 19-brass

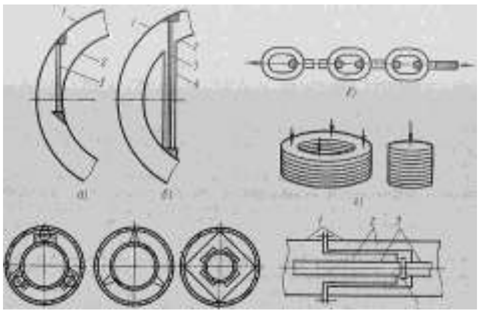

Fig. 6. The elements of thermal bridges for different materials

Heat conductivity of the bridges depends on: cross sections; length; thermal resistance of the contact. The elements are presented by the picture above.

ANALYSIS OF BOLTED CONNECTIONS

In considered bolted connections up to four metals are used:

bolt made of stainless steel
cooper plates
aluminum heat bridge
invar compensate washer

relative thermal shortening range of temperature 300K – 0K

$$\varepsilon = \frac{L_{300K} - L_{0K}}{L_{300K}}.$$

Difference of length that emerge from difference of thermal expansion

$$\Delta L_{\Sigma} = L_{st} \times \varepsilon_{st} - (L_{Cu} \times \varepsilon_{Cu} + L_{A\ell} \times \varepsilon_{A\ell} + L_i \times \varepsilon_i).$$

Relative elongation of bolt.

$$\varepsilon_{sr} = \frac{\Delta L_{\Sigma}}{L_{st}} = \frac{L_{st} \times \varepsilon_{st}}{L_{st}} - \frac{L_{Cu} \times \varepsilon_{Cu} + L_{A\ell} \times \varepsilon_{A\ell} + L_i \times \varepsilon_i}{L_{st}}.$$

Thickness of invar washer.

$$L_i = L_{st} - (L_{Cu} + L_{A\ell}).$$

$$\varepsilon_{sr} = \varepsilon_{st} - \frac{L_{Cu} \times \varepsilon_{Cu} + L_{A\ell} \times \varepsilon_{A\ell} + L_{st} \times \varepsilon_i - L_{Cu} \times \varepsilon_i - L_{A\ell} \times \varepsilon_i}{L_{нж}} =$$

$$= \varepsilon_{st} - \frac{L_{Cu} \times (\varepsilon_{Cu} - \varepsilon_i) + L_{A\ell} \times (\varepsilon_{A\ell} - \varepsilon_i) + L_{st} \times \varepsilon_i}{L_{st}}.$$

Relationship between endurance and tension in the material may be presented by Hook's law. $\varepsilon_{sr} = \dfrac{\sigma}{E}$,

RESULTS OF CALCULATIONS OF BOLT CONNECTIONS.

For brief fore design reduction of contact load may be limited by 30% value a = L_{Al} :L_{Cu}, when e_{sr}=0,3e[΄sr,] is a condition when force of contact load decries to 30%

$$0{,}3 \times [\varepsilon_{sr}] = \varepsilon_{st} - \frac{\varepsilon_{Cu} + \varepsilon_{A\ell} \times \alpha}{1 + \alpha},$$

$$(0{,}3 \times [\varepsilon_{sr}] - \varepsilon_{st}) \times (1 + \alpha) = -\varepsilon_{Cu} - \varepsilon_{A\ell} \times \alpha;$$

$$(0{,}3 \times [\varepsilon_{sr}] - \varepsilon_{st}) \times \alpha + \varepsilon_{A\ell} \times \alpha = -\varepsilon_{Cu} - 0{,}3 \times [\varepsilon_{sr}] + \varepsilon_{st};$$

$$\alpha = -\frac{\varepsilon_{st} - \varepsilon_{Cu} - 0{,}3 \times [\varepsilon_{sr}]}{\varepsilon_{st} - \varepsilon_{A\ell} - 0{,}3 \times [\varepsilon_{sr}]}.$$

Results of calculation for connections on DECRIS-SC
For

L_{Cu}=10mm, e_{Cu} =33,8´10-4;
L_{Al}=1 mm, e_{Al}.=44´10-4;   =5,3´10-4;
e_{st}=33,1´10-

4. $$L_{st} = \frac{10 \times (33{,}8 - 5{,}3) \times 10^{-4} + 1 \times (44 - 5{,}3) \times 10^{-4}}{(33{,}1 - 5{,}3) \times 10^{-4} - 8 \times 10^{-4}} = \frac{285 + 38{,}7}{19{,}8} = 16{,}3\,\text{mm}.$$

$$L_i = 16{,}3 - 10 - 1 = 5{,}3\,\text{mm}.$$

Obtain

$$\varepsilon_{sr} = 33{,}1 \times 10^{-4} - 33{,}8 \times 10^{-4} = -0{,}7 \times 10^{-4}.$$

Acceptable value of bolt relative deformation for preliminary tension is [e_{sr}]=8´10-4.

e_{sr}. temp : e[$_{sr}$]mech=0,7´10-4 : (8´10-4)=0,0875, - weakening of contact is acceptable

e_{sr}=33,1´10-4- 44´10-4= -10,9´10-4> e[$_{sr}$],For aluminum plates we can't use stainless steel bolts.

$$\varepsilon_{sr} = 33{,}1 \times 10^{-4} - \frac{33{,}8 \times 10^{-4} + 44 \times 10^{-4} \times 0{,}1}{1 + 0{,}1} = -1{,}6 \times 10^{-4} < 8 \times 10^{-4}.$$

$$\alpha = -\frac{33{,}1 \times 10^{-4} - 33{,}8 \times 10^{-4} - 0{,}3 \times 8 \times 10^{-4}}{33{,}1 \times 10^{-4} - 44 \times 10^{-4} - 0{,}3 \times 8 \times 10^{-4}} = \frac{3{,}1}{13{,}3} = 0{,}23,$$

At L_{Cu}= 10 mm L_{Al} =2,3 mm

CONTACT FORCE IN DECRIS-S.C. BOLT CONNECTIONS

Calculations have been made for 2-step cryocooler of heat power on 1st and 2nd step respectively: 40K with 30W and 4,2K in 1W.The difference of temperatures on connections DT=0,05 K in 4,2K and 0,5K in 40K.

Heat conductivity of the connection =lQ/DT; for 1st and 2nd step respectively 06=5,0/03=l WxK^{-1}. =l1,0/0=520 WxK^{1-} values of l of cooper contacts in force of

P=45 kG at 78 K (=l0,66 WxK^{-1}) и 4,2 K (=l1,9´10-2 WxK^{-1}).

total contact force on the 1-st step cryocooler's contact

$$P_{\Sigma} = P \times \frac{60}{0{,}66} = 45 \times \frac{60}{0{,}66} = 4090\,\text{kG}.$$

Total surface of cross - section bolts made of the stainless steel for]s[=1600 kG/cm2,

S=4090:1600=2,6 cm2

Total contact force on the 2-st step cryocooler's contact needed – It is too large contact load

$$P_{\Sigma} = 45 \times \frac{20}{1{,}9 \times 10^{-2}} = 47368\,\mathrm{kG}$$

Six M5 bolts of total cross-section surface f= 1,18 cm2 was settled on the 2nd degree collar of cryocooler. The maximum force on the bolts is

Small heat conductivity of cooper contacts in helium temperature obliges to pay special attention on bolt-connections construction. The increase of heat conductivity is possible by enlargement of number of the bolts and their diameter. In DECRIS-S.C. 2nd step collar has been enlarged and eighteen M8 bolts has been used, and that gave cross section of surface 6 cm^2

CONCLUSIONS

1) Method of valuing length of bolts and thickness of invar washer has been conceived
2) Compensatory invar washer may be omitted in bolt connections where thickness of aluminum is not larger than ¼ of cooper thickness. It is enough to clamp bolts to maximum permissible tension value.
3) Properly calculated (in sense of thickness) invar washer enable connections in relatively small forces of clamp bolts.
4) Small heat conductivity of cooper contacts in helium temperature demands special attention while constructing such a center. Covering places of contact with indium and use of proper number of bolts is also specially important.
5) Bolt connections which are used for the most loaded heat bridges of electromagnet DECRIS-SC must have their heat conductance controlled (experimental measurements).

LITERATURE

[1] R. Berman. Some Experiments on Thermal Contact at Low Temperatures. Journal of Applied Physics. Vol. 27, N 4, 1956, pp. 318-321.

[2] Справочник по физико-техническим основам криогеники. Энергоатомиздат, М., 1985, с. 99.

[3] Сосуды и аппараты. Норма и методы расчета на прочность. Госкомитет СССР по стандартам, М., 1980.

5th International Conference **ELMECO**
Nałęczów, Poland
September 2005

STABILIZATION OF ELECTROMAGNETS' SUPERCONDUCTING WINDINGS

H. Malinowski

Electrotechnical Institute, Warsaw, POLAND
E-mail:malin@eltecol.pol.lublin.pl

Keywords: multicharged ion source; superconducting magnet; cryocooler.

INTRODUCTION

Stability of winding in superconducting electromagnet is a basic criterion of its quality. It has direct influence on work and level of electromagnet's safety. The safety can be described by resistance on local changes of winding temperature.Value of destructive energy depends on heat conductivity of the conductor and the winding. It is inevitable to consider large anisotropy of heat conductivity of the winding. The greater stability of the winding is , the lesser is the number of its weak points. Every deformation of the winding, every discontinuity of the superconductor or even local increase of mechanic tension causes reduction of Ic current and it is the source of the weak points.It is crucial in HTS winding. For HTS tape these criterions are significant. Local binding or yield of the conductor causes significant reduction of winding's Ic current.

WINDING OF SUPERCONDUCTING ELECTROMAGNETS

Winding made of LTS conductor. Usually concentrated winding is used for LTS superconductors . This technology is simple

It enables the application of different actions to increase efficiency of heat flow in different directions of the winding. That's the way to gain stability of the winding. Winding made of HTS conductor is typically used as pancake windings. The most common application of HTS tape are pancake windings.

Because of close relation between critical current and yield radius or other deformations, pancakes winding is applied in HTS winding. It enables to limit deformation and to keep high value of Ic current.

In such winding a large anisotropy of heat conduction appears.

When the electromagnet is of large dimensions, such method of construction of the winding requires many soldering points connecting adjacent pancakes. Although the value of the connection's resistance is small, connection of the conductors with steel reinforced tape and large number of such connections result in significant value of total resistance.

Therefore high current value shall cause significant losses of energy in these connections. The larger the electromagnet radius is, the lesser the HTS tape deformation and Ic current reduction is. For concentrated winding, at certain value of the radius, reduction of Ic current for concentrated winding may occur lesser than the reduction caused by rise of temperature of the winding in point of soldering the pancakes elements. Because connection of pancakes in HTS electromagnet by soldering is obligate, resistance must appear on the connections. The manufacturer of the tape advises not to remove the steel reinforcement in point of soldering. Information from Brookhaven says that resistance on such connection has a value of 3,34 uOhm. It can be reduced by enlarging the number of connectors between the sections. Hopefully, the problem doesn't affect HTS electromagnet exploitation in nitrogen bath because of high value of evaporation heat of nitrogen and makes keeping such a winding in superconducting state easy.

Unfortunately, in temperatures below the nitrogen temperature, a problem of the winding's stability appears while cryocooler contact cooling. Local increase of temperature (in soldering point) shall cause limit of Ic current value in HTS conductor.

In such situation it is worth considering applying concentrated winding of HTS conductor. Reduction of Ic current caused by tape deformation cannot be higher than reduction of Ic current caused by temperature rising on the connections.

Results of measurement of resistance on solder connections of HTS tape is shown on fig 1.

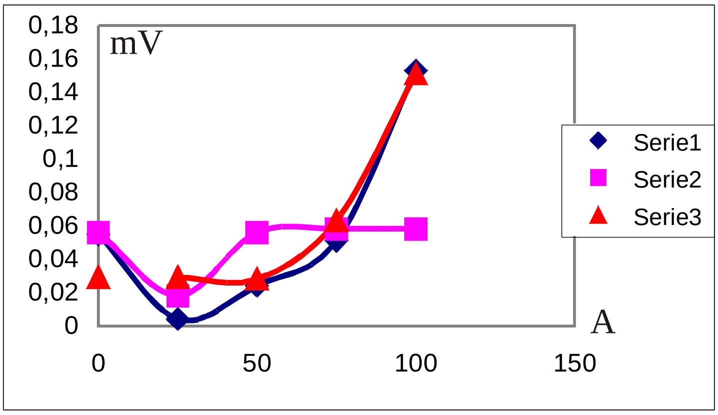

Fig. 1. Tape connected with solder on length between 1 and 2 cm
serie1(Sn 1cm); serie2(Sn 2cm); serie3(In 1cm) Measurement of voltage in mV

SCHEME OF CONCENTRATED WINDING

During concentrated winding of the HTS tape on the electromagnet, the tape is being deformed perpendicularly and parallel to its surface.

Degradation of current and the deformations of the tape diminish with rise of the winding radius.

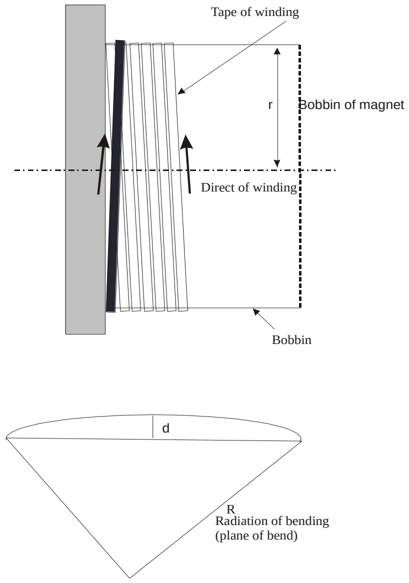

Fig. 2. Experimental stand for testing of HTS tape Ic in relation to size of deformations

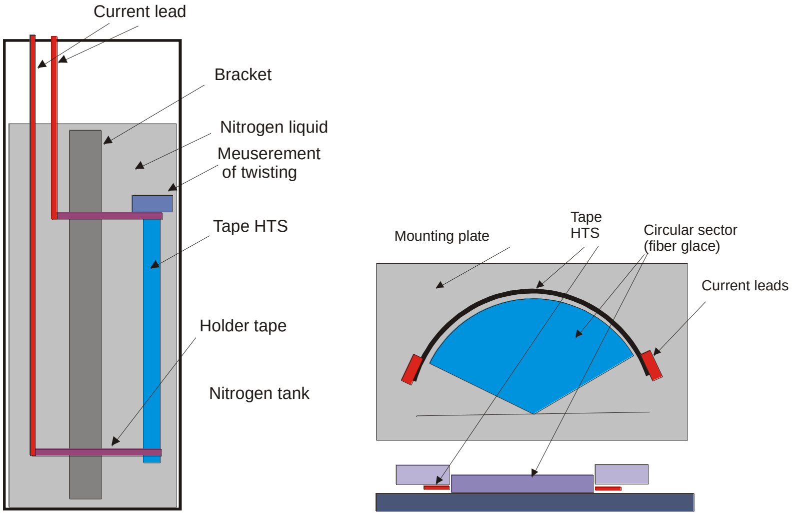

Fig. 2’. Scheme of stand for testing relation of Ic HTS tape of its twist value and its bending radius

Experimental testing of relation of critical current (Ic) of HTS tape to its twist value is shown on the fig. 3.

	twist	
	180 degree	360 degree
I [A]	U [mV]	U [mV]
0	5	2
10	2	2
20	0	1
30	1	1
35	5	1
40	4	1
50	5	1
90	5	4
100	6	9
110	6	17
115	8	27
120	16	41
125	24	64
130	44	119
135	80	163
140	126	249
145	216	391
150	356	639

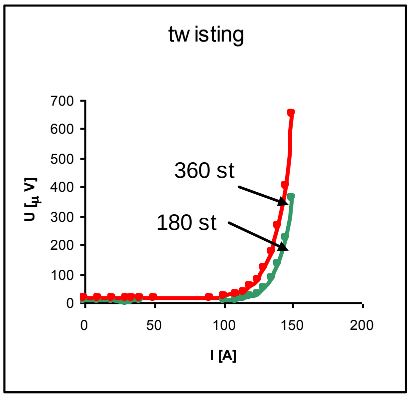

Fig. 3. Results of measurements for HTS tape of length 250 mm (thickness=0,3mm; width=4,1mm; Ic=125A)

Results of experimental testing of Ic of HTS tape in relation to value of its bending is shown on the fig 4 and table bellow.

	Without bending	With bending		After straightening
			repetition	
I [A]	U [mV]	U [mV]	U [mV]	U [mV]
0	9	8	1	9
10		9	2	9
20			8	9
30		10	15	19
35		15	20	28
40	8	21	30	38
45	8	35	40	53
50	9	50	52	68
55	9	65	70	90
60	8	85	85	112
65	9	112	115	142
70	8	148	150	182
75	8	190	194	230
80	9	250	254	300
85	10	310	309	370
90	9	401	395	468
95	9	450		
100	9	620	625	715
105	9	780		
110	10	970	950	1065
115	11	1150		
120	20	1400	1400	1500
125	40	1720	1690	1870
130	75			
135	120			

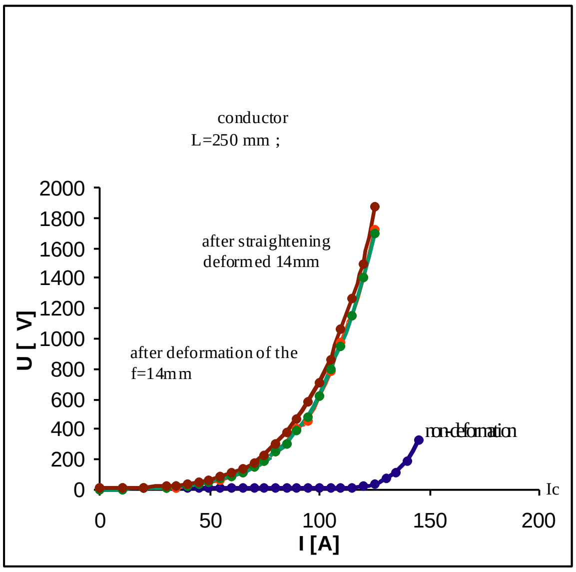

Fig.4. Results of Ic measurement for straight part of HTS tape and after its deformation.Length of HTS tape - 250 mm and width of 4,1 mm and the depth of bending f=14 mm. Description: blue – Ic without bending; green – bended tape; red – Ic after straightening

4. CONCLUSIONS

The manner of realization of HTS electromagnet winding depends on electromagnet radius and requires analysis of losses for each

A large number of connections between elements of the winding (greater number of pancakes), results in rising of total resistance of the winding and amount of heat generated there.

High quality of the connections and enlarged number of connectors for each section results in decrease of total resistance of the connections. Also kind of solder has an influence on the resistance.

In the analysis it is inevitable to take into account the efficiency of cooling down the winding (application of elements improving the cooling between pancakes, improves cooling of the winding, and that results in decrease of current density in it).

LITERATURE

[1] A.M.Archarow, W.P.Bieljakow, E.I.Mikulin, Kriogennye sistiemy. *Moskwa, Maszinostroenie*, 1987

[2] Pod redakcją M.P.Malkowa, Sprawochnik po fizykotechniczekim osnowam kriogeniki, *Moskwa, Energoatomizdat* 1985

[3] Katalog firmy CAN Superconductors, 1999 г

[4] I.A.Glebow, W.N.Szachtarin, J.F. Antonow. Problemy wwoda toka w swerhprowodnikowye ustrojstwa. Hauka, L, 1985, s. 47-50

5th International Conference **ELMECO**
Nałęczów, Poland
September 2005

CRYOCOOLED SUPERCONDUCTING MAGNET SYSTEMS FOR THE DECRIS-SC ION SOURCES

V.M.Drobin, V.V.Seleznev, G.P.Tsvineva, Yu.A.Shishov, V.I.Datskov, V.V.Bekhterev, S.L.Bogomolov, S.N.Dmitriev, A.A.Efremov, B.I.Iakovlev, H.Malinowski

JINR, LHE, Dubna, RUSSIA
JINR, FLNR, Dubna, RUSSIA
Electrotechnical Institute, Warsaw, POLAND
E-mail:malin@eltecol.pol.lublin.pl :

Abstract

Two superconducting magnet systems (SMS) for the ECR ion sources DECRIS-SC and DECRIS-SC2 were designed at the Joint Institute for Nuclear Research, Dubna, Russia. The first one was manufactured and successfully tested in 2004. The peculiarities of this system include the use of a GM cryocooler (1 W at 4.2 K) for the cryostabilization of the magnet and a special configuration of magnetic field required for the ion source. Four coils provide the magnetic field induction on the axes of the source of up to 3 T (the mirror ratio of approximately 6). Prepreg insulation is used for compounding of the magnet's windings which are indirectly cooled in the vacuum. A second SMS for ion source DECRIS-SC2 is currently being prepared. Due to the fact, that the microwave frequency of 14 GHz will be used for ECR plasma heating, the minimum of magnetic field in this region should be in order of 0.4 T. The maximum field on the axes are equal to the values of 1.9 T and 1.4 T in injection and extraction site respectively. The required axial magnetic field is created by a set of four solenoid coils with the inner diameter of 234 mm. The cryostat vacuum vessel will be made from carbon steel and will act as the system's magnetic shield.

Keywords: multicharged ion source; superconducting magnet; cryocooler.

INTRODUCTION

In 2004 a superconducting Electron Cyclotron Resonance Ion Source (Kr^{15+}, Xe^{23+}) DECRIS-SC1 was built and made operational at the Joint Institute for Nuclear Research. High demands for the charge and the intensity of accelerated beams made it necessary to increase the magnetic field of the ion source (up to 3 T).

The main parameters of the magnet are shown in Table 1. The windings are located on a stainless steel former. A copper thermal shield and former are suspended in the vacuum vessel with the help of fiber glass supports. Cryo-stabilization is carried out by a Gifford-MacMahon (GM) cryocooler with 1 W of power at a temperature of 4.2 K. HTS rods are used in the current leads. Passive magnet quench protection is made by using winding sectioning and shunting these sections with cold diodes and resistors. This is complemented by an active quench protection system using normal zone detectors and heaters.

The development phase for the subsequent magnet for the DECRIS-SC2 ion source is now complete. The magnet construction generally resembles the DECRIS-SC1 magnet but at the same time the induction and aperture parameters are decreased and the magnet is more compact. The winding former construction, current leads and cold mass supports are also modified from the previous system.

DECRIS-SC1 MAGNET

Magnet Construction

The magnet (Fig. 1) consists of four coaxial solenoids, the parameters of which are shown in Table 1. The outer solenoids are connected sequentially within the current supply circuit, the internal solenoids have independent power supply and the central solenoid is connected in the opposite direction from the others. The axial component of the magnetic field forms a saddle “trap” for ions. The solenoids 1 are located on a non-magnetic stainless steel former 2, which is free-floating in the vacuum vessel 7 on fibre-glass supports 6. The vacuum vessel 7 is surrounded by the magnetic shield 8. The magnet assembly is protected by the reflective aluminum shield 15 and copper shield 4 cooled from the 1st stage of the cryocooler 10. The copper shield is covered with vacuum multi-layer super-insulation 4.

The former and windings are linked with the 2nd stage of the cryocooler using a thermal conducting linkage 11 from high purity aluminum. Copper plates are screwed to the former containing “cold” diodes 12 and dump resistors 13. The thermal screen is fastened to supports 6. Six HTS current leads 9 are located around the cryocooler head.

The preliminary pumping out of the vacuum vessel is performed by roughing and turbo-molecular pumps 14.

Table 1. Main parameters of magnets DECRIS-SC1/DECRIS-SC2

The name	Unit measures	Value			
No. of sol.		1	2	3	4
ID	mm	281234	280234	280 234	281 234
OD	mm	397 304	396 304	396 304	350 290
Length	mm	80 49	81 56	50 14	80 45,5
Nom. dc	A	60/75			
dc density	A/mm^2	118 152	120 152	119 149	115 152
Bmax on axis	T	2,06 3,0	3,0 3,4	2,8 3,2	0,56 1,5
Inductance	H	33,6 5,02	33,6 6,07	12,2 0,53	11,4 2,62
Stored energy	KJ	60,5 14,1	60,5 17,1	22 1,5	20,5 7,4
Cold Mass	Kg	~ 280 / ~80			

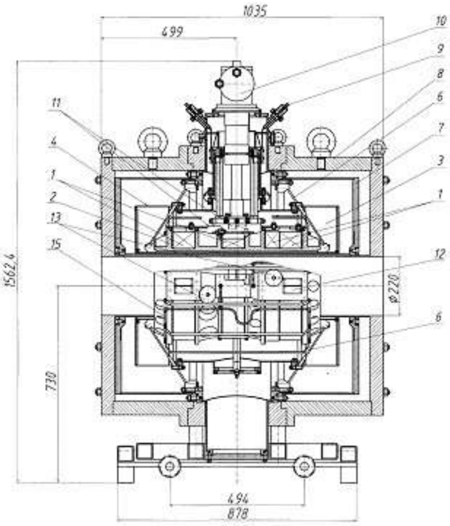

Fig. 1. The scheme of the DECRIS-SC1 magnet (longitudinal section)

Superconducting solenoids

Outokumpu superconducting wire with a diameter of 0.65 mm (0.7 mm insulated) is used for windings, with 6438 filaments (4.7 mkm diameter) and the ratio Cu/NbTi is of 1.9:1. The windings are impregnated using a prepreg glassfibre/epoxy insulation. Aluminum thermal strips are glued to the exterior surface of the windings under a bandage. Each winding is electrically split into 2 or 3 sections which are bridged by "cold" diodes and resistors.

The reserve of the temperature stability has the value of 2.3 K and allows this magnet to operate with increased heat loads.

Electrical power supply and protection of a magnet

The magnet protection system (Fig. 2) contains three normal zone detectors, "cold" diodes, dump resistors and eight resistive heaters installed on the windings. Detectors have a bridging scheme for voltage measurements. The signal from the detectors pass through an amplitude-time analyzer and amplifier and are then passed to a system which controls the disconnection of the power supply from the electrical system and switches on the power supply to the heaters.

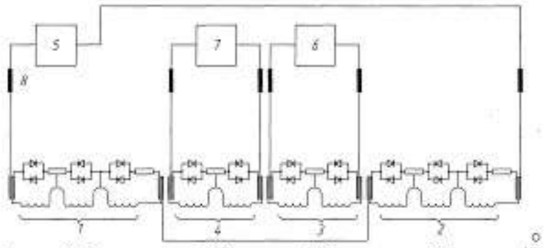

Fig. 2. The electrical circuit for power supply and protection of solenoids:
1,2,3.4 - superconducting solenoids; 5,6,7 - power sources; 8 – HTS section of the current lead; H1,H2 - heaters of 25 Ohm

At 4 K the “cold” diode opens at a voltage of ~ 7 V and allows the winding section to be shunted by resistor of 1 Ohm. The simultaneous heating of all the windings allows the system to avoid any possibility of excessive attractive forces between the suspended magnet assembly and the external magnetic yoke. In the absence of such protection, the forces could exceed one ton and result in the failure of the magnet suspension system.

Current leads

The current leads are produced by CAN [1] and consist of copper braids and a tubular HTS-conductor. Thermal anchors are constructed from foil-laminated insulation material.

Cold mass support

The magnet windings and their former are held in the vacuum vessel with the help of a fibre-glass support system. The copper thermal shield is also hung from the same supports. The supports themselves consist of fibre-glass plates to which are attached copper strips which act as thermal anchors connected by flexible braid to the thermal shield.

The supports are designed to not only bear the weight of the cold mass but also to handle significant axial dynamic forces which can arise from unequal transitions of the windings during a quench.

The supports are tested for durability using an axial load of 1.27 tonne and a radial load of 0.32 tonne.

Monitoring and control

The control of the power supplies to the magnet coils and status monitoring of the entire superconducting system is carried out by a PC. 16 individual temperature sensors are located at strategic points throughout the cold magnet and former assembly, most of which are intended for analysis of complex operations during the testing of the magnet. For long-term monitoring during maintenance only 4-5 sensor readings are required. Calibrated TVO resistors [2] are used as thermometers.

Results of testing

The cooling-down time of the magnet was approximately 120 hours.

During operation the temperatures T1-T6 do not exceed 4 K. It has been determined experimentally that the reserve cryocooler capacity is approximately 0.5 W. The windings 3 and 4 have been tested to a current of 60 A. A current of 45 A was run in all windings simultaneously following adjustment of the protection system. There were no aberrations during normal operation which allowed us to conclude that this magnet system was in good operational condition.

To the present time the ion source magnet DECRIS-SC1 is in maintenance for more than 7000 hours without any operational issues. During this period of time a few planned warm-ups to room temperature and subsequent cooldowns were conducted.

DECRIS-SC2 MAGNET

In 2005 an ion irradiation source DECRIS-CS2 was designed and developed. The main specifications of this magnet are introduced in Table 1. The most significant differences from DECRIS-CS1 magnet are as the following:

- Inductions on the axes of the magnet and the diameter of the aperture have been reduced.
- The vacuum vessel is produced from 08 steel and simultaneously acts as a magnetic shield.
- For support of the cold mass fibre-glass rods are used.

- The quench protection consists of an improved passive part and simplified active part (one block of normal zone detection and 8 heaters in the magnet windings).
- The current leads contain the section with high temperature superconductor tape;
- Windings are split into the sections;
- Cold diodes are used only as protection for the HTS tapes in current leads;
- In the thermal links tapes of high purity aluminium and copper are used.

The magnet construction is introduced in Fig. 3. The power supply scheme is similar to DECRIS-SC1 system and contains 3 current sources. The windings are self-protected as their temperature after a full quench transition is 40-50K and the maximum temperature of the "hottest" point does not exceed ~120K.

For a more homogeneous winding transition into the normal condition additional thermal conductors are used made of pure aluminium.

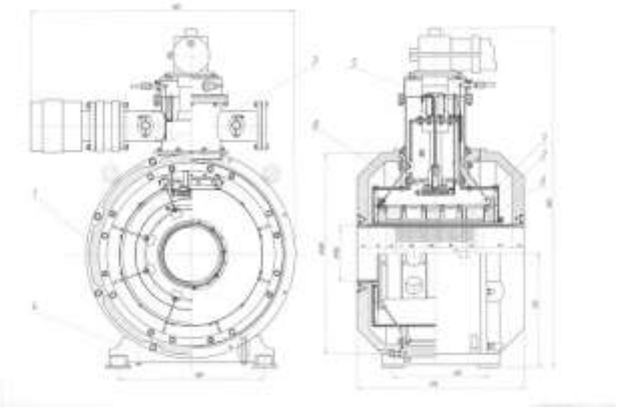

Fig.3. The scheme of the DECRIS-SC2 magnet (longitudinal section)

CONCLUSION

DECRIS-SC1 magnet:

1. Common heat loads are close to estimated values for the DECRIS-SC1 magnet. Total heat load is approximately 0.5 W, thus the temperatures of windings and current leads are optimal.
2. The design of a flexible thermal link between the magnet's elements and the second stage of the cryocooler has been resolved by the use of high purity aluminum.
3. The compensation of the forces in the windings has been successfully resolved and the design of a reliable support system for the magnet assembly has been realized.
4. The quench protection scheme consists of passive protection by means of coil sectioning, diodes and resistors in addition to active protection using a single normal zone detector and a system of coil heaters.

LITERATURE

[1] Catalog of the corporation CAN Superconductors, 1999.

[2] Datskov V.I. Characteristics of Russian carbon resistance (TVO) cryogenic thermometers. In: Proc. ICEC15, Genova, Italy, 1994, p.425-28.